Higher Order Asymptotic Inference in Remote Sensing of Oceanic and Planetary Environments

by

Ioannis Bertsatos

M.Eng., Cambridge University (2002)
B.A., Cambridge University (2002)

Submitted to the Department of Ocean Engineering
in partial fulfillment of the requirements for the degree of

Doctor of Philosophy

at the

MASSACHUSETTS INSTITUTE OF TECHNOLOGY

June 2010

Author .....
Department of Ocean Engineering
May 7, 2010

Certified by .....
Nicholas C. Makris
Professor of Mechanical and Ocean Engineering
Thesis Supervisor

Accepted by .....
David E. Hardt
Chairman, Graduate Committee

Higher Order Asymptotic Inference in Remote Sensing of Oceanic and Planetary Environments

by

Ioannis Bertsatos

Submitted to the Department of Ocean Engineering
on May 7, 2010, in partial fulfillment of the
requirements for the degree of
Doctor of Philosophy

Abstract

An inference method based on higher order asymptotic expansions of the bias and covariance of the Maximum Likelihood Estimate (MLE) is used to investigate the accuracy of parameter estimates obtained from remote sensing measurements in oceanic and planetary environments. We consider the problems of (1) planetary terrain surface slope estimation, (2) Lambertian surface orientation and albedo resolution and (3) passive source localization in a fluctuating waveguide containing random internal waves. In these and other applications, measurements are typically corrupted by signal-independent ambient noise, as well as signal-dependent noise arising from fluctuations in the propagation medium, relative motion between source and receiver, scattering from rough surfaces, propagation through random inhomogeneities, and source incoherence. We provide a methodology for incorporating such uncertainties, quantifying their effects and ensuring that statistical biases and errors meet desired thresholds.

The method employed here was developed by Naftali and Makris[84] to determine necessary conditions on sample size or Signal to Noise Ratio (SNR) to obtain estimates that attain minimum variance, the Cramer-Rao Lower Bound (CRLB), as well as practical design thresholds. These conditions are derived by first expanding the bias and covariance of the MLE in inverse orders of sample size or SNR, where the first-order covariance term is the CRLB. The necessary sample sizes and SNRs are then computed by requiring that (i) the first-order bias and second-order covariance terms are much smaller than the true parameter value and the CRLB, respectively, and (ii) the CRLB falls within desired error thresholds. Analytical expressions have been derived for the asymptotic orders of the bias and covariance of the MLE obtained from general complex Gaussian vectors,[68, 109] which can then be used in many practical problems since (i) data distributions can often be assumed to be Gaussian by virtue of the central limit theorem, and (ii) they allow for both the mean and variance of the measurement to be functions of the estimation parameters, as is the case in the presence of signal-dependent noise.

In the first part of this thesis, we investigate the problem of planetary terrain

surface slope estimation from satellite images. For this case, we consider the probability distribution of the measured photo count of natural sunlight through a Charge-Coupled Device (CCD) and also include small-scale albedo fluctuation and atmospheric haze, besides signal-dependent (or camera shot) noise and signal-independent (or camera read) noise. We determine the theoretically exact biases and errors inherent in photoclinometric surface slope and show when they may be approximated by asymptotic expressions for sufficiently high sample size. We then determine the sample sizes necessary to yield surface slope estimates that have tolerable errors. We show how small-scale albedo variability often dominates biases and errors, which may become an order of magnitude larger than surface slopes when surface reflectance has a weak dependence on surface tilt.

The method described above is also used to determine the errors of Lambertian surface orientation and albedo estimates obtained from remote multi-static acoustic, optical, radar or laser measurements of fluctuating radiance. Such measurements are typically corrupted by signal-dependent noise, known as speckle, which arises from complex Gaussian field fluctuations. We find that single-sample orientation estimates have biases and errors that vary dramatically depending on illumination direction measurement diversity due to the signal-dependent nature of speckle noise and the nonlinear relationship between surface orientation, illumination direction and fluctuating radiance. We also provide the sample sizes necessary to obtain surface orientation and albedo estimates that attain desired error thresholds.

Next, we consider the problem of source localization in a fluctuating ocean waveguide containing random internal waves. Propagation through such a fluctuating environment leads to both the mean and covariance of the received acoustic field being parameter-dependent, which is typically the case in practice. We again make use of the new expression for the second-order covariance of the multivariate Gaussian MLE,[68] which allows us to take advantage of the parameter dependence in both the mean and the variance to obtain more accurate estimates. The degradation in localization accuracy due to scattering by internal waves is quantified by computing the asymptotic biases and variances of source localization estimates. We show that the sample sizes and SNRs necessary to attain practical localization thresholds can become prohibitively large compared to a static waveguide. The results presented here can be used to quantify the effects of environmental uncertainties on passive source localization techniques, such as matched-field processing (MFP) and focalization.

Finally, a method is developed for simultaneously estimating the instantaneous mean velocity and position of a group of randomly moving targets as well as the respective standard deviations across the group by Doppler analysis of acoustic remote sensing measurements in free space and in a stratified ocean waveguide. It is shown that the variance of the field scattered from the swarm typically dominates the range-velocity ambiguity function, but cross-spectral coherence remains and enables high resolution Doppler velocity and position estimation. It is shown that if pseudo-random signals are used, the mean and variance of the swarms' velocity and position can be expressed in terms of the first two moments of the measured range-velocity ambiguity function. This is shown analytically for free space and with Monte-Carlo simulations for an ocean waveguide. It is shown that these expressions can be used to obtain

accurate, with less than 10% error, of a large swarm's instantaneous velocity and position means and standard deviations for long-range remote sensing applications.

Thesis Supervisor: Nicholas C. Makris
Title: Professor of Mechanical and Ocean Engineering

Acknowledgments

I would like to thank my advisor, Prof. Nicholas Makris for his continuing support and motivation throughout the years. Perhaps the greatest benefit of working in the Laboratory for Undersea Remote Sensing has been my experience of his work ethic and sense of perfectionism, which I hope to emulate in the future.

I would also like to thank the members of my thesis committee. Prof. Peter Dahl at the Applied Physics Laboratory of the University of Washington, Prof. Michele Zanolin of Embry-Riddle Aeronautical University, and Prof. Purnima Ratilal of Northeastern University. I was fortunate to interact closely with both Prof. Zanolin and Prof. Purnima early in my graduate career, and I have benefited immensely from these experiences.

Financial support for this work has been provided by Prof. Makris via funds from the ONR Graduate Traineeship Award, and I would like to thank Dr. Ellen Livingston at ONR for her support.

This work would not have been possible without the day to day camaraderie and help of my many colleagues in LURS and the Acoustics Groups at MIT and Northeastern. I would like to thank Yisan Lai, Sunwoong Lee, Joshua Wilson, Tianrun Chen, Deanelle Symonds, Srinivasan Jagannathan, Hadi Tavakoli Nia, Ankita Jain, Anamaria Ignisca, Costas Pelekanakis, Derya Akkaynak, Ninos Donabed, Saomitro Gupta, Mark Andrews, Roger Gong, Ameya Galinde, and Kevin Cockrell. I reserve special thanks for Sunwoong, Dee and Srini who have very kindly put up with my antics for the longest time and have been amazing friends both at and outside of MIT. Srini was also extremely kind to proofread through most of this document and his resilience has been inspiring. I would also like to thank Geoff Fox and of course Leslie Regan, whose administrative help and support has made life at MIT significantly more bearable.

After almost eight years in Cambridge and Boston, there have been a multitude of people, from the most common acquaintances to the closest friends, who have had an impact on my life. These have truly been formative years and I owe a lot

of who I have grown to be today to my friends. Time is short and I am bound to forget one or two people who I hope will forgive me beforehands. I am grateful to Iason, Yannis, Konstantinos, Dimitris, Vasilis, Panayiotis, Olga, Spiros, Alex, Jacob, Ali, Dee, Johnna, Tufool, Shawn, Josh, Justin, Valeria, Augusto, Danny, Yanir, Tim, Laura, Adlar, Costas, Kostas, Nikolas, Ruben, Ioannis, Stella, George, George, Nikolaos. I would also like to thank the whole Sidney-Pacific community and my adopted family, Roger and Dottie Mark. Special thanks to the extended Greek community of Boston. Finally, I would like to recognize the contribution of my friends back in Greece, Kostis, Alex, Markos, Dimitris, Leonidas, Yannis and Giorgos.

It goes without saying that I am forever grateful to my 'old' and 'new' family. My two brothers who I love and care for dearly, Angelos and Konstantinos, and my grandparents. Magdalena, everyday I am reminded how fortunate I am to have you in my life, and everyday my love for you grows. To my parents Ourania and Konstantinos, all I can say is that everything I am and have accomplished in my life, all has been thanks to you.

Contents

List of Figures

List of Tables

Chapter 1

Introduction

In remote sensing applications, parameter estimation often requires the nonlinear inversion of measured data that are randomized by additive signal-independent ambient noise, as well as signal-dependent noise arising from fluctuations in the propagation medium, relative motion between source and receiver, scattering from rough surfaces, propagation through random inhomogeneities, and source incoherence. Parameter estimates obtained from such nonlinear inversions are typically biased and do not attain desired experimental error thresholds. Further, additional errors can easily ensue if both the mean and covariance of the measurement are parameter dependent and this dependence is neglected in either by inappropriately modeling the random measured field as either (i) a deterministic signal vector, or (ii) a fully randomized signal vector with zero mean, both embedded in additive white noise. These approximations are in fact typically employed in ocean acoustic inversions, spectral and radar detection, localization problems, and statistical optics.[104, 49, 30]

For these reasons, a method has been developed for determining necessary conditions on the sample sizes or Signal to Noise Ratios (SNRs) to obtain accurate parameter estimates and aid experimental design.[84] The method is based on asymptotic expansions for the bias and covariance of maximum likelihood estimates (MLEs) in inverse orders of sample size or SNR, where the first-order covariance term is the minimum variance, the Cramer-Rao Lower Bound (CRLB) (see Appendix B). Analytical expressions are provided for the asymptotic orders of the bias and covariance of

MLEs obtained from general complex Gaussian data vectors, which can then be used in many practical problems since (i) data distributions can often be assumed to be Gaussian by virtue of the central limit theorem, and (ii) they allow for *both* the mean and the variance of the measurement to be functions of the estimation parameters, as is the case in the presence of signal-dependent noise.

This approach is based on classical estimation theory,[44, 60] and has already been applied in a variety of problems, including time-delay and Doppler shift estimation,[84] source localization in a deterministic ocean waveguide,[102] pattern recognition in 2-D images,[11] and geoacoustic parameter inversion.[110] All previous applications, however, were chosen so that only the mean or the covariance of the measurement would be parameter dependent, but not both. These are special cases of the problems considered here where signal-dependent noise is typically present: (1) planetary terrain photoclinometric surface slope estimation, (2) Lambertian surface orientation and albedo resolution, and (3) passive source localization in a fluctuating waveguide containing random internal waves.

In planetary terrain surface slope estimation, photoclinometry is typically employed to derive high-resolution elevation maps.[76, 81, 62, 93] For this problem, besides signal-independent (or camera read) noise and signal-dependent (or camera shot) noise, we also incorporate errors due to uncertainties in surface albedo and atmospheric haze. We show that in many practical photoclinometric scenarios the approximate asymptotic biases and errors for a single sample differ dramatically from the exact ones, making asymptotic expressions for errors applicable only when a large number of independent samples is available.

Acoustic, optical, radar and laser images of remote surfaces are typically corrupted by signal-dependent noise known as speckle.[27, 48, 49, 86, 71] Surface orientation and albedo estimates obtained from measurements of fluctuating radiance corrupted by speckle noise are often biased and do not attain minimum variance. The biases and errors of surface and orientation estimates are found to vary signicantly with illumination direction and measurement diversity. This work expands upon work presented by Makris at the SACLANT 1997 conference[73], as well as unpublished

notes of Makris from the Naval Research Laboratory (NRL).

For passive source localization in an ocean waveguide, scattering by internal waves may result in the incoherent intensity or variance of the acoustic field dominating. The ensuing loss of intermodal coherence in the forward propagating field leads to a degradation in the accuracy of localization estimates.[21, 4, 3] We quantify the effect of internal waves on the asymptotic biases and variances of source localization estimates and show that the sample sizes and SNRs necessary to attain practical localization error thresholds can become prohibitively large compared to a static waveguide. The results presented here can be used to quantify the effects of environmental uncertainties on passive source localization techniques, such as matched-field processing (MFP) and focalization,[24] both of which typically utilize line arrays and CW signals.

Finally, we develop a method for estimating the first- and second-order velocity and position statistics of underwater target aggregations, such as groups of Autonomous Underwater Vehicles (AUVs) and fish schools, imaged using a long-range (tens of kilometers), remote sensing system. These estimates are based on analytical expressions for the magnitude squared of the range-velocity ambiguity function for the acoustic field scattered from such target groups. We show that in free space the first two moments of the ambiguity function along constant range and velocity axes are linearly related to the first two moments of the targets' velocity and position given appropriate signal design. We then demonstrate using illustrative examples that in a waveguide it is still possible to obtain such estimates of the velocity and position standard deviations, which can then be used to provide a means for target discimination and classification.

Chapter 2

Statistical Biases and Errors Inherent in Photoclinometric Surface Slope Estimation with Natural Light

2.1 Introduction

High-resolution elevation maps of planetary terrain are typically obtained by the method of photoclinometry [76, 81, 62, 93], which relates variations in surface radiance to variations in surface orientation relative to the light source, typically the Sun, and the optical receiver, typically on a spacecraft [29, 83, 61]. While other methods also exist to produce topographic models, including stereogrammetry and radar altimetry, photoclinometry offers significant advantages since it (1) requires only a single image, and (2) can provide higher resolution measurements [83].

It has been observed, however, that photoclinometry may not work very well under certain lighting conditions that provide little topographic contrast, and that these conditions typically correspond to small incidence angles [28, 36, 57, 61, 62]. Uncertainties in surface albedo may also lead to errors in surface slope estimates

that are significant for small-scale albedo variations [54, 62], but become relatively insignificant for large-scale albedo variations [12].

The primary purpose of the present paper is to provide a formulation of uncertainties and analysis of errors that (1) is consistent with the behavior of the likelihood function [44] of the photoclinometric surface slope estimate that governs the uncertainties, and (2) accounts for all the primary photoclinometric error sources, including albedo, haze, camera read noise and camera shot noise, in a unified manner. Here, classical estimation theory [44, 60] is used to provide a method for determining both the exact and asymptotic biases and errors inherent in a Maximum Likelihood Estimate (MLE) of photoclinometric surface slope given the probability distribution of the measured Charge-Coupled Device (CCD) data and the nonlinear physical model relating the measured CCD data to surface slope by planetary surface reflectance [83]. The formulation also provides bounds on the minimum possible error for any unbiased photoclinometric estimate of surface slope as well as necessary conditions on sample size to attain this error bound, or a desired design threshold on error. The asymptotic biases and errors are determined by series expansion in inverse orders of sample size, where higher order terms vanish in decreasing order as uncertainty decreases until the Cramer-Rao Lower Bound (CRLB) or first-order error term is attained [84]. Since approximations to investigate photoclinometric errors [28, 36, 57, 12, 61, 62] have previously not been formulated in terms of the likelihood function that governs uncertainties, error bounds, asymptotic behavior for decreasing uncertainty, necessary sample sizes, and exact theoretical biases and variances have not been previously provided. We show that in many practical photoclinometric scenarios the approximate asymptotic biases and errors for a single sample differ dramatically from the exact ones, making asymptotic expressions for errors applicable only when a large number of independent samples is available. Moreover, the asymptotic expressions for errors must be formulated in terms of the likelihood function as in Refs. [95, 5, 80, 84] for them to properly converge as uncertainty decreases or sample size increases.

In Section 4.2 we derive the likelihood function, the MLE and biases and errors for photoclinometric surface estimation. The MLE is chosen because it is known to

become asymptotically unbiased and attain the minimum possible mean square error of any unbiased estimate as sample size becomes large or uncertainty becomes small [89, 44]. In Section 4.3 we compute the exact theoretical biases and root mean square errors of the surface slope MLE for various photometric functions and typical values of camera read noise, camera shot noise, atmospheric haze, and albedo variability. We show that the biases and root mean square errors grow rapidly when the dependence of measured intensity on surface slope approaches a constant, and that albedo variability is typically the dominant source of biases and errors. We also present estimation methods for minimizing these biases and errors to obtain surface slope estimates that fall within desired design error thresholds.

2.2 The Likelihood Function and Maximum Likelihood Estimation of Planetary Surface Slopes

In photoclinometry, natural light from a thermal source, such as the Sun or a star, typically acts as the source of planetary surface illumination. Natural light is known to undergo Circular Complex Gaussian Random (CCGR) field fluctuations and exponentially distributed instantaneous intensity fluctuations, as a consequence of the central limit theorem [49]. Spacecraft observations of planetary surfaces are typically made with photon-counting CCD cameras [77, 81], where the number of detected photons is known to follow the conditional Poisson probability distribution for a given average light intensity. Since the average intensity of natural light follows a Gamma distribution, conditional integration over all possible intensities leads to the negative binomial distribution for the photocount [49].

Photocount is related to planetary surface orientation by modeling the reflectance properties of the planetary surface with a photometric function. Many planetary surfaces have been successfully modeled with one or a combination of a such closed-form empirical functions, including Lambert's law, Minnaert's law, and the lunar-Lambert model [83].

In this section, we discuss three common photometric functions used to model planetary surface reflectance. We then use classical estimation theory to derive the likelihood function and MLE for photometric surface slope estimation, the theoretical lower bound on surface slope error, and necessary conditions on sample size to appropriately constrain biases and errors within desired design error thresholds.

2.2.1 Photometric Functions of Planetary Surface Reflectance

The most commonly used photometric function in planetary topography applications is the lunar-Lambert function first introduced in Ref. [82],

$$I(\mu_n, \mu_{0n}, \alpha) = Bo(\alpha) \left[\frac{2L(\alpha)\mu_{0n}}{\mu_n + \mu_{0n}} + (1 - L(\alpha))\mu_{0n} \right] \tag{2.1}$$

where $I(\mu_n, \mu_{0n}, \alpha)$ is the reflectance function, $\mu_n = \cos\epsilon_n$, $\mu_{0n} = \cos\iota_n$, and ϵ_n, ι_n are the emission and incidence angles respectively, as shown in Fig. 2-1. The phase angle α corresponds to the angle between the incidence and emission angles, and $Bo(\alpha) = I(1, 1, \alpha)$ is defined as the intrinsic albedo. $L(\alpha)$ is the ratio of the lunar to the Lambertian component in the lunar-Lambert function, so that in the limit $L(\alpha) \to 0$ the modeled surface is Lambertian, while in the limit $L(\alpha) \to 1$, the surface is lunar. The photometric function is the ratio of the intensity incident at angle ι_n to that reflected to the receiver at emission angle ϵ_n.

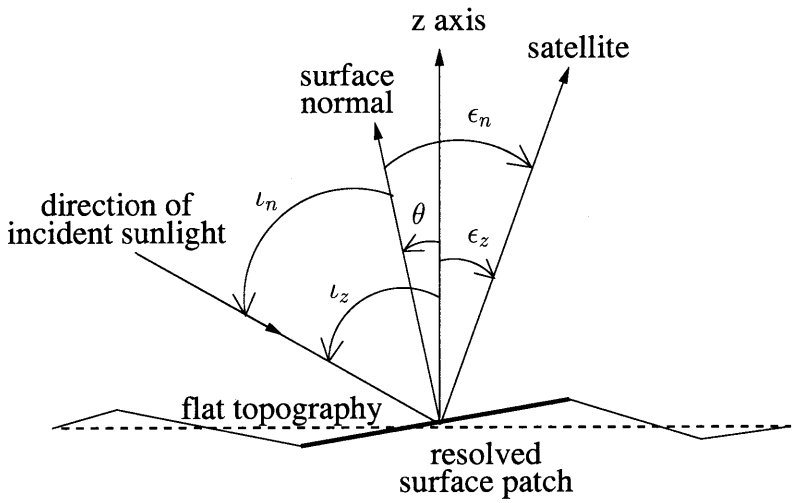

Figure 2-1: Resolved surface element with slope θ to flat topography. The slope, or tilt θ is the angle suspended between the z-axis and the surface normal, measured counter-clockwise. All other angles are measured counter-clockwise from the z-axis or the surface normal direction, as indicated by subscript z or n respectively. The true incident angle is equal to the angle between the z-axis and the incident direction, ι_z, minus surface slope, θ, or $\iota_n = \iota_z - \theta$. Similarly, the true emission angle is equal to the angle between the z-axis and the emission direction, ϵ_z, minus surface slope, θ, or $\epsilon_n = \epsilon_z - \theta$. Specular reflection occurs when $\epsilon_n = -\iota_n$. Given known angles ι_z and ϵ_z, photoclinometry can be used to obtain an estimate of the unknown surface slope θ.

For many planetary surfaces and phase angles, $L(\alpha)$ can be well approximated as a constant L, especially when observations are made over a limited range of incidence angles. Ref. [12], for example, shows that variations in L for Martian terrain lead to small errors of 10% of the $L = 0.55$ mean for Mars Orbiter Camera (MOC) [77] incident angles in the vicinity of 25-45°. Similarly, the effect of large-scale albedo variations, i.e. changes in the value of $Bo(\alpha)$ across the planetary terrain, can be minimized by scaling out the average brightness of the imaged region [12]. Small-scale variations in albedo cannot be similarly accounted for and may lead to much larger errors [54, 62, 12]. Here we model $Bo(\alpha)$ as a Gaussian random variable based on a central limit theorem assumption of many independent sources of albedo variation. The mean is set to the average albedo value across the imaged region and the standard deviation is defined as proportional to a fraction of the mean following calculations presented in Ref. [6] for typical Martian surfaces.

The illumination and zenith direction vectors define the principal plane [88]. It is common in planetary applications for satellite cameras to be close to nadir-looking, so that the difference between the emission angle and its projection on the principal plane is negligible. Assuming that local surface slopes are always in the up- or down-sun direction, which is also the direction where reflectance is most sensitive to slope changes for a Lambertian surface or small emission angles in the lunar-Lambert model of Eq. 2.1 [12, 62], the emission and incidence angles can then be written in terms of slope θ with respect to a flat surface, $\epsilon_n = \epsilon_z - \theta$ and $\iota_n = \iota_z - \theta$. Here ι_z and ϵ_z are defined as the known angles that the incident and emission directions make to the zenith direction, respectively.

With these assumptions, the photometric function can be written as

$$I(\mu_n, \mu_{0n}, \alpha) \equiv I(\theta) = Bof(\theta), \tag{2.2}$$

where

$$f(\theta) = \left[L \frac{\cos(\iota_z - \theta)}{\cos\left(\frac{\iota_z + \epsilon_z}{2} - \theta\right) \cos\left(\frac{\iota_z - \epsilon_z}{2}\right)} + (1 - L)\cos(\iota_z - \theta) \right] \tag{2.3}$$

Surface slope θ can be estimated from knowledge of $I(\theta)$. While surface slopes will be underestimated if their azimuth does not lie in the principal plane, this error is found to be negligibly small for relatively flat topography, as are errors introduced when the satellite viewing direction is off the principal plane [12].

Equation 2.3 is plotted as a function of surface slope θ and incident angle with respect to flat topography ι_z for the parameter L set to 0, 1, and 0.55 in Figs. 2-2(a), 2-3, and 2-4(a), respectively. The case $L = 0.55$ is shown here as an appropriate choice for Martian terrain [12]. For other planetary bodies, Ref. [83] provides best-fit $L(\alpha)$ values for various terrain types. The angle of emission with respect to the z-axis is assumed to be $\epsilon_z \approx 0^o$, which is equivalent to the typical case of a nadir-looking satellite, so that the true emission angle is $\epsilon_n = -\theta$. In all three figures, white dashed lines highlight where the derivative of I with respect to θ is zero so that the dependence of the CCD measurement on surface slope is constant. White dot-dashed lines correspond to the direction of specular reflection, which in this case occurs when $\iota_n = -\epsilon_n = \theta$, or equivalently $\iota_z = \iota_n + \theta = 2\theta$. Finally, black lines denote lines of constant true incidence angle, ι_n, which are described by the equation $\iota_z = \theta + \iota_n$, so that their slope and y-intercept are 1 and ι_n, respectively.

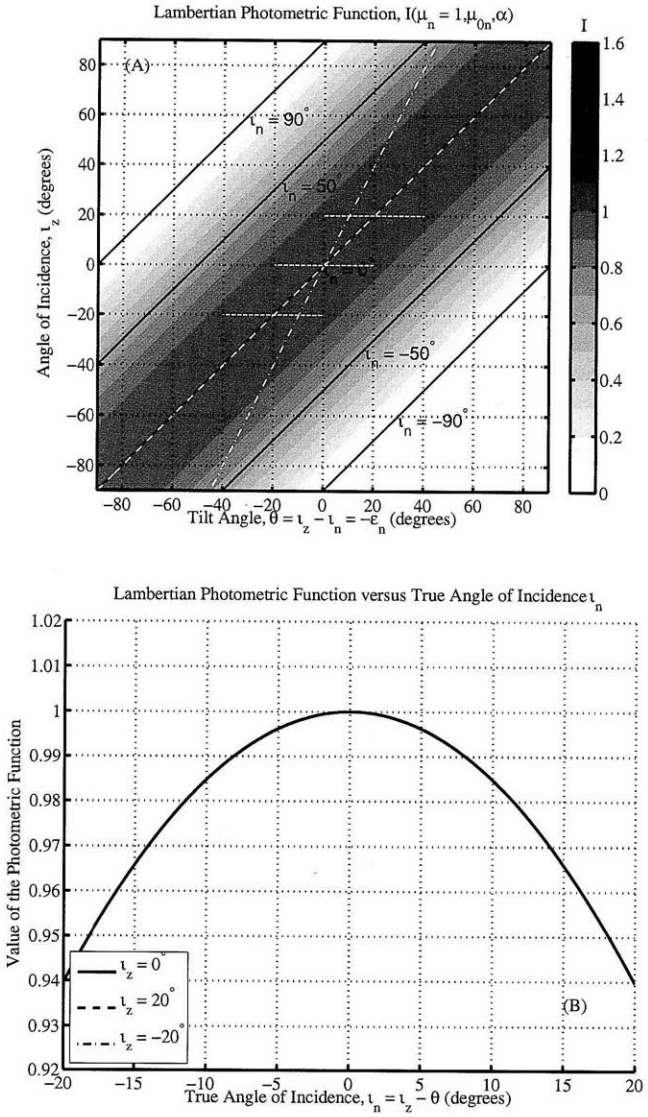

Figure 2-2: Lambertian photometric function given constant albedo, Eq. 2.3 using $L = 0$. (a) 3D representation of the value of Eq. 2.3 for $L = 0$ as a function of surface slope θ, which is the parameter to be estimated, and incident angle with respect to flat topography ι_z. The emission angle ϵ_z is assumed to be zero so that the satellite is nadir-looking. The black lines correspond to lines of constant true incident angle, $\iota_n = \iota_z - \theta$. The regions beyond the $|\iota_n| = 90°$ lines correspond to incidence on the 'back' of the surface patch, so that nothing is reflected towards the receiver and $I = 0$. Superimposed on the plot is the curve along which the derivative of I with respect to θ is zero (white dashed line). Also shown is the line that corresponds to specular reflection, $\epsilon_n = -\iota_n$ (white dot-dashed line). The plot can also be interpreted as a sheared and rotated version of the plot of I versus true incident and emission angle, ι_n and ϵ_n respectively. (b) Three cuts along constant values of incident angle to flat topography, ι_z, for the same photometric function. Each curve is obtained by cutting along the corresponding white dotted line in Fig. 2-2(a) from right to left.

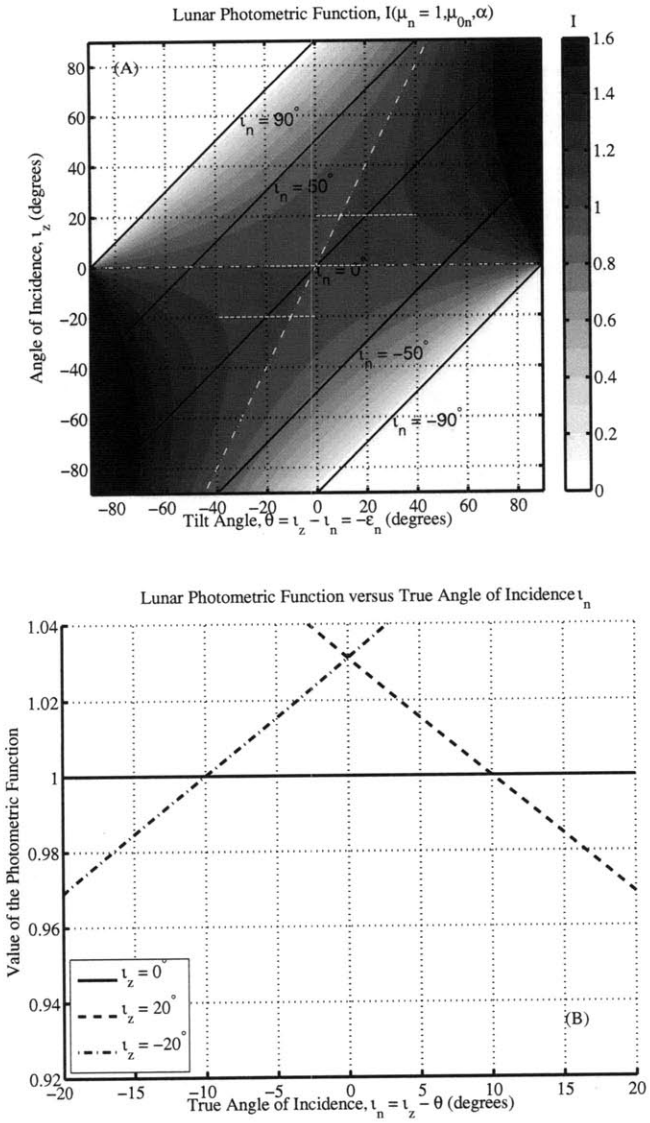

Figure 2-3: The same as Fig. 2-2 for the lunar photometric function given constant albedo, Eq. 2.3 using $L = 1$.

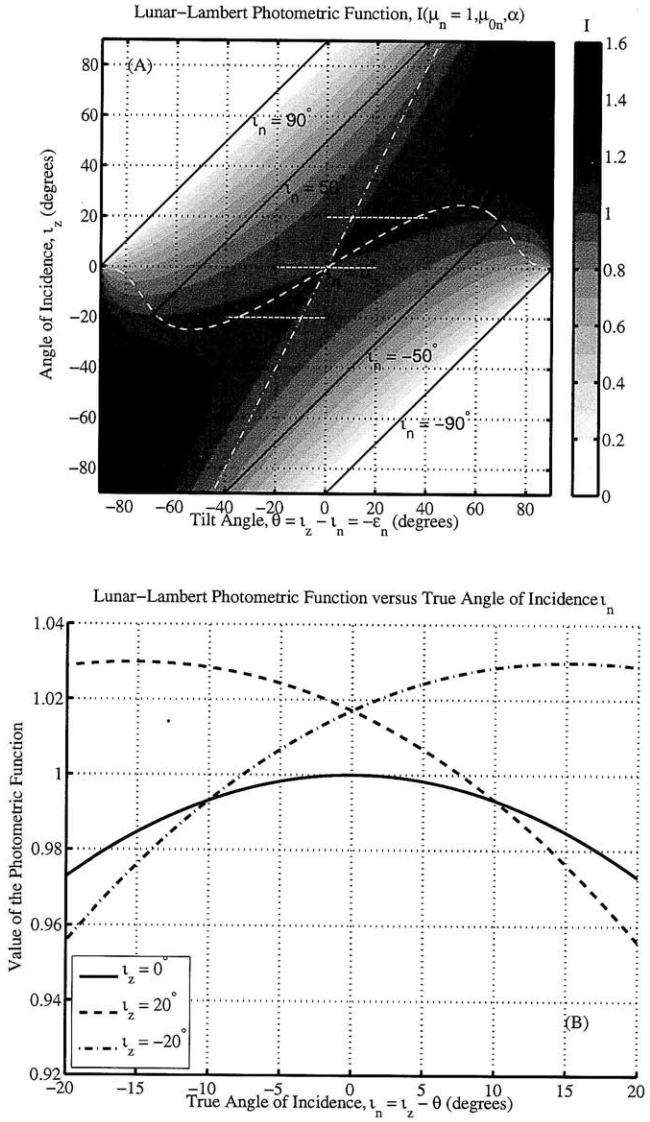

Figure 2-4: The same as Fig. 2-2 for the lunar-Lambert photometric function given constant albedo, Eq. 2.3 using $L = 0.55$, which is a typical value when modeling the reflectance of Martian terrain.

The Lambertian photometric function of Eqs. 2.2-2.3 for $L = 0$ is symmetric about the line where the true incidence angle ι_n equals zero, which is also where $\mathrm{d}I/\mathrm{d}\theta$ is zero, as a consequence of Lambert's cosine law, and as can be seen in Fig. 2-2(a). The lunar photometric function of Eqs. 2.2-2.3 for $L = 1$ is instead antisymmetric about the direction of specular reflection, while its derivative with respect to surface slope goes to zero when the incident and emission directions become collinear, as can be seen in Fig. 2-3(a). For the lunar-Lambert photometric function of Eqs. 2.2-2.3 for $L = 0.55$, the $\mathrm{d}I/\mathrm{d}\theta = 0$ curve (white dashed line) is close to the $\iota_n = 0$ line for small tilt angles θ, while it gradually moves towards the $\iota_z = 0$ line as θ increases, as can be seen in Fig. 2-4(a). For the Martian example of $L = 0.55$, and for small tilt angles, the lunar-Lambert surface then approaches Lambert's cosine law, but becomes similar to a lunar surface as the surface slopes become larger.

The Lambertian, lunar and lunar-Lambert photometric functions are also plotted as functions of the true incidence angle $\iota_n = \iota_z - \theta$, for different values of the angle between the illumination direction and the zenith direction, ι_z, in Figs. 2-2(b)-2-4(b). These plots are constructed by cutting along the white dotted lines of Figs. 2-2(a)-2-4(a) from right to left. Again, we note that the Lambertian photometric function depends only on the value of the true incidence angle ι_n, while the lunar photometric function becomes independent of surface slope when the incident and emission directions are collinear.

2.2.2 The Probability Distribution of CCD Photocount Measurements of Planetary Surface Reflectance

Charge-Coupled Devices (CCDs) typically form the basic recording unit of the high-performance cameras used for space exploration missions [77, 81] by measuring the number of electrons released from a photosurface when an electromagnetic field is incident upon it. This number is linearly proportional to the number of incident photons, which in turn is a function of the average light intensity incident on the photosurface [56], so that the CCD output signal can be parameterized in terms of

average intensity.

Natural light from thermal sources, such as the Sun, is known to follow Circular Complex Gaussian Random (CCGR) field fluctuations by the central limit theorem, so that average intensity is described by the Gamma distribution [49]. Since the number of photon arrivals for a given light intensity is known to be a Poisson random variable, the statistics of CCD-measured photocount then follow the negative binomial distribution [49]. For thermal light at optical frequencies, and for the common integration times of CCDs [77], the discrete negative binomial distribution can be well approximated by the continuous Gaussian probability density (see Appendix C),

$$P_K(K|\theta) = \frac{1}{\sqrt{2\pi}\sigma_K(\theta)} \exp\left(-\frac{1}{2}\left[\frac{K-\overline{K}(\theta)}{\sigma_K(\theta)}\right]^2\right) \tag{2.4}$$

where K is the measured photocount.

The mean and variance of K have been derived in Appendix C (Eqs. C.19, C.20) and are repeated here for convenience

$$\overline{K} = \gamma[I(\theta)+H] = \gamma[\overline{Bo}f(\theta)+H], \tag{2.5}$$

$$\sigma_K^2 = \overline{K} + \overline{K}^2\sigma_{Bo}^2/\overline{Bo}^2 + \sigma_R^2 \tag{2.6}$$

where γ is a known proportionality constant that depends on incident solar flux, camera integration time, pixel surface area and other parameters as described in Eq. C.5, $\overline{Bo}$, σ_{Bo}^2 are the mean and variance of surface albedo, respectively, and H is the expected intensity of atmospheric haze which is assumed to be a known constant [12]. Atmospheric haze is described by a CCGR field that is independent and additive to the CCGR field scattered from the surface which carries reflectance information. The variances or expected intensities of these two fields then add, so that the haze contribution increases the mean and variance of the photocount K. This leads to a dilution of surface reflectance information in the total photocount. Atmospheric haze often contributes minimally to topographic shading [12]. Ref. [63] provides a model for how haze is affected by changes in atmospheric conditions and illumination

geometry.

The photocount variance then has *signal-independent* components due to camera read noise σ_R^2 [56], and atmospheric haze $\sigma_{haze}^2 \equiv \gamma H$, and *signal-dependent* components $\gamma \overline{Bo} f(\theta)$ for shot noise and $\overline{K}^2 \sigma_{Bo}^2 / \overline{Bo}^2$ for albedo uncertainty. The signal-dependent components arise from the Poisson nature of photon statistics, the CCGR fluctuations of the incident field, and the multiplicative dependence of the photometric function on albedo. By defining the Signal to Noise Ratio (SNR) of $K - \gamma H$, or a sample mean of n independent and identically distributed measurements of $K - \gamma H$, as the ratio of the squared mean to variance, SNR is proportional to sample size n. It also becomes large as the mean photocount becomes large and the standard deviation of albedo becomes small compared to the mean albedo.

2.2.3 Maximum Likelihood Estimation

The likelihood function for an estimate of θ is defined as $P_{\mathbf{K}}(\mathbf{K}|\theta)$ evaluated at the measured values of $\mathbf{K}$, where $P_{\mathbf{K}}(\mathbf{K}|\theta)$ is the conditional probability distribution of a data vector $\mathbf{K}$ of independent and identically distributed photocount measurements $K_1, K_2, K_3, \ldots, K_n$ obeying Eqs. 2.4 through 2.6 given surface slope parameter θ. Measurements of random photocount, in the vector $\mathbf{K}$, then contain information about surface slope θ through both the mean and variance of the photocount via Eqs 2.1- 2.6. The MLE $\widehat{\theta}$ is defined as the surface slope that maximizes the likelihood function with respect to θ [89, 44]. The Cramer-Rao Lower Bound (CRLB) is the minimum mean square error attainable by any unbiased estimate, regardless of the method of estimation. The CRLB i^{-1} is the inverse the Fisher information, also known as the expected information, which is defined as $i = \langle l_1^2 \rangle$, where $l(\mathbf{K}|\theta) = \ln P_{\mathbf{K}}(\mathbf{K}|\theta)$ is the log-likelihood function, and $l_j = \frac{\partial^j l(K|\theta)}{\partial \theta^j}$.

If the sample size n is sufficiently large, or uncertainty is sufficiently small, the MLE $\widehat{\theta}$ is *asymptotically* unbiased and obeys the Gaussian distribution

$$P_{\widehat{\theta}}(\widehat{\theta}|\theta) = \sqrt{\frac{i}{2\pi}} \exp\left(-\frac{i}{2}(\widehat{\theta} - \theta)^2\right) \tag{2.7}$$

with variance i^{-1} equal to the CRLB [89, 60], where [70, 71]

$$\begin{aligned} i &= n\left(\frac{1}{\sigma_K^2}\left(\frac{\partial\overline{K}}{\partial\theta}\right)^2 + \frac{1}{2}\left(\frac{\partial\ln(\sigma_K^2)}{\partial\theta}\right)^2\right) \\ &= \frac{n}{\sigma_K^2}\left(\frac{\partial\overline{K}}{\partial\theta}\right)^2\left(1+\frac{1}{2\sigma_K^2}\left[1+2\overline{K}\frac{\sigma_{Bo}^2}{\overline{Bo}^2}\right]^2\right) \end{aligned} \tag{2.8}$$

given the probability distribution for K described in Eq. 2.4-2.6 and Appendix C, Eq. C.18. In the deterministic limit $n \to \infty$, where K is obtained from exhaustive sample averages, $P_{\widehat{\theta}}(\widehat{\theta}|\theta)$ becomes the delta function $\delta(\widehat{\theta}-\theta)$.

In photoclinometry, surface slope estimates are obtained from single images, so the sample size is actually $n = 1$ and the MLE often will be biased and not attain minimum variance. The necessary sample sizes for the MLE to become effectively unbiased and have a Mean Square Error (MSE) that *asymptotically* attains the CRLB are derived in Appendix A.2 and appear in Eqs. A.6b-A.6a. For convenience, we define the necessary minimum sample size, n_b, to obtain an unbiased MLE by conservatively requiring that the first-order bias b_1 (Eq. B.14) be 10 times smaller than the true value of the parameter,

$$n_b = 10\frac{|b_1(\widehat{\theta}|\theta)|}{|\theta|} \tag{2.9}$$

Similarly, the necessary minimum sample size, n_v, for the MSE of an unbiased estimate to attain the CRLB is defined by requiring that the second-order variance var_2 (Eq. B.16) be 10 times smaller than the CRLB,

$$n_v = 10\frac{|var_2(\widehat{\theta}|\theta)|}{var_1(\widehat{\theta}|\theta)} \tag{2.10}$$

where $var_1 = i^{-1}$ is the CRLB (Eq. B.15). In the asymptotic limit as uncertainty decreases, the conditions in Eqs. 2.9-2.10 can also be interpreted in terms of the SNR necessary to obtain an unbiased MLE that attains the CRLB.

2.3 Results and Discussion

In this section we calculate the exact theoretical biases and errors of photoclinometric surface slope estimates for photometric functions following Lambert's law, Minnaert's law, the lunar-Lambert model, for a typical Martian surface imaging scenario (see Appendix C) using the statistical formulation of Section 2.2.3 and the Appendices.

To calculate the exact theoretical bias and Root Mean Square Error (RMSE) of a MLE surface slope estimate $\widehat{\theta}$ it is useful to observe that for $\overline{K} = g(\theta)$ and $\theta = g^{-1}(\overline{K})$, it follows that $\widehat{\theta} = g^{-1}(\widehat{\overline{K}})$ by invariance of the MLE [60] where $\widehat{\overline{K}} = K$ is the MLE of the mean photocount $\overline{K}$. The bias and RMSE of $\widehat{\theta}$ are then given by

$$\text{bias}(\widehat{\theta}) = \theta - \langle\widehat{\theta}\rangle \tag{2.11}$$

$$\text{RMSE}(\widehat{\theta}) = \sqrt{\text{bias}^2(\widehat{\theta}) + \text{var}(\widehat{\theta})} \tag{2.12}$$

where

$$\langle\widehat{\theta}\rangle = \int_0^\infty g^{-1}(K) P_K(K|\theta) \mathrm{d}K \tag{2.13}$$

$$\text{var}(\widehat{\theta}) = \int_0^\infty \left(g^{-1}(K) - \langle\widehat{\theta}\rangle\right)^2 P_K(K|\theta) \mathrm{d}K \tag{2.14}$$

for the conditional probability distribution defined in Eqs. 2.4 through 2.6. The exact theoretical bias and RMSE are calculated using Eqs. 2.11-2.14 for the combined effects of all variance terms in Eq. 2.6 assuming $\sigma_R^2 \approx 6400$ electrons, $\overline{K} \approx O(10^4)$ electrons, $\sigma_{haze}^2 \approx 2000$ electrons, and $\sigma_{Bo} = 0.1 \times \overline{Bo}$ as discussed in Appendix C. Results are shown as a function of the incident angle with respect to the zenith direction, ι_z, and true surface slope θ in Figs. 2-5-2-7.

Both the bias and RMSE of the surface slope estimate increase significantly in the region where the first derivative of I with respect to θ goes to zero, and the measurement becomes 'insensitive' to the parameter to be estimated. For the Lambertian photometric function (Fig. 2-5) the worst errors then occur along the $\iota_n = 0$ line, a consequence of Lambert's cosine law, as expected from Fig. 2-2. For the lunar photo-

metric function (Fig. 2-6), the bias and variance of the estimate are worst along the line $\iota_z = \epsilon_z$ where the incident and observation directions become collinear, as noted in Fig. 2-3. Finally, the worst bias and errors for the lunar-Lambert photometric function (Fig. 2-7) occur along a curve that lies in the region between the $\iota_n = 0$ and $\iota_z = \epsilon_z$ curves, depending on the exact weighting between the Lambertian and lunar functions. By using the full likelihood function for the surface slope estimate $\widehat{\theta}$, we find that previous approximations to the biases and errors typically underestimated their true values by as much as 50%, as can be seen by comparing for example the error ranges shown in Fig.A4a of Ref. [57] to those presented in Fig. 2-7. The first-order error term in Ref. [57], for example, is based on an implicit assumption of additive signal-independent noise, and so is not consistent with the dominant sources of photoclinometric noise, albedo and camera shot noise, which are multiplicative and signal-dependent, and does not equal the first-order term expected from estimation theory, the square root of the CRLB (Eq. B.15).

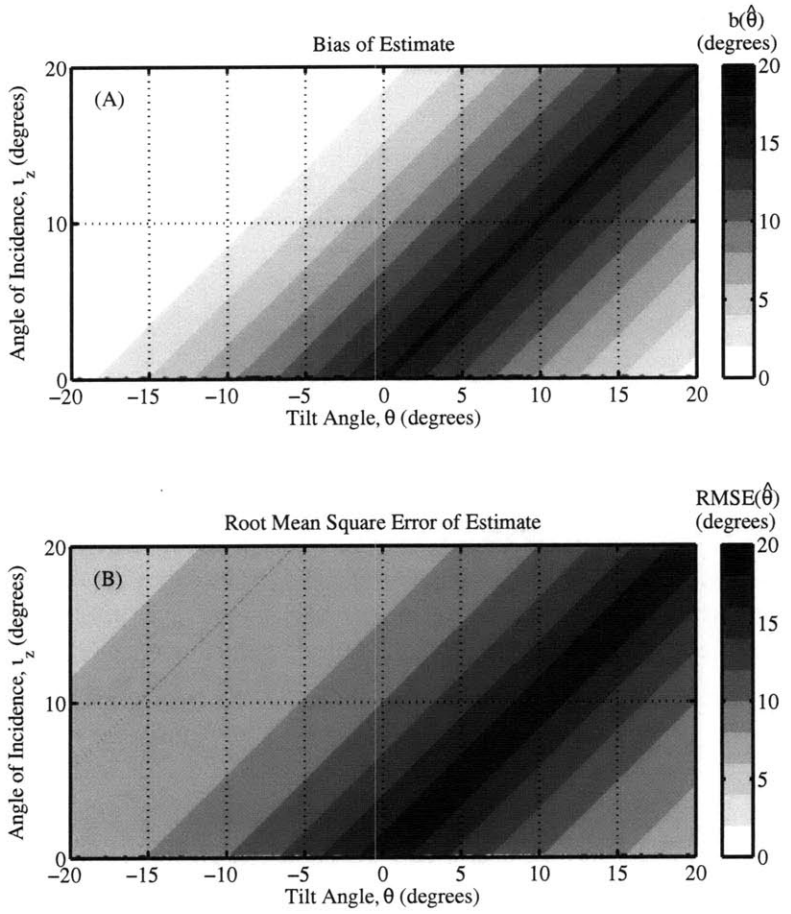

Figure 2-5: Absolute value of the bias and Root Mean Square Error (RMSE) (Eqs. 2.11-2.14) of the Maximum Likelihood Estimate (MLE) of surface slope for the Lambertian photometric function of Fig. 2-2 given typical values for the different sources of noise: (i) CCD camera read noise, $\sigma_R^2 \approx 6400$ electrons, (ii) CCD camera shot noise, $\overline{K} \approx O(10^4)$ electrons, (iii) atmospheric haze, $\sigma_{haze}^2 \approx 2000$ electrons, and (iv) albedo variability, $\sigma_{Bo} = 0.1 \times \overline{Bo}$ (see Appendix C). (a) Bias as a function of incident angle with respect to flat topography ι_z, and true surface slope θ. (b) RMSE as a function of ι_z and θ.

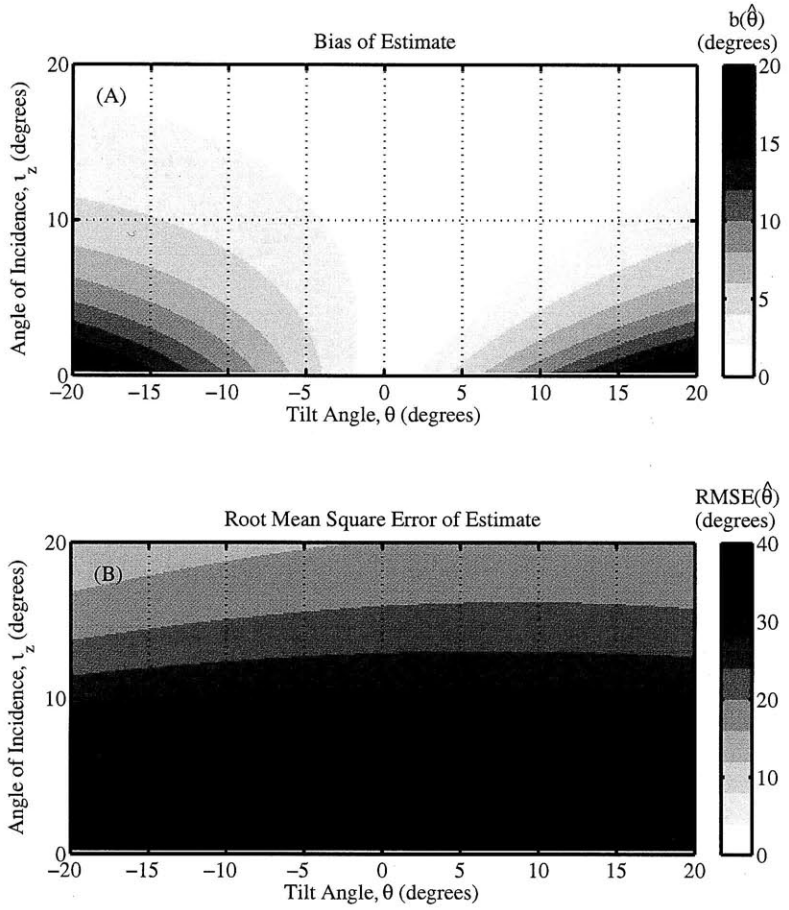

Figure 2-6: The same as Fig. 2-5 for the lunar photometric function of Fig. 2-3.

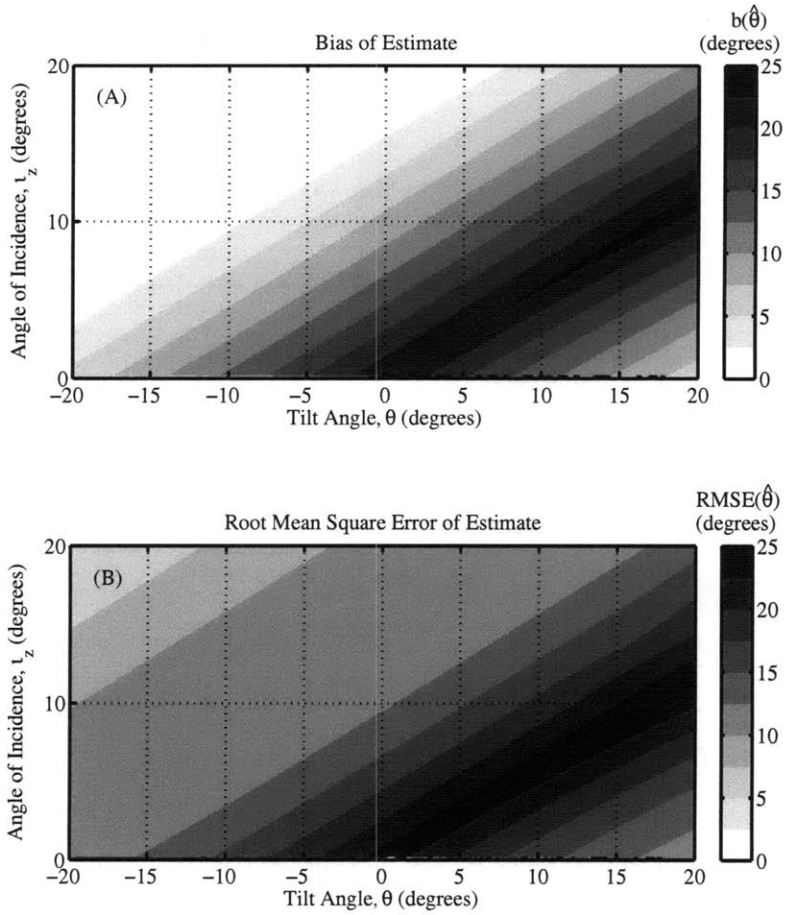

Figure 2-7: The same as Fig. 2-5 for the lunar-Lambert photometric function of Fig. 2-4.

Since the bias and RMSE for the lunar-Lambert photometric function may be as large as 10 degrees or more when the incident angle with respect to the zenith direction, ι_z is less than 20 degrees (Fig. 2-7), obtaining *optimal* estimates may then necessitate averaging over statistically independent measurements. Here, an optimal estimate is defined as one that is unbiased (or has a bias that is negligible compared to the true value of the parameter), and its RMSE attains the the specified design threshold. Statistically independent samples can be obtained, for example, by measuring surface radiance *under different illumination and/or observation conditions*, or by estimating surface slopes over larger regions that can be divided into statistically independent and identically distributed sub-regions. When averaging over a spatial region, the correlation area of albedo variability will limit the total number of statistically independent samples available in that region to the ratio of the total area of the region to the correlation area. The number of samples N necessary to attain the design threshold is given by

$$\sqrt{N} = \frac{\text{RMSE}(\widehat{\theta})}{\text{design threshold}} \tag{2.15}$$

By calculating the sample sizes necessary to *asymptotically* obtain optimal estimates, we find that, while one sample appears to be enough for most illumination conditions, the required number of samples increases significantly in the region of the $\mathrm{d}I/\mathrm{d}\theta = 0$ curve. The necessary sample sizes are computed using Eqs. 2.9-2.10, B.14-B.16, and shown in Figs. 2-8-2-10. In each figure, the white dashed line denotes the curve where $\mathrm{d}I/\mathrm{d}\theta$ goes to zero and more than 10^4 samples are typically required to obtain an estimate that asymptotically becomes unbiased and has a RMSE that attains the square root of the CRLB. In Figs. 2-8(a) and 2-10(a), a ridge occurs at $\theta = 0$, where the denominator vanishes according to our definition for n_b (Eq. 2.9).

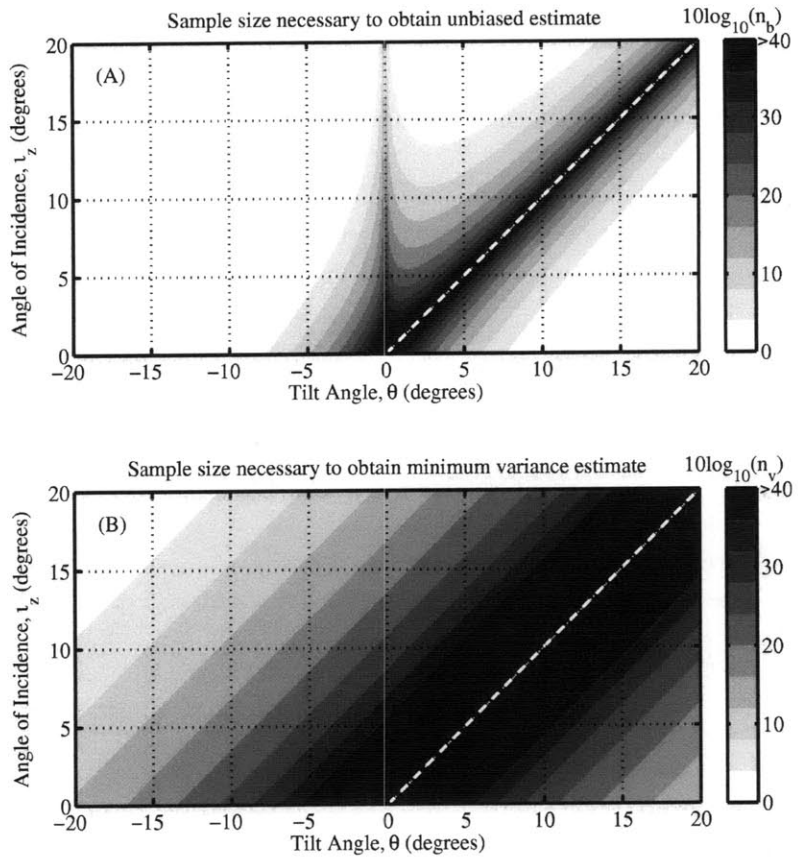

Figure 2-8: Necessary sample sizes to obtain an unbiased estimate of planetary surface slope and for an unbiased estimate to attain the minimum possible RMSE. The planetary surface reflectance is assumed to follow the Lambertian photometric function of Fig. 2-2. (a) $10\log_{10}$ of the necessary sample size for an unbiased estimate $\hat{\theta}$ as a function of incidence angle to flat topography ι_z, and true surface slope θ computed using Eqs. 2.9 and B.14. (b) $10\log_{10}$ of the necessary sample size for an unbiased estimate to attain the minimum possible RMSE as a function of ι_z and θ computed using Eqs. 2.10 and B.15-B.16. The white dashed line indicates the curve along which the derivative of the photometric function with respect to the estimated parameter θ is zero and the necessary sample sizes approach infinity.

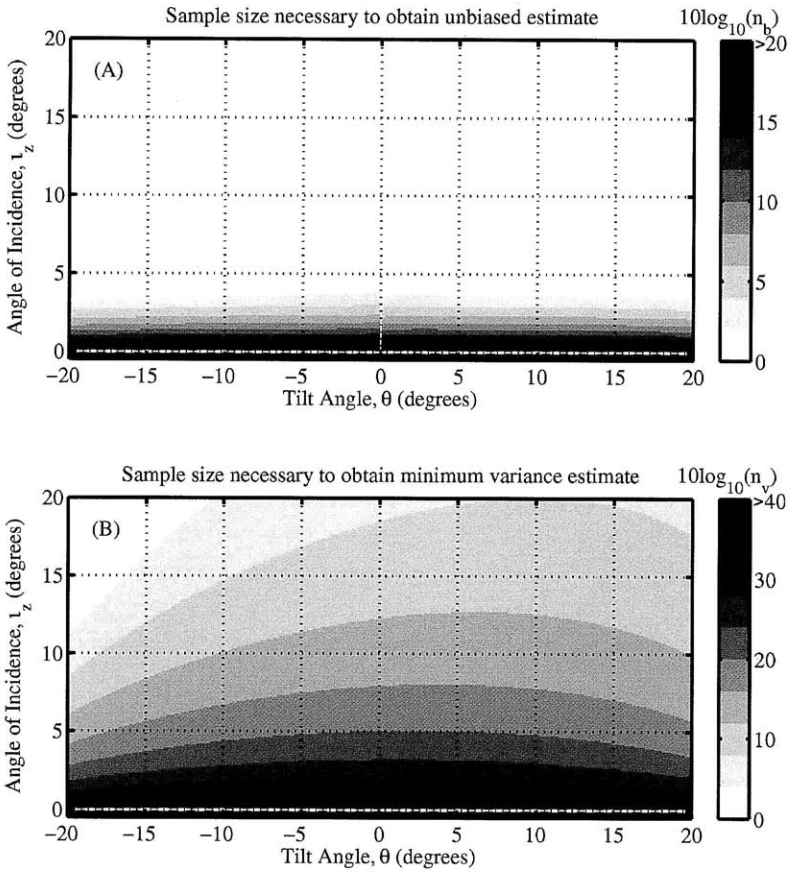

Figure 2-9: The same as Fig. 2-8 for a planetary surface that can be modeled using the lunar photometric function of Fig. 2-3.

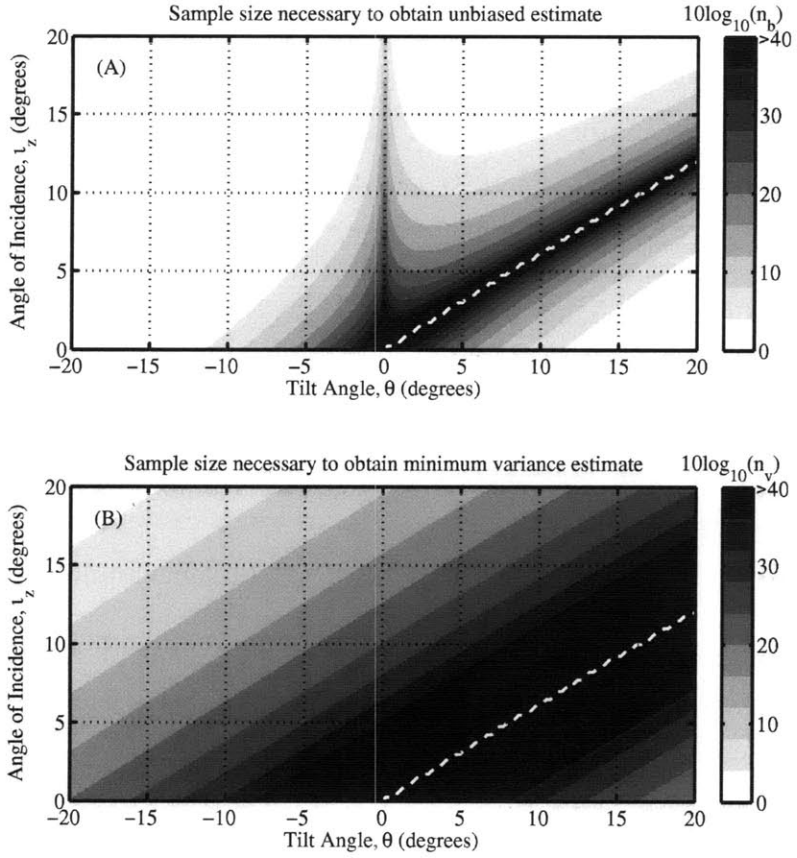

Figure 2-10: The same as Fig. 2-8 for a planetary surface that can be modeled using the lunar-Lambert photometric function of Fig. 2-4, where $L = 0.55$.

Figure 2-11 shows the first-order bias (Eq. B.14) and the square root of the CRLB (Eq. B.15) for the lunar-Lambert photometric function of Eqs. 2.2-2.3 using $L = 0.55$. We find that these asymptotic biases and variances differ dramatically from the exact theoretical values, as can be seen by comparing Figs. 2-11 to 2-7. This is especially evident in two regimes: (1) at large incidence angles, larger than typically 10 degrees, where the asymptotic biases and errors go to zero, and (2) at small incidence angles, where the asymptotic biases and errors very rapidly approach infinity as $\mathrm{d}I/\mathrm{d}\theta$ goes to zero along the white dashed lines in Fig. 2-11. In the special case when n_v samples are available, the RMSE equals the square root of the CRLB. Even then, the CRLB may still be larger than the design threshold, in which case a total of $N = n_v \times n'$ samples would be necessary, where $\sqrt{n'} = \sqrt{\mathrm{CRLB}}/(\text{design threshold})$.

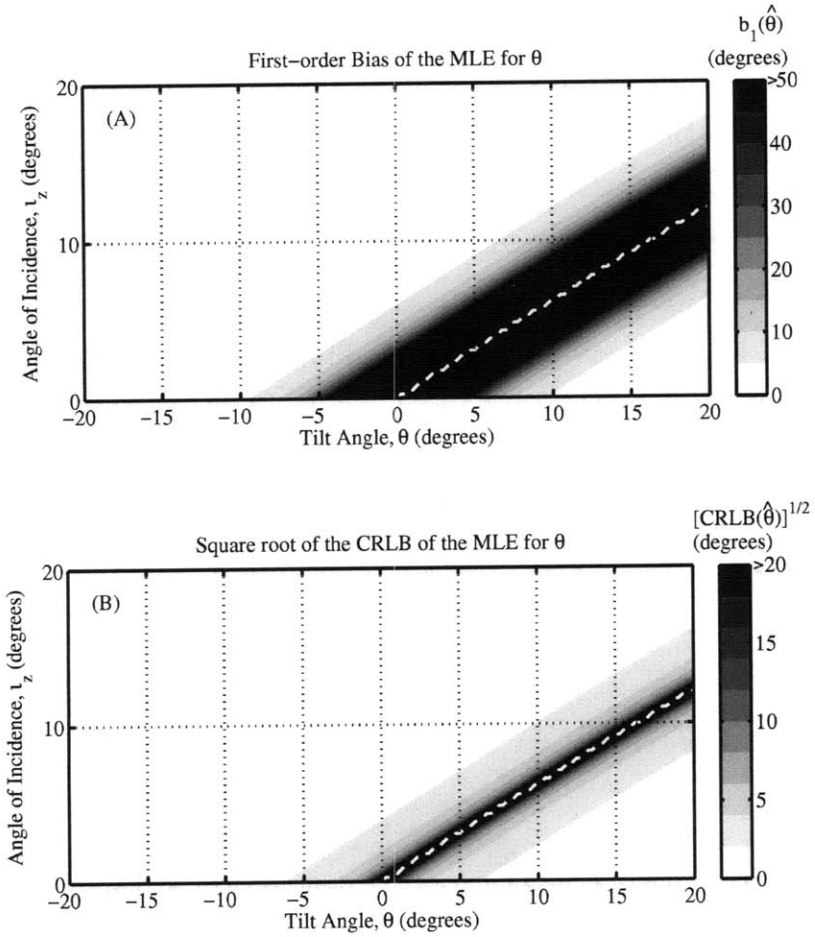

Figure 2-11: Absolute value of the first-order bias and the square root of the CRLB, Eqs. B.14 and B.15, respectively, of the Maximum Likelihood Estimate (MLE) of surface slope for the lunar-Lambert photometric function. (a) First-order bias as a function of incident angle with respect to flat topography ι_z, and true surface slope θ. (b) Square root of the CRLB as a function of ι_z and θ. The white dashed line indicates the curve along which the derivative of the photometric function with respect to the estimated parameter θ is zero and the asymptotic biases and errors approach infinity.

One way of obtaining more independent samples is to tilt the satellite camera to an off-nadir direction. For example, consider the case where the emission direction is at an angle of 20 degrees to the zenith direction, but still lies in the solar plane as defined in Fig. 2-1 and Section 2.2.1. The photometric function, the bias and RMSE (Eqs. 2.11-2.14) of the MLE, and the necessary sample size conditions for this case are shown in Figs. 2-12-2-14.

Comparing Figs. 2-7 and 2-10 to Figs. 2-13 and 2-14, respectively, we find that rotating the camera significantly affects the bias and RMSE, as well as the sample size necessary to obtain an optimal surface slope estimate for given values of ι_z and θ. This example then suggests that carefully designed off-nadir viewing may provide an opportunity for reducing surface slope biases and errors when combined with nadir images.

Depending on the exact experimental conditions, it may be possible to specify a general strategy where an optimal estimate can be obtained from a single sample. For example, for the two cases of the lunar-Lambert function presented here (Figs. 2-4 and 2-12), requiring $|\iota_z| > 30°$, and $|\iota_z| > |\epsilon_z| + 20°$ will allow optimal estimates to be obtained for most values of θ. These two conditions are less stringent than the $|\iota_z| \approx 60° - 75°$, which is typically specified as the optimal regime for photoclinometry [28, 57], where the upper limit typically stems from the need to avoid shadows which are not amenable to investigation. The results presented here (Figs. 2-5-2-7 and 2-13) suggest that photoclinometry may work equally well even at shallower incidence angles.

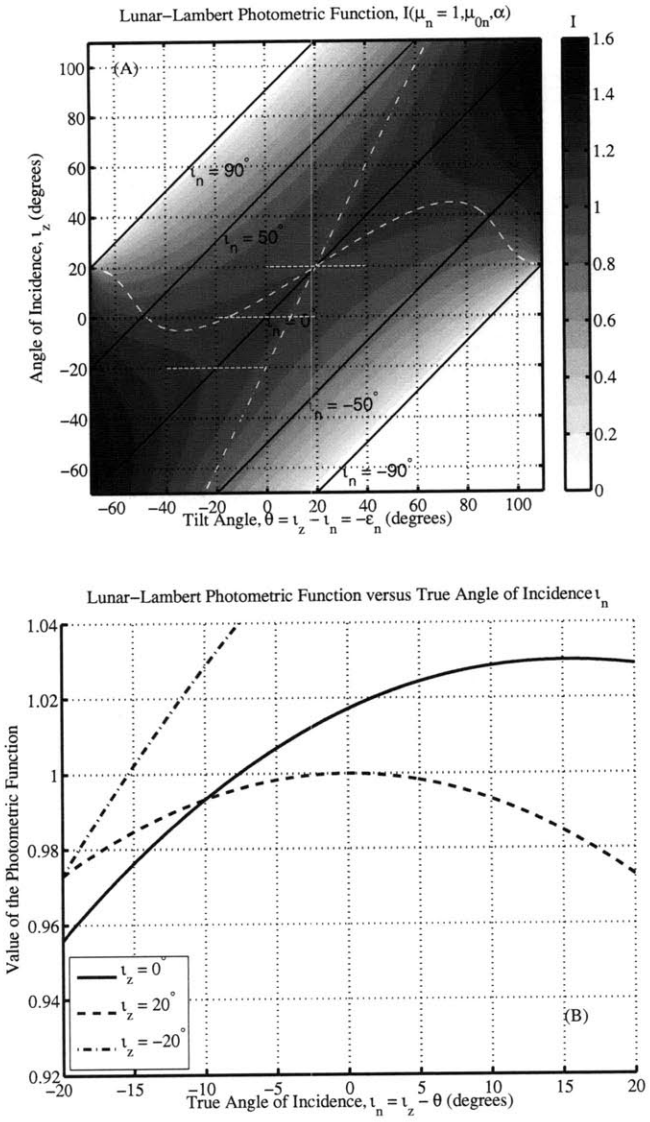

Figure 2-12: The same as Fig. 2-4 for an emission angle $\epsilon_z = 20$ degrees. Again, the regions beyond the $|\iota_n| = 90°$ lines correspond to incidence on the 'back' of the surface patch, so that nothing is reflected towards the receiver and $I = 0$. Note the axes are shifted compared to Fig. 2-4 to ensure the emission direction never lies behind the surface patch.

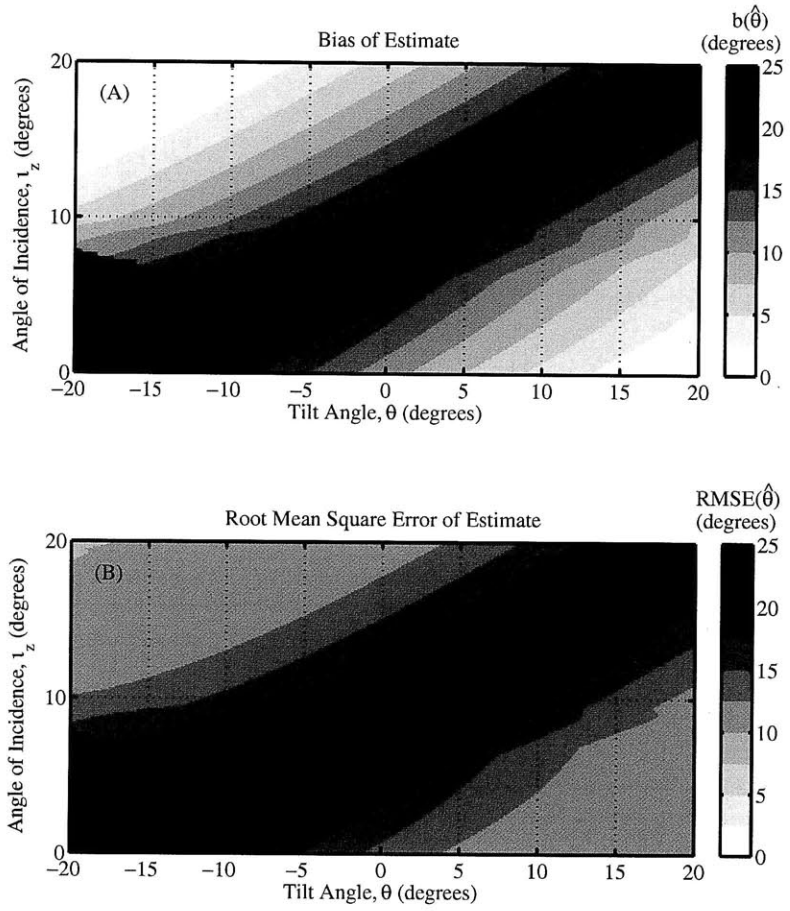

Figure 2-13: The same as Fig. 2-7 for an emission angle $\epsilon_z = 20$ degrees.

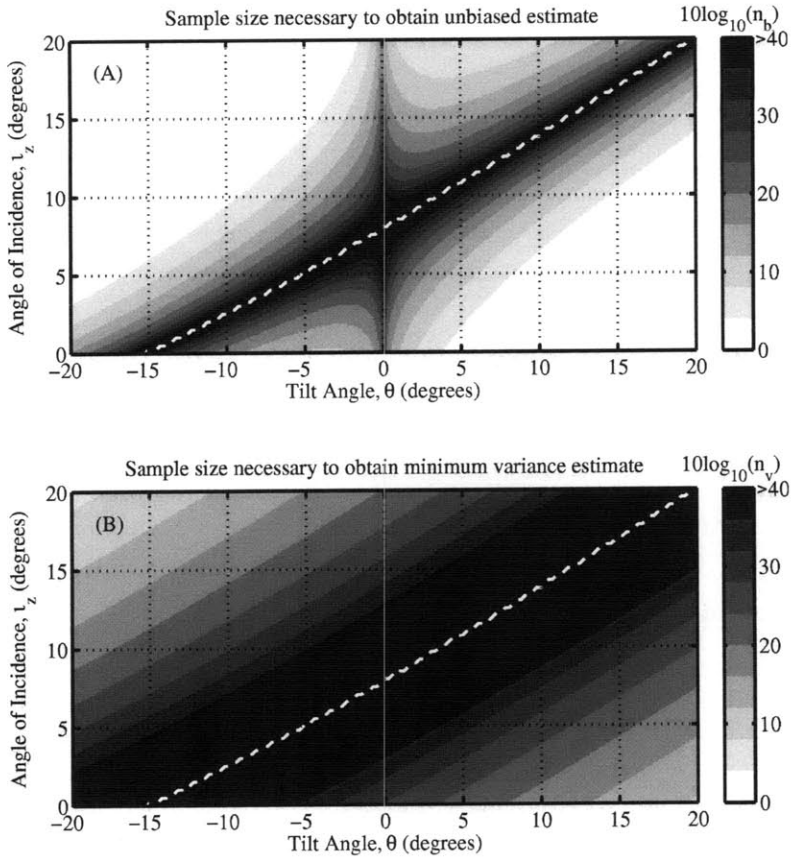

Figure 2-14: The same as Fig. 2-10 for an emission angle $\epsilon_z = 20$ degrees.

2.3.1 Comparison of the Different Sources of Noise or Uncertainty

Here, we examine the biases and errors due to each source of noise or uncertainty described in Section 4.3 acting in the absence of the others. Specifically, biases and errors are calculated with Eqs. 2.11-2.14 by replacing Eq. 2.6 with only the variance term for either (i) read noise, (ii) shot noise, (iii) atmospheric haze, or (iv) albedo variability for each respective case.

As expected, the biases and errors for each noise source increase significantly in the region where the reflectance function has weak dependence on surface slope, as shown in Figures 2-15 and 2-16. The total bias and RMSE for all these error sources has been shown in Fig. 2-7. Biases often dominate the RMSEs.

We find that albedo variability is typically the dominant source of biases and errors, on the order of 10-20° or more at small incidence angles (ι_n smaller than roughly ten degrees), as can be seen from Fig. 2-15(d). Camera shot and read noise are the next most important noise sources, leading to biases and errors on the order of 5° (Fig. 2-15(a-b)). Finally, haze appears to be the least significant source of noise, resulting in biases and errors that are typically on the order of a 1-2°, or approximately an order of magnitude smaller than those due to albedo variability, as can be seen from Fig. 2-15(c). This last result is in agreement with previous literature [62], where errors due to haze have typically been found to comprise less than 20% of the total error when accurately modeled. Note however that haze effects may increase significantly in magnitude during dust storms [20].

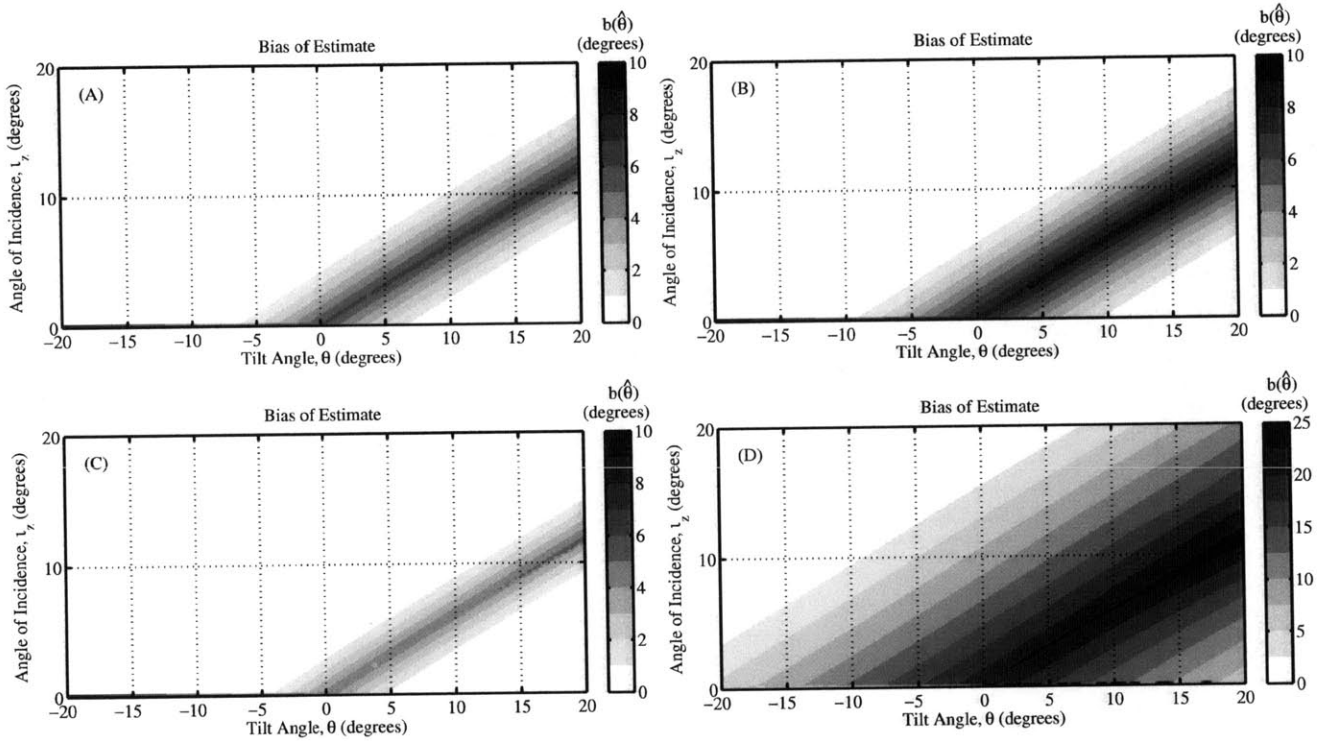

Figure 2-15: Absolute value of the bias (Eqs. 2.11 and 2.13) of the MLE of surface slope for the lunar-Lambert photometric function, given typical values for the different sources of noise: (i) CCD camera read noise, $\sigma_R^2 \approx 6400$ electrons, (ii) CCD camera shot noise, $\overline{K} \approx O(10^4)$ electrons, (iii) atmospheric haze, $\sigma_{haze}^2 \approx 2000$ electrons, and (iv) albedo variability, $\sigma_{Bo} = 0.1 \times \overline{Bo}$ (see Appendix C). The emission angle is again assumed to be zero, and $L = 0.55$. The total bias has been shown in Fig. 2-7(a).

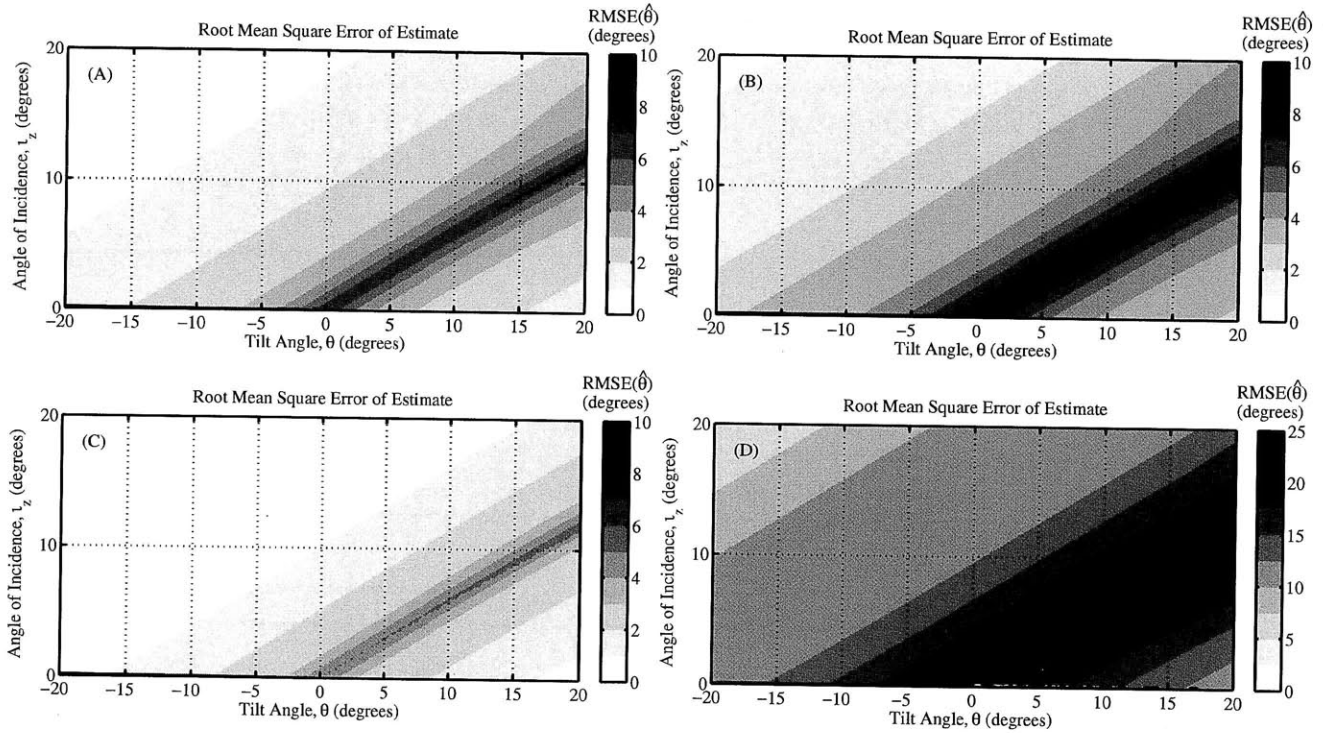

Figure 2-16: RMSE (Eqs.2.12 and 2.13-2.14) of the MLE of surface slope for the lunar-Lambert photometric function, given typical values for the different sources of noise: (i) CCD camera read noise, $\sigma_R^2 \approx 6400$ electrons, (ii) CCD camera shot noise, $\overline{K} \approx O(10^4)$ electrons, (iii) atmospheric haze, $\sigma_{haze}^2 \approx 2000$ electrons, and (iv) albedo variability, $\sigma_{Bo} = 0.1 \times \overline{Bo}$ (see Appendix C). The emission angle is again assumed to be zero, and $L = 0.55$. The total RMSE has been shown in Fig. 2-7(b).

Since the ratio of the albedo to the shot noise contribution of the photocount variance from Eq. 2.6 is $\overline{K}\frac{\sigma_{Bo}^2}{\overline{Bo}^2}$, we expect that albedo noise should dominate the variance of the photocount K if the standard deviation of albedo uncertainty is larger than $\frac{1}{\sqrt{\overline{K}}}$ times the mean albedo, or roughly 1% of the mean albedo for the mean photocount used here of $\overline{K} \approx O(10^4)$, given sufficiently low read and haze noise contributions. This is indeed found to be the case in Figs. 2-15-2-16 where $\sigma_{Bo} = 0.1 \times \overline{Bo}$, for our typical Martian scenario. For much lower albedo uncertainty of $\sigma_{Bo} = 0.005 \times \overline{Bo}$, as reported for Miranda [51], the total bias and error are instead dominated by shot noise, which can be seen by comparing the black dashed lines to the gray dash-dotted lines in Fig. 2-17 which shows a cut through Figs. 2-7 and 2-15-2-16 along the line $\iota_z = 12°$.

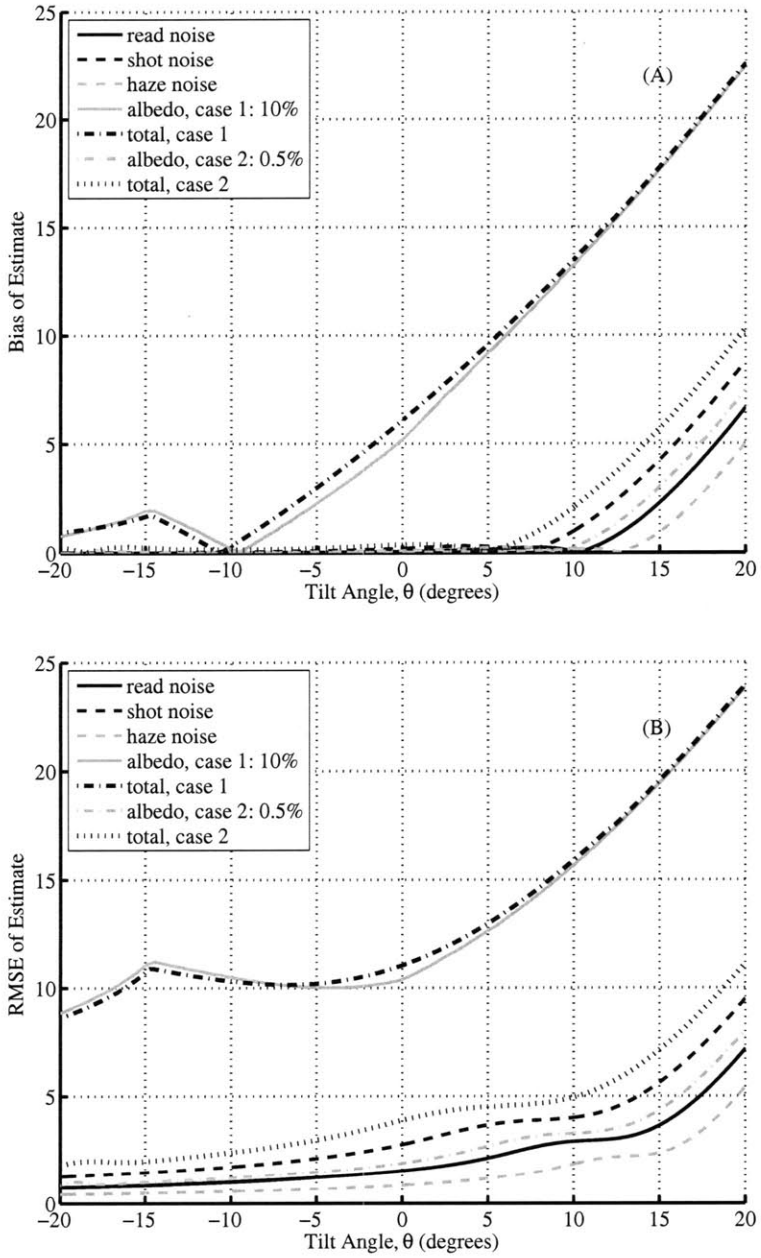

Figure 2-17: Horizontal cuts along $\iota_z = 12°$ in Figs. 2-7 and 2-15-2-16. The bias and error due to small-scale albedo variability such that $\sigma_{Bo} = 0.005 \times \overline{Bo}$, as well as the total bias and error in this case are also shown.

2.4 Conclusions

Both theoretically exact and asymptotic biases and errors inherent in photoclinometric estimation of planetary surface orientation from Charge-Coupled Device (CCD) measurements are calculated using an approach developed from classical estimation theory. The approach can be used to determine the accuracy of topographic reconstructions and aid in experimental design.

The likelihood function governing statistical fluctuations of a photoclinometric slope estimate is derived, including uncertainty due to camera shot noise, camera read noise, small-scale albedo fluctuations and atmospheric haze. The derivation incorporates common photometric models of planetary surface reflectance and the known probability distributions of CCD measurements of natural light. From this, bounds on the minimum mean square error of any unbiased estimate of photoclinometric surface slope are derived, as are necessary conditions to attain these bounds and constrain errors within desired design thresholds. Approximate asymptotic biases and errors for low uncertainty (1) are formulated in terms of the likelihood function to insure proper convergence with decreasing uncertainty, and (2) typically differ dramatically from the exact ones, making them applicable only when a large number of independent samples is available. Biases and errors are shown to typically become much larger than surface slopes for illuminations and observations where planetary reflectance is weakly dependent on surface slope, near inflection points of the photometric function.

The approach developed here provides a unified method for quantitatively comparing the biases and errors from different sources of uncertainty in a photoclinometric estimate. Albedo variability, for example, is shown to typically dominate estimate biases and errors when the standard deviation of albedo uncertainty is larger than approximately $\frac{1}{\sqrt{K}}$ times the mean albedo in the imaged region, for CCD photocount K, while other error sources such as shot noise may become dominant for very low albedo uncertainty.

Chapter 3

Resolving Lambertian Surface Orientation from Fluctuating Radiance

3.1 Introduction

Acoustic, optical, radar and laser images of remote surfaces are typically corrupted by signal-dependent noise known as speckle. This noise arises when wavelength scale roughness on the surface causes a random interference pattern in the field scattered from it by an active system. Relative motion between source, surface and receiver, or source incoherence causes the received field to fluctuate over time with circular complex Gaussian random (CCGR) statistics.[27, 48, 49, 86, 71] Underlying these fluctuations, however, is the expected radiance of the surface, from which its orientation may be inferred. In many cases of practical importance, Lambert's Law is appropriate for such inference because variations in the projected area of a surface patch, as a function of source and receiver orientation, often cause the predominant variations in its radiance.

The aim of this paper is to provide a method for estimating remote surface orientation and albedo from measurements of fluctuating radiance that are corrupted by

speckle noise. The ability to accurately resolve remote surface orientation from measurements of fluctuating radiance is not only of great importance to ocean acoustics,[105, 58] but also to optics,[14, 106] medical ultrasound,[101] planetary terrain surveillance,[33, 37] and machine vision.[53] Due to the signal-dependent nature of speckle noise, and the nonlinear relationship between surface orientation, illumination direction and radiance,[87] surface orientation estimates based on a single sample typically have large biases and mean square errors (MSEs). Given the probability distribution of surface radiance and the physical model relating it to surface orientation and albedo, maximum likelihood estimates (MLEs) are derived and their biases and variances are expanded in terms of the likelihood function.[95, 5, 80, 84] The likelihood function governs the physical and statistical behavior of surface orientation estimates, so that the expansions presented here are guaranteed to converge in inverse orders of sample size or Signal to Noise Ratio (SNR). Analytical expressions are then derived for the sample sizes or SNRs necessary to obtain estimates that are in the asymptotic regime where biases are negligible and MSEs attain minimum variance. The biases and errors are found to vary signicantly with illumination direction and measurement diversity. In a particularly compelling example, it is shown that the minimum error in estimating the angle of incidence with respect to a Lambertian surface is at best proportional to the *cotangent* of this angle, so that surface orientation varies from irresolvable at normal incidence to perfectly resolvable at shallowest grazing. A preliminary investigation of surface orientation estimation from fluctuating intensity presented by Makris at the SACLANT 1997 conference[73] determined sample size conditions by a Taylor series approach that is not guaranteed to converge in inverse orders of sample size as the approach here does since it did not involve the expansion of the likelihood function. The special case of deterministic data, which corresponds to infinite SNR, has been treated by Horn.[53]

In Section 3.2, we present the necessary Radiometry background and describe how measurements of surface radiance are typically obtained, and in Section 3.3, we give the probability density for such radiometric measurements. In Section 3.4, we review estimation theory and the maximum likelihood method, and determine necessary

conditions on sample size or SNR to obtain estimates of the desired accuracy. Finally, in Section 3.5 we present illustrative examples of estimating surface orientation and albedo.

3.2 Radiometry

The flux $d\Phi$, received in a acoustic, optical, radar or laser beam of solid angle $d\beta$, is related to the area of the resolved surface patch dA_β (Fig. 3-1), the local surface radiance L_β, and the solid angle subtended by the receiver aperture $d\Omega$, by the linear equation

$$d\Phi = dA_\beta L_\beta d\Omega. \tag{3.1}$$

The solid angle subtended by the receiver aperture from the surface patch dA_β is $d\Omega = \cos\psi_r \, dA/r^2$, where dA is the area of the aperture, $\cos\psi_r$ is the foreshortening of the surface patch with respect to the receiver, ψ_r is the scattering angle, and r is the range to the aperture. The intensity of the received beam is then

$$I_\beta = \frac{d\Phi}{dA} = dA_\beta L_\beta \frac{\cos\psi_r}{r^2}. \tag{3.2}$$

Assuming that the receiver is of sufficiently high resolution that it resolves an elemental surface patch dA_β, that is locally planar and small enough so that

$$d\beta = dA_\beta \frac{\cos\psi_r}{r^2}, \tag{3.3}$$

surface radiance can be directly measured by the receiver as

$$\frac{dI_\beta}{d\beta} = L_\beta. \tag{3.4}$$

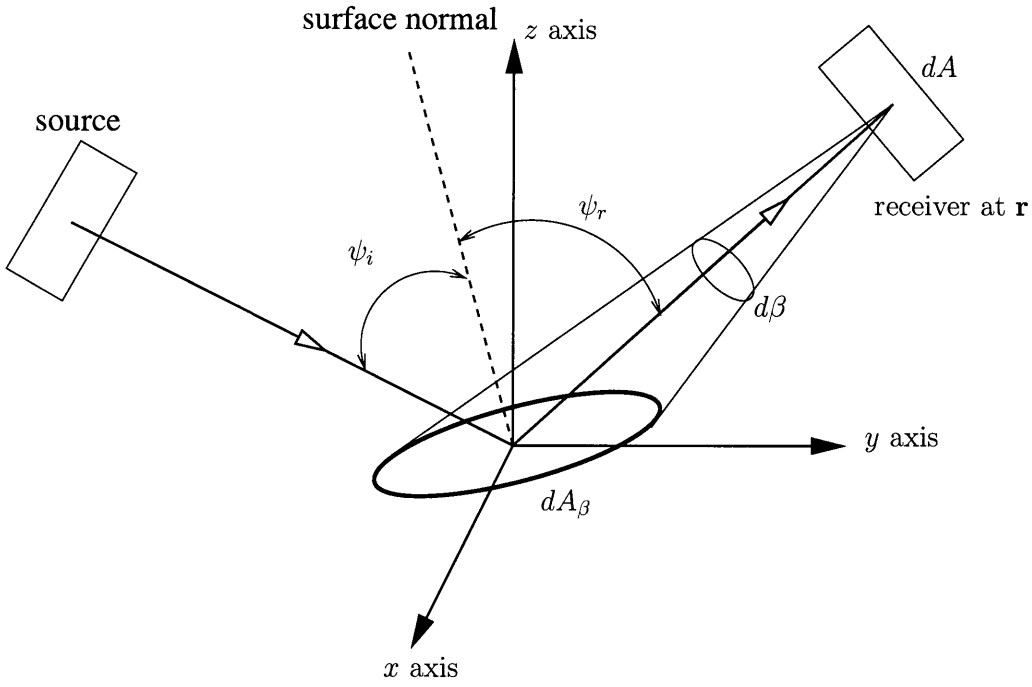

Figure 3-1: Resolved surface patch.

For a Lambertian surface,

$$L_\beta = \rho E \cos\psi_i, \tag{3.5}$$

so that the radiance measured in a acoustic, optical, radar or laser image of the scene L_β, is independent of the viewing direction ψ_r. It follows a linear relationship with the foreshortening $\cos\psi_i$ of the surface patch, the surface irradiance E, and the surface bidirectional reflectance distribution function ρ which is $1/\pi$ for a perfectly reflecting Lambertian surface. Here ψ_i is the angle of incident insonification and E is defined as incident flux per unit area on the surface of albedo $\pi\rho$.

3.3 The Likelihood Function and Measurement Statistics

Let the stochastic measurement vector $\mathbf{R}$ contain the independent statistics R_k whose expected values $\sigma_k(\mathbf{a}) = \langle R_k \rangle$ are linearly related to measured surface radiance, where the vector $\mathbf{a}$ contains the surface orientation parameters a_r to be estimated from the measurements $\mathbf{R}$ for $r = 1, 2, 3 \ldots Q$. More succinctly, let $\boldsymbol{\sigma}(\mathbf{a}) = \langle \mathbf{R} \rangle$.

Assuming the R_k are corrupted by Circular Complex Gaussian Random (CCGR) field fluctuations, the conditional probability distribution for the measurements $\mathbf{R}$ given parameter vector $\mathbf{a}$ is the product of gamma distributions[71, 70]

$$P_{\mathbf{R}}(\mathbf{R};\mathbf{a}) = \prod_{k=1}^{M} \frac{(\frac{\mu_k}{\sigma_k(\mathbf{a})})^{\mu_k} (R_k)^{\mu_k - 1} \exp(-\mu_k \frac{R_k}{\sigma_k(\mathbf{a})})}{\Gamma(\mu_k)}. \tag{3.6}$$

The quantity μ_k is the number of coherence cells in the measurement average used to obtain R_k,[71, 70] the variance of which is given by σ_k^2/μ_k. It is important to note that μ_k is then also equal to the squared-mean-to-variance ratio, or Signal to Noise Ratio (SNR), defined as $\langle R_k \rangle^2 / (\langle R_k^2 \rangle - \langle R_k \rangle^2)$. For example, μ_k equals the time-bandwidth product of the received field if each R_k is obtained from a continuous but finite-time average. Additionally, μ_k can be interpreted as the number of stationary

speckles averaged over a finite spatial aperture in the image plane or the number of stationary multi-look images averaged for a particular scene.[70]

3.4 Classical Estimation Theory and a Higher Order Asymptotic Approach to Inference

The Maximum Likelihood Estimator (MLE) $\hat{\mathbf{a}}$, for the parameter set $\mathbf{a}$, maximizes the log-likelihood function $l(\mathbf{R};\mathbf{a}) = \ln\left(P_{\mathbf{R}}(\mathbf{R};\mathbf{a})\right)$ with respect to $\mathbf{a}$. The Cramer-Rao Lower Bound (CRLB) $\mathbf{i}^{-1}$ is the minimum mean square error attainable by any unbiased estimate, regardless of the method of estimation. The CRLB is the inverse of the Fisher information matrix, also known as the expected information, the elements of which are given by $i_{bc} = \langle l_b l_c \rangle$, where $l_r = \frac{\partial l(\mathbf{R};\mathbf{a})}{\partial a_r}$ and a_r is the rth component of $\mathbf{a}$.

For sufficiently large sample size, μ_k, the MLE is asymptotically unbiased and follows the Gaussian distribution

$$P_{\hat{\mathbf{a}}}(\hat{\mathbf{a}};\mathbf{a}) = \sqrt{\frac{|\mathbf{i}|}{(2\pi)^M}} \exp\left(-\frac{1}{2}(\hat{\mathbf{a}}-\mathbf{a})^T \mathbf{i} (\hat{\mathbf{a}}-\mathbf{a})\right), \tag{3.7}$$

with variance $\mathbf{i}^{-1}$ equal to the CRLB,[89, 60], where[71, 70]

$$i_{bc} = \sum_{k=1}^{M} \left(\mu_k \frac{\partial \ln \sigma_k(\mathbf{a})}{\partial a_b} \frac{\partial \ln \sigma_k(\mathbf{a})}{\partial a_c}\right), \tag{3.8}$$

$$i^{bc} \equiv [\mathbf{i}^{-1}]_{bc} = \sum_{k=1}^{M} \left(\frac{(\sigma_k(\mathbf{a}))^2}{\mu_k} \frac{\partial a_b}{\partial \sigma_k(\mathbf{a})} \frac{\partial a_c}{\partial \sigma_k(\mathbf{a})}\right) \tag{3.9}$$

given the probability ditribution for $\mathbf{R}$ described in Eq. 3.6. In the deterministic limit $\mu_k \to \infty$, where the R_k are obtained from exhaustive sample averages, $P_{\hat{\mathbf{a}}}(\hat{\mathbf{a}};\mathbf{a})$ becomes the delta function $\delta(\hat{\mathbf{a}}-\mathbf{a})$.

Expressions for the asymptotic orders of the MLE bias and variance have been derived in detail in Ref. [84] and are summarized in Appendix B. For the statistical

model of Eq. 3.6,

$$b_1(\hat{a}_r;\mathbf{a},\boldsymbol{\mu},1) = -\sum_{k=1}^{M}\frac{1}{2}\frac{\sigma_k^2}{\mu_k}\frac{\partial^2 a_r}{\partial\sigma_k^2}, \tag{3.10}$$

$$var_1(\hat{a}_r;\mathbf{a},\boldsymbol{\mu},1) = \sum_{k=1}^{M}\frac{\sigma_k^2}{\mu_k}\left(\frac{\partial a_r}{\partial\sigma_k}\right)^2, \tag{3.11}$$

$$var_2(\hat{a}_r;\mathbf{a},\boldsymbol{\mu},1) = \sum_{k=1}^{M}\frac{1}{\mu_k^2}\left[2\sigma_k^3\frac{\partial a_r}{\partial\sigma_k}\frac{\partial^2 a_r}{\partial\sigma_k^2}+\sigma_k^4\frac{\partial a_r}{\partial\sigma_k}\frac{\partial^3 a_r}{\partial\sigma_k^3}+\frac{1}{2}\sigma_k^4\left(\frac{\partial^2 a_r}{\partial\sigma_k^2}\right)^2\right] \tag{3.12}$$

where b_1 is the first-order MLE bias, and var_1, var_2 are the first- and second-order MLE covariance, respectively.

As shown in Appendix B, assuming for simplicity that $\mu_k = \mu$ for all k, the MLE bias and variance can then also be expressed as asymptotic series in inverse powers of μ,

$$\text{bias}(\hat{a}_r,\boldsymbol{\mu},1) = \frac{b_1(\hat{a}_r;\mathbf{a},\mathbf{e},1)}{\mu}+\frac{b_2(\hat{a}_r;\mathbf{a},\mathbf{e},1)}{\mu^2}+O(\mu^{-3}), \tag{3.13}$$

$$\text{var}(\hat{a}_r,\boldsymbol{\mu},1) = \frac{var_1(\hat{a}_r;\mathbf{a},\mathbf{e},1)}{\mu}+\frac{var_2(\hat{a}_r;\mathbf{a},\mathbf{e},1)}{\mu^2}+O(\mu^{-3}), \tag{3.14}$$

where the components of the vector $\mathbf{e}$ are $e_k = 1$ for $k = 1,2,\ldots,M$. To simplify notation, let $var_j(\hat{a}_r;\mathbf{a},\mathbf{e},1) \equiv var_k(\hat{a}_r;\mathbf{a})$ and $b_j(\hat{a}_r;\mathbf{a},\mathbf{e},1) \equiv b_j(\hat{a}_r;\mathbf{a})$.

The value of μ necessary for $\hat{a}_r$ to become *asymptotically* unbiased is found by conservatively requiring the first-order bias to be an order of magnitude smaller than the true value of the parameter,

$$\mu = 10\left|\frac{b_1(\hat{a}_r;\mathbf{a})}{a_r}\right| = 10\left|\frac{\sum_{k=1}^{M}\sigma_k^2\frac{\partial^2 a_r}{\partial\sigma_k^2}}{2a_r}\right| \tag{3.15}$$

Similarly, the value of μ necessary for the MLE variance to *asymptotically* attain the CRLB is found by requiring the second-order variance to be an order of magnitude

smaller than the first-order variance, so that

$$\mu = 10\frac{|var_2(\hat{a}_r;\mathbf{a})|}{var_1(\hat{a}_r;\mathbf{a})} = 10\frac{\left|\sum_{k=1}^{M} 2\sigma_k^3 \frac{\partial a_r}{\partial \sigma_k}\frac{\partial^2 a_r}{\partial \sigma_k^2} + \sigma_k^4 \frac{\partial a_r}{\partial \sigma_k}\frac{\partial^3 a_r}{\partial \sigma_k^3} + \frac{1}{2}\sigma_k^4\left(\frac{\partial^2 a_r}{\partial \sigma_k^2}\right)^2\right|}{\sum_{k=1}^{M}\sigma_k^2\left(\frac{\partial a_r}{\partial \sigma_k}\right)^2} \tag{3.16}$$

Only for values of μ satisfying these conditions is it possible for the variance to be in the asymptotic regime where it is unbiased and continuously attains the CRLB.[84, 102, 110]

3.5 Inferring Lambertian Surface Orientation

For measurement k, a collimated source with known unit incident direction $\mathbf{s_k}$ irradiates a planar Lambertian surface with unknown unit normal vector $\mathbf{n}$. For each measurement, the receiver measures Lambertian surface radiance from any hemispherical position within view of the surface. For convenience, a Cartesian coordinate system (x, y, z) is adopted, with the origin in the center of the resolved surface patch, as shown in Fig.3-1. Because surface incident irradiance E_k is presumed known, given knowledge of source power, directionality, and transmission characteristics to the surface, it can be deterministically scaled out of the measured surface radiance leaving $\sigma_{L_k} = \langle L_k \rangle / E_k$. When signal-independent additive CCGR noise of intensity $\sigma_{N_k} d\beta_k E_k$ is also measured with the radiant field from the surface, the expected measurement vector $\langle \mathbf{R} \rangle$ becomes $\boldsymbol{\sigma}(\mathbf{a}) = \boldsymbol{\sigma}_L(\mathbf{a}) + \boldsymbol{\sigma}_N$.

Lambert's Law for the expected radiometric component of the data is then

$$\langle \mathbf{R} \rangle_L = \boldsymbol{\sigma}_L(\mathbf{a}) = [\sigma_1(\mathbf{a}), \ldots, \sigma_M(\mathbf{a})]^T = \mathbf{S}\mathbf{x}, \tag{3.17}$$

where the matrix $\mathbf{S}$ is defined by

$$\mathbf{S}^T = [\mathbf{s_1}\ \mathbf{s_2}\ \mathbf{s_3} \ldots \mathbf{s_M}], \tag{3.18}$$

and the vector $\mathbf{x}$ equals $\rho\mathbf{n}$.

The general problem is to determine both the Lambertian surface normal vector $\mathbf{n}$ and the albedo $\pi\rho$ from the fluctuating measurements $\mathbf{R}$. The surface normal is typically expressed in terms of the surface gradient components

$$\mathbf{n}^T = [-p_n \ -q_n \ 1]/(1 + p_n^2 + q_n^2)^{1/2}, \tag{3.19}$$

where

$$p_n = \frac{\partial z}{\partial x}, \ \ q_n = \frac{\partial z}{\partial y}, \tag{3.20}$$

or in terms of spherical coordinates

$$\mathbf{n}^T = [\cos\phi_n \sin\theta_n \ \ \sin\phi_n \sin\theta_n \ \ \cos\theta_n]. \tag{3.21}$$

3.5.1 Maximum Likelihood Estimates of Surface Orientation and Albedo

The 3-D parameter vector $\mathbf{x}$ is to be estimated from the potentially over-determined M-D measurement vector $\mathbf{R}$. From Eqs. 3.8 and 3.17, the mean square error bound on any unbiased estimate $\tilde{\mathbf{x}}$ is

$$\langle(\tilde{\mathbf{x}} - \mathbf{x})(\tilde{\mathbf{x}} - \mathbf{x})^T\rangle \geq \mathbf{J}_{\mathbf{x}}^{-1} = \left[\mathbf{S}^T\mathbf{J}_{\boldsymbol{\sigma}}\mathbf{S}\right]^{-1}, \tag{3.22}$$

where $[\mathbf{J}_{\boldsymbol{\sigma}}]_{ij} = \delta_{ij}\mu_{ij}/\sigma_i^2$ is infinite when all incident vectors $\mathbf{s}_k$ are tangent to $\mathbf{n}$ in the absence of signal-independent noise.

To derive the maximum likelihood estimate (MLE) of the vector $\mathbf{x} = \rho\mathbf{n}$, he probability distribution for $\mathbf{R}$ in Eq. 3.6 is rewritten as

$$P_{\mathbf{R}}(\mathbf{R};\mathbf{x}) = \prod_{k=1}^{M} \frac{(\frac{\mu_k}{\sigma_k(\mathbf{x})})^{\mu_k}(R_k)^{\mu_k - 1}\exp(-\mu_k\frac{R_k}{\sigma_k(\mathbf{x})})}{\Gamma(\mu_k)}. \tag{3.23}$$

The MLE $\hat{x}_r$ maximizes the log-likelihood function $ln(P_{\mathbf{R}}(\mathbf{R};\mathbf{x}))$ with respect to x_r,

so that it satisfies

$$\frac{\partial ln(P_{\mathbf{R}}(\mathbf{R};\mathbf{x}))}{\partial x_r} = \sum_{k=1}^{M} \frac{\mu_k}{\sigma_k}\left[\frac{R_k}{\sigma_k} - 1\right]\frac{\partial \sigma_k}{\partial x_r}\bigg|_{x_r=\hat{x}_r} = 0 \tag{3.24}$$

where $\frac{\partial \sigma_k}{\partial x_r}$ is the (k,r) element of $\mathbf{S}$. Considering all the elements of $\mathbf{x}$, Eq. 3.24 can be rewritten in vector form as

$$\sum_{k=1}^{M}(\mathbf{S}_k)^T\frac{\mu_k}{\sigma_k}\bigg|_{\mathbf{x}=\hat{\mathbf{x}}} = \sum_{k=1}^{M}(\mathbf{S}_k)^T\frac{\mu_k R_k}{\sigma_k^2}\bigg|_{\mathbf{x}=\hat{\mathbf{x}}} \tag{3.25}$$

$$\left[\mathbf{S}^T\mathbf{J}_{\boldsymbol{\sigma}}\boldsymbol{\sigma}\right]\big|_{\mathbf{x}=\hat{\mathbf{x}}} = \left[\mathbf{S}^T\mathbf{J}_{\boldsymbol{\sigma}}\mathbf{R}\right]\big|_{\mathbf{x}=\hat{\mathbf{x}}} \tag{3.26}$$

where $\mathbf{S}_k$ is the kth row of $\mathbf{S}$. The MLE, given linearity between $\mathbf{x}$ and $\boldsymbol{\sigma}$ is then given by

$$\hat{\mathbf{x}} = \left[\mathbf{S}^T\mathbf{J}_{\boldsymbol{\sigma}}\mathbf{S}\right]^{-1}\mathbf{S}^T\mathbf{J}_{\boldsymbol{\sigma}}(\mathbf{R} - \boldsymbol{\sigma}_N), \tag{3.27}$$

is unbiased and attains the error bound $\mathbf{J}_{\mathbf{x}}^{-1}$ of Eq. 3.22.

Given this information, the MLEs for albedo $\pi\hat{\rho} = \pi\,|\hat{\mathbf{x}}|$, surface normal $\mathbf{n} = \hat{\mathbf{x}}/\hat{\rho}$, cone and polar angles $\hat{\theta}_n = \cos^{-1}\hat{n}_3$, $\hat{\phi}_n = \tan^{-1}\frac{\hat{n}_2}{\hat{n}_1}$, and surface gradient components $\hat{p}_n = -\frac{\hat{n}_1}{\hat{n}_3}$, $\hat{q}_n = -\frac{\hat{n}_2}{\hat{n}_3}$, however, are not generally unbiased and do not generally have minimum variance except for sufficiently large sample sizes.

Taking the case where $\mathbf{R}$ is a 3-D vector and $\boldsymbol{\sigma}_N$ is negligible, for example, the joint distribution for $\hat{\mathbf{x}}$ is

$$P_{\hat{\mathbf{x}}}(\hat{\mathbf{x}}|\mathbf{x}) = |\mathbf{s}_1 \cdot \mathbf{s}_2 \times \mathbf{s}_3|\, P_R(\mathbf{S}\hat{\mathbf{x}}|\boldsymbol{\sigma}), \tag{3.28}$$

which leads to the respective joint distributions

$$P_{grad}(\hat{p}_n, \hat{q}_n, \hat{\rho}|p_n, q_n, \rho) = \\ = \frac{P_{\hat{\mathbf{x}}}(-\hat{\rho}\hat{p}_n(1+\hat{p}_n^2+\hat{q}_n^2)^{-1/2},\ -\hat{\rho}\hat{q}_n(1+\hat{p}_n^2+\hat{q}_n^2)^{-1/2},\ \hat{\rho}(1+\hat{p}_n^2+\hat{q}_n^2)^{-1/2}|\mathbf{x})}{|\hat{\rho}^2(1+\hat{p}_n^2+\hat{q}_n^2)^{-3/2}|}, \tag{3.29}$$

and

$$P_{polar}(\hat{\theta}_n, \hat{\phi}_n, \hat{\rho}|\theta_n, \phi_n, \rho) = \\ = \frac{P_{\hat{\mathbf{x}}}(\hat{\rho}\cos\hat{\phi}_n \sin\hat{\theta}_n,\ \hat{\rho}\sin\hat{\phi}_n \sin\hat{\theta}_n,\ \hat{\rho}\cos\hat{\theta}_n|\mathbf{x})}{\left|\hat{\rho}^2 \sin^2\hat{\theta}_n\right|}, \tag{3.30}$$

for the gradient and polar coordinate MLEs.

Returning to the general case when $\mathbf{R}$ is an M-D vector, the asymptotic maximum likelihood distributions for surface orientation and albedo follow Eq. 3.7 when Eqs. 3.15 and 3.16 are satisfied.

3.5.2 The Angle of Incidence

Suppose that the angle of incidence ψ is to be estimated from a single measurement R, with mean $\sigma = \rho\cos\psi$ and variance σ^2/μ, given that the albedo $\pi\rho$ is known. From Eq. 3.8, the resulting mean-square error bound is the inverse of the (scalar) Fisher information

$$\langle(\tilde{\psi} - \psi)^2\rangle \geq i^{-1} = \frac{(\cos\psi + \sigma_N)^2}{\mu \sin^2\psi}, \tag{3.31}$$

for any unbiased estimate $\tilde{\psi}$, which becomes

$$\langle(\tilde{\psi} - \psi)^2\rangle \geq i^{-1} = \frac{\cot^2\psi}{\mu}, \tag{3.32}$$

when the signal-independent noise is negligible. These expressions show resolution of the incident angle to be highest when the Lambertian surface is illuminated at shallow grazing and lowest when the surface is illuminated near normal incidence. This can be motivated physically by noting that for shallow grazing angle illumination Lambert's Law has a first order dependence that is proportional to the incident angle. Conversely, for illumination near normal incidence Lambert's Law is independent of the incident angle to first order. It is also significant that when the root mean square error (RMSE) bound is finite, it can be reduced in proportion to the square-root of

the sample size μ averaged to obtain the radiometric statistic R, as shown in detail in Section 3.4.

The MLE for the angle of incidence is

$$\hat{\psi} = \cos^{-1}\left(\frac{R - \sigma_N}{\rho}\right) \tag{3.33}$$

Many of the potential benefits and difficulties associated with maximum likelihood estimation can be illustrated by examining the statistical properties of $\hat{\psi}$.

For the remainder of this section, let σ_N be negligible, as may be expected in practical imaging systems expect at shallow grazing where ψ is very near $\pi/2$. First of all, because R is a gamma variate and can take on any positive definite value, the estimate $\hat{\psi}$ is real for $0 \leq R/\rho \leq 1$ and imaginary for $R/\rho > 1$. The probability that $\hat{\psi}$ is real is found to be $\gamma(\mu, \mu/\cos\psi)/\Gamma(\mu)$ by appropriately integrating $P_R(R|\psi)$. But this leaves finite probability $\Gamma(\mu, \mu/\cos\psi)/\Gamma(\mu)$ that $\hat{\psi}$ is imaginary. More specifically, let the statistic $\hat{\psi} = \hat{\psi}_r + \hat{\psi}_i$, where $\hat{\psi}_r$, $\hat{\psi}_i$ are the real and imaginary parts of $\hat{\psi}$ respectively. Then the statistic $\hat{\psi}$ is distributed according to

$$P_{\hat{\psi}}(\hat{\psi};\psi) = \rho \sin\hat{\psi} P_R(\rho\cos\hat{\psi};\psi) \qquad \text{over } 0 \leq \hat{\psi} \leq \pi/2, \tag{3.34}$$

for $\hat{\psi}$ real, and

$$P_{\hat{\psi}}(\hat{\psi};\psi) = \rho \sinh\hat{\psi} P_R(\rho\cosh\hat{\psi};\psi) \qquad \text{over } 0 \leq \hat{\psi} \leq \infty, \tag{3.35}$$

for $\hat{\psi}$ imaginary. The probability $\Gamma(\mu, \mu/\cos\psi)/\Gamma(\mu)$ that $\hat{\psi}$ is imaginary decreases as the angle of incidence ψ and sample size μ increase, as does the bias of $\hat{\psi}$.

Apparently, CCGR fluctuations in the radiant field can lead to unphysical MLEs of the incident angle ψ. This can be remedied by reconditioning the MLE, given ancillary information[44] that $\hat{\psi}$ is real, so that

$$P_{\hat{\psi},Re}(\hat{\psi};\psi) \equiv P_{\hat{\psi}}(\hat{\psi}|\hat{\psi} = \Re\{\hat{\psi}\};\psi) = \rho\sin\hat{\psi} P_R(\rho\cos\hat{\psi};\psi)\frac{\Gamma(\mu)}{\gamma(\mu, \mu/\cos\psi)}, \tag{3.36}$$

for $0 \leq \hat{\psi} \leq \pi/2$. Similarly, the probability that $\hat{\psi}$ is imaginary is defined as

$$P_{\hat{\psi},Im}(\hat{\psi};\psi) \equiv P_{\hat{\psi}}(\hat{\psi}|\hat{\psi} = \Im\{\hat{\psi}\};\psi) = \rho \sinh\hat{\psi} P_R(\rho\cosh\hat{\psi};\psi)\frac{\Gamma(\mu)}{\Gamma(\mu,\mu/\cos\psi)}, \quad (3.37)$$

For sufficiently large sample size μ, the relationship between MLE $\hat{\psi}$ and data $\mathbf{R}$ approaches linearity, so that $\hat{\psi}$ obeys the Gaussian distribution

$$P_{\hat{\psi},G}(\hat{\psi};\psi) = \sqrt{\frac{\mu}{2\pi\cot^2\psi}}\exp\left(-\frac{1}{2}\mu\frac{(\hat{\psi}-\psi)^2}{\cot^2\psi}\right), \quad (3.38)$$

with bias vanishing and variance equaling the inverse Fisher information, $\cot^2\psi/\mu$.

Figure 3-2 shows the probability densities of Eq. 3.36 (dash-dot line), Eq. 3.37 (dash line), and Eq. 3.38 (solid line) for $\psi = 30°$. As the sample size μ increases, the correlation between $P_{\hat{\psi},G}$ and $P_{\hat{\psi},Re}$ approaches one, while $P_{\hat{\psi},Im}$ goes to zero. For the value of ψ used in these plots, a sample size of approximately 320 is necessary for the correlation between $P_{\hat{\psi},G}$ and $P_{\hat{\psi},Re}$ to become larger than 0.99. As the true value ψ increases, the necessary sample size to achieve a good correlation is found to decrease, as discussed earlier.

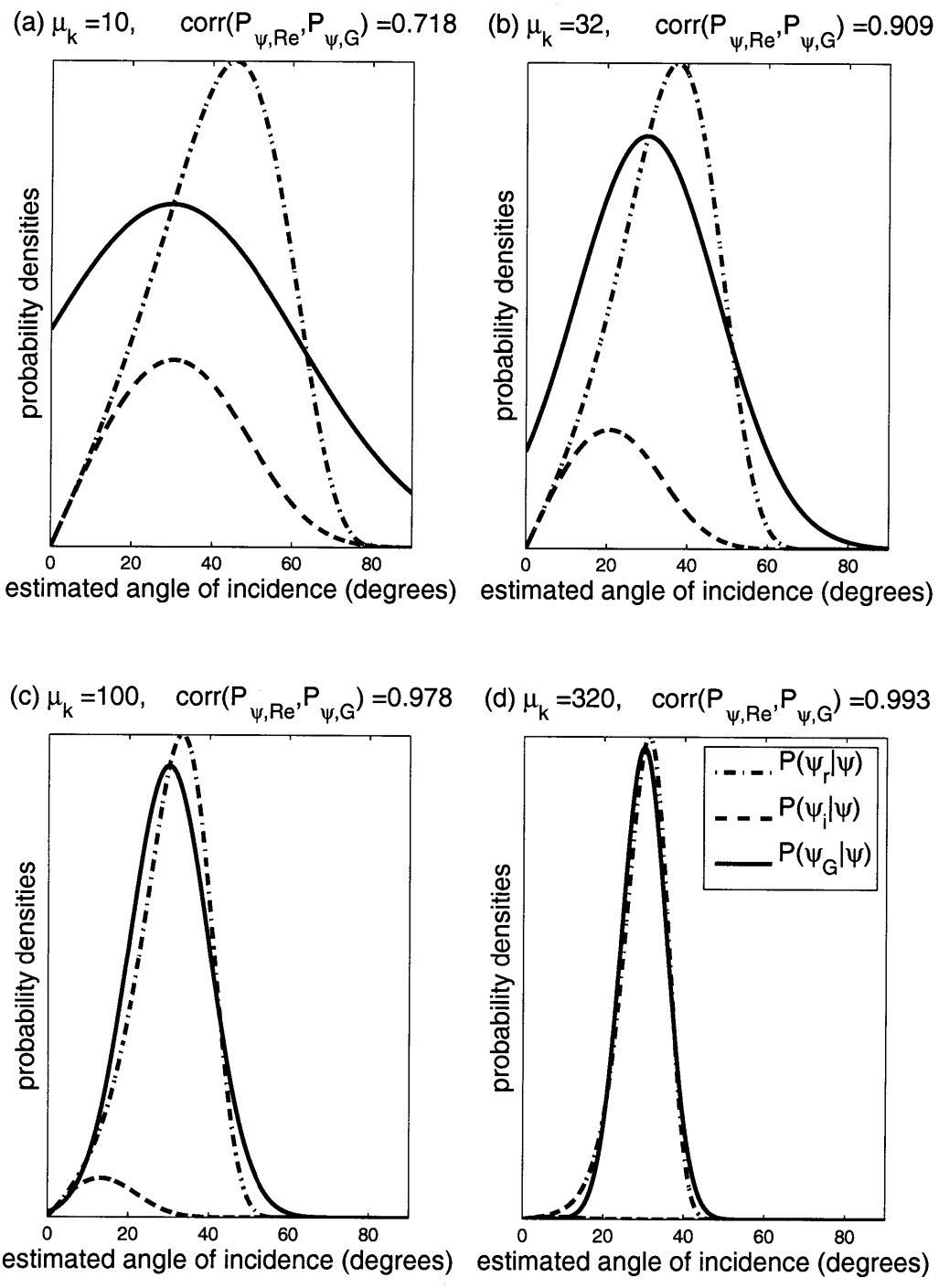

Figure 3-2: Probability densities given real, imaginary or Gaussian constraint on parameter estimate.

Following Section 3.4, $\hat{\psi}$ is effectively unbiased when

$$\mu \gg \left| \frac{\cot^3 \psi}{2\psi} \right|, \tag{3.39}$$

and effectively attains the bound $i^{-1} = \cot^2 \psi / \mu$ when

$$\mu \gg \left| \cot^2 \psi \left(3 + \frac{7}{2} \cot^2 \psi \right) \right|. \tag{3.40}$$

As the above expressions show, the sample size necessary for $\hat{\psi}$ to behave as a minimum variance, unbiased estimate varies nonlinearly from unity at shallow grazing angles to infinity near normal incidence.

Figure 3-3 shows the sample sizes necessary for the MLE to become asymptotically unbiased (Eq. 3.39, dash line), for the MLE variance to asymptotically attain the CRLB (Eq. 3.40, dash-dot line), and for the correlation between $P_{\hat{\psi},G}$ and $P_{\hat{\psi},Re}$ to be greater than 0.99 (solid line), as functions of the angle of incidence ψ. The curves have been truncated so that the minimum necessary sample size is 1. For most values of ψ, achieving a minimum variance estimate also ensures that an unbiased estimate is obtained that approximately obeys the Gaussian distribution of Eq. 3.38. For shallow-grazing incidence angles (ψ approaching 90 degrees), the sample size necessary for $P_{\hat{\psi},G}$ to be a good approximation to $P_{\hat{\psi},Re}$ becomes the limiting condition.

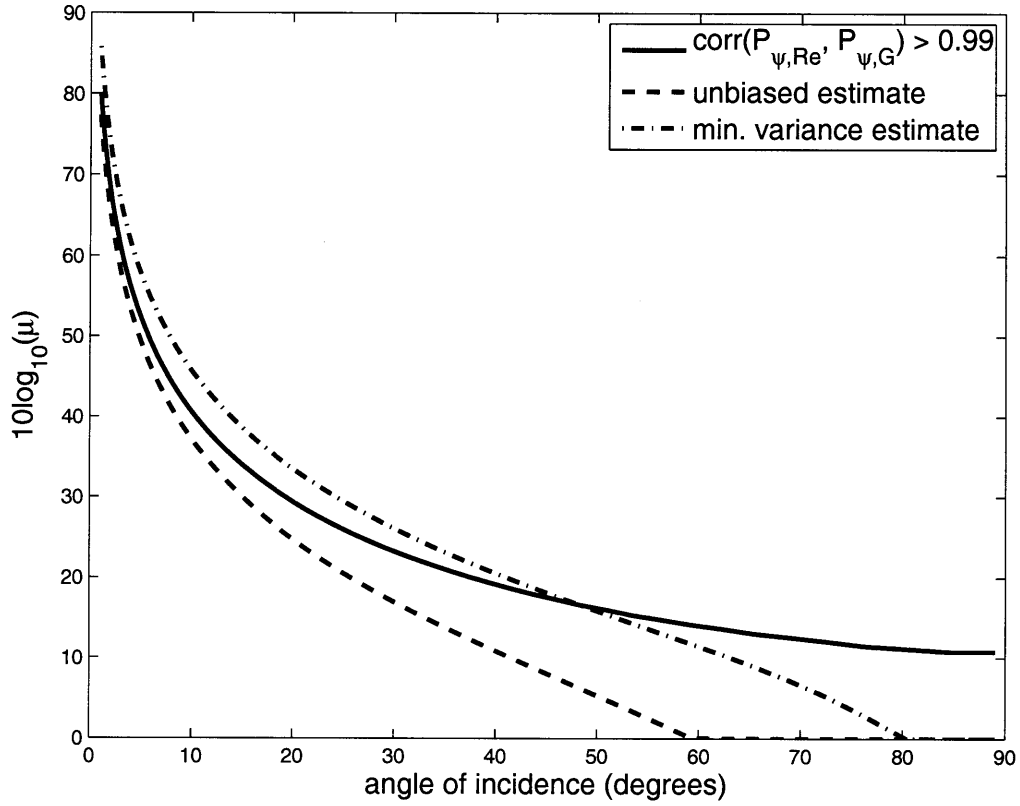

Figure 3-3: Comparison of the necessary sample sizes to achieve (a) a correlation greater than 0.99 between $P_{\hat{\psi},Re}(\hat{\psi};\psi)$ and $P_{\hat{\psi},G}(\hat{\psi};\psi)$, (b) an unbiased estimate, (c) an estimate that attains the minimum possible variance.

3.5.3 3-D Surface Orientation and Albedo

Two independent measurements of surface radiance with distinct illumination can lead to at most two unique solutions for the two components of Lambertian surface orientation.[53] This ambiguity in surface orientation can be easily resolved if one of the solutions places the surface out of the view of the observer. Otherwise, the ambiguity can be resolved if a third measurement is made under distinct illumination. These observations can be geometrically motivated by considering the intersection of the cones formed by appropriately rotating the Lambertian surface normals about the source direction for each measurement given the slope estimated from that measurement. Here, specific examples of resolution bounds on orientation estimation are presented, as well as expressions for the CRLBs for cone and polar angles, surface gradients and/or albedo given two or three measurements of surface radiance.

For surface gradient $\mathbf{a}^T = [p\ q\ r]$, or polar coordinate $\mathbf{a}^T = [\theta\ \phi\ \rho]$ parameterizations, the mean square error bound on any unbiased estimate $\tilde{\mathbf{a}}$ is

$$\langle(\tilde{\mathbf{a}} - \mathbf{a})(\tilde{\mathbf{a}} - \mathbf{a})^T\rangle \geq \mathbf{J}_{\mathbf{a}}^{-1} = \frac{\partial \mathbf{a}}{\partial \mathbf{x}} \mathbf{J}_{\mathbf{x}}^{-1} \frac{\partial \mathbf{a}}{\partial \mathbf{x}}^T, \tag{3.41}$$

where $\mathbf{J}_{\mathbf{x}}$ is given in Eq. 3.22. The bound $\mathbf{J}_{\mathbf{a}}^{-1}$ becomes singular when all the $\mathbf{s}_k$ are coplanar but not tangent to the surface for non-zero $\boldsymbol{\sigma}_N$, or when the Jacobian $\left|\frac{\partial \mathbf{a}}{\partial \mathbf{x}}\right|$ is singular. When $\boldsymbol{\sigma}_N$ vanishes, $|\mathbf{J}_x|^{1/2}|\mathbf{J}_{\boldsymbol{\sigma}}|^{-1/2}$ can be interpreted as the effective weighted volume of incident vectors $\mathbf{s}_k$. For example, when $\mathbf{R}$ is a 3-D vector, the bound $\mathbf{J}_{\mathbf{x}}^{-1}$ is

$$[\mathbf{J}_x^{-1}]_{ij} = \frac{\frac{\sigma_1^2}{\mu_1}[\mathbf{s}_2 \times \mathbf{s}_3]_i[\mathbf{s}_2 \times \mathbf{s}_3]_j + \frac{\sigma_2^2}{\mu_2}[\mathbf{s}_3 \times \mathbf{s}_1]_i[\mathbf{s}_3 \times \mathbf{s}_1]_j + \frac{\sigma_3^2}{\mu_3}[\mathbf{s}_1 \times \mathbf{s}_2]_i[\mathbf{s}_1 \times \mathbf{s}_2]_j}{(\mathbf{s}_1 \cdot \mathbf{s}_2 \times \mathbf{s}_3)^2}, \tag{3.42}$$

so that $|\mathbf{J}_x|^{1/2}|\mathbf{J}_{\boldsymbol{\sigma}}|^{-1/2}$ simply is the volume $(\mathbf{s}_1 \cdot \mathbf{s}_2 \times \mathbf{s}_3)^2$ of the parallelepiped of incident vectors. Behavior of the Jacobian $\left|\frac{\partial \mathbf{a}}{\partial \mathbf{x}}\right|$ depends upon the final coordinates $\mathbf{a}$, as can be seen from the respective forms $(p^2 + q^2 + 1)^{3/2}/\rho^2$ and $1/(\rho^2 \sin^2\theta)$ for the surface gradient and polar systems.

Assume that the measurements R_k have the same number of coherence cells,

$\mu_k = \mu$ for all k. The stereo case is considered where three measurements R_1, R_2 and R_3 are used to compute the two parameters a_1 and a_2. Let $a_1 = \alpha$ and $a_2 = \beta$ be the Lambertian surface orientations (azimuth and elevation angles, or surface gradients). The abbreviation $C_k = \sigma_k(\alpha, \beta) = \cos\psi[k]$ is used, where $\psi[k]$ denotes the angle of incidence for the k^{th} measurement. It is also convenient to define the vector $\mathbf{L}$ to have the elements $L_k = \ln C_k$, which contain the natural logarithms of the positive semi-definite measurement cosines. With this definition, the CRLB's for the general Lambertian surface orientations α and β are

$$E[(\hat{\alpha} - \alpha)^2] \geq \frac{1}{\mu} \frac{\left|\frac{\partial \mathbf{L}}{\partial \beta}\right|^2}{\left|\frac{\partial \mathbf{L}}{\partial \alpha} \times \frac{\partial \mathbf{L}}{\partial \beta}\right|^2}, \tag{3.43}$$

$$E[(\hat{\beta} - \beta)^2] \geq \frac{1}{\mu} \frac{\left|\frac{\partial \mathbf{L}}{\partial \alpha}\right|^2}{\left|\frac{\partial \mathbf{L}}{\partial \alpha} \times \frac{\partial \mathbf{L}}{\partial \beta}\right|^2}. \tag{3.44}$$

The bounds only depend upon the cosine between the source direction and Lambertian surface normal for each measurement, C_k, and the respective partial derivatives of these cosines with respect to the two orientation parameters to be estimated. It is relatively easy to determine conditions in which these expressions will attain limiting values due to the positive semi-definiteness of terms in the numerators and denominators. For example, the bounds are infinite when all three measurements are coplanar with the surface normal, such that $\mathbf{n} \cdot (\mathbf{s}[1] \times \mathbf{s}[2]) = \mathbf{n} \cdot (\mathbf{s}[2] \times \mathbf{s}[3]) = 0$. However, the bounds are not necessarily infinite for coplanar illumination directions that are not also coplanar with the surface normal, i.e. for $\mathbf{s}[1] \cdot (\mathbf{s}[2] \times \mathbf{s}[3]) = 0$, but $\mathbf{n} \cdot (\mathbf{s}[1] \times \mathbf{s}[2]) \neq 0$, or $\mathbf{n} \cdot (\mathbf{s}[2] \times \mathbf{s}[3]) \neq 0$. The bounds are zero when any of the two direction cosines C_1, C_2, C_3 are zero and the two respective illumination directions for these have differing polar angles.

It is also possible to estimate the albedo when three measurements with unique illumination directions are available. Let $a_3 = \rho$ be the surface albedo. It is useful to define the unit all-measurements-equal vector $\mathbf{E}$ by its components such that $E_k = 1$

for $k = 1, 2, 3$. With this definition, the CRLB's for estimation of α, β, ρ are given by

$$E[(\hat{\alpha} - \alpha)^2] \geq \frac{1}{\mu} \frac{\left| \frac{\partial \mathbf{L}}{\partial \beta} \times \mathbf{E} \right|^2}{\left[\left(\frac{\partial \mathbf{L}}{\partial \alpha} \times \frac{\partial \mathbf{L}}{\partial \beta} \right) \cdot \mathbf{E} \right]^2}, \tag{3.45}$$

$$E[(\hat{\beta} - \beta)^2] \geq \frac{1}{\mu} \frac{\left| \frac{\partial \mathbf{L}}{\partial \alpha} \times \mathbf{E} \right|^2}{\left[\left(\frac{\partial \mathbf{L}}{\partial \alpha} \times \frac{\partial \mathbf{L}}{\partial \beta} \right) \cdot \mathbf{E} \right]^2}. \tag{3.46}$$

$$E[(\hat{\rho} - \rho)^2] \geq \frac{\rho^2}{\mu} \frac{\left| \frac{\partial \mathbf{L}}{\partial \alpha} \times \frac{\partial \mathbf{L}}{\partial \beta} \right|^2}{\left[\left(\frac{\partial \mathbf{L}}{\partial \alpha} \times \frac{\partial \mathbf{L}}{\partial \beta} \right) \cdot \mathbf{E} \right]^2}, \tag{3.47}$$

It is noteworthy that the bound for ρ is a function of the surface orientation components α and β, as well as ρ. While the bounds for α and β given in Eqs. 3.45 and 3.46 are independent of the value of ρ, they are affected by uncertainty in the value of ρ, and Eqs. 3.43 and 3.44 are no longer applicable. These particular bounds for α and β are infinite when all three illumination directions are coplanar such that $\mathbf{s}[1] \cdot (\mathbf{s}[2] \times \mathbf{s}[3]) = 0$, even if the directions are not coplanar to the surface normal. Additionally, these bounds for α and β can be zero when any of the two direction cosines are zero.

Note that for the CRLB for ρ to be given by ρ^2/μ, and thereby be otherwise independent of Lambertian surface orientation, it is sufficient to have

$$\left(\frac{\partial \mathbf{L}}{\partial \alpha} \times \frac{\partial \mathbf{L}}{\partial \beta} \right) \cdot \mathbf{P} \left(\frac{\partial \mathbf{L}}{\partial \alpha} \times \frac{\partial \mathbf{L}}{\partial \beta} \right) = 0, \tag{3.48}$$

where the permutation matrix is defined as

$$\mathbf{P} = \begin{bmatrix} 0 & 1 & 0 \\ 0 & 0 & 1 \\ 1 & 0 & 0 \end{bmatrix}. \tag{3.49}$$

For example the CRLB for ρ is given by ρ^2/μ when any two of the measurement cosines C_1, C_2, C_3 are equal to zero.

Eqs. 3.45-3.47 are useful in providing a geometric interpretation of the CRLB for α, β and ρ given three measurements. For example, consider the conditions leading to the limiting values of zero and infinity for the bounds. Inspection of the positive semi-definite numerators and denominators of Eqs. 3.45-3.47 motivates consideration of the following two cases: (1) the partial derivative of the logarithmic measurement vector with respect to the orientation component α or β respectively is orthogonal to the all-measurements-equal vector; (2) the cross product of the partial derivatives of the logarithmic measurement vector with respect to the α and β orientations is orthogonal to the all-measurements-equal vector. When (1) is true but (2) is not, the respective bound on orientation component β or α is zero. When (1) is not true but (2) is true the bound on either orientation is infinite. As noted before, this occurs when the illumination directions for all measurements are coplanar with the surface normal. When both (1) and (2) are true, the bound on α or β depends only on the number of coherence cells.

Figures 3-4-3-6 show the CRLBs of Eqs. 3.45 - 3.47 and the necessary sample sizes of Eq. 3.15 and 3.16 for the x- and y-gradients, and surface albedo ρ. These computations exhibit the dramatic nonlinear variations in the sample sizes necessary to obtain accurate estimates of Lambertian surface orientation and albedo from multi-static acoustic, optical, radar or laser images corrupted by signal-dependent speckle noise.

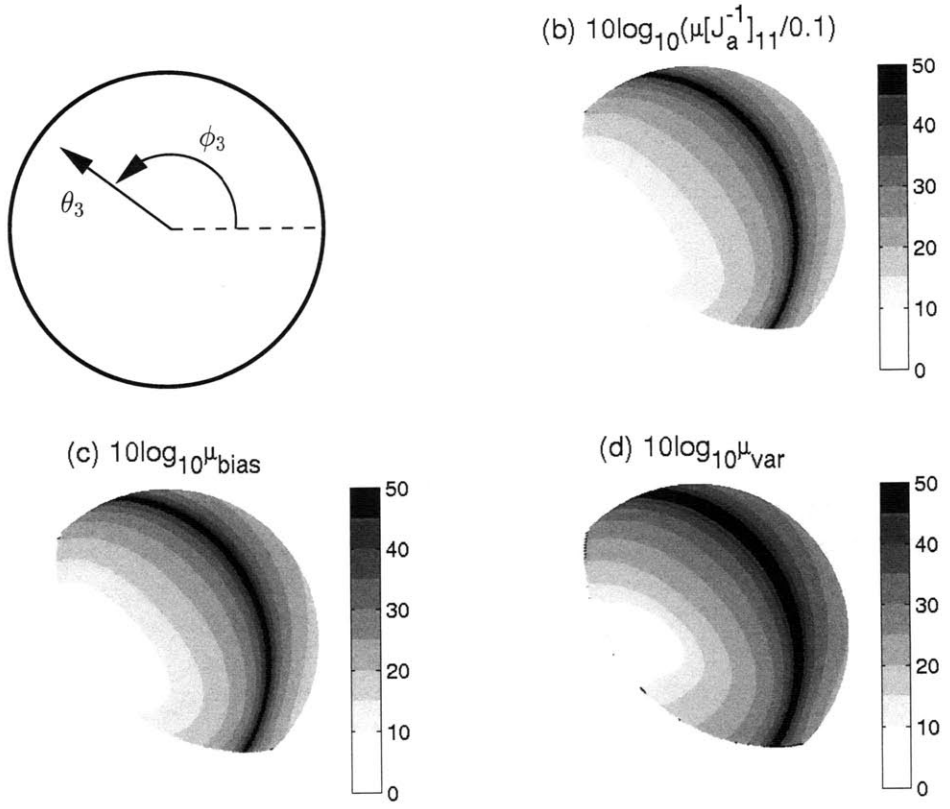

Figure 3-4: A visualization for $\mathbf{a}$ corresponding to the surface gradient parameterization for a 3-D measurement vector $\mathbf{R}$ with $\boldsymbol{\sigma}_N$ negligible and Lambertian surface defined by the polar coordinate parameterization ($\theta_n = \pi/4$, $\phi_n = \pi/4$, $\rho = 0.6$). Incident vectors $\mathbf{s}_1$ and $\mathbf{s}_2$ are fixed at $(\sqrt{2/3},\ -\sqrt{1/6},\ \sqrt{1/6})$ and $(\sqrt{1/6},\ \sqrt{2/3},\ \sqrt{1/6})$ respectively, but $\mathbf{s}_3$ is allowed to vary as in (a) where the positive z-axis is central and points out of the page. (b) The bound $[\mathbf{J}_a^{-1}]_{11}$ on the x-gradient, $a_1 = p$, including full 3-D coupling. Only values where $\mathbf{s}_3 \cdot \mathbf{n}$ is positive and the Lambertian surface is in view from the positive z-axis are shown. Optimal resolution occurs when $\mathbf{s}_3$ is tangent to the Lambertian surface along the x-axis (horizontal), for the p-bound, and the y-axis (vertical) for the q-bound (see Fig. 3-5(b)), with sign so as to maximize the volume of incident vectors. Poorest resolution occurs when the volume of incident vectors approaches zero, as realized along the dark arc. (c) The sample size necessary for the MLE $\hat{a}_1 = \hat{p}$ to be effectively unbiased, from Eq. 3.15. (d) The sample size necessary, from Eq. 3.16, for $\hat{p}$ to effectively attain the bound given in (b).

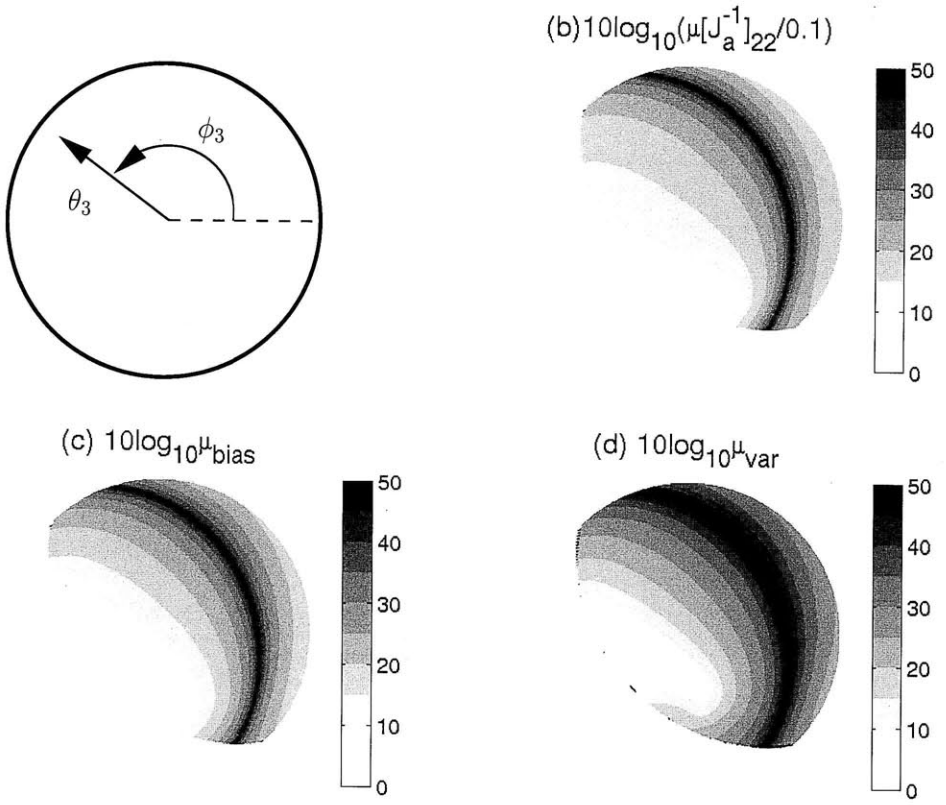

Figure 3-5: Same as Fig. 3-4 for estimation of the y-gradient, $a_2 = q$.

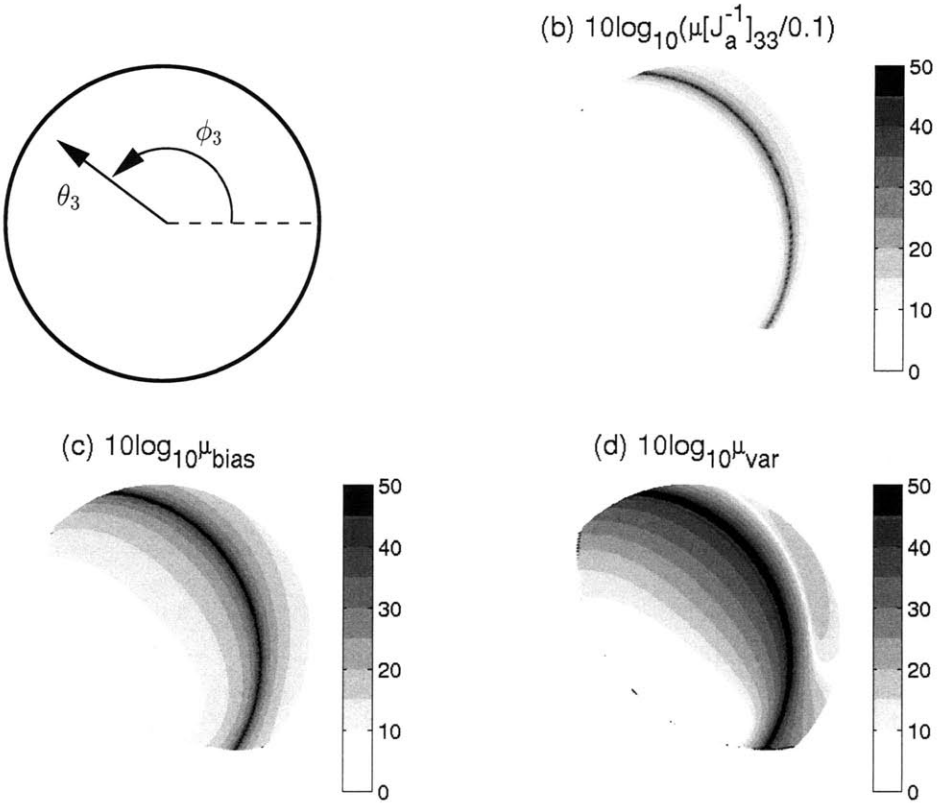

Figure 3-6: Same as Fig. 3-4 for estimation of the albedo, $a_3 = \rho$.

3.6 Conclusions

A maximum likelihood method for estimating remote surface orientation from multi-static acoustic, optical, radar or laser images is derived. It is assumed that the images are corrupted by signal-dependent noise, known as speckle, arising from complex Gaussian field fluctuations, and that the surface properties are effectively Lambertian. Surface orientation estimates for a single sample are shown to have biases and errors that vary dramatically depending on illumination direction. This is due to the signal-dependent nature of speckle noise and the nonlinear relationship between surface orientation, illumination direction and fluctuating radiance. The minimum number of independent samples necessary for maximum likelihood estimates to be asymptotically unbiased and attain classical estimation theory's lower bound on resolution as well as practical design thresholds are derived.

In a particularly compelling example, it is shown that the minimum error in estimating the angle of incidence of a Lambertian surface is at best proportional to the cotangent of this angle. The greatest accuracy occurs for estimates obtained from shallow illumination angles where Lambert's Law shows its greatest sensitivity to surface illumination, while poorest resolution occurs near normal incidence where sensitivity is the least. For the general stereo case where at least three measurements are used to estimate 3-D surface orientation and albedo, the minimum mean square error is shown to be inversely proportional to the volume delimited by the unit normals of incident illumination. As a result, the number of samples or SNR necessary to accurately estimate surface orientation and albedo is shown to become arbitrarily large as the illumination directions approach the coplanar limit, while accurate stereo resolution of 3-D surface orientation and albedo is shown to be possible even with a single sample given illumination directions of sufficient diversity and shallow angle incidence.

Chapter 4

General Second-Order Covariance of Gaussian Maximum Likelihood Estimates Applied to Passive Source Localization in Fluctuating Waveguides

4.1 Introduction

In remote sensing applications, parameter estimation often requires the nonlinear inversion of measured data that are randomized by additive signal-independent ambient noise, as well as signal-dependent noise arising from fluctuations in the propagation medium. Parameter estimates obtained from such nonlinear inversions are typically biased and do not attain desired experimental error thresholds. For this reason, necessary conditions have been developed on sample size or Signal to Noise Ratio (SNR) to obtain accurate estimates and aid experimental design.[84]

These conditions are derived by first expanding the bias and covariance of maximum likelihood estimates (MLEs) in inverse order of sample size or SNR, where the

first-order covariance term is the minimum variance, the Cramer-Rao Lower Bound (CRLB), which is also the minimum mean square error (MSE) of any unbiased estimate regardless of the method of estimation. It is then required that (i) the first-order bias term and the second-order covariance term become much smaller than the true value of the parameter and the CRLB, respectively, and (ii) the CRLB falls within desired error thresholds.

Here, we provide an analytical expression for the second-order covariance term of MLEs obtained from general complex Gaussian data vectors, which can then be used in many practical problems since (i) data distributions can often be assumed to be Gaussian by virtue of the central limit theorem, and (ii) it allows for *both* the mean and the variance of the measurement to be functions of the estimation parameters, as is the case in the presence of signal-dependent noise. For example, the expression can be used to aid the design of many experiments in a variety of fields where nonlinear inversions are typically performed and data are often corrupted by signal-dependent noise, such as ocean acoustics, geophysics, statistical signal processing and optics.[104, 49, 30]

We then consider the problem of source localization in a fluctuating ocean waveguide containing random internal waves and calculate the minimum array-gain-augmented Signal to Additive Noise Ratio (SANR) necessary for accurate localization. The fluctuating ocean waveguide is modeled using analytical expressions for the mean, mutual intensity, and spatial covariance of the acoustic field forward propagated through random 3-D internal waves in a stratified ocean waveguide for a continuous wave (CW) narrowband signal.[21] This model provides an analytical treatment of the loss of intermodal coherence in the forward propagating field due to scattering by internal waves. While the ensuing degradation in localization performance may be expected,[4, 3] the exact effect of internal waves is here quantified for the first time by computing the asymptotic biases and variances of source localization estimates. The results presented here can be used to quantify the effects of environmental uncertainties on passive source localization techniques, such as matched-field processing (MFP) and focalization,[24] both of which typically utilize line arrays and CW signals.

Incomplete or imprecise knowledge of environmental parameters and randomness in the propagation environment are known to seriously deteriorate the performance of MFP, which has been investigated extensively in the past.[103, 46, 97, 43, 94, 42, 108, 107, 96, 111] MFP has been demonstrated in a number of theoretical and experimental scenarios involving fluctuating or unknown environments,[42, 96, 111] but with significant localization ambiguities due to multimodal propagation and environmental mismatch. For example, in Ref. [111] it was shown that given $10\log_{10}$SNR of more than 20 dB, peaks in the MFP ambiguity surface occured at the true source range, but significant sidelobes were also observed at other ranges. All past experimental demonstrations of MFP have used SNRs that have exceeded the minimum levels necessary for accurate localization derived here.

Previously, the performance of passive source localization techniques was investigated by deriving CRLBs in a non-fluctuating waveguide.[4] Later it was shown that these were single-sample bounds,[72] multiple sample bounds were derived,[72, 41] and it was shown that stationary averaging could reduce the bounds to zero.[72] Asymptotic statistics were then used to derive necessary conditions on sample size for errors to attain the CRLB and these were applied to source localization in a non-fluctuating waveguide.[102] Our approach is based on classical estimation theory,[84] is independent of the estimation technique and has already been applied in a variety of other problems, including time-delay and Doppler shift estimation,[84] pattern recognition in 2-D images,[11] geoacoustic parameter inversion, [110] and planetary terrain surface slope estimation.[8] In all previous applications except the last, however, the measurement was modeled as either (i) a deterministic signal vector, or (ii) a fully randomized signal vector with zero mean, both embedded in additive white noise. These are special cases of the scenario considered here where *both* the mean and the variance of the measurement are parameter-dependent, which is necessary to properly model acoustic propagation through a fluctuating waveguide that leads to a signal-dependent noise component. The methodology presented here can then be used in any experimental design to ensure that statistical biases and errors meet necessary error thresholds.

In Section 4.2, we first review the first-order bias and first-order covariance of MLEs given general multivariate Gaussian data. We then provide a new analytic expression for the second-order covariance. In Section 4.3, we calculate the MLE statistics and determine necessary conditions on sample size or SNR to obtain estimates that meet any design error threshold in a deterministic and a random waveguide.

4.2 General Asymptotic Expansions for the Bias and Covariance of the MLE

In this section, we first review the asymptotic expansions for the bias and covariance of the MLE. We also summarize the conditions necessary for an MLE to become asymptotically unbiased and have a variance that attains the CRLB. We then provide a new expression for the second-order covariance of the MLE given general multivariate Gaussian random data and describe how these measurements are obtained.

4.2.1 General Multivariate Gaussian Data

The general bias and variance expressions of Eqs. (A.8-A.10) are now applied to the specific case of data that obey the conditional Gaussian probability density[60]

$$p(\mathbf{X};\boldsymbol{\theta}) = \frac{1}{(2\pi)^{nN/2}|\mathbf{C}(\boldsymbol{\theta})|^{n/2}} \exp\left\{ -\frac{1}{2}\sum_{j=1}^{n}(\mathbf{X}_j - \boldsymbol{\mu}(\boldsymbol{\theta}))^T\mathbf{C}(\boldsymbol{\theta})^{-1}(\mathbf{X}_j - \boldsymbol{\mu}(\boldsymbol{\theta}))\right\} \tag{4.1}$$

where $\mathbf{C}$ is the real-valued covariance matrix, and $\boldsymbol{\mu}$ is the real-valued mean of the real random data. Similarly to the work of Ref. [102], in the present study of underwater localization, $\mathbf{X}_j$ represents the real and imaginary parts of the narrow-band acoustic data collected across an array of $N/2$ sensors around the given harmonic-source frequency, and the parameter set $\boldsymbol{\theta}$ represents the range and depth of the acoustic source.

The first-order bias has already been provided in Eq. (7) of Ref. [84] and is repeated

below

$$b_1(\hat{\theta}^r;\boldsymbol{\theta},n) \;=\; -\frac{1}{2}i^{ra}i^{bc}\Big(\boldsymbol{\mu}_{bc}\mathbf{C}^{-1}\boldsymbol{\mu}_a - \boldsymbol{\mu}_b(\mathbf{C}^{-1})_a\boldsymbol{\mu}_c + \frac{1}{2}tr(\check{\mathbf{C}}_{bc}\check{\mathbf{C}}_a)\Big), \qquad (4.2)$$

Typically, as discussed in the Introduction, both the data mean and covariance in Eq. (4.1) are functions of the desired parameter set $\boldsymbol{\theta}$. This necessitates evaluation of the joint moments in Eq. (A.10) as shown in Ref. [68] and summarized in Appendix B. The second-order covariance of the MLE given multivariate Gaussian random data is given by[68]

$$\begin{aligned}
var_2(\hat{\theta}^r;\boldsymbol{\theta},n) = {} & -i^{rr} + i^{rm}i^{rm}i^{ab}\Big[\boldsymbol{\mu}_{ma}\mathbf{C}^{-1}\boldsymbol{\mu}_{mb} - \boldsymbol{\mu}_{mm}\mathbf{C}^{-1}\boldsymbol{\mu}_{ab} - \boldsymbol{\mu}_{mab}\mathbf{C}^{-1}\boldsymbol{\mu}_m \\
& + tr(\check{\mathbf{C}}_m\check{\mathbf{C}}_m\check{\mathbf{C}}_a\check{\mathbf{C}}_b) + tr(\check{\mathbf{C}}_m\check{\mathbf{C}}_a\check{\mathbf{C}}_m\check{\mathbf{C}}_b) + tr(\check{\mathbf{C}}_{ab}\check{\mathbf{C}}_m\check{\mathbf{C}}_m) - tr(\check{\mathbf{C}}_{ma}\check{\mathbf{C}}_m\check{\mathbf{C}}_b) \\
& - tr(\check{\mathbf{C}}_{ma}\check{\mathbf{C}}_b\check{\mathbf{C}}_m) + \frac{1}{2}tr(\check{\mathbf{C}}_{ma}\check{\mathbf{C}}_{mb}) - \frac{1}{2}tr(\check{\mathbf{C}}_{mm}\check{\mathbf{C}}_{ab}) - \frac{1}{2}tr(\check{\mathbf{C}}_{mab}\check{\mathbf{C}}_m) \\
& + 4\boldsymbol{\mu}_{ma}(\mathbf{C}^{-1})_m\boldsymbol{\mu}_b + 2\boldsymbol{\mu}_{ma}(\mathbf{C}^{-1})_b\boldsymbol{\mu}_m - \boldsymbol{\mu}_{ab}(\mathbf{C}^{-1})_m\boldsymbol{\mu}_m + \boldsymbol{\mu}_a(\mathbf{C}^{-1})_{mm}\boldsymbol{\mu}_b \\
& + \boldsymbol{\mu}_m(\mathbf{C}^{-1})_a(\mathbf{C}^{-1})_b\boldsymbol{\mu}_m + 2\boldsymbol{\mu}_m(\mathbf{C}^{-1})_a(\mathbf{C}^{-1})_m\boldsymbol{\mu}_b + \boldsymbol{\mu}_a(\mathbf{C}^{-1})_m(\mathbf{C}^{-1})_m\boldsymbol{\mu}_b\Big] \\
& + i^{rm}i^{rm}i^{ab}i^{cd}\Big\{\boldsymbol{\mu}_{ma}\mathbf{C}^{-1}\boldsymbol{\mu}_c\Big[- \boldsymbol{\mu}_{md}\mathbf{C}^{-1}\boldsymbol{\mu}_b - 2\boldsymbol{\mu}_b(\mathbf{C}^{-1})_d\boldsymbol{\mu}_m - 4\boldsymbol{\mu}_b(\mathbf{C}^{-1})_m\boldsymbol{\mu}_d \\
& \quad - tr(\check{\mathbf{C}}_{md}\check{\mathbf{C}}_b) + tr(\check{\mathbf{C}}_{bd}\check{\mathbf{C}}_m) + tr(\check{\mathbf{C}}_m\check{\mathbf{C}}_b\check{\mathbf{C}}_d) + tr(\check{\mathbf{C}}_m\check{\mathbf{C}}_d\check{\mathbf{C}}_b)\Big] \\
& + \boldsymbol{\mu}_{ac}\mathbf{C}^{-1}\boldsymbol{\mu}_m\Big[\frac{1}{2}\boldsymbol{\mu}_{bd}\mathbf{C}^{-1}\boldsymbol{\mu}_m + 2\boldsymbol{\mu}_{mb}\mathbf{C}^{-1}\boldsymbol{\mu}_d + \frac{1}{2}tr(\check{\mathbf{C}}_{bd}\check{\mathbf{C}}_m) - tr(\check{\mathbf{C}}_m\check{\mathbf{C}}_b\check{\mathbf{C}}_d) \\
& \quad + tr(\check{\mathbf{C}}_{mb}\check{\mathbf{C}}_d)\Big] + tr(\check{\mathbf{C}}_m\check{\mathbf{C}}_a\check{\mathbf{C}}_c)\Big[\boldsymbol{\mu}_m(\mathbf{C}^{-1})_b\boldsymbol{\mu}_d + \boldsymbol{\mu}_m(\mathbf{C}^{-1})_d\boldsymbol{\mu}_b + 3\boldsymbol{\mu}_b(\mathbf{C}^{-1})_m\boldsymbol{\mu}_d \\
& \quad - \frac{1}{2}\big(tr(\check{\mathbf{C}}_m\check{\mathbf{C}}_b\check{\mathbf{C}}_d) + tr(\check{\mathbf{C}}_m\check{\mathbf{C}}_d\check{\mathbf{C}}_b) - tr(\check{\mathbf{C}}_{md}\check{\mathbf{C}}_b) - tr(\check{\mathbf{C}}_{mb}\check{\mathbf{C}}_d) + tr(\check{\mathbf{C}}_{bd}\check{\mathbf{C}}_m)\big)\Big] \\
& + tr(\check{\mathbf{C}}_{ma}\check{\mathbf{C}}_c)\Big[- \frac{1}{4}tr(\check{\mathbf{C}}_{md}\check{\mathbf{C}}_b) - \boldsymbol{\mu}_m(\mathbf{C}^{-1})_d\boldsymbol{\mu}_b - 2\boldsymbol{\mu}_b(\mathbf{C}^{-1})_m\boldsymbol{\mu}_d\Big] \\
& - \frac{3}{2}\boldsymbol{\mu}_a(\mathbf{C}^{-1})_m\boldsymbol{\mu}_c\boldsymbol{\mu}_b(\mathbf{C}^{-1})_m\boldsymbol{\mu}_d + tr(\check{\mathbf{C}}_{ac}\check{\mathbf{C}}_m)\Big[\frac{1}{2}tr(\check{\mathbf{C}}_{mb}\check{\mathbf{C}}_d) + \frac{1}{8}tr(\check{\mathbf{C}}_{bd}\check{\mathbf{C}}_m)\Big] \\
& + \boldsymbol{\mu}_m(\mathbf{C}^{-1})_a\boldsymbol{\mu}_c\Big[- \boldsymbol{\mu}_m(\mathbf{C}^{-1})_d\boldsymbol{\mu}_b - 2\boldsymbol{\mu}_b(\mathbf{C}^{-1})_m\boldsymbol{\mu}_d\Big] \\
& + \Big[\boldsymbol{\mu}_{cd}\mathbf{C}^{-1}\boldsymbol{\mu}_a - \boldsymbol{\mu}_c(\mathbf{C}^{-1})_a\boldsymbol{\mu}_d + \frac{1}{2}tr(\check{\mathbf{C}}_{cd}\check{\mathbf{C}}_a)\Big]\Big[\frac{1}{2}tr(\check{\mathbf{C}}_{mm}\check{\mathbf{C}}_b) + \frac{1}{2}tr(\check{\mathbf{C}}_{mb}\check{\mathbf{C}}_m) \\
& \quad - tr(\check{\mathbf{C}}_m\check{\mathbf{C}}_m\check{\mathbf{C}}_b) + \boldsymbol{\mu}_{mm}\mathbf{C}^{-1}\boldsymbol{\mu}_b + \boldsymbol{\mu}_{mb}\mathbf{C}^{-1}\boldsymbol{\mu}_m + \boldsymbol{\mu}_m(\mathbf{C}^{-1})_m\boldsymbol{\mu}_b\Big]\Big\} \qquad (4.3)
\end{aligned}$$

where subscripts indicate derivatives with respect to the specified indices, $tr(\mathbf{C})$

stands for the trace of $\mathbf{C}$, and the auxiliary term $\check{\mathbf{C}}_R$ is defined in Eq. (B.1c) for an arbitrary set of indices R. As shown in Appendix B, the above expression can be used even if the random data are not distributed in a Gaussian form, provided that they can be expressed as functions of Gaussian random variables with a Jacobian of the transformation that is independent of the parameter set $\boldsymbol{\theta}$.[68] Equation (4.3) can be used to calculate the second-order MLE covariance in applications where *both* the data mean and covariance are functions of the estimated parameters.

4.2.2 Mean and Variance of the Measured Field

We consider a vertical receiving array employed to localize a harmonic source in a fluctuating ocean waveguide. The mean and covariance of the measured field can then be obtained from the analytical expressions provided in Ref. [21] and summarized in Appendix D. Equation (D.1) defines the qth element of the vector $\overline{\boldsymbol{\mu}}$ for $q = 1, 2, 3, \ldots, N/2$, where $N/2$ is the number of hydrophones in the receiving array. Similarly, Eq. (D.4) defines the (q, p) element of the covariance matrix $\overline{\mathbf{C}}$ for $q, p = 1, 2, 3, \ldots, N/2$. In the above, we have defined the complex mean $\overline{\boldsymbol{\mu}}$ and covariance $\overline{\mathbf{C}}$ that are related to the real mean $\boldsymbol{\mu}$ and covariance $\mathbf{C}$ of Eq. (4.1) by the following expressions:[60]

$$\boldsymbol{\mu} = \begin{bmatrix} \mathrm{Re}(\overline{\boldsymbol{\mu}}) \\ \mathrm{Im}(\overline{\boldsymbol{\mu}}) \end{bmatrix}, \qquad \mathbf{C} = \frac{1}{2} \begin{bmatrix} \mathrm{Re}(\overline{\mathbf{C}}) & -\mathrm{Im}(\overline{\mathbf{C}}) \\ \mathrm{Im}(\overline{\mathbf{C}}) & \mathrm{Re}(\overline{\mathbf{C}}) \end{bmatrix} + \sigma_{an}^2 \mathbf{I} \tag{4.4}$$

where $\mathbf{I}$ is the identify matrix and σ_{an}^2 is defined as the instantaneous variance of the additive noise on each hydrophone. The expressions above are valid under the assumption that the complex Fourier transform of the data measured at each hydrophone follow a circularly complex Gaussian random process[49] when the mean is subtracted. Evaluation of Eqs. (A.8-A.10) requires knowledge of the higher-order derivatives of $\boldsymbol{\mu}$ and $\mathbf{C}$ with respect to parameters ρ and z_0, which are provided in Appendix D.

The SNR and Signal to Additive Noise Ratio (SANR) for a single sample collected

across the array are then defined as

$$SNR[1] = \frac{\sum_{q=1}^{N/2} |\langle \Psi_T(\mathbf{r}_q|\mathbf{r}_0)\rangle|^2}{\sum_{q=1}^{N/2} [\mathrm{Var}(\Psi_T(\mathbf{r}_q|\mathbf{r}_0)) + \sigma_{an}^2]} = \frac{tr(|\overline{\boldsymbol{\mu}}|^2)}{tr(\overline{\mathbf{C}}) + N\sigma_{an}^2/2} \tag{4.5}$$

$$SANR[1] = \frac{\sum_{q=1}^{N/2} [|\langle \Psi_T(\mathbf{r}_q|\mathbf{r}_0)\rangle|^2 + \mathrm{Var}(\Psi_T(\mathbf{r}_q|\mathbf{r}_0))]}{N\sigma_{an}^2/2} = \frac{tr(|\overline{\boldsymbol{\mu}}|^2) + tr(\overline{\mathbf{C}})}{N\sigma_{an}^2/2} \tag{4.6}$$

Since the total received intensity is given by the numerator of Eq. (4.6), we adopt the convention[102] of setting the SANR[1] of the field across the array to unity *for a source located at r = 1 km range and any depth z*, to maintain consistency between the different waveguides examined in the next section. The definition provided in Eq. (4.6) does not account for potential improvements due to array gain. For a uniform array of $N/2$ elements, the SANR[1] can be array-gain-augmented by $(N/2)$ for the ideal case of a plane wave signal embedded in spatially uncorrelated white noise.[104] For a deterministic signal embedded in additive white noise, the covariance matrix $\mathbf{C}$ reduces to $\sigma_{an}^2\mathbf{I}$ so that SNR and SANR are equal and proportional to sample size,[102]

$$n = \frac{SANR}{SANR[1]} \tag{4.7}$$

The sample size conditions in Eqs. (A.6) and (A.7) can then also be written in terms of SANR and SANR[1]. For general multivariate Gaussian data, this simple proportionality is only approximately valid when the signal-dependent noise contribution to the covariance is weak.

4.3 Illustrative Examples

Here we demonstrate how the methodology presented in Section A and the expression for the MLE second-order covariance in Eq. (4.3) can be used to specify conditions on sample size or SNR to obtain accurate source localization estimates in a fluctuating ocean waveguide. The effects of the loss of coherence in the forward propagating field are quantified by (i) calculating these sample sizes and SNRs, as well as the

asymptotic biases and variances of source localization MLEs, and (ii) comparing them to those for a static waveguide. In the latter, the measured acoustic field is fully coherent, and the source localization problem reduces to that of parameter estimation given a deterministic signal embedded in white additive Gaussian noise. Such a problem was treated for a different waveguide, source frequency and receiving array in Ref. [102], and results are presented here for comparison with the fluctuating waveguide case considered. In the fluctuating waveguide, both the mean and the variance of the measurement are parameter dependent so that Eq. (4.3) must be used to correctly calculate the asymptotic MLE variance. The internal wave height standard deviation is chosen to be greater than the acoustic wavelength so that the waveguide becomes highly randomized within a few kilometers of the source,[21] and the effects of environmental uncertainty on source localization can be distinguished.

The simple two-layer waveguide used in Ref. [21] is again employed here to model internal waves in a shallow-water continental shelf environment. Figure 4-1 shows the selected sound speed profile, bottom composition and internal wave characteristics. The origin of the coordinate system is placed at the sea surface. The z axis points downward and normal to the interface between horizontal strata. The water depth is H and the boundary separating the upper and lower medium is at depth $z = D$. Let coordinates of the source be defined by $\mathbf{r_0} = (-\rho_0, 0, z_0)$, and receiver coordinates by $\mathbf{r} = (0, 0, z)$. Spatial cylindrical (ρ, ϕ, z) and spherical systems (r, θ, ϕ) are defined by $x = r\sin\theta\cos\phi$, $y = r\sin\theta\sin\phi$, $z = r\cos\theta$, and $\rho = x^2 + y^2$. The horizontal and vertical wave number components for the nth mode are, respectively, $\xi_n = k\sin\alpha_n$ and $\gamma_n = k\cos\alpha_n$, where α_n is the elevation angle of the mode measured from the z axis. Here, $0 \leq \alpha_n \leq \pi/2$ so that down- and up-going plane wave components of each mode will then have elevation angles α_n and $\pi - \alpha_n$, respectively. The azimuth angle of the modal plane wave is denoted by β, where $0 \leq \beta \leq 2\pi$. The geometry of spatial and wave number coordinates is shown in Ref. [74].

For single frequency simulations, we employ a 415 Hz monopole source and a 10-element vertical array in a 100 m deep waveguide. The water column is comprised of a warm upper layer with density $d_1 = 1024$ kg/m^3 and source speed $c_1 = 1520$

m/s overlying a cool lower layer with density $d_2 = 1025$ kg/m^3 and sound speed $c_2 = 1500$ m/s. The boundary between the layers is at a depth of $D = 30$ m, and the attenuation in both layers is $\alpha = 6{\times}10^{-5}$ dB/λ. The spacing of the array elements is 1.5 m ($\lambda/2 \approx 1.8$ m) with the shallowest element at 43.5 m, so that the array is centered in the water-column. The ocean bottom is a fluid half space with a sound speed of $c_b = 1700$ m/s, a density of $d_b = 1.9$ kg/m^3, and an attenuation of $\alpha_b = 0.8$ dB/wavelength, which are representative values for sandy environments.

Note that the results presented in this paper are not representative of the performance of the waveguide invariant[23, 15] or the array invariant,[65] since the former uses acoustic intensity data versus range and frequency and the latter employs beam-time or coherent hydrophone data over time. Here, we instead consider instantaneous measurements of the acoustic field due to a CW source made with a vertical line array. The results presented here can also be used for broadband signals when matched-field processing is performed separately for each frequency component and the computed ambiguity surfaces are then combined incoherently. This is commonly known as incoherent processing,[111, 98] even though each separate frequency bin is still processed coherently before the correlation values of the data and replica fields are averaged. For a broadband signal that consists of M_f frequency bins, incoherent averaging means that the effective sample size equals $n \times M_f$, so that conditions on the necessary sample sizes can be found by scaling the right hand sides of Eqs. (A.6a), (A.6b) and (A.7) by $1/M_f$.

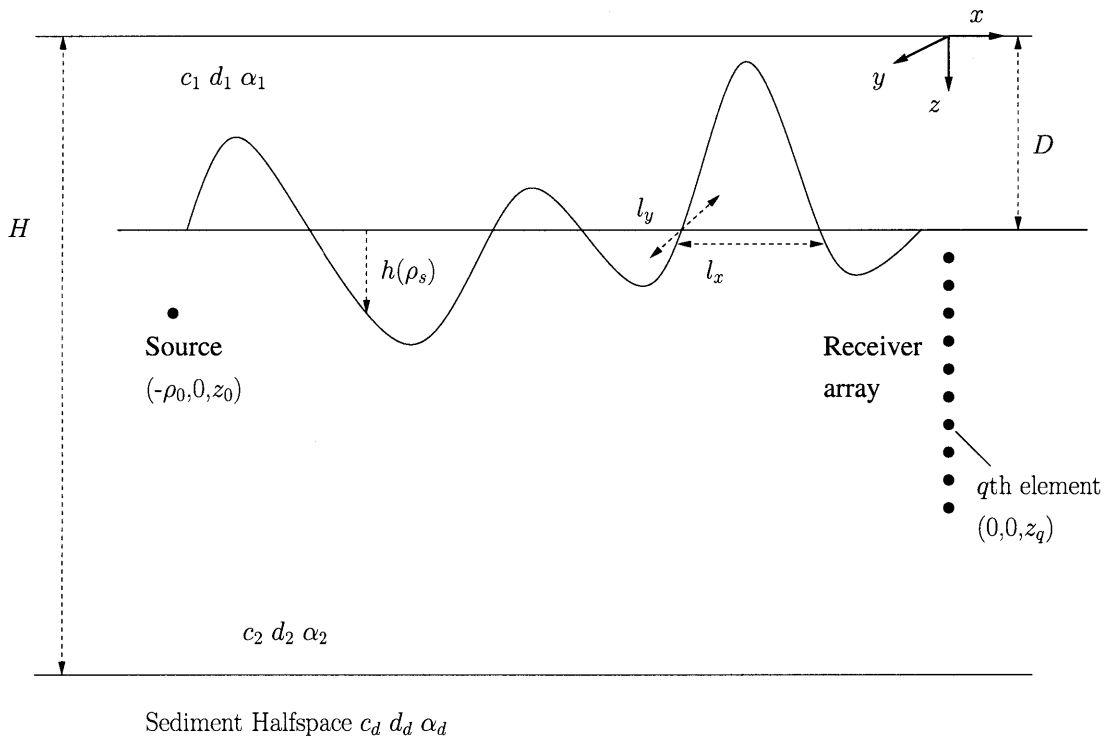

Figure 4-1: Geometry of an ocean waveguide environment with two-layer water column of total depth $H = 100$ m, and upper layer depth of $D = 30$ m. The bottom sediment half-space is composed of sand. The internal wave disturbances have coherence length scales l_x and l_y in the x and y directions, respectively, and are measured with positive height h measured downward from the interface between the upper and lower water layers.

4.3.1 Undisturbed Waveguide

For the undisturbed static waveguide, coherent interference between the waveguide modes leads to a range- and depth-dependent structure in the total acoustic field intensity which maintains a modal coherence pattern over very long ranges with the SANR range-depth pattern of Fig. 4-2. The SANR[1] is computed using Eq. (4.6) and plotted as a function of source-receiver range and source depth for the shallow water waveguide of Fig. 4-1 when there are no internal waves present. The source level is fixed as a constant over range so that $10\log_{10}$SANR[1] is 0 dB across the array for a source-receiver range of 1 km. For the static waveguide, the covariance of the acoustic field measurement in Eq. (4.4) reduces to $\mathbf{C} = \sigma_{an}^2\mathbf{I}$ so that SNR[1] and SANR[1] in Eqs. (4.5-4.6) are equivalent. For the array of 10 elements considered here, the array-gain-augmented SANR[1] is higher than the SANR[1] shown in Fig. 4-2 by a factor of 10.

The first-order bias, first-order covariance (CRLB) and second-order covariance of the MLEs for source range and depth are plotted in Fig. 4-3, given a source fixed at 50 m depth and a sample size of $n = 1$. The asymptotic bias and the square root of the CRLB for a range estimate are very small, typically less than 10 m even at ranges beyond 30-40 km, while the corresponding quantities for a depth estimate (Fig. 4-3(b)) reach values comparable to the waveguide depth of 100 m. This suggests that it may be possible to obtain unbiased range MLEs from a single sample, whereas depth MLEs will have significant biases, *given the SANR[1] in Fig. 4-2.* The second-order covariance exceeds the CRLB for both the range and depth MLE even at a few kilometers from the source, so that the variance of MLEs obtained from a single sample will not in general attain the CRLB. The CRLB and the second-order covariance approximately coincide where $10\log_{10}$SANR[1] is about -5 dB, which is where the array-gain-augmented $10\log_{10}$SANR[1] equals 5 dB. Increasing the arrain gain could help obtain single-sample MLEs that attain the CRLB at longer ranges from the source.

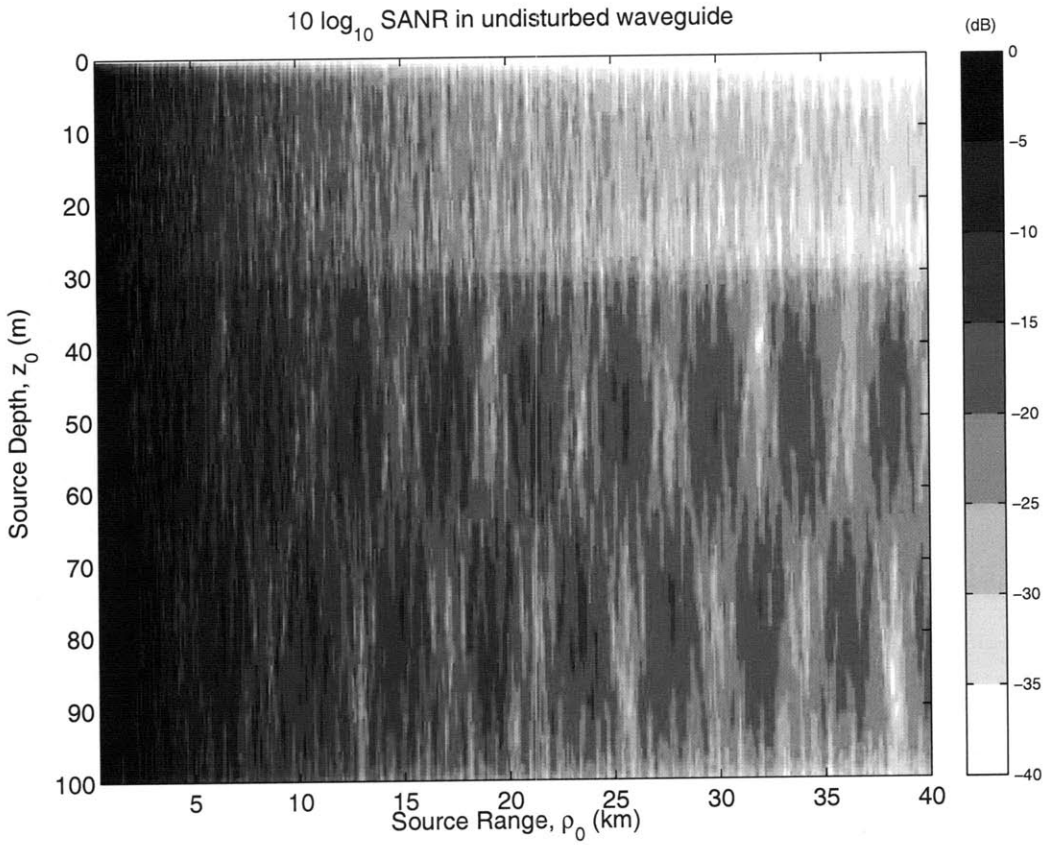

Figure 4-2: Signal to Additive Noise Ratio (SANR) at 415 Hz in an undisturbed waveguide with no internal waves. The SANR received at the 10-element vertical array described in Section 4.3 is plotted as a function of source range ρ_0 and depth z_0. The observed range-depth pattern is due to the underlying modal coherence structure of the total acoustic field intensity. The receiver array is centered at $\rho = 0$ m and $z = 50$ m. The source level is fixed as a constant over range so that $10\log_{10}\text{SANR}[1]$ is 0 dB at 1 km source range at all source depths. For the undisturbed waveguide, SANR is equivalent to Signal to Noise Ratio (SNR).

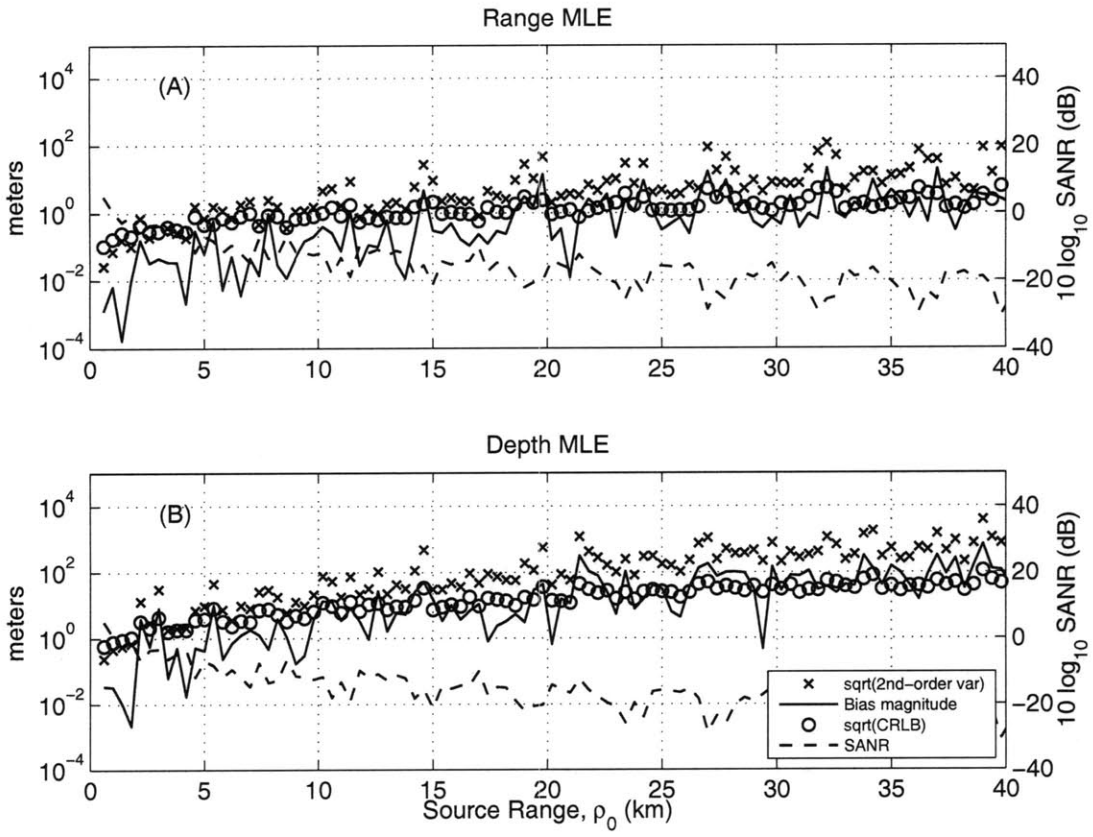

Figure 4-3: Ocean acoustic localization MLE behavior given a single sample for (a) range estimation and (b) depth estimation for a 415 Hz source placed at 50 m depth in an undisturbed waveguide with no internal waves. The MLE first-order bias magnitude (solid line), square root of the CRLB (circle marks) and square root of the second-order variance (cross marks), as well as the measured Signal to Additive Noise Ratio (SANR, dashed line) are plotted as functions of source range. Given the necessary sample size conditions in Eq. (A.6), whenever the first-order bias and the second-order variance attain roughly 10% of the true parameter value and the CRLB, respectively, more than a single sample will be needed to obtain unbiased, minimum variance MLEs. The source level is fixed as a constant over range so that $10\log_{10}\text{SANR}[1]$ is 0 dB at 1 km source range.

The results shown here are consistent with those of Figs. 2 and 4 of Ref. [102] for a deterministic source signal in a static waveguide, as expected. Since the bias and variance terms in the asymptotic expansions of the MLE moments, e.g. Eq. (A.3), always depend on inverse order of sample size n, the asymptotic statistics of the MLE for any arbitrary n can be obtained by shifting the curves in Fig. 4-3 according to the order of the term involved and the value of n desired for a given SANR[1]. For the static waveguide, the data covariance $\mathbf{C}$ is parameter independent, in which case the MLE bias and covariance can also be expanded in inverse orders of SNR.[68] The necessary sample sizes given throughout this section can then also be interpreted in terms of necessary SNR or SANR. Increasing SANR by a factor of 10 in Fig. 4-3, for example, would reduce the first-order bias and the CRLB by one order of magnitude, and the second-order covariance by two orders of magnitude, as seen by replacing n in Eqs. (A.2) and (A.3) with SANR/SANR[1] (Eq. (4.7)). Minimum variance range MLEs could then be obtained from a single sample up to the maximum range for which the second-order covariance and the CRLB are equal in Fig. 4-3, i.e. 8 km, given such a factor of 10 increase in SANR.

Figure 4-4 shows the sample size n necessary to obtain an unbiased source range MLE whose MSE attains the CRLB and has $\sqrt{\text{CRLB}} \leq 100$ m. It also shows that for fixed SANR, n fluctuates as a function of source range due to the modal interference structure of the static waveguide. If the received $10\log_{10}$SANR is fixed at 0 dB for all ranges between 1 and 50 km, then to obtain a source range estimate of 100 m accuracy for 95% of the ranges either (a) 20 samples are needed, or (b) given a single sample a $10\log_{10}$SANR of 13 dB (Eq. (4.7)) is necessary.

Figure 4-5(a-b) shows the square root of the single-sample CRLB for source range and depth estimation. The sample sizes necessary to obtain unbiased source range and depth estimates that asymptotically attain the CRLB are given by the maximum of n_b, n_v in Eq. (A.6) and shown in Fig. 4-5(c-d). They are found to be roughly inversely proportional to SANR[1] and are typically much larger than one, as expected from Fig. 4-3. We find that the necessary sample size is at least an order of magnitude larger in the upper waveguide layer where SANR[1] decreases more rapidly, as can

be seen in Fig. 4-2. Given sufficient source level, however, accurate range MLEs may be obtained from a single sample at any desired source-receiver separation. For example, increasing source level so that $10\log_{10}$SANR at 1 km range is 40 dB should be sufficient to accurately estimate the range of a source at any depth and ranges up to roughly 30 km, according to Fig. 4-5 and Eq. (4.7).

Given the sample sizes in Fig. 4-5(c), for example, the source range MLE will be in the asymptotic regime where its variance continuously attains the CRLB, which is the minimum possible mean square error (MSE) of an unbiased estimate, regardless of the method of estimation. Since the CRLB is inversely proportional to sample size, as shown in Eq. (A.3), conditions can be specified on sample size for the MLE error to meet any desired threshold. It is then possible to determine whether these conditions can be met in practice, since the number of statistically independent samples of the received acoustic signal is limited by the ratio of the measurement time window to the coherence time scale of acoustic field intensity,[71, 84] which can also be calculated.[22]

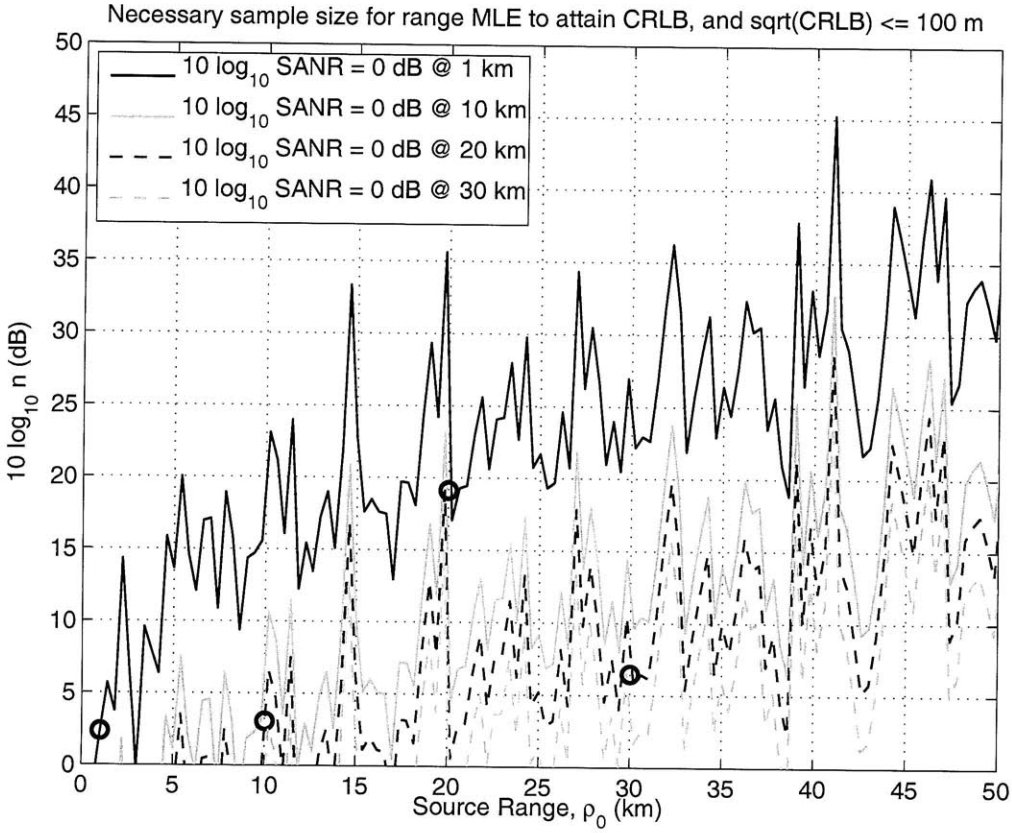

Figure 4-4: Undisturbed waveguide. $10\log_{10} n$, where $n = \{\max[n_b, n_v] \times n'\}$ is the sample size necessary to obtain an unbiased source range MLE whose MSE attains the CRLB and has $\sqrt{\text{CRLB}} \leq 100$ m, where n_b, n_v, n' are calculated using Eqs. (A.6) and (A.7), given a 415 Hz source at 50 m depth. Source level is fixed as a constant over range so that $10\log_{10}$SANR is 0 dB at 1, 10, 20, and 30 km source range (black circles), respectively, for the four curves shown.

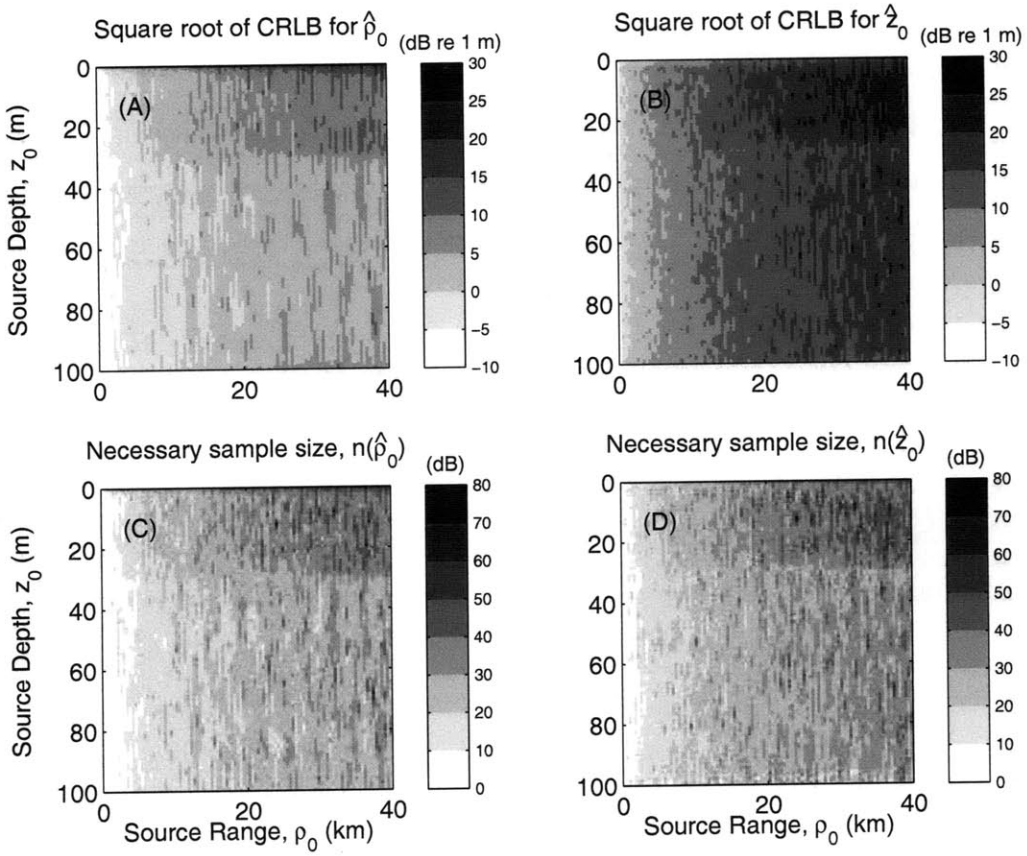

Figure 4-5: Undisturbed waveguide. $10\log_{10}$ of the square root of the CRLB for (a) source range $\hat{\rho}_0$, (b) source depth $\hat{z}_0$ MLEs given a single sample. $10\log_{10}(\max[n_b, n_v])$, the sample sizes or SNRs necessary to obtain (c) source range, (d) source depth MLEs that become unbiased and have MSEs that attain the CRLB. Given any design error threshold, the sample size necessary to obtain an accurate source range or depth MLE is then equal to $(\max[n_b, n_v]) \times n'$, where $n' = CRLB(\max[n_b, n_v])/(\text{design threshold})^2$. The source level is fixed as a constant over range so that $10\log_{10}$SANR[1] is 0 dB at 1 km source range at all source depths.

The temporal coherence scale of acoustic field fluctuations for a shallow-water continental shelf environment such as the one considered here is on the order of minutes,[22] so that the calculated necessary sample sizes imply that accurate source localization may not be practical at ranges greater than 20 km *given the SANR[1] in Fig. 4-2*, since stationary averaging over time periods on the order of hours may then be necessary.

4.3.2 Waveguide Containing Internal Waves

The fluctuating waveguide considered here is the same as that in Ref. [21]. The variance of the acoustic field intensity, or incoherent intensity, starts dominating the expected total intensity for ranges beyond roughly a few kilometers in the upper layer and 20 km in the lower waveguide layer, as seen in Fig. 4-6(c). The SNR[1] and SANR[1] are computed using Eqs. (4.5-4.6), respectively, and are plotted together with the ratio of coherent to incoherent intensity in Fig. 4-6(a-c) as functions of source-receiver range and source depth for a waveguide containing random internal waves. The forward propagated field quickly loses its modal coherence structure and follows a decaying trend with local oscillations over range due to scattering by random 3-D internal waves. The internal wave disturbances have a height standard deviation of $\eta_h = 4$ m and coherence lengths of $l_x = l_y = 100$ m.[21] In this random waveguide, there is no longer a simple linear relationship between SNR[1] and SANR[1], but $10\log_{10}$SNR[1] can be approximated as equal to $10\log_{10}$SANR[1] minus 4-5 dB for ranges beyond roughly 30 km, as can be seen by comparing Figs. 4-6(a)-(b), as well as in Fig. 4-7.

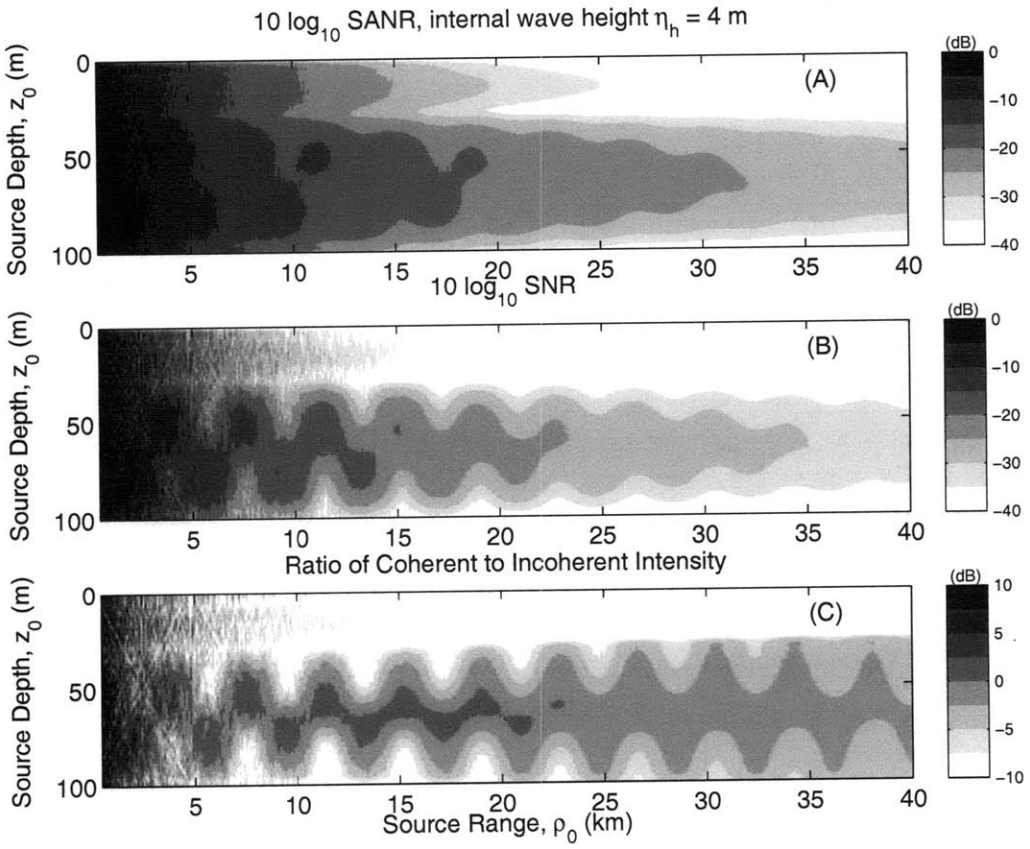

Figure 4-6: (a) Signal to Additive Noise Ratio (SANR), (b) Signal to Noise Ratio (SNR), and (c) the ratio of coherent to incoherent intensity at 415 Hz in a waveguide containing random internal waves. The internal wave disturbances have a height standard deviation of $\eta_h = 4$ m and coherence lengths of $l_x = l_y = 100$ m. This medium is highly random so that incoherent intensity dominates at all depths beyond about 20 km. The total received intensity, given by the numerator of SANR in Eq. (4.6) follows a decaying trend with local oscillations over range. All quantities are plotted as functions of source range ρ_0 and depth z_0 received at the 10-element vertical array described in Section 4.3. The receiver array is centered at $\rho = 0$ m and $z = 50$ m. The source level is fixed as a constant over range so that $10\log_{10}$SANR[1] is 0 dB at 1 km source range at all source depths.

The loss of coherence in the forward propagated field has severe effects on localization accuracy, as shown in Fig. 4-7 where the first-order bias, first-order covariance (CRLB) and second-order covariance of source position MLEs are plotted given a source fixed at 50 m depth and a sample size of $n = 1$. While the asymptotic bias and square root of the CRLB of the source range estimate (Fig. 4-7(a)) are still found to be relatively small, on the order of 10 m for source-receiver ranges greater than about 20 km, the square root of the second-order range variance has increased by approximately an order of magnitude from the static waveguide case. The asymptotic bias and variances of the source depth MLE have all increased by an order of magnitude or more, as seen by comparing Figs. 4-7(b) and 4-3(b). Similarly to the undisturbed waveguide scenario, increasing the array gain could help improve the accuracy of source localization MLEs.

Given Eq. (A.6b), significantly larger sample sizes will be necessary to obtain unbiased range MLEs that attain the minimum possible mean square error compared to the static waveguide case. It will also be practically impossible to attain an accurate source depth estimate from a single sample for ranges greater than a couple of kilometers, given the SANR[1] in Fig. 4-6. For a given SANR[1], the asymptotic statistics of the MLE for any arbitrary n can be obtained by shifting the curves in Fig. 4-7 according to the order of the term involved and the value of n desired. For this random waveguide, the data covariance $\mathbf{C}$ is parameter dependent and the MLE bias and covariance cannot be readily expanded in inverse orders of SANR.[68] We find that increasing SANR by a factor of 10 in Fig. 4-7 reduces the first-order bias and the CRLB by roughly one order of magnitude, and the second-order covariance by approximately two orders of magnitude, as in the deterministic waveguide case. Minimum variance range MLEs can then be obtained from a single sample up to the maximum range for which the second-order covariance and the CRLB are equal in Fig. 4-7, i.e. 5 km, given such a factor of 10 increase in SANR.

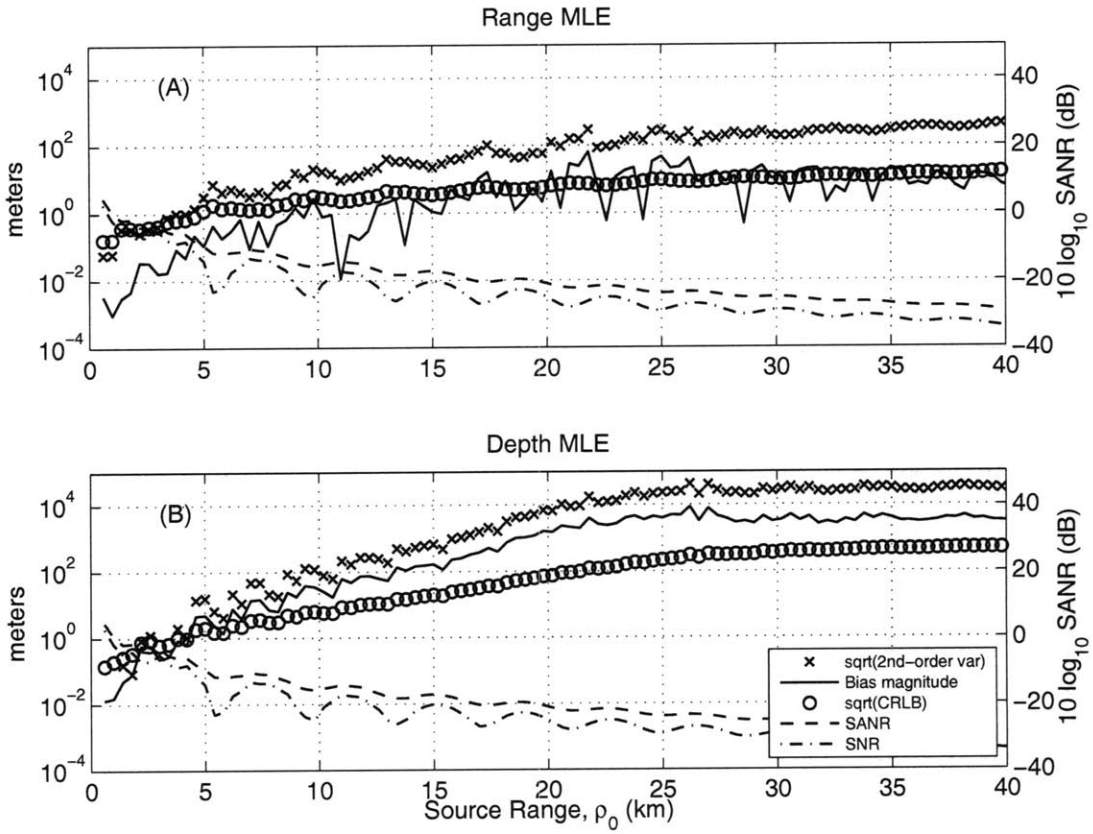

Figure 4-7: Ocean acoustic localization MLE behavior given a single sample for (a) range estimation and (b) depth estimation for a 415 Hz source placed at 50 m depth in a waveguide containing random internal waves. The internal wave disturbances have a height standard deviation of $\eta_h = 4$ m and coherence lengths of $l_x = l_y = 100$ m. The MLE first-order bias magnitude (solid line), square root of the CRLB (circle marks) and square root of the second-order variance (cross marks), as well as the Signal to Additive Noise Ratio (SANR, dashed line) and Signal to Noise Ratio (SNR, dash-dotted line) are plotted as functions of source range. Other than the first-order bias and CRLB of the range MLE, the remaining quantities have increased by at least an order of magnitude when compared to the static waveguide scenario in Fig. 4-3. Given the necessary sample size conditions in Eq. (A.6), whenever the first-order bias and the second-order variance attain roughly 10% of the true parameter value and the CRLB, respectively, more than a single sample will be needed to obtain unbiased, minimum variance MLEs. The source level is fixed as a constant over range so that $10\log_{10}\text{SANR}[1]$ is 0 dB at 1 km source range.

Figure 4-8 shows the sample size n necessary to obtain an unbiased source range MLE whose MSE attains the CRLB and has $\sqrt{\text{CRLB}} \leq 100$ m. It also shows that for fixed SANR, n remains approximately constant as function of source range in the fluctuating waveguide, since the forward propagated field now follows a smoother trend with range than the undisturbed waveguide due to scattering by random 3-D internal waves. If the received $10\log_{10}$SANR is fixed at 0 dB for the four source ranges investigated in Fig. 4-8 (1, 10, 20, and 30 km), then to obtain a source range estimate of 100 m accuracy either (a) 20 samples are needed, or (b) given a single sample a $10\log_{10}$SANR of 13 dB (Eq. (4.7)) is necessary.

The presence of internal waves may severely affect the ability to obtain accurate estimates of source position in practice, as can be deduced from Fig. 4-9(a-b) which shows the square root of the single-sample CRLB for source range and depth estimation. The sample sizes necessary to obtain unbiased source range and depth estimates which asymptotically attain the CRLB are shown in Fig. 4-9(c-d) and are typically much larger than one, as expected from Fig. 4-7.

The minimum error of an unbiased source range MLE is on the order of tens of meters even at ranges beyond 20 km for a source in the lower waveguide layer, as expected from Fig. 4-7(a), but may become as high as several hundred meters for a source in the upper layer where the SANR[1] is much lower, as seen in Fig. 4-6. The minimum error of an unbiased source depth MLE has increased from the undisturbed waveguide case by at least an order of magnitude, as expected from Fig. 4-7(b). The sample sizes necessary to attain either of these CRLBs have also increased by an order of magnitude or more from those corresponding to the static waveguide scenario, Fig. 4-5. These increases in the CRLBs and the necessary sample sizes to attain them are particularly pronounced in the upper layer of the waveguide and the middle of the lower layer at about 65 m, since those are the regions of most rapid SNR[1] and SANR[1] decrease, and also where the received intensity is weakly dependent on source depth and range.

The calculated necessary sample sizes suggest that it becomes practically impossible to accurately estimate source position for ranges greater than a few kilo-

meters for the specific receiver array, waveguide, source frequency and type of instantaneous measurements considered *given the SANR[1] in Fig. 4-6(a)* and typical acoustic field coherent scales,[21] since stationary averaging over tens of hours may be required. The examples presented here illustrate passive source localization scenarios typical of matched-field processing (MFP) and focalization[24] in fluctuating waveguides.[21, 67, 45, 64] They not only provide a quantitative demonstration of the degradation in localization accuracy due to the presence of internal waves, but can also be used to assess the effects of environmental uncertainties on parameter estimation.

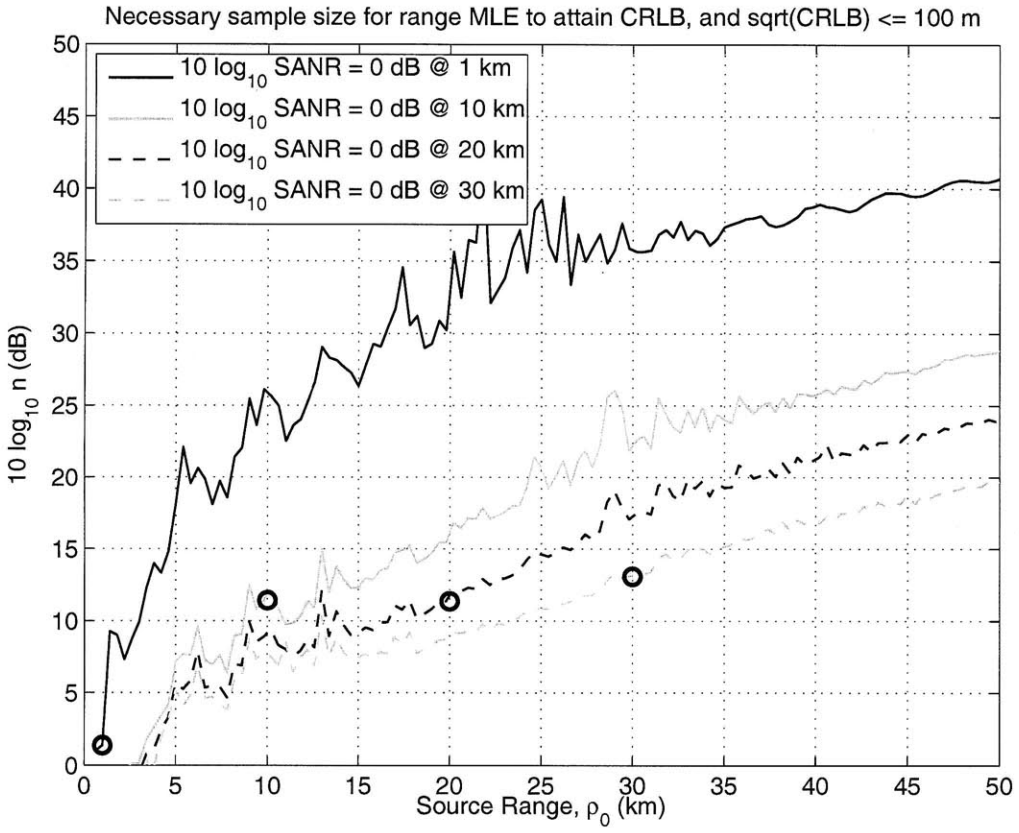

Figure 4-8: Fluctuating waveguide containing internal waves. $10\log_{10} n$, where $n = \{\max[n_b, n_v] \times n'\}$ is the sample size necessary to obtain an unbiased source range MLE whose MSE attains the CRLB and has $\sqrt{\text{CRLB}} \leq 100$ m, and n_b, n_v, n' are calculated using Eqs. (A.6) and (A.7), given a 415 Hz source placed at 50 m depth. Source level is fixed as a constant over range so that $10\log_{10}$SANR is 0 dB at 1, 10, 20, and 30 km source range (black circles), respectively, for the four curves shown.

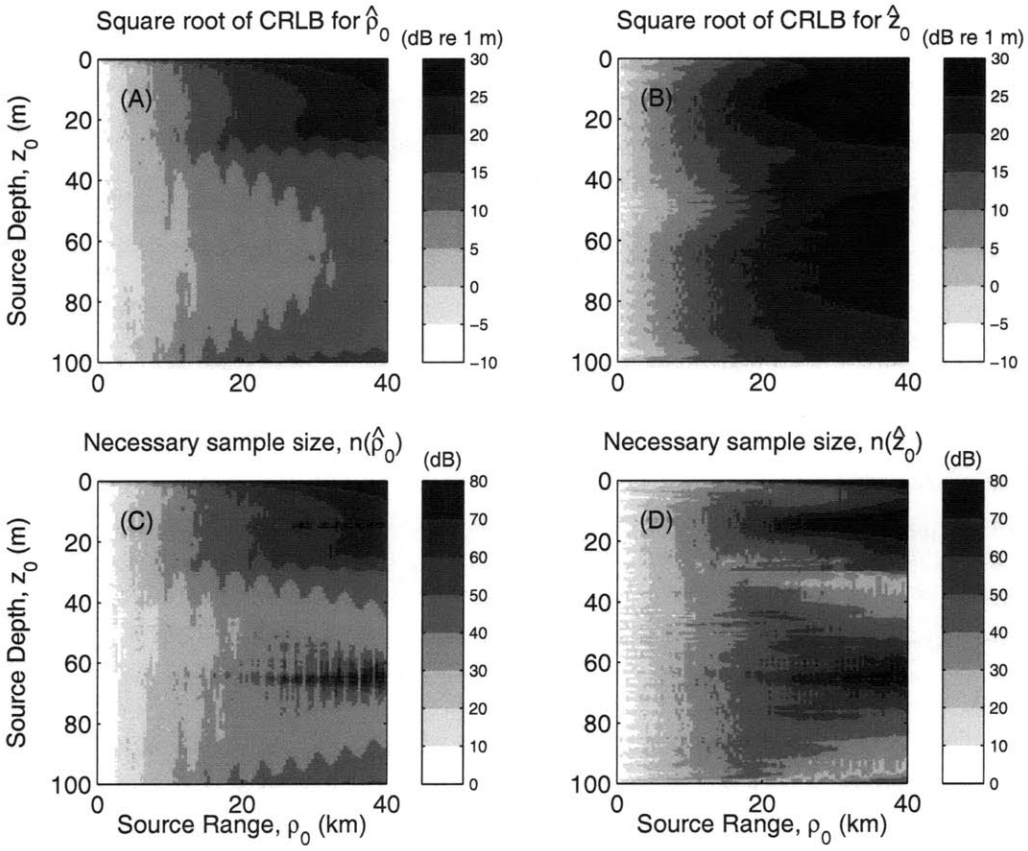

Figure 4-9: Fluctuating waveguide containing internal waves. $10\log_{10}$ of the square root of the CRLB for (a) source range $\hat{\rho}_0$, (b) source depth $\hat{z}_0$ MLEs given a single sample. $10\log_{10}(\max[n_b, n_v])$, the sample sizes or SNRs necessary to obtain (c) source range, (d) source depth MLEs that become unbiased and have MSEs that attain the CRLB. Given any design error threshold, the sample size necessary to obtain an accurate source range or depth MLE is then equal to $(\max[n_b, n_v]) \times n'$, where $n' = CRLB(\max[n_b, n_v])/(\text{design threshold})^2$. The internal wave disturbances have a height standard deviation of $\eta_h = 4$ m and coherence lengths of $l_x = l_y = 100$ m. The source level is fixed as a constant over range so that $10\log_{10}$SANR[1] is 0 dB at 1 km source range at all source depths.

Importance of the joint-moment terms in calculating the second-order covariance

Here, we show the benefits of employing the expression for the MLE second-order covariance in Eq. (4.3) that can be used to determine necessary sample size conditions for accurate estimation given measurements whose mean and covariance are *both* parameter dependent. If the physical environment leads to parameter dependence in both the mean and covariance and this dependence is neglected in either, then large errors can easily ensue, as demonstrated for the physical scenario considered in Section 4.3.2. Neglecting the parameter dependence in either the covariance or the mean is equivalent to approximating the underwater acoustic measurement as either (i) a deterministic signal vector, or (ii) a fully randomized signal vector with zero mean, both embedded in additive white noise.

These two common approximations to the received field may lead to significant miscalculations of the CRLB and the necessary sample sizes of Eq. (A.6), as can be seen by comparing Figs. 4-7 and 4-9 to Figs. 4-10-4-11 and 4-12-4-13, respectively. Note that the asymptotic biases and variances for source range and depth MLEs (Fig. 4-10(a-b), respectively) are of the same order of magnitude as those for the undisturbed waveguide in Fig. 4-3. This is expected since neglecting parameter dependence in the covariance $\mathbf{C}$ is equivalent to assuming a static waveguide where the only noise is purely white additive. The asymptotic biases and variances for the case where $\boldsymbol{\mu}$ is assumed parameter independent (Fig. 4-11(a-b)) are instead found to be many orders of magnitude larger. The observed increase is much larger than the decrease in SANR[1] and SNR[1], and suggests that the covariance of the measurement is only weakly dependent on source range and depth. The differences observed between Figs. 4-10 and 4-11 are consistent with those observed between Figs. 2 and 3 of Ref. [102], where the biases of the MLE obtained from a purely random signal are found to be much larger than those obtained from an equivalent deterministic signal, and range estimation is more severely affected.

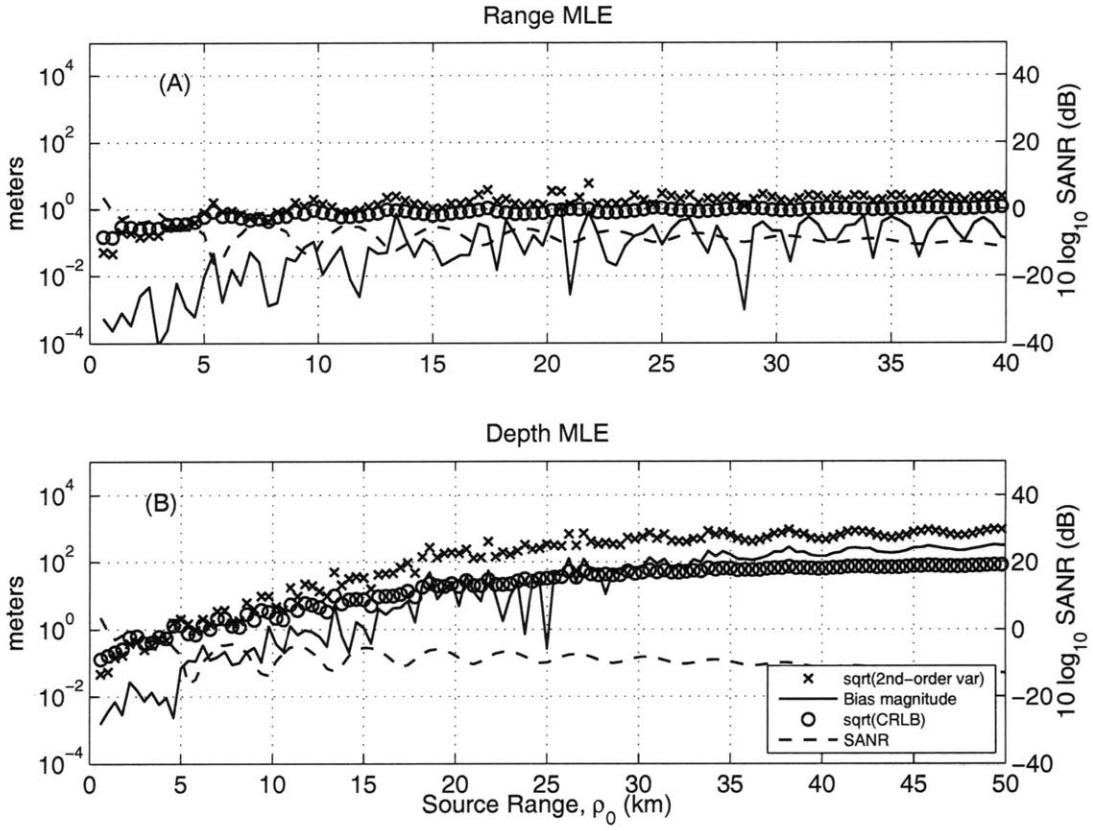

Figure 4-10: The same as Fig. 4-7, but here the covariance $\mathbf{C}$ of the measurement is assumed parameter independent so that its derivatives in Eqs. 4.2-4.3 are set to zero. The asymptotic biases and variances of source range and depth MLEs are typically underestimated, as seen by comparing with Fig. 4-7. This scenario is equivalent to incorrectly assuming the received measurement is a deterministic signal embedded in purely additive white noise, in which case the SANR and SNR of the measurement are equal and the two curves coincide.

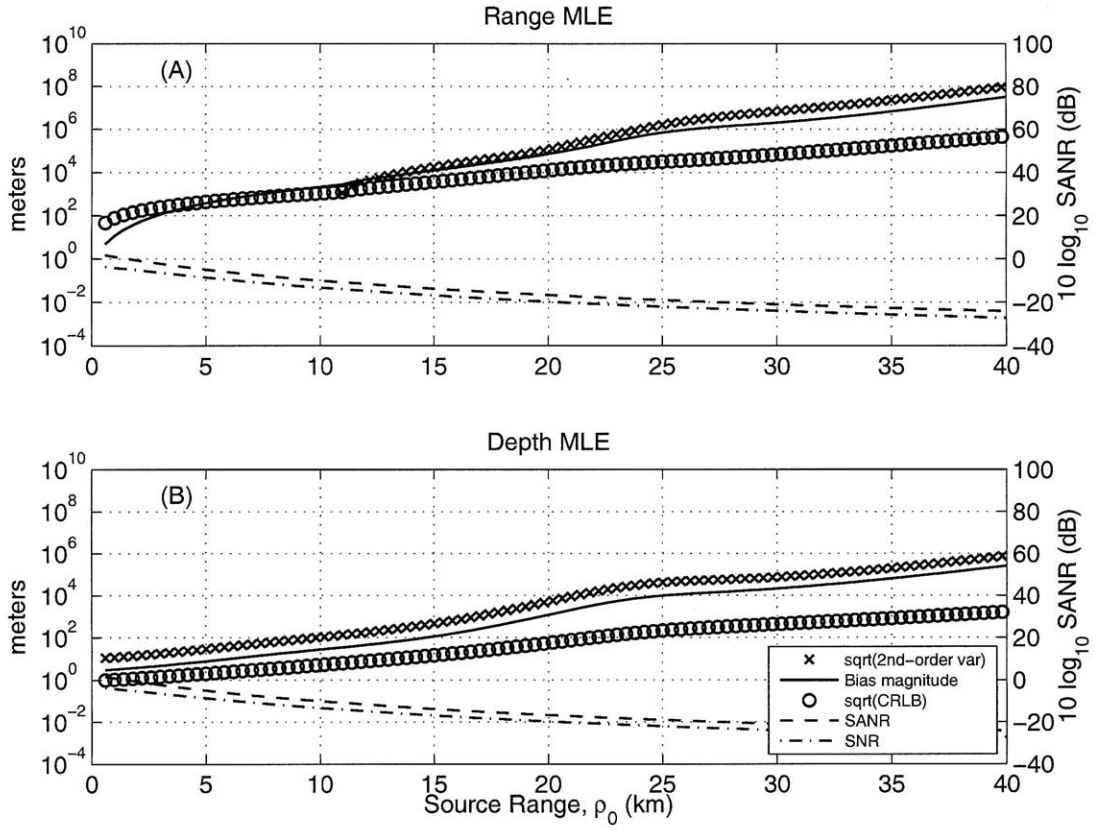

Figure 4-11: The same as Fig. 4-7, but here the mean $\boldsymbol{\mu}$ of the measurement is assumed parameter independent so that its derivatives in Eqs. 4.2-4.3 are set to zero. The asymptotic biases and variances of source range and depth MLEs may be significantly overestimated, as seen by comparing with Fig. 4-7. This scenario is equivalent to incorrectly assuming the received measurement is purely random with zero mean, embedded in additive white noise.

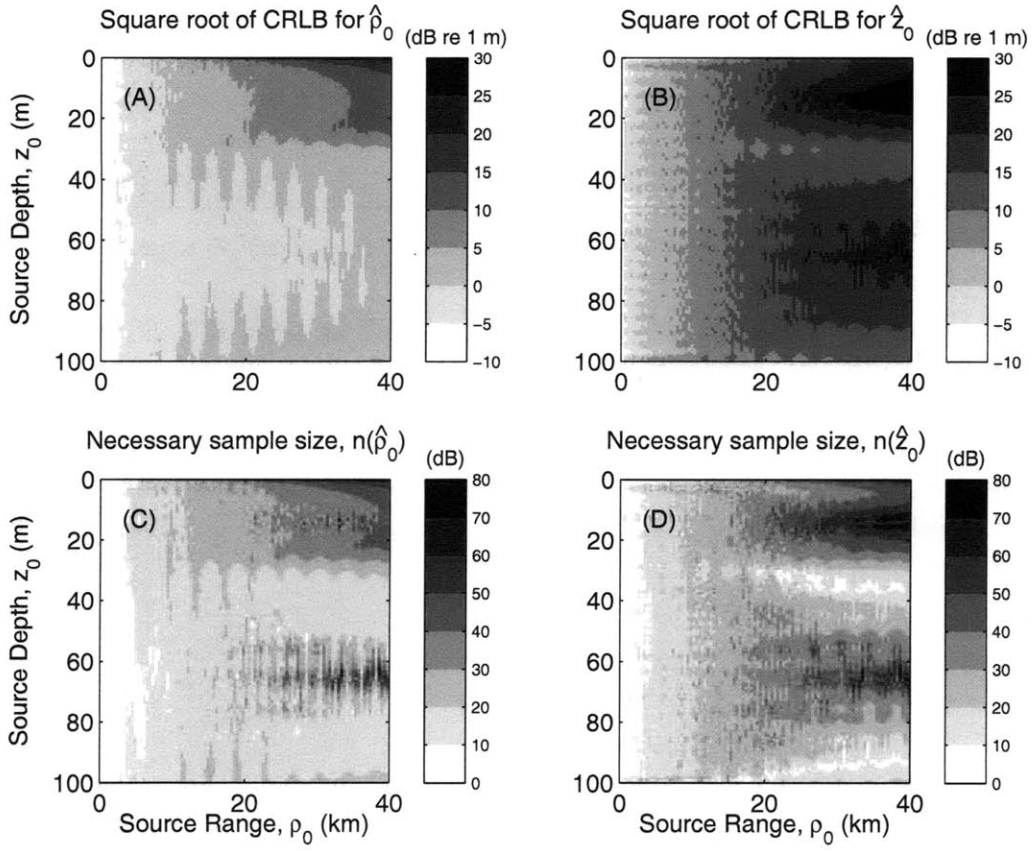

Figure 4-12: The same as Fig. 4-9, but here the covariance $\mathbf{C}$ of the measurement is assumed parameter independent so that its derivatives in Eqs. 4.2-4.3 are set to zero. The CRLB and the sample sizes necessary to attain it are underestimated when compared with Fig. 4-9. This scenario is equivalent to incorrectly assuming the received measurement is a deterministic signal embedded in purely additive white noise.

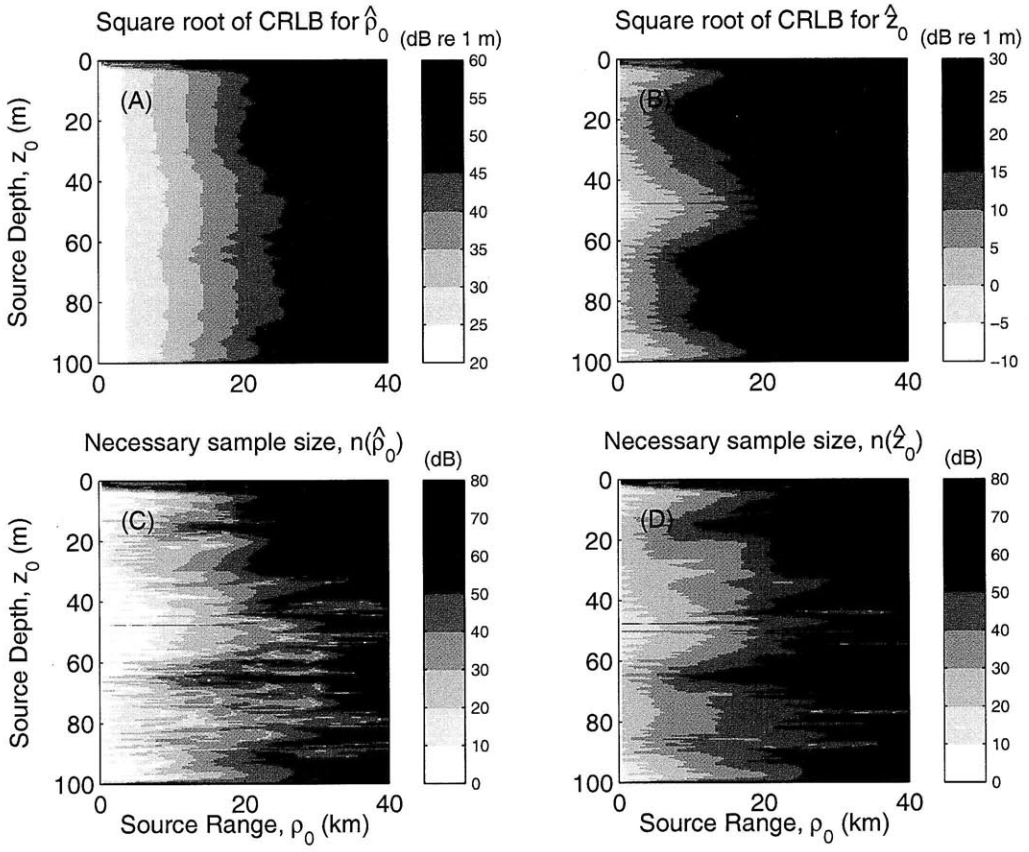

Figure 4-13: The same as Fig. 4-9, but here the mean $\boldsymbol{\mu}$ of the measurement is assumed parameter independent so that its derivatives in Eqs. 4.2-4.3 are set to zero. The CRLB and the sample sizes necessary to attain it are overestimated when compared with Fig. 4-9. This scenario is equivalent to incorrectly assuming the received measurement is purely random with zero mean, embedded in additive white noise.

Both approximations to the measured signal model are inappropriate for determining the sample sizes required to obtain MLEs of source position that attain desired error thresholds. The minimum errors for unbiased estimates of source position given a single sample are shown in Figs. 4-12(a-b) and 4-13(a-b). The sample sizes necessary to attain either of these CRLBs are given in Figs. 4-12(c-d) and 4-13(c-d). Setting the derivatives of $\mathbf{C}$ in Eqs. 4.2-4.3 to zero results in underestimating the sample size required to obtain an accurate estimate of source range by a factor of typically 10^2, as seen by comparing Figs. 4-10(a) and 4-12(a) to Figs. 4-7(a) and 4-9(a), *given the SANR[1] in Fig. 4-6(a).* Similarly, setting instead the derivatives of $\boldsymbol{\mu}$ to zero leads to an overestimation of this sample size by a factor of at least 10^7, *given the SANR[1] in Fig. 4-6(a).* In the latter case, the degradation in range estimation is especially notable and minimum errors are now at least as large as tens of kilometers beyond 20 km from the source, having increased by several orders of magnitude from those calculated in Section 4.3.2.

4.3.3 Discussion

We have calculated the sample sizes or SANRs necessary to obtain accurate source localization estimates in a static and a fluctuating waveguide, given a 415 Hz source and an $N/2 = 10$ element array in Section 4.3.1 and 4.3.2. As a rough design rule, we find that in the lower layer of both the undisturbed and fluctuating waveguide, source range can be typically estimated to within $100 \times M$ m if the received $10\log_{10}$SANR at a single hydrophone is at least $(13 + 10\log_{10} 20/N' - 20\log_{10} M)$ dB, given a single sample and a vertical array of $N'/2$ elements. The necessary SANRs for both the undisturbed and fluctuating waveguide follow the same design rule because they have similar range-averaged behavior.

The necessary sample sizes or SANRs presented here are consistent with those reported in experimental studies. For example, in Ref. [96], the authors localize a source at a range of 5 km with an accuracy of approximately 200 m using single measurements at similar frequencies as investigated here from a 32-element array, despite uncertainties in the sound speed profile. The effective $10\log_{10}$SANR of their

multi-spectral measurement is roughly 16 dB at a single hydrophone, which is much higher than the $(13 + 10\log_{10}(10/32) - 20\log_{10} 2) \approx 2$ dB estimated from our rough design rule for accurate source localization in a fluctuating waveguide.

4.4 Conclusions

A method is provided for determining necessary conditions on sample size or Signal to Noise Ratio (SNR) to obtain accurate parameter estimates from remote sensing measurements in a fluctuating ocean waveguide. These conditions are derived by first expanding the bias and covariance of maximum likelihood estimates (MLEs) in inverse orders of sample size or SNR, where the first-order term in the covariance expansion is the minimum mean square error (MSE) of any unbiased estimate, the Cramer-Rao Lower Bound (CRLB). Necessary sample sizes or SNRs are then determined by requiring (i) the first-order bias term and the second-order covariance term to be much smaller than the true value of the parameter and the CRLB, respectively, and (ii) the CRLB to fall within desired error thresholds. An analytical expression is provided for the second-order covariance of MLEs obtained from general complex Gaussian data vectors, which can be used in many practical problems since (i) data distributions can often be assumed to be Gaussian by virtue of the central limit theorem, and (ii) it allows for *both* the mean and the variance of the measurement to be functions of the estimation parameters. By comparing the asymptotic biases and errors of MLEs, and the sample sizes or SNRs necessary to attain accurate estimates in a static waveguide and in the presence of internal waves, it is then possible to quantitatively assess the effects of environmental uncertainties on parameter estimation.

Here, we consider the problem of source localization in a fluctuating waveguide containing random internal waves, which we model using the analytical expressions provided in Ref. [21] for the mean, mutual intensity, and spatial covariance of the acoustic field forward propagated through random 3-D internal waves in a stratified ocean waveguide for a continuous wave (CW) narrowband signal. The loss of coherence in the foward propagating field due to scattering by internal waves may

have severe consequences on parameter estimation and lead to significant losses in localization ability with narrowband vertical array measurements for fixed source and receiver. We determine the sample sizes and SNRs necessary to obtain accurate source localization estimates in an undisturbed waveguide and find that the median necessary sample size or SNR increases by at least an order magnitude in a fluctuating waveguide, when internal wave fluctuations result in the incoherent intensity component dominating the total acoustic field intensity. Past experiments demonstrating localization with matched-field processing (MFP) in random or fluctuating environments have used SNRs that exceeded the derived conditions and so have not tested the limits of passive detection and localization. In practice, many stealthy or distant sources will have much lower SNRs than have been used in current experiments, and so would likely require impractically long stationary averaging periods for localization to be possible. The results shown here provide an example of how asymptotic statistics can be used in experimental design to ensure that statistical biases and errors meet pre-determined error thresholds.

We also demonstrate the advantages of using the expression for the second-order covariance presented here, which accounts for parameter dependence on both the mean and the variance of the measurement. This is achieved by comparing the asymptotic biases and errors to those calculated when either the covariance or the mean of the measurement is incorrectly assumed to be parameter independent. Such approximations are often necessary to model the measured field in fluctuating environments when it is not possible to determine the parameter dependence of both its mean and variance. Using the analytical tools developed here, we can instead take advantage of the parameter dependence of both the mean and variance of the measured field to obtain more accurate parameter estimates. We find that modeling the measurement as a deterministic signal vector leads to significantly underestimating both the CRLB as well as the sample size or SNR required to attain it. Similarly, modeling the measurement as a zero-mean, fully randomized signal vector results in a gross overestimation of the CRLB and the required sample size or SNR to attain it.

Chapter 5

Estimating the Instantaneous Velocity of Randomly Moving Target Swarms in a Stratified Ocean Waveguide by Doppler Analysis

5.1 Introduction

Many animal species and man-made targets assemble in large organized groups,[19, 99] such as schools of fish,[75, 100, 52] swarms of insects,[13] Autonomous Underwater Vehicles,[59] bats,[10] and flocks of birds.[35] Determining the velocity fields of such aggregations is of interest for ecosystem sensing, environmental sustainability, as well as clutter mitigation. Free-space Doppler analysis is typically used to observe and determine the motion of target swarms in both the atmosphere, e.g. rain droplets,[31] and in the ocean, e.g. plankton.[69] Here, we show that this is possible because cross-spectral coherence remains in the variance of the ambiguity function of the field scattered from such swarms and enables high resolution Doppler velocity and position

estimation. We also develop a method to estimate the mean of the instantaneous velocity and position of a random target group, as well as their respective *standard deviations* across the group, with a long-range acoustic remote sensing system in both free space and in a stratified ocean waveguide representative of typical continental shelf environments.

We show that the variance of the field scattered from large swarms of randomly distributed moving targets typically dominates the range-velocity ambiguity function when the spatial extent of the swarm is much larger than the wavelength. This is achieved by deriving analytical expressions for the expected value and the expected square magnitude of the ambiguity function in terms of the targets' velocity and position probability densities relative to a stationary monostatic remote sensing system. Domination of the variance in the scattered field intensity has previously been shown to occur for the special case of large aggregations of immobile targets where no Doppler shifts occur.[1]

It is shown that for appropriate signal design, such as pseudo-random signals, the mean and variance of the swarm's velocity and position can be expressed in terms of the first two moments of the measured range-velocity ambiguity function. This is shown analytically for free space and with Monte-Carlo simulations for an ocean waveguide. We refer to simultaneous estimation of the group's velocity and position from ambiguity surface moments as the Moment Method. Illustrative examples are then presented for migrating and non-migrating groups of randomly moving targets in free space and in a stratified, range-independent waveguide. Simultaneous estimates of the mean velocity and position can also be obtained by finding the velocity and position that correspond to the peak of the ambiguity function's expected square magnitude, which we refer to as the Peak Method. For a single deterministic target in a waveguide, it has been shown that a relatively accurate estimate of the target velocity can be obtained by measuring the Doppler shifted spectrum of its scattered field.[92, 91] Here we instead consider scattering from a group of random targets, simultaneously resolve both instantaneous velocity and position means of the group, as well as their and standard deviations through the Moment Method. We show

that estimates of the mean velocity obtained via the Moment Method are at least as accurate as estimates based on the Peak Method.

In Section 5.2 and the Appendices, we derive analytical expressions for the statistical moments of the field scattered from a source of arbitrary spectrum by a single moving target in free space or a stratified range-independent waveguide, given random target velocity and position. We then derive the expected value and expected square magnitude of the range-velocity ambiguity function for the total field scattered from a group of random targets. We then show that the first and second moments of the ambiguity function's expected square magnitude along constant range and velocity axes in free space are linear functions of the group's velocity and position means and standard deviations for the Costas sequence, a pseudo-random signal described in Appendix E.3. In Section 5.3, we demonstrate both the Peak and Moment methods via illustrative examples in free space and an ocean waveguide.

5.2 Determining Target Velocity Statistics from Doppler Shift and Spread

We assume a group of N targets are randomly distributed in volume V centered at the origin $\mathbf{0}$, which is in the far field of a stationary monostatic source/receiver system at range $\mathbf{r}$, as shown in Fig. 5-1. We consider a remote sensing sonar platform that consists of a point source collocated with a horizontal receiving array, such as that shown in Fig. 5-2. We define $\mathbf{u}_q^0$ as the random initial position of the qth target, and v_q as the random speed of the qth target *towards* the source/receiver system. We assume that the target positions and velocities are independent and identically distributed (i. i. d.) random variables with probability densities $P_{\mathbf{u}}(\mathbf{u}_q^0)$ and $P_v(v_q)$, which are inherent properties of the target group. We define the means and standard deviations for $\mathbf{u}_q^0$, v_q to be $\boldsymbol{\mu}_{\mathbf{u}}$, $\boldsymbol{\sigma}_{\mathbf{u}}$ and μ_v, σ_v, respectively. We also assume that the targets move at low Mach numbers, which is typical for biological scatterers, e.g. fish at velocities of order 1 m/s.[55, 85, 26] As detailed in Appendix

E, v_q is defined to be the velocity component parallel to $\mathbf{r}$, which is assumed to be constant during the time necessary for the sound signal to travel through the resolution footprint of the remote sensing system. For simplicity, we assume that all targets have the same scatter function, and for the frequencies considered, they scatter omnidirectionally. We assume target velocities follow Gaussian probability densities, and set the velocity means to correspond to typical fish group swimming speeds, in illustrative examples. A target group is then defined to be migrating by setting the velocity standard deviation to be approximately 10% of the mean velocity. Similarly, a group is defined to be randomly swarming if the velocity standard deviation is much larger than the velocity mean. Targets are assumed to be uniformly distributed within 100 m about a nominal range of 15 km from the remote sensing system. For waveguide examples, we consider the waveguide of Fig. 5-2, which is representative of continental shelf environments, and assume targets are uniformly distributed in depth between 70 and 90 m. For free space examples, we use the sane distributions. Finally, areal number densities are chosen so that acoustic returns from the target groups will stand above background reverberation,[40] based on past OAWRS field data from the New Jersey Continental Shelf and the Gulf of Maine.[38, 39] For herring we then assume an areal number density of 2 fish/m^2, while for tuna we consider imaging a single school consisting of roughly 100 individuals.[40]

In all examples, we employ the specific signal design described in Appendix E.3, which has center frequency of 1.6 kHz, bandwidth of roughly 20 Hz, velocity resolution of approximately 0.17 m/s, and range resolutions of about 43 m, which is smaller than the range dimension of the targets' spatial distribution. The target distribution scenarios are summarized in Table 5.1, and the source signal and remote sensing system parameters are given in Table 5.2.

Table 5.1: Target Distribution Scenarios

	Case A Migrating Herring	Case B Swarming Herring	Case C Migrating Tuna
Velocity Mean, μ_v	0.2 m/s	0 m/s	1.5 m/s
Velocity Standard Deviation, σ_v	0.025 m/s	0.5 m/s	0.1 m/s
Areal Number Density, or Number of Targets	2 fish/m^2		1 school (100 fish)
Position Mean, $\boldsymbol{\mu}_\mathbf{u}$ (from the origin $\mathbf{0}$, see Figs. 5-1 and 5-2)	$\mathbf{0}$		
Target Range Distribution (from the mean position $\boldsymbol{\mu}_\mathbf{u}$)	Uniform, $\pm$ 50 m		
Target Depth Distribution (for waveguide examples, see Fig. 5-2)	Uniform, 70-90 m		
Target Cross-Range Extent	Exceeds remote sensing system's cross-range resolution		

Table 5.2: Remote Sensing System Properties

Signal Design	7-pulse Costas sequence (see Appendix E.3)
Center Frequency	1.6 kHz
Bandwidth	$\approx$ 20 Hz
Range Resolution, Δu	$\approx$ 43 m
Cross-Range Resolution (at 15 km range)	$\approx$ 100 m
Velocity Resolution, Δv	$\approx$ 0.17 m/s
Source/Receiver Range (from the origin $\mathbf{0}$, see Figs. 5-1 and 5-2)	15 km
Source/Receiver Depth (for waveguide examples, see Fig. 5-2)	20 m

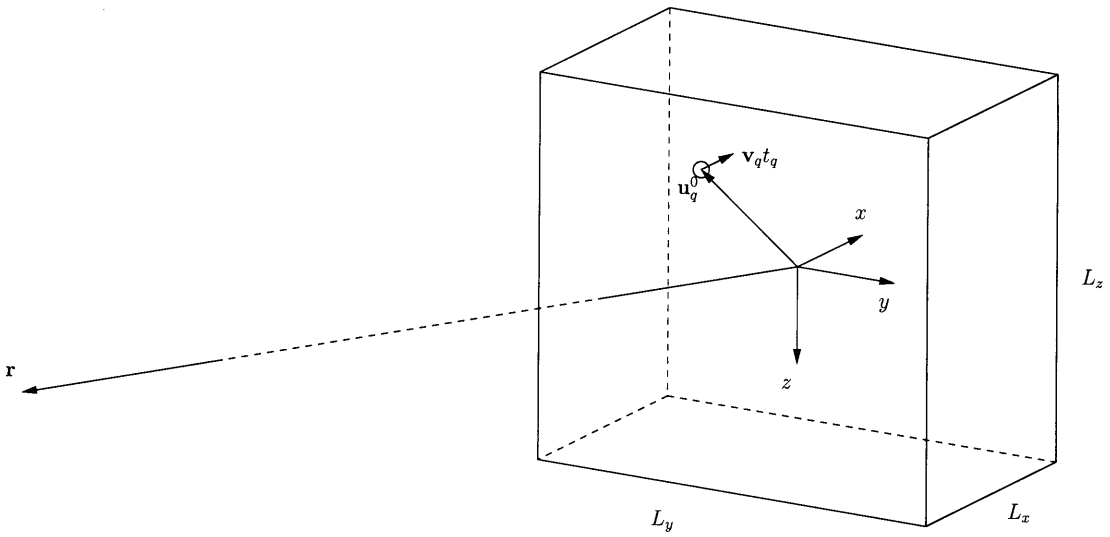

Figure 5-1: Sketch of the resolution footprint volume enclosing a target with initial offset u_q^0 from the coordinate system origin and velocity v_q. The variables L_x, L_y, and L_z denote the dimensions of the footprint volume in x, y, z coordinates, respectively. The position mean and standard deviation are $\boldsymbol{\mu}_\mathbf{u}$, $\boldsymbol{\sigma}_\mathbf{u}$, while the velocity mean and standard deviation are μ_v, σ_v.

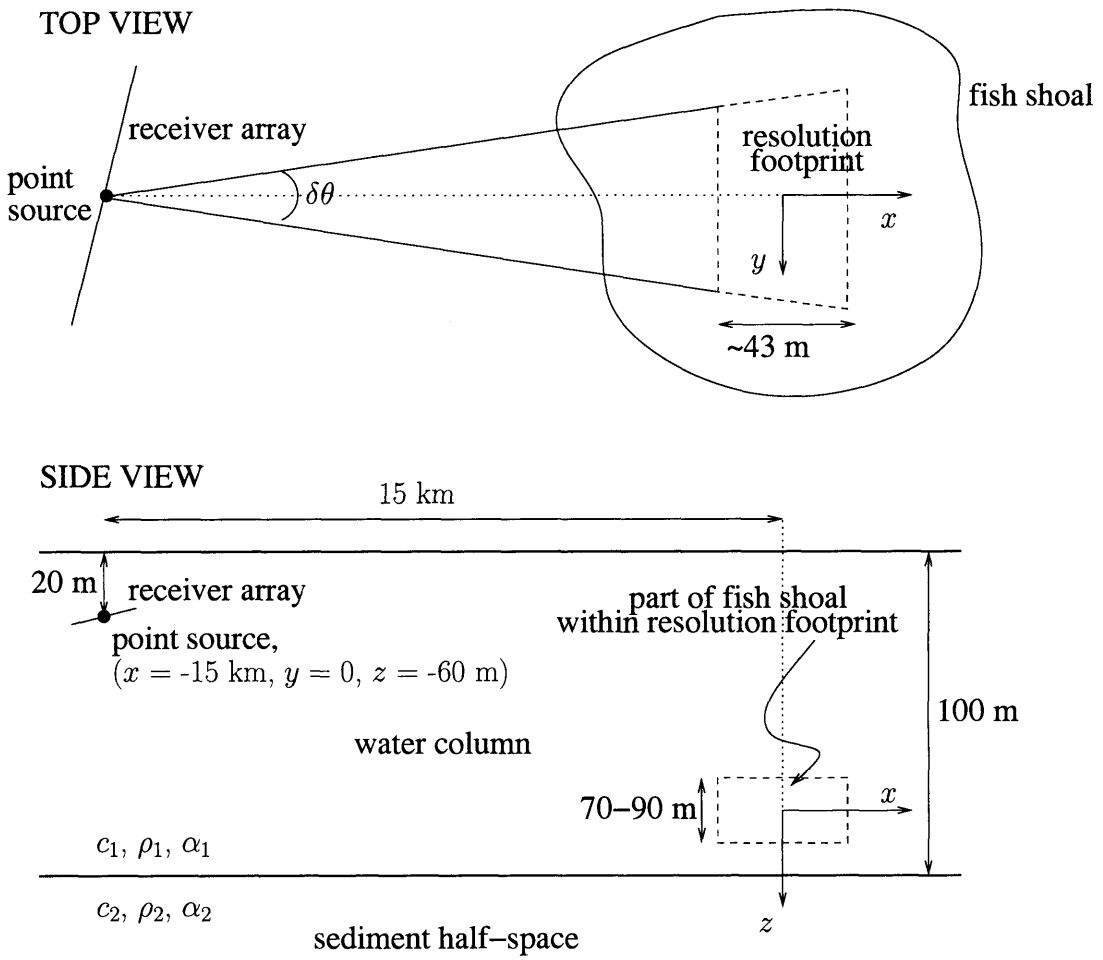

Figure 5-2: Sketch of waveguide geometry and sound speed profile. The locations of the fish shoal, the source/receiver imaging system and the resolution footprint with respect to the coordinate system (x, y, z) are also shown. The coordinate system coincides with that of Fig. 5-1. The sound speed in the water column is constant, $c_1 = 1500$ m/s, and the sound speed in the sediment half-space is $c_2 = 1700$ m/s. The density ρ_1 and attenuation α_1 in the water column are 1 kg/m^3 and 6×10^{-5} dB/λ_1, respectively, where λ_1 is the wavelength in the watercolumn. The sediment half-space has density $\rho_2 = 1.9$ kg/m^3, and attenuation $\alpha_2 = 0.8$ dB/λ_2, representative of sand, where λ_2 is the wavelength in the bottom sediment.

5.2.1 Free Space

The field scattered from the qth target due to a harmonic source of frequencey f and unit amplitude, can be written as[92]

$$\Phi_{s,q}(\mathbf{r},t;f) = \frac{S(\bar{f})}{\bar{k}} G(\mathbf{r}|\mathbf{0},\bar{f}) G(\mathbf{0}|\mathbf{r},f) e^{-i2\pi\bar{f}t} e^{-i2\pi(\bar{f}+f)\hat{\mathbf{i}}_r\cdot\mathbf{u}_q^0/c} \tag{5.1}$$

where $\bar{f} \approx f(1+2v_q/c)$ is the Doppler-shifted frequency of the scattered field, c is the sound speed in the medium, $S(f)$ is the target's planewave scattering function, and $G(\mathbf{0}|\mathbf{r},f)$ is the free space Green's function between the source and the origin evaluated at frequencey f. For a broadband source with dimensionless source function $q(t) \Leftrightarrow Q(f)$, the scattered field is given by Fourier synthesis as

$$\Psi_{s,q}(\mathbf{r},t) = \int \mathrm{d}f Q(f) \Phi_{s,q}(\mathbf{r},t;f) \tag{5.2}$$

where $\Leftrightarrow$ denotes Fourier transform pairs $q(t) = \int Q(f) e^{-i2\pi ft}\mathrm{d}f$, $Q(f) = \int q(t) e^{i2\pi ft}\mathrm{d}t$.

The ambiguity function is defined as

$$\begin{aligned} \Psi_{s,q}(\tau,\nu) &= \int_{-\infty}^{\infty} \Psi_{s,q}(\mathbf{r},t) q^*(t-\tau) e^{i2\pi\nu t}\mathrm{d}t \\ &= \int_{-\infty}^{\infty} \Psi_{s,q}(\mathbf{r},f') Q^*(f'-\nu) e^{-i2\pi(f'-\nu)\tau}\mathrm{d}f' \end{aligned} \tag{5.3}$$

where ν is the Doppler shift and τ is the time delay defined such that $\tau = 0$ corresponds to the time instant the signal is transmitted from the source. The ambiguity function has units of Pa/Hz and can also be interpreted in terms of target velocity and position by using the transformations $v = c\nu/(2f_c)$ and $u = c\tau/2$, where v, u are the target's velocity and position, and f_c is the signal's center frequency. The mean and second moment of the ambiguity function $\Psi_{s,q}(\tau,\nu)$ are derived analytically in

Appendix E.1 and are given by

$$\begin{aligned}\langle \Psi_{s,q}(\tau,\nu)\rangle &= \int_{-\infty}^{\infty} \frac{S(f')}{k'} G(\mathbf{r}|\mathbf{0},f') Q^*(f'-\nu) e^{-i2\pi(f'-\nu)\tau} \\ &\quad \times \int G(\mathbf{0}|\mathbf{r}, f'(1+2v_q/c)^{-1}) Q(f'(1+2v_q/c)^{-1}) \\ &\quad \times U_q(f'\hat{\mathbf{i}}_r/c, v_q) P_v(v_q) \mathrm{d}v_q \mathrm{d}f' \end{aligned} \tag{5.4}$$

$$\begin{aligned}\langle |\Psi_{s,q}(\tau,\nu)|^2\rangle &= \int_{-\infty}^{\infty}\int_{-\infty}^{\infty} \frac{S(f_1)}{k_1} G(\mathbf{r}|\mathbf{0},f_1) Q^*(f_1-\nu) \frac{S^*(f_2)}{k_2^*} G^*(\mathbf{r}|\mathbf{0},f_2) Q(f_2-\nu) \\ &\quad \times e^{-i2\pi(f_1-f_2)\tau} \int G(\mathbf{0}|\mathbf{r}, f_1(1+2v_q/c)^{-1}) Q(f_1(1+2v_q/c)^{-1}) \\ &\quad \times G^*(\mathbf{0}|\mathbf{r}, f_f(1+2v_q/c)^{-1}) Q^*(f_2(1+2v_q/c)^{-1}) \\ &\quad \times U_q((f_1-f_2)\hat{\mathbf{i}}_r/c, v_q) P_v(v_q) \mathrm{d}v_q \mathrm{d}f_1 \mathrm{d}f_2 \end{aligned} \tag{5.5}$$

where f', f_1 or f_2 correspond to received frequencies, and $Q(f)$ is the source spectrum. The variable U_q is defined analytically in Eq. (E.4) and is the characteristic function for probability density $P_{\mathbf{u}}(\mathbf{u}_q^0)$, so that it can be interpreted as the Fourier transform of the target's spatial distribution. For the whole group of N targets, we find $|\langle \Psi_s(\tau,\nu)\rangle|^2 = N^2 |\langle \Psi_{s,q}(\tau,\nu)\rangle|^2$, and (see Appendix E.1),

$$\langle |\Psi_s(\tau,\nu)|^2\rangle = N\langle |\Psi_{s,q}(\tau,\nu)|^2\rangle + N(N-1)|\langle \Psi_{s,q}(\tau,\nu)\rangle|^2 \tag{5.6}$$

The expected square magnitude of the ambiguity function is then the sum of: (i) a second moment term proportional to N due to scattering from each target, and (ii) a mean-squared term proportional to N^2 due to interaction of the fields scattered from different targets.[90]

For target groups large compared to the wavelength, the source spectrum Q and the targets' spatial spectrum U_q tend to be non-overlapping band-limited functions of frequency whose products tend to zero in Eq. (5.4), leading to a negligible mean. This is not the case in Eq. (5.5) where the peaks of Q and U_q overlap because evaluation of U_q at the frequency difference enables cross-spectral coherence. The variance then

typically dominates the second moment.[1] This is shown in Fig. 5-3 for the Case A target distribution scenario that represents migrating herring (Table 5.1), given the source signal and remote sensing system parameters in Table 5.2, where we find that the magnitude squared of the expected value of the ambiguity function, $|\langle\Psi_s(\tau,\nu)\rangle|^2$ is typically about 20 dB smaller than the expected square magnitude of the ambiguity function, $\langle|\Psi_s(\tau,\nu)|^2\rangle$. From Eq. (5.6), this means that for this case we would require a 100-fold increase in population density for the magnitude squared of the mean ambiguity function to dominate.

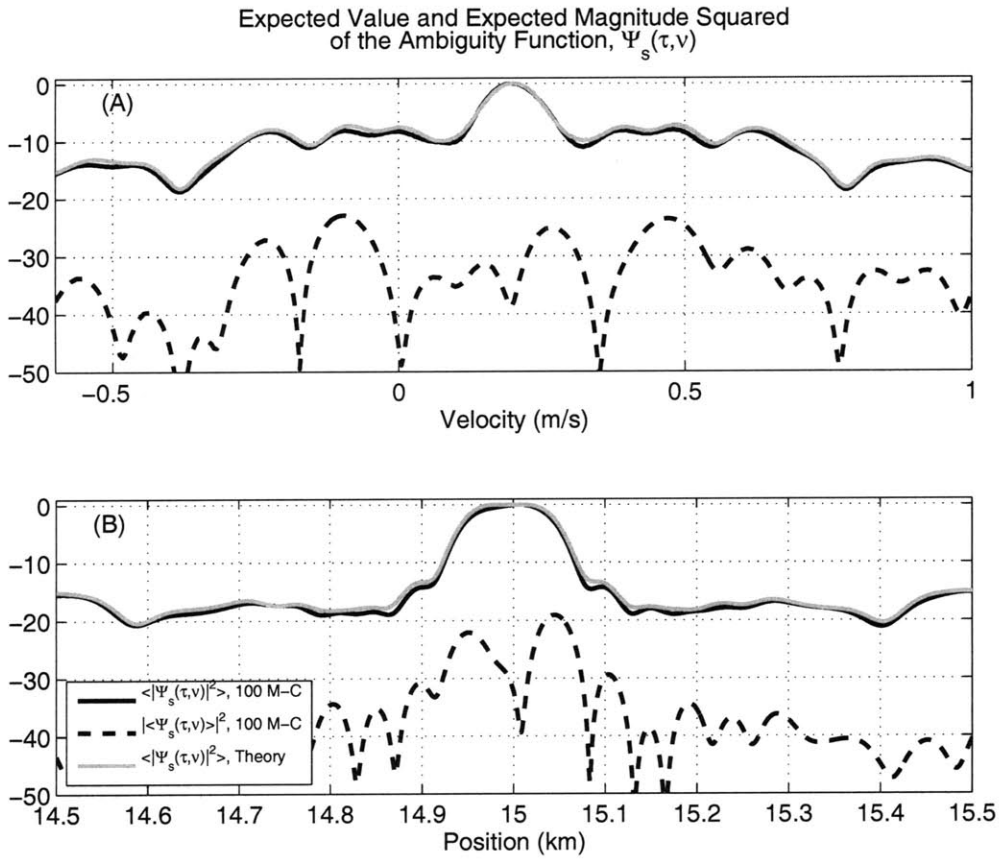

Figure 5-3: Free Space. Expected value (black dashed line) and expected square magnitude (black solid line) of the ambiguity function via 100 Monte-Carlo simulations for the field scattered from a random aggregation of targets following the Case A scenario described in Table 5.1. The source signal and remote sensing system parameters are given in Table 5.2. The expected square magnitude of the ambiguity function based on the analytical expressions of Eqs. (5.4-5.5) and (5.6) is also shown (gray line) and is found to be in good agreement with the Monte-Carlo result. The variance of the ambiguity function dominates the total intensity and the magnitude squared of the ambiguity function's expected value is negligible.

Estimating Target Position and Velocity Statistics

Equations (5.4) and (5.5) cannot typically be evaluated analytically. A significant simplication is however possible in the case of specially designed source signals whose spectra can be approximated as

$$\begin{aligned} Q(f) &= \sum_{n=0}^{M-1} a_n e^{i2\pi(f-f_n)h_n} \text{sinc}\left(\pi(f-f_n)T\right) \\ &\approx \sum_{n=0}^{M-1} a_n e^{i2\pi(f-f_n)h_n} \delta(f-f_n), \end{aligned} \tag{5.7}$$

where a_n is the coefficient of the nth frequency component, f_n, for $n = 1, 2, \ldots, M$, and h_n, T are known constants. Equation (5.7) is approximately valid, for example, for spectra that consist of a series of windowed harmonic waves, such as the Costas sequence described in Appendix E.3. For such spectra, the expected square magnitude of the ambiguity function is given by

$$\begin{aligned} \langle|\Psi_{s,q}(\tau,\nu)|^2\rangle &= \sum_{n=0}^{M-1}\sum_{m=0}^{M-1}\sum_{l=0}^{M-1}\sum_{j=0}^{M-1} a_n^* a_m a_l a_j^* \left[\frac{S(f_n+\nu)}{2\pi(f_n+\nu)/c}\right]\left[\frac{S^*(f_l+\nu)}{2\pi(f_l+\nu)/c}\right] \\ &\quad \times G(\mathbf{r}|\mathbf{0}, f_n+\nu) G^*(\mathbf{r}|\mathbf{0}, f_l+\nu) G(\mathbf{0}|\mathbf{r}, f_m) G^*\left(\mathbf{0}|\mathbf{r}, \frac{f_l+\nu}{f_n+\nu} f_m\right) \\ &\quad \times \delta\left(\frac{f_l+\nu}{f_n+\nu} f_m - f_j\right) U_q\left(\left[f_n + f_m - f_l - \frac{f_l+\nu}{f_n+\nu} f_m\right]\hat{\mathbf{i}}_r/(2c), 0\right) \\ &\quad \times e^{-i2\pi(f_n-f_l)\tau} P_v\left(\frac{c}{2}\left[\frac{f_n+\nu}{f_m} - 1\right]\right) \end{aligned} \tag{5.8}$$

When the dimensions of the swarm are much larger than the acoustic wavelength, the first two moments of Eq. (5.8) along constant Doppler shift ν and constant time delay τ axes can be analytically expressed in terms of the targets' position and velocity first and second statistical moments (see Appendix E.1). Taking moments along a

constant-τ axis,

$$\begin{aligned}
\nu_1 &= \int \nu \langle |\Psi_{s,q}(\tau,\nu)|^2 \rangle \mathrm{d}\nu \approx b_1 \left\{ \left[\sum_{n=0}^{M-1} \sum_{m=0}^{M-1} \frac{2f_m}{c} (f_m - f_n) \right] + \left[M \sum_{m=0}^{M-1} \left(\frac{2f_m}{c} \right)^2 \right] \mu_v \right\} \\
&\approx c_1 + d_1 \mu_v, \qquad (5.9a) \\
\nu_2 &= \int \nu^2 \langle |\Psi_{s,q}(\tau,\nu)|^2 \rangle \mathrm{d}\nu \approx b_1 \left\{ \left[\sum_{n=0}^{M-1} \sum_{m=0}^{M-1} \frac{2f_m}{c} (f_m - f_n)^2 \right] \right. \\
&\quad \left. + \left[\sum_{n=0}^{M-1} \sum_{m=0}^{M-1} 2 \left(\frac{2f_m}{c} \right)^2 (f_m - f_n) \right] \mu_v + \left[M \sum_{m=0}^{M-1} \left(\frac{2f_m}{c} \right)^3 \right] (\mu_v^2 + \sigma_v^2) \right\} \\
&\approx c_2 + d_2 \mu_v + e_2 (\mu_v^2 + \sigma_v^2), \qquad (5.9b)
\end{aligned}$$

where the ambiguity function has been normalized so that $\int \langle |\Psi_{s,q}(\tau,\nu)|^2 \rangle \mathrm{d}\nu = 1$. The coefficient b_1 is given by

$$b_1 = \left[M \sum_{m=0}^{M-1} \frac{2f_m}{c} \right]^{-1} \qquad (5.10)$$

The coefficients c_1, d_1, c_2, d_2, e_2 can be calculated analytically given a specific signal design, and then used to provide estimates of the target's mean velocity and its standard deviation given measurements of ν_1 and ν_2. For the purposes of this paper, we employ the Costas sequence design detailed in Appendix E.3 that satisfies Eq. (5.7), and for which the coefficients are given in Table 5.3. In the illustrative examples of Section 5.3.1, we assume the form of Eq. (5.9) holds and use it to estimate the velocity means and standard deviations. Estimates obtained via the Moment Method are found in Section 5.3.1 to be very accurate, with errors typically smaller than 10%.

Table 5.3: Coefficients of Eq. (5.9).

c_1	d_1	c_2	d_2	e_2
0.0156	2.1334	0.5822	0.1333	4.5512

Similarly, for the moments of the expected square magnitude of the ambiguity

function over time delay τ, we find

$$\tau_1 = \int \tau \langle |\Psi_{s,q}(\tau,\nu)|^2 \rangle \mathrm{d}\tau = \left(r + \hat{\mathbf{i}}_r \cdot \boldsymbol{\mu}_{\mathbf{u}}\right) \frac{1}{c} \sum_{n=0}^{M-1} \sum_{m=0}^{M-1} d_{n,m}, \tag{5.11a}$$

$$\tau_2 = \int \tau^2 \langle |\Psi_{s,q}(\tau,\nu)|^2 \rangle \mathrm{d}\tau = \left([\hat{\mathbf{i}}_r \cdot \boldsymbol{\sigma}_{\mathbf{u}}]^2 + [r + \hat{\mathbf{i}}_r \cdot \boldsymbol{\mu}_{\mathbf{u}}]^2\right) \frac{2}{c^2} \sum_{n=0}^{M-1} \sum_{m=0}^{M-1} d_{n,m} \tag{5.11b}$$

where the ambiguity function has again been normalized so that $\int \langle |\Psi_{s,q}(\tau,\nu)|^2 \rangle \mathrm{d}\tau = 1$. The coefficients $d_{n,m}$ are given by

$$d_{n,m} = P_v\left(\frac{c}{2}\left[\frac{f_n + \nu}{f_m} - 1\right]\right) \tag{5.12}$$

Equation (5.11) shows that the moments of the ambiguity function's expected square magnitude along a constant Doppler shift axis are linearly related to the targets' position mean and variance. Note that as long as the absolute value of the mean position estimate is less than or equal to the length scale of the resolution footprint, then for practical purposes the targets have been accurately localized.

5.2.2 Waveguide

As in Section 5.2.1, we assume a group of N targets is randomly distributed within volume V in the far-field of a monostatic source/receiver system in a stratified range-independent waveguide. We also assume that targets scatter omnidirectionally for the frequencies considered. Under these conditions, the field scattered from the qth target, due to a harmonic source at angular frequency Ω, can be found by adapting Eq. (59) of Ref. [92] to account for the case of a monostatic ($\mathbf{r}_0 = \mathbf{r}$), stationary ($v_0 = v = 0$) system and for the change of the coordinate system origin from the target centroid to the center of the resolution footprint,

$$\Phi_{s,q}(\mathbf{r},t;\Omega) = 4\pi \sum_l \sum_m \frac{S(\omega_{m,l,q})}{k(\omega_{m,l,q})} \Phi_{s,q}^{l,m}(\mathbf{r},\Omega,\omega_{m,l,q}) e^{-i\omega_{m,l,q}t} \tag{5.13}$$

where $\omega_{m,l,q} = \Omega + v_q[\xi_l(\Omega) + \xi_m(\Omega)]$ is the Doppler shifted frequency due to target motion, ξ is the wavenumber, $S(\omega)$ is the target's planewave scattering function, l, m are indices corresponding to the incoming and outgoing modes, respectively, and the variable $\Phi_{s,q}^{l,m}$ describing propagation to and from the target is defined explicitly in Eq. (E.30). Note that both the scattering function and the wavenumber are evaluated at the Doppler shifted frequency $\omega_{m,l,q}$ due to modal propagation. The mean and second moment of the ambiguity function of the back-scattered field are derived analytically in Appendix E.2 and are given by

$$\begin{aligned}\langle \Psi_{s,q}(\tau,\nu)\rangle &= \frac{1}{\pi}\int_{-\infty}^{\infty}\frac{S(\omega')}{k(\omega')}Q^*(\omega'-2\pi\nu)e^{-i(\omega'-2\pi\nu)\tau} \\ &\quad\times\int\sum_l\sum_m Q(\omega'(1+v_q(1/v_l^G+1/v_m^G))^{-1})U_q^{l,m}(\omega',v_q)P_v(v_q)\mathrm{d}v_q\mathrm{d}\omega'\end{aligned} \tag{5.14}$$

$$\begin{aligned}\langle|\Psi_{s,q}(\tau,\nu)|^2\rangle &= \frac{1}{\pi^2}\int_{-\infty}^{\infty}\int_{-\infty}^{\infty}\frac{S(\omega_1)}{k(\omega_1)}Q^*(\omega_1-2\pi\nu)\frac{S^*(\omega_2)}{k^*(\omega_2)}Q(\omega_2-2\pi\nu)e^{-i(\omega_1-\omega_2)\tau} \\ &\quad\times\int\sum_l\sum_m\sum_n\sum_p Q(\omega_1(1+v_q(1/v_l^G+1/v_m^G))^{-1})U_q^{l,m,n,p}(\omega_1,\omega_2,v_q) \\ &\quad\times Q^*(\omega_2(1+v_q(1/v_n^G+1/v_p^G))^{-1})P_v(v_q)\mathrm{d}v_q\mathrm{d}\omega_1\mathrm{d}\omega_2\end{aligned} \tag{5.15}$$

where ω', ω_1 or ω_2 correspond to received frequencies,[92] v_m^G is the group velocity of the mth mode, and $Q(f)$ is the source spectrum. As in the free space case, the ambiguity function can also be interpreted in terms of target velocity and position by using the transformations $v = v_1^G\nu/(2f_c)$ and $u = v_1^G\tau/2$, where v, u are the target's velocity and position, and f_c is the signal's center frequency. The variables $U_q^{l,m}$ and $U_q^{l,m,n,p}$ are defined in Eqs. (E.34) and (E.38), respectively, and are characteristic functions for the qth target's initial position $\mathbf{u}_q^0$ given its probability density function, $P_{\mathbf{u}}(\mathbf{u}_q^0)$. They can be interpreted as Fourier transforms of the target's spatial distribution and are evaluated at the Doppler shifted frequencies $\omega_{m,l,q}$ and $\omega_{p,n,q}$ so that they are functions of the modes l, m, n, p.

For a group containing N targets, we again have $|\langle\Psi_s(\tau,\nu)\rangle|^2 = N^2|\langle\Psi_{s,q}(\tau,\nu)\rangle|^2$

and $\langle|\Psi_s(\tau,\nu)|^2\rangle = N\langle|\Psi_{s,q}(\tau,\nu)|^2\rangle + N(N-1)|\langle\Psi_{s,q}(\tau,\nu)\rangle|^2$. As in the free space case, the expected square magnitude of the ambiguity function is the sum of a second moment term proportional to N and a mean-squared term proportional to N^2, where the variance term typically dominates for groups large compared to the wavelength,[1] as shown for the Case A target distribution scenario that represents migrating herring (Table 5.1) in Fig. 5-4. The source signal and remote sensing system parameters are given in Table 5.2. We note that the targets appear to be closer to the source/receiver by roughly 40 m, but this is approximately equal to the length scale of the system's resolution footprint, so for practical purposes the targets are still accurately localized.

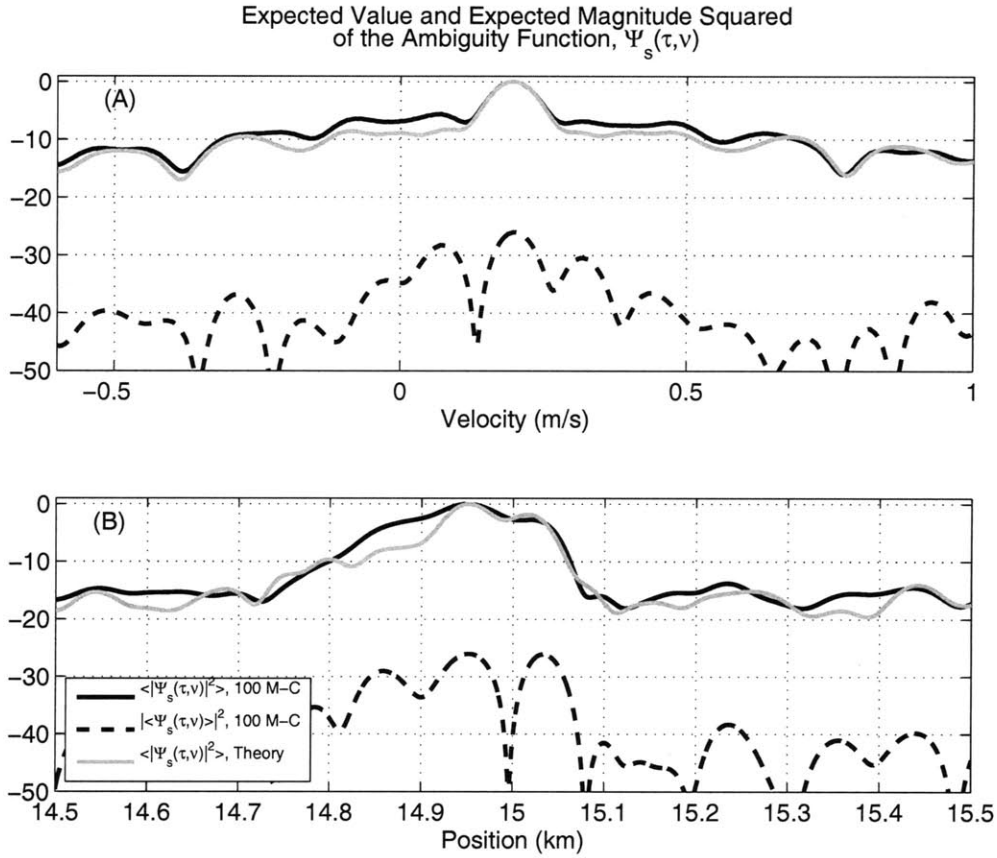

Figure 5-4: Waveguide. Expected value (black dashed line) and expected square magnitude (black solid line) of the ambiguity function via 100 Monte-Carlo simulations for the field scattered from a random aggregation of targets following the Case A scenario described in Table 5.1. The cross-range resolution is set to be such that the fish areal number density is 2 fish/m^2. The source signal and remote sensing system parameters are given in Table 5.2. The expected magnitude of the ambiguity function based on evaluating Eqs. (5.14-5.15) and (5.6) is also shown (gray line) and is found to be in good agreement with the Monte-Carlo result. The variance of the ambiguity function dominates the total intensity and the magnitude squared of the ambiguity function's expected value is negligible.

Estimating Target Position and Velocity Statistics

As in the free space case, Eqs. (5.14) and (5.15) cannot typically be analytically evaluated. A significant simplification is however possible in the case of some specially designed source spectra, such as Costas sequences, which can be written in the form of Eq. (5.7), $Q(\Omega) = \sum_{n=0}^{M-1} a_n e^{i(\Omega-\Omega_n)H_n}\delta(\Omega-\Omega_n)$. The second moment of the ambiguity function is then given by (see Appendix E.2),

$$\begin{aligned}\langle|\Psi_{s,q}(\tau,\nu)|^2\rangle &= \sum_{n'}^{M-1}\sum_{m'}^{M-1}\sum_{l'}^{M-1}\sum_{j'}^{M-1}\frac{a^*_{n'}a_{m'}a_{l'}a^*_{j'}}{\pi^2}\left[\frac{S(\omega_{n'}+2\pi\nu)}{(\omega_{n'}+2\pi\nu)/c}\right]\left[\frac{S^*(\omega_{l'}+2\pi\nu)}{\omega_{l'}+2\pi\nu)/c}\right] \\ &\quad\times\delta\left(\frac{\omega_{j'}}{\omega_{m'}}-\frac{\omega_{l'}+2\pi\nu}{\omega_{n'}+2\pi\nu}\right)e^{-i(\omega_{n'}-\omega_{l'})\tau} \\ &\quad\times\sum_l\sum_m\sum_n\sum_p U_q^{l,m,n,p}(\omega_{n'}+2\pi\nu,\omega_{l'}+2\pi\nu,\tilde{v}_q)P_v(\tilde{v}_q)\end{aligned} \tag{5.16}$$

where $a_{n'}$ are the coefficients of the $\omega_{n'}$ frequency components for $n' = 1, 2, \ldots, M$, and

$$\tilde{v}_q = \left(\frac{\omega_{n'}+2\pi\nu}{\omega_{m'}}-1\right)(1/v_l^G + 1/v_m^G)^{-1} \tag{5.17}$$

Despite this simplified form, it is still not straightforward to derive analytical expressions for the moments along time delay τ and Doppler shift ν. We note, however, that

$$\begin{aligned}&U_q^{l,m,n,p}(\omega_{n'}+2\pi\nu,\omega_{l'}+2\pi\nu,\tilde{v}_q) \equiv \\ &\quad\equiv\frac{1}{V}\int_V \Phi_{s,q}^{l,m}(\mathbf{r},\omega_{m'},\omega_{n'}+2\pi\nu)\Phi_{s,q}^{*n,p}(\mathbf{r},\omega_{j'},\omega_{l'}+2\pi\nu)\mathrm{d}^3\mathbf{u}_q^0,\end{aligned} \tag{5.18}$$

which is not a function of target velocity, so that Eq. (5.16) for the waveguide has many similarities with Eq. (5.8) for the free space case. In the illustrative examples of Section 5.3.2, we assume the form of Eq. (5.9) still holds and use the coefficients of Table 5.3 for free space to estimate the velocity means and standard deviations in a waveguide.

5.3 Illustrative Examples

Here, we demonstrate how the position and velocity mean and standard deviation of a group of targets can be simultaneously estimated in free space and in a typical continental-shelf environment. We examine the three target scenarios described in Table 5.1, which are illustrative of long-range remote sensing of marine life in the ocean. In all the examples, we employ the Costas sequence design detailed in Appendix E.3 and the remote sensing system parameters summarized in Table 5.2. The mean of the ambiguity function and its expected square magnitude are found by evaluating either Eqs. (5.4 - 5.5) for free space, or Eqs. (5.14 - 5.15) for the waveguide scenario via 100 Monte-Carlo simulations. We then evaluate the moments of the ambiguity function square magnitude along constant time delay and Doppler shift axes. Estimates of the targets' velocity and position mean and standard deviation are obtained via the Moment Method by inverting Eqs. (5.9) and (5.11), using coefficients from Table 5.3,

$$\hat{\mu}_{v,j} = \frac{\nu_1 - c_1}{d_1}, \tag{5.19a}$$

$$\hat{\sigma}_{v,j} = \sqrt{\frac{\nu_2 - c_2 - d_2\hat{\mu}_{v,j} - e_2\hat{\mu}_{v,j}^2}{e_2}}, \tag{5.19b}$$

$$\hat{\mathbf{i}}_r \cdot \hat{\boldsymbol{\mu}}_{\mathbf{u}} = \frac{c\tau_1}{d_3} - r, \tag{5.19c}$$

$$\hat{\mathbf{i}}_r \cdot \boldsymbol{\sigma}_{\mathbf{u}} = \sqrt{\frac{c^2\tau_2}{2d_3} - \left[r + \hat{\mathbf{i}}_r \cdot \boldsymbol{\mu}_{\mathbf{u}}\right]^2} \tag{5.19d}$$

where

$$d_3 = \sum_{n=0}^{M-1}\sum_{m=0}^{M-1} d_{n,m}, \tag{5.20}$$

$d_{n,m}$ has been defined in Eq. (5.12), and j corresponds to one Monte-Carlo simulation. For the coefficients c_1 through e_2, we use the analytically calculated values for free space given in the first row of Table 5.3. Estimates of the mean velocity and position are also obtained by simply finding the peak of the ambiguity function square

magnitude, which we refer to as the Peak Method and define by

$$\langle |\Psi_{s,q}(\tau,\nu)|^2 \rangle \big|_{\nu=2\hat{\mu}'_{v,j} f_c/c}\,, \tag{5.21a}$$

$$\langle |\Psi_{s,q}(\tau,\nu)|^2 \rangle \big|_{\tau=2\hat{\boldsymbol{\mu}}'_{\mathbf{u},j}/c}\,, \tag{5.21b}$$

For each estimated quantity, $N_{MC} = 100$ Monte-Carlo simulations are used to calculate the estimate's sample mean and sample variance, and so investigate how such estimates perform in both free space and waveguide environments. For example,

$$\langle \hat{\mu}_v \rangle = \frac{1}{N_{MC}} \sum_{j=1}^{N_{MC}} \hat{\mu}_{v,j}, \tag{5.22a}$$

$$\mathrm{var}(\hat{\mu}_v) = \frac{1}{N_{MC}} \sum_{j=1}^{N_{MC}} \left(\hat{\mu}_{v,j} - \langle \hat{\mu}_v \rangle\right)^2 \tag{5.22b}$$

The free space results are presented here for comparison with those in a waveguide, since analytical expressions for the moments of the expected square magnitude of the ambiguity function have been derived only for free space. For the waveguide scenarios, we check whether estimates of the velocity and position mean and standard deviation can be obtained via the Moment Method using the analytical expressions derived in free space, Eqs. (5.9) and (5.11), and Table 5.3.

5.3.1 Free Space

The expected square magnitude of the ambiguity function, as well as constant-velocity and constant-position cuts through its maximum for a typical migrating shoal of herring (Table 5.1, Case A) are shown in Fig. 5-5, given the signal and remote sensing system parameters summarized in Table 5.2. Estimates of the velocity and position mean are obtained via the Moment Method (Eqs. (5.19a) and (5.19c)), as well as via the Peak Method (Eq. (5.21)). The Moment Method and Eqs. (5.19b) and (5.19d) are then used to estimate the velocity and position standard deviation.

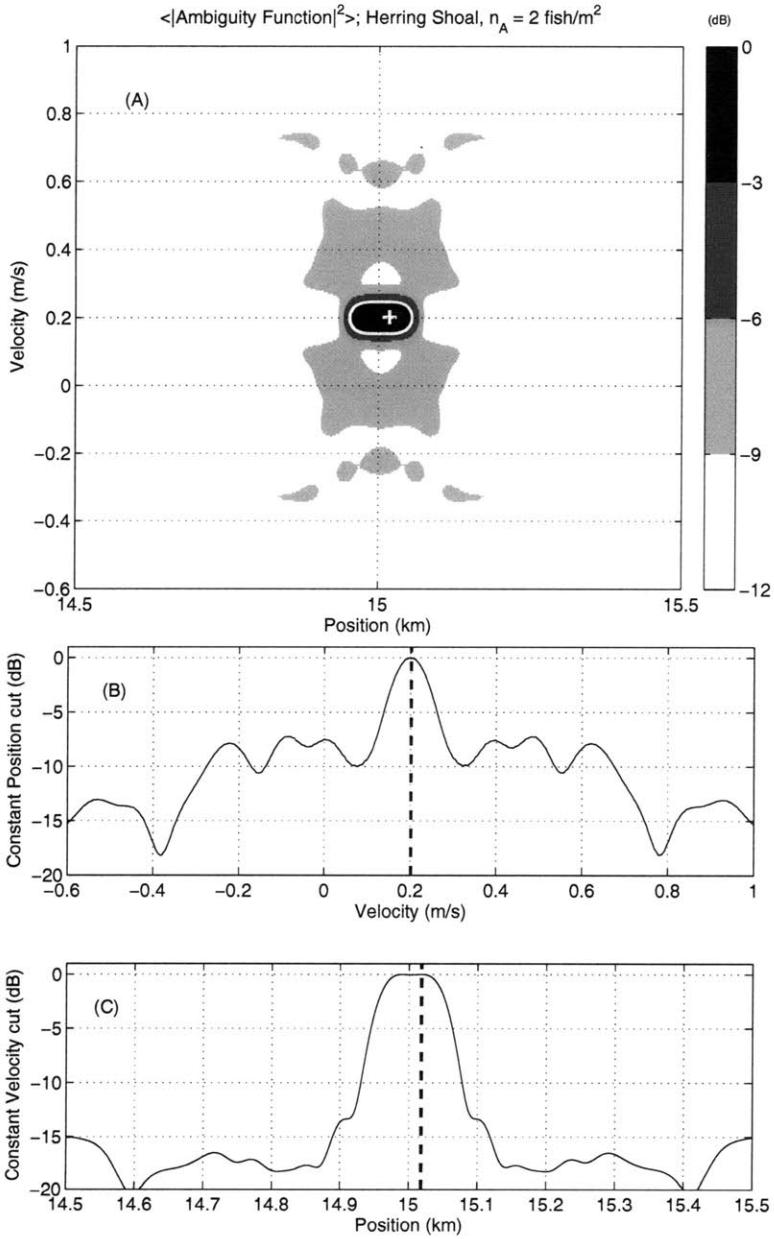

Figure 5-5: Free Space. The strength of the sidelobes is much less than half that of the main lobe and the Moment Method provides accurate velocity and position estimates, as shown in Fig. 5-6. (a) Expected value of the ambiguity function square magnitude for the pressure field scattered from a shoal of migrating herring (Table 5.1, Case A) and given the source signal and remote sensing system parameters in Table 5.2. The white curve indicates 3 dB-down contour(s), which may be used to roughly delimit the target shoal. The maximum of the ambiguity surface is shown by a white cross. (b, c) Constant-velocity and constant-position cuts through the point indicated by the white cross in (a). Dashed lines indicate the mean position and velocity estimates based on the maximum value of the ambiguity surface (Peak Method).

The sample means and sample standard deviations, e.g. Eqs. (5.22a) and (5.22b), of these estimates are shown in Fig. 5-6. We find that estimates of the velocity and position mean based on the Moment Method are at least as accurate as those based on the Peak Method. For mean velocity, only the case of the swarming herring demonstrates an observable bias which is likely due to the very large standard deviation of the targets' velocity for that scenario. As long as the estimate of mean position is within the 40 m resolution footprint of the remote sensing system, for practical purposes, the target group has been accurately localized. This is the case for all the examples considered here, as shown in Fig. 5-6. Estimates of the velocity standard deviation for Cases A, B and C are very distinct. This suggests that in free space it may be possible to use the Moment Method to help identify and classify dynamic behavior.

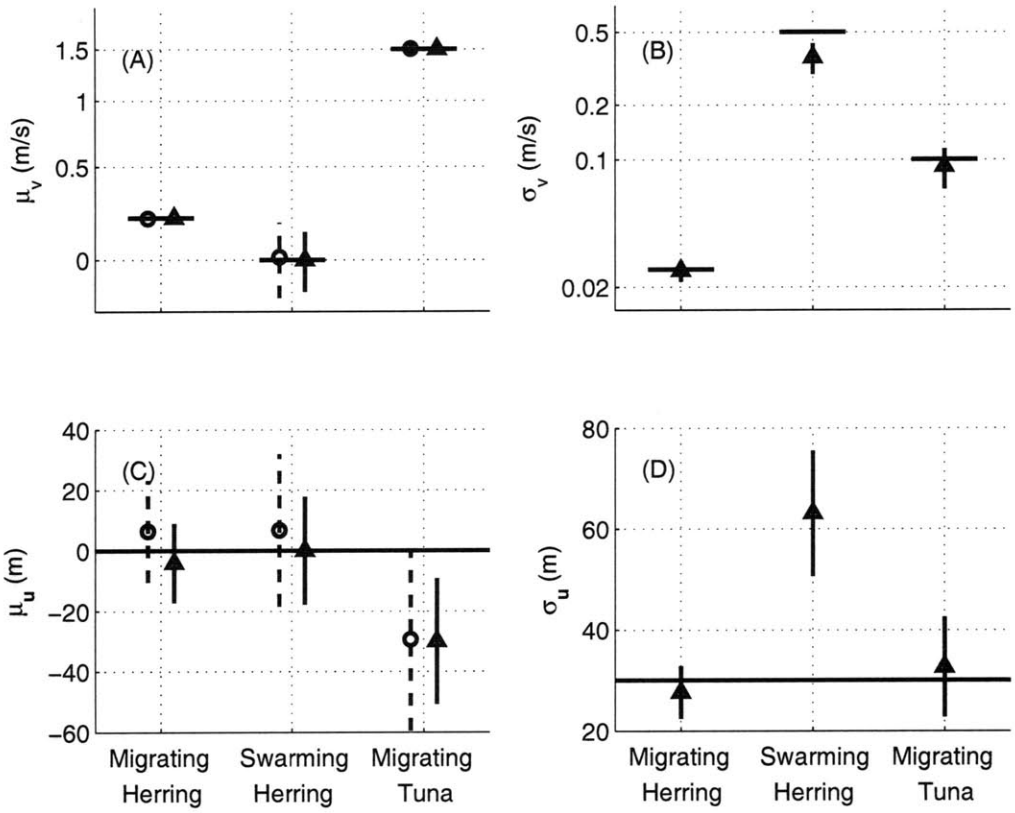

Figure 5-6: Free Space. Estimates of the velocity and position mean and standard deviation for simulated migrating and swarming herring shoals, and a migrating school of tuna (Table 5.1), given the source signal and remote sensing system parameters summarized in Table 5.2. Target positions are localized within the remote sensing system's resolution footprint, and velocity estimate errors are typically less than roughly 10%. Horizontal lines indicate true values. (a, b) Estimates of the targets' velocity mean and standard deviation. Triangles and solid vertical lines indicate the sample means and sample standard deviations of estimates obtained via the Moment Method (Eqs. (5.19a) and (5.19b)), using 100 Monte-Carlo simulations. Circles and dashed lines indicate the sample mean and sample standard deviation for estimates of the mean velocity obtained via the Peak Method (Eq. (5.21a)), i.e. by locating the maximum of the ambiguity function square magnitude (white cross in Fig. 5-5(a)). (c, d) Same as (a, b) but for estimates of the group's position mean and standard deviations obtained via both the Moment (triangles and solid vertical lines) and Peak (circles and dashed lines) methods.

5.3.2 Waveguide

We consider the same cases (Table 5.1) as in Section 5.3.1 for free space, with the same source signal and remote sensing system parameters (Table 5.2), but now in the waveguide of Fig. 5-2. For the case of a migrating herring shoal (Table 5.1, Case A), we find that the Peak and Moment methods provide accurate velocity and position estimates, even though the ambiguity function square magnitude now exhibits more significant sidelobes, as shown in Fig. 5-7.

These estimates for all cases are shown in Fig. 5-8. We find that the free space expressions and coefficients for the Moment Method of Eqs. (5.9), (5.11) and Table 5.3 provide very good estimates of the mean velocity and position of the groups and their standard deviation in a stratified range-independent waveguide environment. Estimates of the velocity mean and standard deviation are found to typically be within 10% of their true values, and the targets are accurately localized within the system's resolution footprint. Estimates of the velocity standard deviation for the three different cases considered are found to be distinct, which suggests that it may be possible to classify dynamic behavior through instantaneous Doppler measurements.

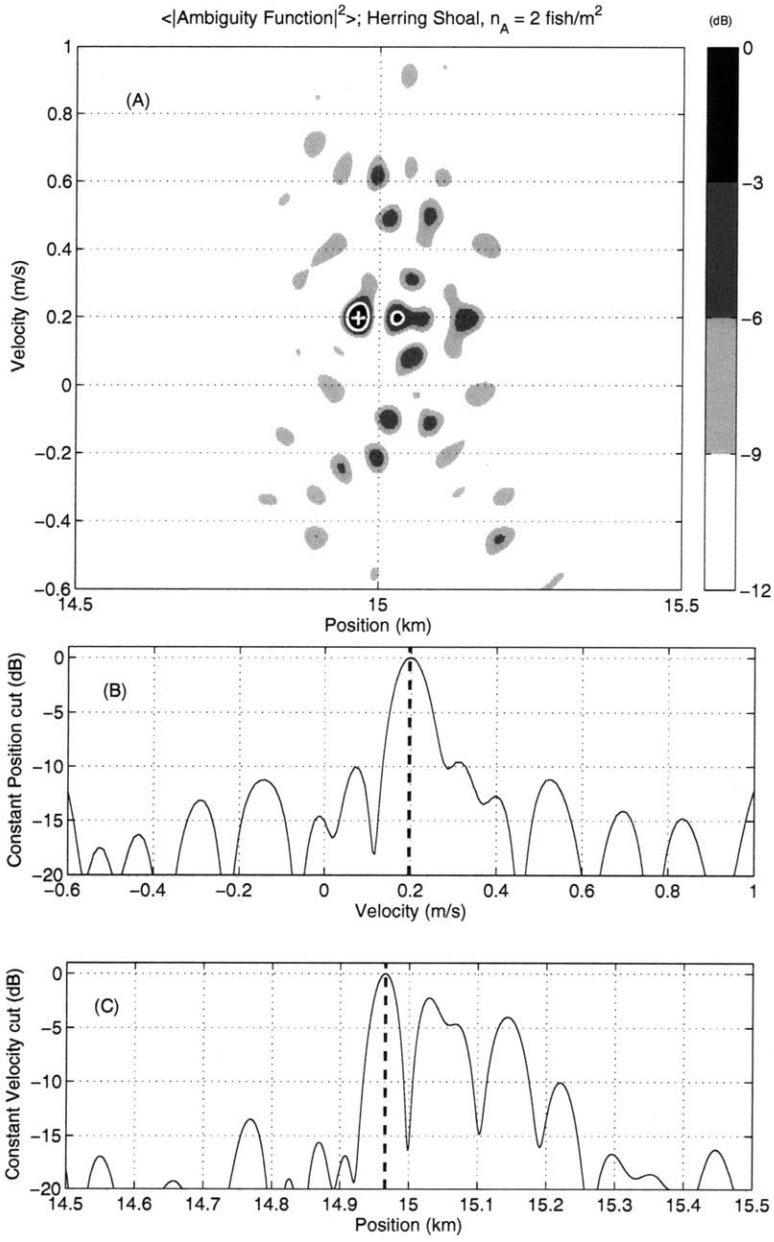

Figure 5-7: Waveguide. There is now more energy in the sidelobes of the ambiguity function compared to Fig. 5-5, but both the Peak and Moment methods still provide accurate velocity and position estimates as seen in Fig. 5-8. (a) Expected value of the ambiguity function square magnitude for the pressure field scattered from a shoal of migrating herring (Table 5.1, Case A) and given the source signal and remote sensing system parameters in Table 5.2. The fish are assumed to be submerged in the waveguide of Fig. 5-2. The cross-range resolution is set to be such that the fish areal number density is 2 fish/m^2. The white curve indicated 3 dB-down contour(s), which may be used to roughly delimit the target shoal. The maximum of the ambiguity surface is shown by a white cross. (b, c) Constant-velocity and constant-position cuts through the point indicated by the white cross in (a). Dashed lines indicate the mean position and velocity estimates based on the maximum value of the ambiguity surface (Peak Method).

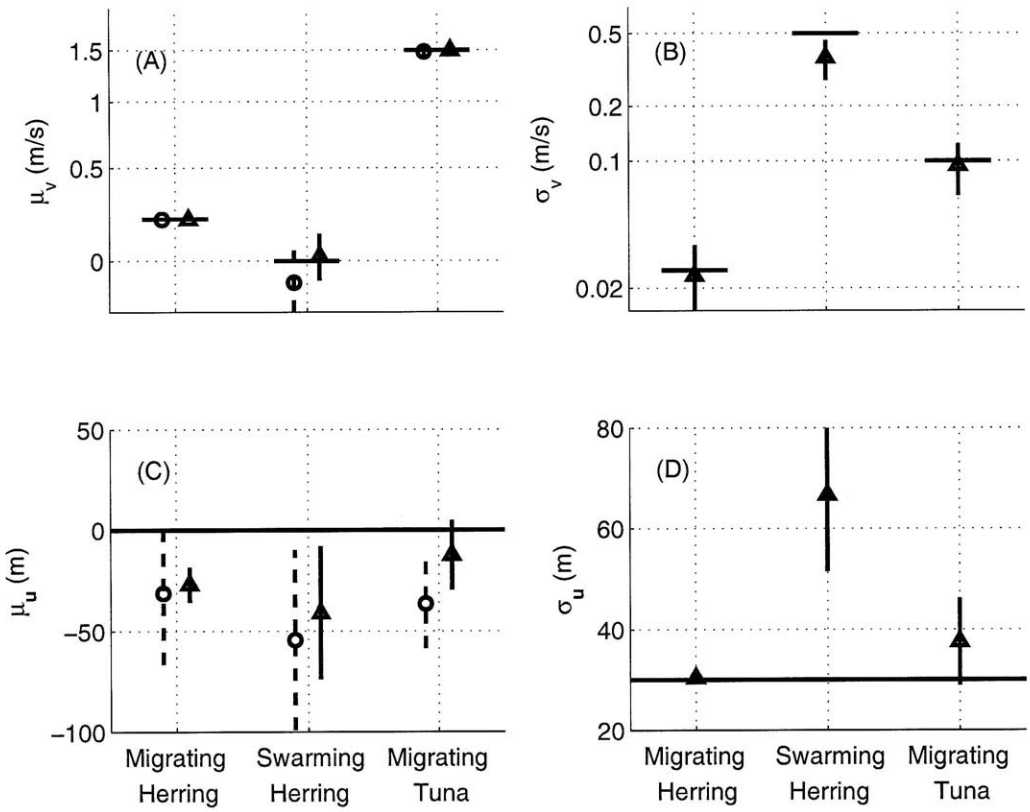

Figure 5-8: Waveguide. Estimates of the velocity and position mean and standard deviation for simulated migrating and swarming herring shoals, and a migrating school of tuna (Table 5.1), given the source signal and remote sensing system parameters summarized in Table 5.2. Target positions are localized within the remote sensing system's resolution footprint, and velocity estimate errors are typically less than roughly 10%. Horizontal lines indicate true values. (a, b) The sample means and sample standard deviations of estimates of the tagets' velocities mean and standard deviation obtained via the Moment Method (Eqs. (5.19a) and (5.19b), triangles and solid vertical lines). Also the sample mean and sample standard deviation of the target mean velocity estimate obtained via the Peak Method (Eq. (5.21a), circles and dashed lines), i.e. by locating the maximum of the ambiguity function (white cross in Fig. 5-7). (c, d) Same as (a, b) but for estimates of the group's position mean and standard deviations obtained via both the Moment (triangles and solid vertical lines) and Peak (circles and dashed lines) methods.

5.4 Conclusions

We showed that for typical remote sensing scenarios of large aggregations of randomly distributed moving targets where the group dimensions are much larger than the acoustic wavelength, the variance of the scattered field dominates the range-velocity ambiguity function, but cross-spectral coherence remains and enables high resolution Doppler velocity and position estimation. We then developed a method for simultaneously and instantaneously estimating the means and standard deviations of the velocity and position of groups of self-propelled underwater targets from moments of the measured range-velocity ambiguity function. This Moment Method is based on analytic expressions for the expected square magnitude of the range-velocity ambiguity function *in free space.* It was shown that for pseudo-random signals, such as Costas sequences, the moments of the ambiguity function's expected square magnitude along constant time delay and Doppler shift are linear functions of the mean and variance of the targets' velocity and position. We also described an alternative Peak Method that can be used to estimate the targets' mean velocity and position.

Both methods were shown to perform well not only in free space, but in a typical continental shelf ocean waveguide also. In particular, for typical long-range imaging scenarios, exceeding 10 km, the target groups were accurately localized within the remote sensing system's resolution footprint with simultaneous velocity mean and standard deviation estimates for the group within 10% of the true values. We found that the estimates obtained via the Moment Method were at least as accurate as those provided by the Peak Method. The performance of both methods is dependent on maintaining low sidelobes in the ambiguity surface. Since it is only possible to measure the targets' velocity component *relative* to the system, at least two sources or receivers must be used to estimate horizontal velocity vectors.

Chapter 6

Conclusion

In this thesis, we investigated the biases and errors inherent in parameter estimates obtained from nonlinear inversions of measured data that are randomized by additive signal-independent ambient noise, as well as signal-dependent noise arising due to propagation through fluctuating media and random inhomogeneities, relative motion between source and receiver, scattering from rough surfaces and source incoherence. Three problems were considered where signal-dependent noise is typically present: (1) passive source localization in a fluctuating waveguide containing random internal waves, (2) Lambertian surface orientation and albedo resolution, and (3) planetary terrain photoclinometric surface slope estimation. For each of these problems, we first expand the bias and covariance of Maximum Likelihood Estimates (MLEs) in inverse orders of sample size or Signal to Noise Ratio (SNR). We then determine necessary conditions on sample size or SNR to obtain accurate parameter estimates, following the approach of Ref. [84], which is based on classical estimation theory and is independent of the estimation technique. The results presented here can be used in experimental design to ensure that statistical biases and errors meet pre-determined error thresholds.

The biases and errors of photoclinometric surface slope MLEs are shown to typically become much larger than surface slopes for illuminations and observations where planetary reflectance is weakly dependent on surface slope. Further, the asymptotic biaeses and errors are shown to typically differ dramatically from the exact ones,

making them applicable only when a large number of independent samples is available. For this problem, a unified method is provided for quantitatively comparing the biases and errors from different sources of uncertainty, including signal-independent (camera read) noise, signal-dependent (camera shot) noise, as well as noise due to scall-scale albedo fluctuations and atmospheric haze. Albedo variability is shown to typically dominate estimate biases and errors.

The minimum number of independent samples or SNR necessary for Lambertian surface orientation and albedo MLEs to be asymptotically unbiased and attain classical estimation theory's lower bound on resolution as well as practical design thresholds are derived. Single-sample MLEs are shown to have biases and errors that vary dramatically depending on illumination direction. The number of samples or SNR necessary to accurately estimate surface orientation and albedo is shown to become arbitrarily large as the illumination directions approach the coplanar limit, while accurate stereo resolution of 3-D surface orientation and albedo is shown to be possible even with a single sample given illumination directions of sufficient diversity and shallow angle incidence.

For passive source localization, we quantify the effects of the loss of coherence in the forward propagated field due to scattering by random 3-D internal waves, and find that there may be significant losses in localization ability with narrowband vertical array measurements for fixed source and receiver. The sample sizes necessary to obtain accurate source position estimates increase by at least an order of magnitude, when compared to the static waveguide case. It may then no longer be possible to attain the requisite number of independent samples since stationary averaging may be necessary over time periods on the order of hours. We also demonstrate the advantages of using analytical tools that can take advantage of the parameter dependence of both the mean and variance of the measured field by comparing the asymptotic biases and errors to those calculated when either the covariance or the mean of the measurement is incorrectly assumed to be parameter independent.

Finally, we also developed a method for estimating the means and standard deviations of the velocity and position of self-propelled underwater target groups imaged

using Ocean Acoustic Waveguide Remote Sensing (OAWRS). This method is based on analytical expressions of the range-velocity ambiguity function for the acoustic field scattered from such target groups. For free space, we showed that the moments of the range-velocity ambiguity function magnitude squared are linearly related to the targets' velocity and position mean and variance. We also demonstrated that the method performs well in a typical continental shelf environment and the velocity mean and standard deviation can typically be estimated within 10% of their true values. Estimates of the second order velocity statistics may offer new possibilities for clutter discrimination and classification.

Appendix A

Asymptotic Bias and Variance of the MLE and the Sample Sizes Necessary for Accurate Parameter Estimation

A.1 Asymptotic Expansions of the MLE Bias and Variance

Following the theory and notation adopted in Ref. [84], assume an experimental measurement that consists of a set of n independent and identically distributed N-dimensional real-valued random data vectors $\mathbf{X}_j$ obeying the conditional probability density $p(\mathbf{X};\boldsymbol{\theta})$, where $\mathbf{X} = [\mathbf{X}_1^T, \ldots, \mathbf{X}_n^T]$ and $\boldsymbol{\theta}$ is an m-dimensional parameter vector. Also let $\boldsymbol{\nu}^T = [\nu_1, \nu_2, \ldots, \nu_N]$ be the vector of samples ν_k used to obtain the measurement $X_{j,k}$ for $k = 1, 2, \ldots, N$ and all $j = 1, 2, \ldots, n$.

The MLE $\hat{\boldsymbol{\theta}}$ of $\boldsymbol{\theta}$ is the maximum of the log-likelihood function $l(\boldsymbol{\theta}) = \ln(p(\mathbf{X};\boldsymbol{\theta}))$ with respect to $\boldsymbol{\theta}$.[89, 5, 44] The first-order parameter derivative of the log-likelihood function is defined as $l_r = \partial l(\boldsymbol{\theta})/\partial\theta^r$, where θ^r is the rth component of $\boldsymbol{\theta}$. The elements of the expected information matrix, also known as the Fisher information

matrix, are given by $i_{rs} = \langle l_r l_s \rangle$, and the elements of its inverse by $i^{rs} = [\mathbf{i}^{-1}]_{rs}$, where $\mathbf{i}^{-1}$ is the CRLB,[89, 60, 104] and $\langle \ldots \rangle$ signifies expected value. Moments of the log-likelihood derivatives are defined by $\upsilon_R \equiv \langle l_R \rangle$, and joint moments by $\upsilon_{R_1,R_2,\ldots,R_M} = \langle l_{R_1} l_{R_2} \ldots l_{R_M} \rangle$, where R_i is an arbitrary set of indices.[84, 102]

The moments of $\hat{\theta}^r$ for $r = 1, \ldots, m$ can then be expressed as a series of inverse powers of the sample size n,[84, 102] provided that the required derivatives of the likelihood function exist.[95] The MLE bias is then given by[110, 8]

$$\text{bias}(\hat{\theta}^r, \boldsymbol{\nu}, n) = b_1(\hat{\theta}^r; \boldsymbol{\theta}, \boldsymbol{\nu}, n) + b_2(\hat{\theta}^r; \boldsymbol{\theta}, \boldsymbol{\nu}, n) + \text{Higher Order terms}, \tag{A.1}$$

where $b_j(\hat{\theta}^r; \boldsymbol{\theta}, \boldsymbol{\nu}, n) = b_j(\hat{\theta}^r; \boldsymbol{\theta}, \boldsymbol{\nu}, 1)/n^j$, so that

$$\text{bias}(\hat{\theta}^r, \boldsymbol{\nu}, n) = \frac{b_1(\hat{\theta}^r; \boldsymbol{\theta}, \boldsymbol{\nu}, 1)}{n} + \frac{b_2(\hat{\theta}^r; \boldsymbol{\theta}, \boldsymbol{\nu}, 1)}{n^2} + \mathrm{O}(n^{-3}), \tag{A.2}$$

where $\mathrm{O}(n^{-3})$ represents integer powers n^{-3} and higher. Similarly, the MLE variance can be written as

$$\text{var}(\hat{\theta}^r, \boldsymbol{\nu}, n) = \frac{var_1(\hat{\theta}^r; \boldsymbol{\theta}, \boldsymbol{\nu}, 1)}{n} + \frac{var_2(\hat{\theta}^r; \boldsymbol{\theta}, \boldsymbol{\nu}, 1)}{n^2} + \mathrm{O}(n^{-3}) \tag{A.3}$$

where the first term on the right hand side of Eq. (A.3) is the CRLB, which is the asymptotic value of the variance when sample size n and SNR become large and also the minimum possible mean square error (MSE) of an unbiased estimate.

A.2 Necessary Sample Sizes to Attain Design Error Thresholds

The value of n necessary for the MLE to become asymptotically unbiased is found by requiring the first-order bias to be much smaller than the true value of the parameter

$$n \gg \left| \frac{b_1(\hat{\theta}^r; \boldsymbol{\theta}, \boldsymbol{\nu}, 1)}{\theta^r} \right| \tag{A.4}$$

Similarly, the value of n necessary for the MLE variance to asymptotically attain the CRLB is found by requiring the second-order variance to be much smaller than the first-order, so that

$$n \gg \frac{|var_2(\hat{\theta}^r; \boldsymbol{\theta}, \boldsymbol{\nu}, 1)|}{var_1(\hat{\theta}^r; \boldsymbol{\theta}, \boldsymbol{\nu}, 1)} \tag{A.5}$$

Only for values of n satisfying these conditions is it possible for the estimate to be in the asymptotic regime where it is unbiased and it continuously attains the CRLB,[84, 102, 110] so that it has the minimum possible mean square error. Following established convention,[102, 110] we determine the sample sizes necessary to obtain an unbiased, minimum variance MLE by requiring the first-order bias and the second-order variance to be an order of magnitude smaller than the true value of the parameter and the first-order variance, respectively,

$$n_b \equiv 10 \left| \frac{b_1(\hat{\theta}^r; \boldsymbol{\theta}, \boldsymbol{\nu}, 1)}{\theta^r} \right| \tag{A.6a}$$

$$n_v \equiv 10 \frac{|var_2(\hat{\theta}^r; \boldsymbol{\theta}, \boldsymbol{\nu}, 1)|}{var_1(\hat{\theta}^r; \boldsymbol{\theta}, \boldsymbol{\nu}, 1)}, \tag{A.6b}$$

In this thesis, conditions on sample size or SNR for parameter estimates to attain specified design error thresholds are calculated by requiring that (i) n meets the conditions in Eq. (A.6), and (ii) the CRLB is smaller than the desired error threshold. The sample size necessary to obtain accurate parameter estimates is then given by $(\max[n_b, n_v]) \times n'$, where

$$n' = \frac{\text{CRLB}(\max[n_b, n_v])}{(\text{design threshold})^2} \tag{A.7}$$

A.3 Expressions for the Asymptotic Orders of the MLE Bias and Variance

Expressions for $b_1(\hat{\theta}^r;\boldsymbol{\theta},\boldsymbol{\nu},n)$, $var_1(\hat{\theta}^r;\boldsymbol{\theta},\boldsymbol{\nu},n)$ and $var_2(\hat{\theta}^r;\boldsymbol{\theta},\boldsymbol{\nu},n)$ have been derived in terms of tensors in the form of $\upsilon_{R_1,R_2,\ldots,R_M}$ corresponding to moments of the log-likelihood derivatives,[84, 68] as summarized below

$$b_1(\hat{\theta}^r;\boldsymbol{\theta},\boldsymbol{\nu},n) = \frac{1}{2}i^{ra}i^{bc}(\upsilon_{abc}+2\upsilon_{ab,c}) \tag{A.8}$$

$$var_1(\hat{\theta}^r;\boldsymbol{\theta},\boldsymbol{\nu},n) = i^{rr} \tag{A.9}$$

$$\begin{aligned} var_2(\hat{\theta}^r;\boldsymbol{\theta},\boldsymbol{\nu},n) = & -i^{rr} \\ & +i^{rm}i^{rm}\Big[i^{pq}\Big(2\upsilon_{mq,m,p}+\upsilon_{mmpq}+3\upsilon_{mq,pm}+2\upsilon_{mmp,q}+\upsilon_{mpq,m}\Big) \\ & +i^{pz}i^{qt}\Big(\upsilon_{mpt}\upsilon_{m,q,z}+\upsilon_{mpm}\upsilon_{qzt}+\frac{5}{2}\upsilon_{mpq}\upsilon_{mzt}+2\upsilon_{m,qz}\upsilon_{mtp} \\ & +2\upsilon_{mmt}\upsilon_{qz,p}+6\upsilon_{mt,z}\upsilon_{mpq}+\upsilon_{m,mt}\upsilon_{pqz}+2\upsilon_{mq,z}\upsilon_{pt,m} \\ & +2\upsilon_{mq,m}\upsilon_{pt,z}+\upsilon_{mq,p}\upsilon_{mt,z}\Big)\Big] \end{aligned} \tag{A.10}$$

Here, as elsewhere, the Einstein summation convention is used, where summation over indices appearing both as superscript and subscript is implied. These expressions are evaluated for the case of multivariate Gaussian data in Appendix B.

Appendix B

Joint Moments for Asymptotic Gaussian Inference

B.1 Analytical Tensor Expressions for General Multivariate Gaussian Data

Before giving the explicit expressions for the first order bias and the second order covariance, we define the auxiliary quantities

$$N_{ab} = \frac{1}{2}\mathbf{C}^{-1}\boldsymbol{\mu}_{ab} + (\mathbf{C}^{-1})_b\boldsymbol{\mu}_a = \frac{1}{2}\mathbf{C}^{-1}\frac{\partial^2\boldsymbol{\mu}}{\partial\vartheta^a\partial\vartheta^b} + \frac{\partial\mathbf{C}^{-1}}{\partial\vartheta^b}\frac{\partial\boldsymbol{\mu}}{\partial\vartheta^a} \tag{B.1a}$$

$$\begin{aligned} M_{abc} &= \frac{1}{3}\mathbf{C}^{-1}\boldsymbol{\mu}_{abc} + (\mathbf{C}^{-1})_c\boldsymbol{\mu}_{ab} + (\mathbf{C}^{-1})_{bc}\boldsymbol{\mu}_a \\ &= \frac{1}{3}\mathbf{C}^{-1}\frac{\partial^3\boldsymbol{\mu}}{\partial\vartheta^a\partial\vartheta^b\partial\vartheta^c} + \frac{\partial\mathbf{C}^{-1}}{\partial\vartheta^c}\frac{\partial^2\boldsymbol{\mu}}{\partial\vartheta^a\partial\vartheta^b} + \frac{\partial^2\mathbf{C}^{-1}}{\partial\vartheta^b\partial\vartheta^c}\frac{\partial\boldsymbol{\mu}}{\partial\vartheta^a} \end{aligned} \tag{B.1b}$$

$$\check{\mathbf{C}}_{a_1..a_p} = \mathbf{C}^{-1}\mathbf{C}_{a_1..a_p} = \mathbf{C}^{-1}\frac{\partial^p\mathbf{C}}{\partial\vartheta^{a_1}..\partial\vartheta^{a_p}} \tag{B.1c}$$

$$\tilde{\mathbf{C}}_{a_1..a_p} = \mathbf{C}(\mathbf{C}^{-1})_{a_1..a_p} = \mathbf{C}\frac{\partial^p\mathbf{C}^{-1}}{\partial\vartheta^{a_1}..\partial\vartheta^{a_p}} \tag{B.1d}$$

$$\beta_{abc} = tr\Big(\frac{\partial^2}{\partial\vartheta^b\partial\vartheta^c}[\mathbf{C}^{-1}\frac{\partial\mathbf{C}}{\partial\vartheta^a}]\Big) + tr\Big(\mathbf{C}\frac{\partial^3\mathbf{C}^{-1}}{\partial\vartheta^a\partial\vartheta^b\partial\vartheta^c}\Big) \tag{B.1e}$$

and specify that we will write the tensors as a principal group of terms plus the terms obtained by a rearrangement of the indexes using the notation described in Table B.1. If more than one of the symmetry prescriptions appear in the same tensor, it means

that the total number of terms contained is the product of the number of terms generated by each symmetry. As a reminder, for the terms where the sample size n is not explicitly shown, we write a square bracket beside it containing the corresponding power. For example, $\upsilon_{ab}\upsilon_{cd}[2]$ is proportional to n^2 since it is the product of two terms proportional to n.

Table B.1: Legend of Index Rearrangement

$A_{a_1,a_2,...,a_m}$, perm$(a_1, a_2, ..., a_m)$:	Add the terms with permutated indexes
$A_{a_1,a_2,...,a_m}$, rot$(a_1, a_2, ..., a_m)$:	Add the terms with rotated indexes
$A_{a_1,a_2,...,a_m}$, $(a_i \leftrightarrow a_j)$:	Add the terms with indexes a_i and a_j inverted

The tensors are then given by

$$\upsilon_{a,b} = -\upsilon_{ab} = \mathbf{i}_{ab} = n[\boldsymbol{\mu}_a^T \mathbf{C}^{-1} \boldsymbol{\mu}_b + \frac{1}{2} tr(\check{\mathbf{C}}_a \check{\mathbf{C}}_b)] \tag{B.2a}$$

$$\upsilon_{abc} = n[-\boldsymbol{\mu}_{ab}^T \mathbf{C}^{-1} \boldsymbol{\mu}_c - \boldsymbol{\mu}_a^T (\mathbf{C}^{-1})_b \boldsymbol{\mu}_c + \frac{2}{3} tr(\check{\mathbf{C}}_a \check{\mathbf{C}}_b \check{\mathbf{C}}_c) - \frac{1}{2} tr(\check{\mathbf{C}}_{ab} \check{\mathbf{C}}_c)], \quad \text{rot}(a, b, c) \tag{B.2b}$$

$$\upsilon_{ab,c} = n[{N_{ab}}^T \boldsymbol{\mu}_c + \frac{1}{4} tr(\tilde{\mathbf{C}}_{ab} \tilde{\mathbf{C}}_c)], \ (a \leftrightarrow b) \tag{B.2c}$$

$$\upsilon_{a,b,c} = n[-\frac{1}{2} \boldsymbol{\mu}_a^T (\mathbf{C}^{-1})_b \boldsymbol{\mu}_c + \frac{1}{6} tr(\check{\mathbf{C}}_a \check{\mathbf{C}}_b \check{\mathbf{C}}_c)], \ \text{perm}(a, b, c) \tag{B.2d}$$

$$\upsilon_{abcd} = n \left[-\frac{1}{8} \boldsymbol{\mu}_{ab}^T \mathbf{C}^{-1} \boldsymbol{\mu}_{cd} - \frac{1}{6} \boldsymbol{\mu}_{abc}^T \mathbf{C}^{-1} \boldsymbol{\mu}_d - \frac{3}{8} tr(\check{\mathbf{C}}_a \check{\mathbf{C}}_b \check{\mathbf{C}}_c \check{\mathbf{C}}_d) + \frac{1}{2} tr(\check{\mathbf{C}}_{ab} \check{\mathbf{C}}_c \check{\mathbf{C}}_d) \right.$$
$$\left. -\frac{1}{16} tr(\check{\mathbf{C}}_{ab} \check{\mathbf{C}}_{cd}) - \frac{1}{12} tr(\check{\mathbf{C}}_{abc} \check{\mathbf{C}}_d) - \frac{1}{2} \boldsymbol{\mu}_{ab}^T (\mathbf{C}^{-1})_c \boldsymbol{\mu}_d - \frac{1}{4} \boldsymbol{\mu}_a^T (\mathbf{C}^{-1})_{bc} \boldsymbol{\mu}_d \right], \quad \text{perm}(a, b, c, d) \tag{B.2e}$$

$$\upsilon_{a,b,c,d} = \frac{1}{8} \upsilon_{a,b} \upsilon_{c,d}[2] + n[\frac{1}{2} \boldsymbol{\mu}_a^T \mathbf{C}^{-1} \tilde{\mathbf{C}}_b \tilde{\mathbf{C}}_c \boldsymbol{\mu}_d + \frac{1}{8} tr(\check{\mathbf{C}}_a \check{\mathbf{C}}_b \check{\mathbf{C}}_c \check{\mathbf{C}}_d)], \quad \text{perm}(a, b, c, d) \tag{B.2f}$$

$$\upsilon_{ab,c,d} = \frac{1}{4} \upsilon_{ab} \upsilon_{c,d}[2] - n \left[\frac{1}{8} tr(\tilde{\mathbf{C}}_c \tilde{\mathbf{C}}_d \tilde{\mathbf{C}}_{ab}) + \frac{1}{8} tr(\tilde{\mathbf{C}}_c \tilde{\mathbf{C}}_{ab} \tilde{\mathbf{C}}_d) \right.$$
$$\left. + N_{ab}^T \tilde{\mathbf{C}}_d \boldsymbol{\mu}_c + \frac{1}{4} \boldsymbol{\mu}_c^T \mathbf{C}^{-1} \tilde{\mathbf{C}}_{ab} \boldsymbol{\mu}_d \right], \ (a \leftrightarrow b)(c \leftrightarrow d) \tag{B.2g}$$

$$\upsilon_{ab,cd} = \frac{1}{4}\upsilon_{ab}\upsilon_{cd}[2] + n[\frac{1}{8}tr(\tilde{\mathbf{C}}_{ab}\tilde{\mathbf{C}}_{cd}) + N_{ab}^T\mathbf{C}N_{cd}],\ (a \leftrightarrow b)(c \leftrightarrow d) \quad \text{(B.2h)}$$

$$\upsilon_{abc,d} = n[\frac{1}{6}tr(\tilde{\mathbf{C}}_{abc}\tilde{\mathbf{C}}_{d}) + M_{abc}^T\boldsymbol{\mu}_d],\ \mathrm{rot}(a,b,c) \quad \text{(B.2i)}$$

$$\begin{aligned}\upsilon_{abcde} = n\Bigg[&-\frac{1}{24}\boldsymbol{\mu}_{abcd}^T\mathbf{C}^{-1}\boldsymbol{\mu}_e - \frac{1}{12}\boldsymbol{\mu}_{abc}^T\mathbf{C}^{-1}\boldsymbol{\mu}_{de} - \frac{1}{48}tr(\check{\mathbf{C}}_{abcd}\check{\mathbf{C}}_e)\\ &-\frac{1}{24}tr(\check{\mathbf{C}}_{abc}\check{\mathbf{C}}_{de}) + \frac{1}{6}tr(\check{\mathbf{C}}_{abc}\check{\mathbf{C}}_d\check{\mathbf{C}}_e) + \frac{1}{4}tr(\check{\mathbf{C}}_{ab}\check{\mathbf{C}}_{cd}\check{\mathbf{C}}_e)\\ &-\frac{3}{4}tr(\check{\mathbf{C}}_{ae}\check{\mathbf{C}}_b\check{\mathbf{C}}_c\check{\mathbf{C}}_d) + \frac{2}{5}tr(\check{\mathbf{C}}_a\check{\mathbf{C}}_b\check{\mathbf{C}}_c\check{\mathbf{C}}_d\check{\mathbf{C}}_e) - \frac{1}{12}\boldsymbol{\mu}_a^T(\mathbf{C}^{-1})_{bcd}\boldsymbol{\mu}_e\\ &-\frac{1}{8}\boldsymbol{\mu}_{ab}^T\mathbf{C}^{-1}\tilde{\mathbf{C}}_c\boldsymbol{\mu}_{de} - \frac{1}{6}\boldsymbol{\mu}_{abc}^T\mathbf{C}^{-1}\tilde{\mathbf{C}}_d\boldsymbol{\mu}_e - \frac{1}{4}\boldsymbol{\mu}_{ab}^T\mathbf{C}^{-1}\tilde{\mathbf{C}}_{cd}\boldsymbol{\mu}_e\Bigg],\\ &\mathrm{perm}(a,b,c,d,e)\end{aligned} \quad \text{(B.2j)}$$

$$\upsilon_{abc,d,e} = \frac{1}{6}\upsilon_{d,e}\upsilon_{abc}[2] - n[\frac{1}{6}tr(\tilde{\mathbf{C}}_{abc}\tilde{\mathbf{C}}_d\tilde{\mathbf{C}}_e) + \frac{1}{6}\boldsymbol{\mu}_d^T\mathbf{C}^{-1}\tilde{\mathbf{C}}_{abc}\boldsymbol{\mu}_e + M_{abc}^T\tilde{\mathbf{C}}_e\boldsymbol{\mu}_d],\ \mathrm{rot}(a,b,c)(d \leftrightarrow e) \quad \text{(B.2k)}$$

$$\upsilon_{abc,de} = \frac{1}{6}\upsilon_{de}\upsilon_{abc}[2] + n[\frac{1}{12}tr(\tilde{\mathbf{C}}_{abc}\tilde{\mathbf{C}}_{de}) + M_{abc}^T\mathbf{C}N_{de}],\ \mathrm{rot}(a,b,c)(d \leftrightarrow e) \quad \text{(B.2l)}$$

$$\upsilon_{ab,cd,e} = \frac{1}{4}\upsilon_{ab}\upsilon_{cd,e}[2] - \frac{n}{2}[\frac{1}{4}tr(\tilde{\mathbf{C}}_{ab}\tilde{\mathbf{C}}_e\tilde{\mathbf{C}}_{cd}) + N_{ab}^T\tilde{\mathbf{C}}_{cd}\boldsymbol{\mu}_e + N_{ab}^T\tilde{\mathbf{C}}_e\mathbf{C}N_{cd}],\ (a \leftrightarrow b)(c \leftrightarrow d)(ab \leftrightarrow cd) \quad \text{(B.2m)}$$

$$\begin{aligned}\upsilon_{ab,c,d,e} = &(\frac{1}{12}\upsilon_{ab}\upsilon_{c,d,e} + \frac{1}{4}\upsilon_{d,e}\upsilon_{ab,c})[2] + \frac{n}{2}\Bigg[\frac{1}{2}tr(\tilde{\mathbf{C}}_{ab}\tilde{\mathbf{C}}_c\tilde{\mathbf{C}}_d\tilde{\mathbf{C}}_e)\\ &+2N_{ab}^T\tilde{\mathbf{C}}_e\tilde{\mathbf{C}}_c\boldsymbol{\mu}_d + \boldsymbol{\mu}_d^T\mathbf{C}^{-1}\tilde{\mathbf{C}}_c\tilde{\mathbf{C}}_{ab}\boldsymbol{\mu}_e\Bigg],\ (a \leftrightarrow b)\mathrm{perm}(c,d,e)\end{aligned} \quad \text{(B.2n)}$$

$$\begin{aligned}\upsilon_{abc,d,e,f} = &(\frac{1}{18}\upsilon_{abc}\upsilon_{d,e,f} + \frac{1}{6}\upsilon_{abc,d}\upsilon_{e,f})[2] + \frac{n}{6}\Big[tr(\tilde{\mathbf{C}}_{abc}\tilde{\mathbf{C}}_d\tilde{\mathbf{C}}_e\tilde{\mathbf{C}}_f)\\ &+6M_{abc}^T\tilde{\mathbf{C}}_e\tilde{\mathbf{C}}_f\boldsymbol{\mu}_d + \boldsymbol{\mu}_d^T\mathbf{C}^{-1}\tilde{\mathbf{C}}_f\tilde{\mathbf{C}}_{abc}\boldsymbol{\mu}_e + \boldsymbol{\mu}_d^T\mathbf{C}^{-1}\tilde{\mathbf{C}}_{abc}\tilde{\mathbf{C}}_f\boldsymbol{\mu}_e\Big],\\ &\mathrm{rot}(a,b,c)\mathrm{perm}(d,e,f)\end{aligned} \quad \text{(B.2o)}$$

$$\begin{aligned}\upsilon_{ab,cd,e,f} = &\frac{1}{16}\upsilon_{ab}\upsilon_{cd}\upsilon_{e,f}[3]\\ &+(\frac{\upsilon_{ab}}{8}(\upsilon_{cd,e,f} - \upsilon_{cd}\upsilon_{e,f}) + \frac{\upsilon_{e,f}}{16}(\upsilon_{cd,ab} - \upsilon_{cd}\upsilon_{ab}) + \frac{1}{8}\upsilon_{ab,e}\upsilon_{cd,f})[2]\\ &+n\Bigg[\frac{3}{16}tr(\tilde{\mathbf{C}}_{ab}\tilde{\mathbf{C}}_{cd}\tilde{\mathbf{C}}_e\tilde{\mathbf{C}}_f) + \frac{1}{2}N_{cd}^T\tilde{\mathbf{C}}_e\tilde{\mathbf{C}}_f\mathbf{C}N_{ab} + \frac{1}{8}\boldsymbol{\mu}_d{}^T\mathbf{C}^{-1}\tilde{\mathbf{C}}_{ab}\tilde{\mathbf{C}}_{cd}\boldsymbol{\mu}_f\\ &+\boldsymbol{\mu}_e{}^T\mathbf{C}^{-1}\tilde{\mathbf{C}}_f\tilde{\mathbf{C}}_{cd}\mathbf{C}N_{ab}\Bigg],\ (a \leftrightarrow b)(c \leftrightarrow d)(e \leftrightarrow f)(ab \leftrightarrow cd)\end{aligned} \quad \text{(B.2p)}$$

$$\begin{aligned}\upsilon_{ab,cd,ef,g} = &\frac{\upsilon_{ab}\upsilon_{cd}\upsilon_{ef,g}}{16}[3] + \frac{\upsilon_{ab}\upsilon_{cd,ef,g} + \upsilon_{ab,g}\upsilon_{ef,cd} - 3\upsilon_{ab,g}\upsilon_{cd}\upsilon_{ef}}{16}[2]\\ &+\frac{n}{4}\Bigg[\frac{1}{4}tr(\tilde{\mathbf{C}}_{ab}\tilde{\mathbf{C}}_{cd}\tilde{\mathbf{C}}_{ef}\tilde{\mathbf{C}}_g) + N_{ab}^T\tilde{\mathbf{C}}_{cd}\tilde{\mathbf{C}}_{ef}\boldsymbol{\mu}_g + N_{ab}^T\tilde{\mathbf{C}}_{cd}\tilde{\mathbf{C}}_g\mathbf{C}N_{ef}\\ &+N_{ab}^T\tilde{\mathbf{C}}_g\tilde{\mathbf{C}}_{cd}\mathbf{C}N_{ef}\Bigg],\ (a \leftrightarrow b)(c \leftrightarrow d)(e \leftrightarrow f)\mathrm{perm}(ab,cd,ef)\end{aligned} \quad \text{(B.2q)}$$

$$
\begin{aligned}
\upsilon_{abcd,e,f,g} &= \left(\frac{\upsilon_{abcd}\upsilon_{e,f,g}}{144} + \frac{\upsilon_{abcd,g}\upsilon_{e,f}}{48}\right)[2] + n\left[\frac{1}{48}tr(\tilde{\mathbf{C}}_e\tilde{\mathbf{C}}_f\tilde{\mathbf{C}}_g\tilde{\mathbf{C}}_{abcd})\right. \\
&\quad + [\frac{1}{6}\boldsymbol{\mu}_a^T\mathbf{C}^{-1}\tilde{\mathbf{C}}_{bcd} + \frac{1}{6}\boldsymbol{\mu}_{abc}^T\mathbf{C}^{-1}\tilde{\mathbf{C}}_d + \frac{1}{4}\boldsymbol{\mu}_{ab}^T\mathbf{C}^{-1}\tilde{\mathbf{C}}_{cd} + \frac{1}{24}\boldsymbol{\mu}_{abcd}^T\mathbf{C}^{-1}]\tilde{\mathbf{C}}_e\tilde{\mathbf{C}}_f\boldsymbol{\mu}_g \\
&\quad \left. + \frac{1}{24}\boldsymbol{\mu}_e^T\mathbf{C}^{-1}\tilde{\mathbf{C}}_{abcd}\tilde{\mathbf{C}}_f\boldsymbol{\mu}_g\right], \ \mathrm{perm}(a,b,c,d)\mathrm{perm}(g,e,f) \qquad \text{(B.2r)} \\
\upsilon_{abc,de,f,g} &= \frac{\upsilon_{abc}\upsilon_{de}\upsilon_{f,g}}{12}[3] \\
&\quad + \frac{\upsilon_{de}\upsilon_{abc,f,g} + \upsilon_{abc}\upsilon_{de,f,g} + \upsilon_{f,g}\upsilon_{abc,de} + 2\upsilon_{abc,f}\upsilon_{de,g} - 3\upsilon_{de}\upsilon_{abc}\upsilon_{f,g}}{12}[2] \\
&\quad + n\left[M_{abc}^T\tilde{\mathbf{C}}_f\tilde{\mathbf{C}}_g\mathbf{C}N_{de} + \frac{1}{3}{N_{de}}^T\tilde{\mathbf{C}}_f\tilde{\mathbf{C}}_{abc}\boldsymbol{\mu}_g + \frac{1}{3}{N_{de}}^T\tilde{\mathbf{C}}_{abc}\tilde{\mathbf{C}}_f\boldsymbol{\mu}_g\right. \\
&\quad + \frac{1}{6}\boldsymbol{\mu}_f^T\mathbf{C}^{-1}\tilde{\mathbf{C}}_{abc}\tilde{\mathbf{C}}_{de}\boldsymbol{\mu}_g + \frac{1}{6}\boldsymbol{\mu}_f^T\mathbf{C}^{-1}\tilde{\mathbf{C}}_{de}\tilde{\mathbf{C}}_{abc}\boldsymbol{\mu}_g + \frac{1}{2}M_{abc}^T\tilde{\mathbf{C}}_{de}\tilde{\mathbf{C}}_f\boldsymbol{\mu}_g \\
&\quad \left. + \frac{1}{2}M_{abc}^T\tilde{\mathbf{C}}_f\tilde{\mathbf{C}}_{de}\boldsymbol{\mu}_g + \frac{1}{4}tr(\tilde{\mathbf{C}}_{abc}\tilde{\mathbf{C}}_{de}\tilde{\mathbf{C}}_f\tilde{\mathbf{C}}_g)\right], \\
&\quad \mathrm{rot}(a,b,c)(f \leftrightarrow g)(d \leftrightarrow e) \qquad \text{(B.2s)}
\end{aligned}
$$

The expressions given above are in a form suitable for analyzing situations where the parametric dependence is on both the mean vector $\boldsymbol{\mu}$ and the covariance matrix $\mathbf{C}$. The formalism can also be readily adapted to the case where only the mean vector or the covariance depends on the parameters by setting the derivatives of the covariance matrix or the mean vector to zero, respectively.

Substituting for the tensors of Eq. (B.2) into Eqs. (A.8) and (A.10), expressions are obtained for the first-order bias and second-order covariance of the MLE given general multivariate Gaussian data. The former has been stated in Eq. (7) of Ref. [84], while the latter is now shown here. For the diagonal terms of the second order covariance matrix we obtain Eq. (4.3).

B.2 Deriving Tensor Expressions for non-Gaussian Data

The explicit expressions of the tensors evaluated for general Gaussian random variables can also be used for random data that are not distributed in a Gaussian form provided that they can be expressed as functions of Gaussian random vari-

ables with a Jacobian of the transformation that is independent of the parameters to be estimated.[68] This result is then used to prove that the asymptotic orders of the MLE bias and variance are expressible in inverse orders of SNR when the measurement data follows the gamma distribution of Eq. (3.6).

Consider for example a single vector sample composed of $Y_1, \ldots, Y_b$ arbitrary random variables which can be expressed in terms of $u_1, \ldots, u_q$ Gausssian random variables ($q \geq b$). Assume the Jacobian of the transformation is independent of the m-dimensional parameter vector $\boldsymbol{\theta}$. The mapping is assumed to be one-to-one between $\mathbf{u} = [u_1, \ldots, u_q]^T$ and $\mathbf{Y} = [Y_1, \ldots, Y_b]^T$ (for $q = b$), or between $\mathbf{u}$ and $\mathbf{Y}' \equiv [\mathbf{Y}, \boldsymbol{\Omega}]^T = [Y_1, \ldots, Y_b, \Omega_1, \ldots, \Omega_{q-b}]^T$ (for $q > b$), with $\Omega_1, \ldots, \Omega_{q-b}$ some arbitrary random variables that are not dependent on the parameter vector $\boldsymbol{\theta}$. For the general case of $q > b$, the parameter independent Jacobian of the transformation is $J' = \left|\frac{\partial \mathbf{u}}{\partial \mathbf{Y}'}\right|$. Under these assumptions, we have the following identity which holds for the expectation of any function of derivatives of the likelihood function with respect to the parameters,[68]

$$\begin{aligned}
\langle f \rangle_{\mathbf{Y}} &= \int f\left(\frac{\partial ln(p(\mathbf{Y};\boldsymbol{\theta}))}{\partial \theta_i}, \cdots, \frac{\partial^d ln(p(\mathbf{Y};\boldsymbol{\theta}))}{\partial \theta_i^d}\right) p(\mathbf{Y};\boldsymbol{\theta}) \mathrm{d}\mathbf{Y} \\
&= \int\int f\left(\frac{\partial ln(p(\mathbf{Y};\boldsymbol{\theta})p(\boldsymbol{\Omega}))}{\partial \theta_i}, \cdots, \frac{\partial^d ln(p(\mathbf{Y};\boldsymbol{\theta})p(\boldsymbol{\Omega}))}{\partial \theta_i^d}\right) p(\mathbf{Y};\boldsymbol{\theta}) p(\boldsymbol{\Omega}) \mathrm{d}\mathbf{Y} \mathrm{d}\boldsymbol{\Omega},
\end{aligned} \tag{B.3}$$

for all $i = 1, 2, \ldots, m$, where the last equality is introduced so as to make the transformation between $\mathbf{Y}'$ and $\mathbf{u}$, since $p(\mathbf{Y};\boldsymbol{\theta})p(\boldsymbol{\Omega}) = p(\mathbf{u}(\mathbf{Y}, \boldsymbol{\Omega};\boldsymbol{\theta}))J'$ and $\boldsymbol{\Omega}$ is parameter independent. Equation (B.3) can then be written as

$$\begin{aligned}
\langle f \rangle_{\mathbf{Y}} &= \int\int f\left(\frac{\partial ln(p(\mathbf{u}(\mathbf{Y}, \boldsymbol{\Omega});\boldsymbol{\theta})J')}{\partial \theta_i}, \cdots, \frac{\partial^d ln(p(\mathbf{u}(\mathbf{Y}, \boldsymbol{\Omega});\boldsymbol{\theta})J')}{\partial \theta_i^d}\right) \\
&\qquad \times p(\mathbf{u}(\mathbf{Y}, \boldsymbol{\Omega});\boldsymbol{\theta}) J' \mathrm{d}\mathbf{Y} \mathrm{d}\boldsymbol{\Omega} \\
&= \int f\left(\frac{\partial ln(p(\mathbf{u};\boldsymbol{\theta}))}{\partial \theta_i}, \cdots, \frac{\partial^d ln(p(\mathbf{u};\boldsymbol{\theta}))}{\partial \theta_i^d}\right) p(\mathbf{u};\boldsymbol{\theta}) \mathrm{d}\mathbf{u} \\
&= \langle f \rangle_{\mathbf{u}}
\end{aligned} \tag{B.4}$$

The expected value of any function of derivatives of the likelihood function for $\mathbf{Y}$ with respect to the parameters $\boldsymbol{\theta}$ can then be written as the same function of derivatives of the likelihood function for $\mathbf{u}$. Since the asymptotic orders are function of expectations that have the same structure as Eq. (B.3), the asymptotic orders of the MLE of a parameter $\boldsymbol{\theta}$ can be computed from measurements of the non-Gaussian quantity $\mathbf{Y}$.

For example, the MLE of a scalar parameter θ from an observation Y distributed as a Gamma with parameter dependent mean $\sigma(\theta)$,

$$p(Y;\theta) = \left(\frac{n}{\sigma(\theta)}\right)^n \frac{Y^{n-1}}{\Gamma(n)} \exp\left(-\frac{nY}{\sigma(\theta)}\right) \tag{B.5}$$

can be computed using the set of Gaussian random variables $u_1, \ldots, u_{2n}$

$$p(u_1, \ldots, u_{2n}; \theta) = \prod_{i=1}^{2n} \frac{1}{\sqrt{\pi\sigma(\theta)}} \exp\left(-\frac{u_i^2}{\sigma(\theta)}\right) \tag{B.6}$$

B.2.1 Expansion of Bias and Variance in Inverse Orders of Sample Size or SNR for Gamma-Distributed Intensity Data

For the problem of surface orientation considered in Chapter 3, the M-dimensional measurements $\mathbf{R}$, given parameter vector $\mathbf{a}$, are distributed according to the product of gamma distributions of Eq. 3.6. The parameter $\mathbf{a}$ can be estimated using the set of Gaussian random variables $x_{1,1}, \ldots, x_{1,2\mu_1}, x_{2,1}, \ldots, x_{2,2\mu_2}, \ldots, x_{M,1}, \ldots, x_{M,2\mu_M}$, such that

$$P_{\mathbf{x}}(x_{1,1}, \ldots, x_{M,2\mu_M}; \mathbf{a}) = \prod_{k=1}^{M} \left(\prod_{i=1}^{2\mu_k} \frac{1}{\sqrt{\pi\sigma_k(\mathbf{a})}} \exp\left(-\frac{x_{k,i}^2}{\sigma_k(\mathbf{a})}\right) \right). \tag{B.7}$$

where σ_k is the mean of R_k and also twice the variance of $x_{k,i}$ for $i = 1, \ldots 2\mu_k$. Assuming that $\mu_k = \mu$ for all k, Eq. B.7 then becomes

$$P_{\mathbf{x}}(\mathbf{x}_1, \ldots, \mathbf{x}_{2\mu}; \mathbf{a}) = \frac{1}{(2\pi)^{M\mu}|\mathbf{C}(\mathbf{a})|^{\mu}} \exp\left(-\frac{1}{2}\sum_{j=1}^{2\mu} \mathbf{x}_j^T \mathbf{C}(\mathbf{a})^{-1} \mathbf{x}_j\right) \tag{B.8}$$

where $\mathbf{x}_j = [x_{1,j}, \ldots, x_{M,j}]^T$ is the jth sample of the M-dimensional data vector for $j = 1, \ldots, 2\mu$, and the M-dimensional covariance matrix $\mathbf{C}(\mathbf{a})$ has elements $\mathbf{C}_{kl} = \delta_{kl}\sigma_k/2$. Using this notation, the M-dimensional measurement $\mathbf{R}$, with parameter-dependent mean $\boldsymbol{\sigma}(\mathbf{a})$, can be replaced by the measurement $\mathbf{x}$ obtained from $n' = 2\mu$ independent and identically distributed M-dimensional vectors, where the parameter dependence is instead on the covariance of the data, $\mathbf{C}(\mathbf{a})$.

The asymptotic orders of the MLE bias and variance for the rth component of the parameter vector $\mathbf{a}$ can then be calculated using the existing expressions provided in Ref. [84] after substituting for $n' = 2\mu$ and $\mathbf{C}_{kl} = \delta_{kl}\sigma_k/2$. These asymptotic expansions are in inverse orders of the sample size n', and therefore in inverse orders of μ. Since μ is the SNR of the gamma-distributed $\mathbf{R}$ measurement, the MLE bias and variance given data that follow a gamma distribution can be written as asymptotic series in inverse orders of SNR,

$$\text{bias}(\widehat{a}_r, \boldsymbol{\mu}, M = 1) = \frac{b_1(\widehat{a}_r; \mathbf{a}, \mathbf{e}, 1)}{\mu} + \frac{b_2(\widehat{a}_r; \mathbf{a}, \mathbf{e}, 1)}{\mu^2} + O(\mu^{-3}), \tag{B.9}$$

$$\text{var}(\widehat{a}_r, \boldsymbol{\mu}, M = 1) = \frac{var_1(\widehat{a}_r; \mathbf{a}, \mathbf{e}, 1)}{\mu} + \frac{var_2(\widehat{a}_r; \mathbf{a}, \mathbf{e}, 1)}{\mu^2} + O(\mu^{-3}), \tag{B.10}$$

where the vector $\mathbf{e}$ with components $e_k = 1$ signifies the 'all-measurements-equal' case of $\mu_k = \mu$ for all $k = 1, 2 \ldots M$

For example, consider the Fisher information and the first order bias. The Fisher information matrix has elements

$$i_{bc} = (2\mu) \sum_{k=1}^{M} \frac{1}{2} \left(\frac{1}{(\sigma_k(\mathbf{a}))^2} \frac{\partial \sigma_k(\mathbf{a})}{\partial a_b} \frac{\partial \sigma_k(\mathbf{a})}{\partial a_c} \right), \tag{B.11}$$

and is equal to Eq. 3.8, as expected. The first order bias using the gamma distribution of Eq. 3.6 is given by

$$b_1(\hat{a}^r) = -\frac{1}{2} i^{ra} i^{bc} \sum_{k=1}^{M} \left(\frac{\mu}{(\sigma_k(\mathbf{a}))^2} \frac{\partial \sigma_k(\mathbf{a})}{\partial a^a} \frac{\partial^2 \sigma_k(\mathbf{a})}{\partial a^b \partial a^c} \right). \tag{B.12}$$

which reduces to Eq. B.14 after substituting for i^{ra}, i^{bc}. Using the Gaussian distribu-

tion of Eq. B.8,

$$b_1(\hat{a}^r) = -\frac{1}{4} i^{ra} i^{bc} \sum_{k=1}^{M} \left(\frac{2\mu}{(\sigma_k(\mathbf{a}))^2} \frac{\partial \sigma_k(\mathbf{a})}{\partial a^a} \frac{\partial^2 \sigma_k(\mathbf{a})}{\partial a^b \partial a^c} \right). \tag{B.13}$$

which equals Eq. B.12, as expected.

B.2.2 Analytical Expressions of the Asymptotic MLE Bias and Variance for CCD Measurements of Surface Reflectance

For the statistical model of Eq. C.18

$$\begin{aligned}
b_1(\widehat{\theta}|\theta) &= -\frac{1}{2}(i^{-2})[\upsilon_{1,2} + \frac{1}{2}\nu_1\nu_2 + \upsilon_{1,1}\nu_1], && \text{(B.14)}\\
var_1(\widehat{\theta}|\theta) &= i^{-1}, && \text{(B.15)}\\
var_2(\widehat{\theta}|\theta) &= (i^{-3})[2\nu_1^4 - 5\upsilon_{1,2}\nu_1 + 6\upsilon_{1,1}\nu_1^2 - \frac{1}{2}\nu_1\nu_3 \\
&\qquad -\upsilon_{1,1}\nu_2 - \upsilon_{1,3} - \nu_1^2\nu_2] \\
&\quad +(i^{-4})[\frac{7}{2}\upsilon_{1,2}^2 + \frac{7}{2}\upsilon_{1,1}\nu_1^2\nu_2 + 7\upsilon_{1,1}\upsilon_{1,2}\nu_1 \\
&\qquad +\frac{7}{8}\nu_1^2\nu_2^2 + \frac{7}{2}\upsilon_{1,2}\nu_1\nu_2 - \frac{11}{2}\upsilon_{1,1}^2\nu_1^2 \\
&\qquad -6\upsilon_{1,1}\nu_1^4 - \nu_1^6] && \text{(B.16)}
\end{aligned}$$

where

$$\begin{aligned}
\upsilon_{a,b} &= \frac{1}{\sigma_K^2} \frac{\partial^a \overline{K}}{\partial \theta^a} \frac{\partial^b \overline{K}}{\partial \theta^b} && \text{(B.17)}\\
\nu_c &= \frac{1}{\sigma_K^2} \frac{\partial^c \sigma_K^2}{\partial \theta^c} && \text{(B.18)}
\end{aligned}$$

and i is the Fisher information given by Eq. 2.8.

Appendix C

Statistics of CCD Measurements of Surface Reflectance

We show that a CCD photocount measurement, K, of planetary surface reflectance from a natural light source approximately follow a Gaussian distribution. The derivation incorporates surface albedo variability, as well as CCD camera read and shot noise, and atmospheric haze noise. The number of photoevents K recorded by CCD cameras is directly proportional to incident intensity [56]. The averaged intensity incident on a photosurface of area A in the time interval $(t_0,\ t_0 + \tau)$ is a random variable

$$W|Bo = \frac{1}{\tau A} \int\int\int_{t_0}^{t_0+\tau} \mathscr{I}(x, y; t|Bo)\ \mathrm{d}t\ \mathrm{d}x\ \mathrm{d}y \tag{C.1}$$

where $\mathscr{I}(x, y; t|Bo)$ is the random instantaneous intensity at time t and location $(x,\ y)$ on the photosurface given albedo Bo. For satellite imaging of a planetary surface under the illumination-observation scenario described in Fig. 2-1, the expected value of $\mathscr{I}(x, y; t|Bo)$ is proportional to the surface reflectance function $I(\mu_n, \mu_{0n}, \alpha)$ times the incident solar flux $\mathscr{I}_0$ [79], where the latter is assumed to be a known constant, plus the mean intensity from atmospheric haze H. The surface reflectance function can be expressed as $I(\mu_n, \mu_{0n}, \alpha) = Bof(\theta)$ (Eq. 2.3), where Bo is the random surface albedo and θ is the unknown planetary surface slope. Atmospheric haze is described

by a CCGR field that is independent and additive to the CCGR field from the surface, so that the field variances, or equivalently the mean instantaneous intensities of each add.

The probability distribution of $W|Bo$ for polarized thermal light is given by the Gamma distribution [49],

$$P_{W|Bo}(W|Bo) = \begin{cases} \left(\frac{\zeta}{\overline{W}_{Bo}}\right)^{\zeta} \frac{W^{\zeta-1}\exp\left(-\zeta\frac{W}{\overline{W}_{Bo}}\right)}{\Gamma(\zeta)} & \text{for } W \geq 0 \\ 0 & \text{for } W < 0 \end{cases} \tag{C.2}$$

where $\overline{W}_{Bo} \equiv \langle W|Bo\rangle = \int W P_{W|Bo}(W|Bo)\mathrm{d}W = \mathscr{I}_0[Bof(\theta) + H]$, and H is the expected intensity of atmospheric haze which is assumed to be a known constant [12]. The variable ζ is the number of coherence cells in the intensity average [49] which is equal to the squared-mean-to-variance ratio, or Signal to Noise Ratio (SNR) of $W|Bo$, defined as $\langle W|Bo\rangle^2/(\langle W|Bo^2\rangle - \langle W|Bo\rangle^2)$. For example, ζ equals the time-bandwidth product of the received field if $W|Bo$ is obtained from a finite-time average [70]. Additionally, ζ can be interpreted as the number of stationary speckles averaged over a finite spatial aperture in the image plane or the number of stationary multi-look images averaged for a particular scene [2, 70].

The probability of observing K photoevents follows the conditional Poisson distribution [49]

$$P_{K|W,Bo}(K|W,Bo) = \frac{(\overline{K}_{W,Bo})^K}{K!}\mathrm{e}^{-\overline{K}_{W,Bo}} \tag{C.3}$$

where $\overline{K}_{W,Bo} = \beta\tau AW$. The proportionality constant β is given by $\beta = \frac{\eta}{h\overline{\nu}}$, where h is Planck's constant ($6.626\text{x}10^{-34}$ Joule-s), $\overline{\nu}$ is the mean optical frequency of radiation, and η is the quantum efficiency that represents the average number of photoevents produced by each incident photon ($0 \leq \eta \leq 1$). From Eqs. C.2 and C.3, the probability

of observing K photoevents then follows the negative binomial distribution

$$\begin{aligned} P_{K|Bo}(K|Bo) &= \int_{-\infty}^{\infty} P_{K|W,Bo}(K|W,Bo)P_{W|Bo}(W|Bo)\mathrm{d}W \\ &= \frac{\Gamma(K+\zeta)}{\Gamma(K+1)\Gamma(\zeta)}\left[1+\frac{\zeta}{\overline{K}_{Bo}}\right]^{-K}\left[1+\frac{\overline{K}_{Bo}}{\zeta}\right]^{-\zeta} \end{aligned} \tag{C.4}$$

where $\overline{K}_{Bo} = \beta\tau A\overline{W}_{Bo} \equiv \gamma[Bof(\theta)+H]$, and we have defined for convenience the proportionality constant γ

$$\gamma \equiv \beta\tau A\mathscr{I}_0 = \frac{\eta}{h\overline{\nu}}\tau A\mathscr{I}_0 \tag{C.5}$$

For $\zeta \gg 1$, the Gamma distribution of Eq. C.2 approximates a delta function [78], $P_{W|Bo}(W|Bo) = \delta(W-\overline{W}_{Bo})$, so that the negative binomial distribution for K (Eq. C.4) approaches a Poisson distribution. To show this, let $q = \overline{K}_{Bo}/\zeta$. The first cumulant of the negative binomial distribution for K conditional on Bo is given by $\lambda_1(K|Bo) = \zeta q$, and the rest by the recursion equation

$$\lambda_{j+1}(K|Bo) = q(q+1)\frac{\mathrm{d}\lambda_j(K|Bo)}{\mathrm{d}q}, \tag{C.6}$$

so that

$$\lambda_n(K|Bo) = \zeta(q+\sum_{j=2}^{n} a_j q^j) \qquad \text{for } n \geq 2, \tag{C.7}$$

where the a_j are constants. For thermal light at optical frequencies, and for the common integration times of CCDs, ζ is very large, usually in the order of 10^{10}, while maximum values for $\overline{K}_{Bo}$ are typically much smaller, around 10^4. For $\zeta \gg \overline{K}_{Bo}$, q tends to 0 and $\lambda_n(K|Bo) \approx \zeta q$ for all n, so that the cumulants of $K|Bo$ become equal to those of a Poisson distributed random variable with mean $\zeta q = \overline{K}_{Bo}$, which is random since Bo is a random variable.

The total probability distribution for K is also approximately Gaussian by virtue of the central limit theorem. To show this, we first calculate the cumulants κ_n of the

photocount K using the law of total cumulance [17],

$$\kappa_n(K) \equiv \kappa_1(K_1, \ldots, K_n) = \sum_{\pi} \kappa_1(\lambda_1(K_{\pi 1}|Bo), \ldots, \lambda_1(K_{\pi j}|Bo)) \tag{C.8}$$

where the summation is defined over all possible *partitions* π of the set $\{1, \ldots, n\}$ of indices. For each partition π, sub-blocks are denoted by $\pi 1, \ldots, \pi j$, so that for example, if $n = 3$ and $\pi = \{2 \text{ indices, } 1 \text{ index}\}$, the sub-blocks are $\pi_1 = \{[1,2], 3\}$, $\pi_2 = \{[1,3], 2\}$, and $\pi_3 = \{[2,3], 1\}$. We then define $K_1 = K_2 = \ldots = K_n = K$. Equation C.8 reduces to the well known laws of *iterated expectations* and *total variance* for $n = 1$, 2 [9]. The cumulants for K are given by,

$$\begin{aligned}
\kappa_1(K) &= \langle \overline{K}_{Bo} \rangle, & \text{(C.9)} \\
\kappa_2(K) &= \langle \overline{K}_{Bo} \rangle + \mathrm{var}(\overline{K}_{Bo}), & \text{(C.10)} \\
&\vdots & \\
\kappa_n(K) &= \langle \overline{K}_{Bo} \rangle + b_n \mathrm{var}(\overline{K}_{Bo}) & \text{(C.11)}
\end{aligned}$$

where the b_n are constants and we have made use of $\kappa_j(\overline{K}_{Bo}) = 0$ for all $j \geq 3$, since Bo has been assumed to follow a Gaussian distribution with mean $\overline{Bo}$ and variance σ^2_{Bo}.

Defining a new random variable

$$U = \frac{(K - \overline{K})}{\sqrt{\overline{K}} \left(1 + \overline{K}\sigma^2_{Bo}/\overline{Bo}^2\right)^{1/2}} \tag{C.12}$$

where $\overline{K} = \langle \overline{K}_{Bo} \rangle = \gamma[\overline{Bo} f(\theta) + H]$, the cumulant generating function of U is given by

$$\begin{aligned}
g_U(\phi) &= \ln \langle \mathrm{e}^{\phi U} \rangle \\
&= -\phi \frac{\sqrt{\overline{K}}}{(1 + \overline{K}\sigma^2_{Bo}/\overline{Bo}^2)^{1/2}} + g_K \left(\frac{\phi}{\sqrt{\overline{K}}(1 + \overline{K}\sigma^2_{Bo}/\overline{Bo}^2)^{1/2}} \right), & \text{(C.13)}
\end{aligned}$$

where $g_K(\phi)$ is the cumulant generating function of K. The cumulants of U are then

given by

$$u_j = \left.\frac{\mathrm{d}^j g_U(\phi)}{\mathrm{d}\phi^j}\right|_{\phi=0} = \frac{1}{\left[\sqrt{\overline{K}}(1+\overline{K}\sigma_{Bo}^2/\overline{Bo}^2)^{1/2}\right]^j}\left(-\overline{K}^j \left.\frac{\mathrm{d}^j\phi}{\mathrm{d}\phi^j}\right|_{\phi=0} + \kappa_j(K)\right), \quad \text{(C.14)}$$

so that

$$\begin{aligned} u_1 &= 0, && \text{(C.15)} \\ u_2 &= 1, && \text{(C.16)} \\ &\vdots \\ u_n &= \frac{\overline{K}(1+c_n\overline{K}\sigma_{Bo}^2/\overline{Bo}^2)}{\left[\sqrt{\overline{K}}(1+\overline{K}\sigma_{Bo}^2/\overline{Bo}^2)^{1/2}\right]^n} \qquad \text{for } n \geq 2, && \text{(C.17)} \end{aligned}$$

where the c_n are constants. For very large values of $\overline{K}$, u_n approaches 0 for $n > 2$, so that U and consequently K become Gaussian random variables.

The discrete probability density for K is then well approximated by the continuous Gaussian probability distribution,

$$P_K(K|\theta) = \frac{1}{\sqrt{2\pi}\sigma_K(\theta)} \exp\left(-\frac{1}{2}\left[\frac{K-\overline{K}(\theta)}{\sigma_K(\theta)}\right]^2\right) \quad \text{(C.18)}$$

where

$$\begin{aligned} \overline{K} &= \gamma[\overline{Bo}f(\theta)+H], && \text{(C.19)} \\ \sigma_K^2 &= \overline{K}+\overline{K}^2\sigma_{Bo}^2/\overline{Bo}^2+\sigma_R^2 && \text{(C.20)} \end{aligned}$$

are the mean and variance of K respectively, σ_R^2 is an additive signal-independent variance term due to CCD camera read noise, and we define $\sigma_{haze}^2 \equiv \gamma H$ as the noise term due to the known atmospheric haze expected intensity H.

In order to determine appropriate noise levels and the scaling factor γ, we consider as an example the HiRISE camera of the latest Mars Reconnaissance Orbiter (MRO) mission [7, 81], where Ref. [7] specifies read noise σ_R to be roughly 80 electrons r.m.s.,

and imply in Fig. 12 a γ ranging from roughly 20000 electrons for the blue-green and NIR bands to 70000 electrons for the red (pan) band. The mean photocount, $\overline{K}$, is then on the order of 10^4 electrons.

A typical value for the contribution of atmospheric haze to the total measured signal in images of Mars may be inferred from Table I of Ref. [16]. Accounting for the gain of Mariner's camera [34], we find that the atmospheric haze component, σ^2_{haze}, is typically on the order of 2000 electrons, or roughly 10% of the mean signal expected using the blue-green HiRISE band. For albedo variability, the mean $\overline{Bo}$ is normalized to one and the standard deviation σ_{Bo} is specified as 10% of the mean following calculations presented in Ref. [6] for typical Martian surfaces. Albedo variability then results in a variance that is on the order of 10^6 electrons.

The integration time or shutter speed of the HiRISE camera is $\tau \geq 76$ μsec and the optical bandwidth is $\nu_B \approx 10^{14}$ Hz or greater, depending on the exact band used. The value of ζ is then in the order of 10^{10}, while $\overline{K}$ is in the order of 10^4, so that the negative binomial distribution of Eq. C.4 is well approximated by the Gaussian distribution of Eq. C.18. In this paper, we consider CCD measurements in the blue-green and/or the NIR band.

Appendix D

Received Pressure Field in a Fluctuating Ocean Waveguide

D.1 Mean, Covariance of the Forward Propagated Field, and their Derivatives

Here, we review the analytical expressions for the mean field, variance, and expected total intensity of the forward field propagated through an ocean waveguide containing random internal waves. These expressions will be used to calculate the mean vector $\boldsymbol{\mu}$ and the covariance matrix $\mathbf{C}$ in Eq. (4.1), and determine their derivatives with respect to source range and depth. We employ the formulation developed in Refs. [21] and [90], where it is assumed that the internal wave inhomogeneities follow a stationary random process in space. Referring to Fig. 4-1, for a source at $\mathbf{r}_0 = (-\rho_0, 0, z_0)$, the mean forward field received by the qth hydrophone array element at $\mathbf{r}_q = (0, 0, z_q)$ is given by Eq. (83) of Ref. [90]

$$\langle \Psi_T(\mathbf{r}_q|\mathbf{r}_0)\rangle = \sum_n \Psi_i^{(n)}(\mathbf{r}_q|\mathbf{r}_0) \mathrm{e}^{i\int_{-\rho_0}^{0} \nu_n(\rho_s)\mathrm{d}\rho_s}, \tag{D.1}$$

where ρ_s is the horizontal location of the internal wave inhomogeneity, and

$$\Psi_i^{(n)}(\mathbf{r}_q|\mathbf{r}_0) = 4\pi \frac{i}{d(z_0)\sqrt{8\pi}} \mathrm{e}^{-i\pi/4} u_n(z_q) u_n(z_0) \frac{\mathrm{e}^{i\xi_n \rho_0}}{\sqrt{\xi_n \rho_0}} \tag{D.2}$$

is the incident field contribution from mode n given no inhomogeneities in the medium, $d(z_0)$ is the density at the source depth z_0, $u_n(z)$ is the modal amplitude at depth z, ξ_n is the horizontal wave number, and ν_n is the change in the horizontal wave number due to multiple scattering from the inhomogeneities. As detailed in Ref. [90], the modal horizontal wave number change is complex, and it leads to both dispersion and attenuation in the mean forward field. Analytic expressions for ν_n are provided in Eqs. (56) and (60) of Ref. [90] for compact inhomogeneities that obey a stationary random process in depth and for general inhomogeneities with arbitrary depth dependence, respectively.

The variance of the forward field at the receiver is given by Eq. (84) of Ref. [90]

$$\begin{aligned} \mathrm{Var}(\Psi_T(\mathbf{r}_q|\mathbf{r}_0)) \;=\; & \sum_n \frac{2\pi}{d^2(z_0)} \frac{1}{|\xi_n|\rho_0} |u_n(z_0)|^2 |u_n(z_q)|^2 \\ & \times \mathrm{e}^{-2\Im\left\{\xi_n \rho_0 + \int_{-\rho_0}^0 \nu_n(\rho_s) \mathrm{d}\rho_s\right\}} \left(\mathrm{e}^{\int_{-\rho_0}^0 \mu_n(\rho_a) \mathrm{d}\rho_a} - 1 \right), \end{aligned} \tag{D.3}$$

where μ_n is defined in Ref. [90] as the exponential coefficient of modal field variance, and $\Im\{\ldots\}$, $\Re\{\ldots\}$ correspond to the imaginary and real part, respectively. The variance of the forward field depends on the first- and second-order moments of the scatter function density of the random medium. Analytic expressions for μ_n for general surface and volume inhomogeneities are provided in Eqs. (74) and (77) of Ref. [90] for fully correlated and uncorrelated scatterers, respectively.

The covariance of the forward fields received at $\mathbf{r}_q$ and $\mathbf{r}_p$ is given by Eq. (104) of

Ref. [90]

$$\begin{aligned}
&\mathrm{Cov}(\Psi_T(\mathbf{r}_q|\mathbf{r}_0), \Psi_T(\mathbf{r}_p|\mathbf{r}_0)) = \\
&\quad = \sum_n \frac{2\pi}{d^2(z_0)} \frac{1}{|\xi_n|\rho_0} |u_n(z_0)|^2 u_n(z_q) u^*(z_p) \mathrm{e}^{-2\Im\{\xi_n\}\rho_0} \\
&\quad \times \exp\left(\int_{-\rho_0}^{0} (i\Re\{\nu_{n,q}(\rho_s) - \nu_{n,p}(\rho_s)\} - \Im\{\nu_{n,q}(\rho_s) + \nu_{n,p}(\rho_s)\}) \mathrm{d}\rho_s \right) \\
&\quad \times \left(\mathrm{e}^{\int_{-\rho_0}^{0} \mu_{n,q,p}(\rho_s) \mathrm{d}\rho_s} - 1 \right)
\end{aligned} \tag{D.4}$$

The mean forward field of Eq. (D.1) is also called the coherent field, the magnitude square of which is proportional to coherent intensity. The variance of the forward field in Eq. (D.3) provides a measure of the incoherent intensity. The total intensity of the forward field is the sum of the coherent and incoherent intensities. As shown in Ref. [21], the coherent field tends to dominate at short ranges from the source and in slightly random media, while the incoherent field tends to dominate in highly random media. It should be noted that in a nonrandom waveguide $\mu_n = 0$ so that the variance of the forward field is zero, from Eq. (D.3). This is expected since the field is fully coherent in this case.

D.1.1 Derivatives of the Mean Field with Respect to Source Range and Depth

Going back to Eq. (D.1), the modal amplitude $u_n(z)$ is defined as

$$u_n(z) = \left[N^{(1)} \mathrm{e}^{i\Re\{\gamma_n\}z} - N^{(2)} \mathrm{e}^{-i\Re\{\gamma_n\}z} \right] \mathrm{e}^{-\Im\{\gamma_n\}z}. \tag{D.5}$$

We will assume that

$$\int_{-\rho_0}^{0} \nu_n(\rho_s) \mathrm{d}\rho_s = \nu_n \rho_0, \quad \text{and} \tag{D.6a}$$

$$\frac{\partial d(z_0)}{\partial z_0} = 0, \tag{D.6b}$$

so that

$$\langle \Psi_T(\mathbf{r}|\mathbf{r_0}) \rangle = \sum_{n=1}^{\infty} C_n(z) f_n(z_0) g_n(\rho_0), \tag{D.7}$$

where the following quantities have been defined

$$C_n(z) = 4\pi \frac{i}{d(z_0)\sqrt{8\pi\xi_n}} \mathrm{e}^{-i\pi/4} u_n(z), \tag{D.8a}$$

$$f_n(z_0) = u_n(z_0) \tag{D.8b}$$

$$g_n(\rho_0) = \frac{1}{\sqrt{\rho_0}} \mathrm{e}^{i(\xi_n + \nu_n)\rho_0}. \tag{D.8c}$$

The derivatives of the mean field with respect to source depth and range can then be simply expressed in terms of derivatives of $f_n(z_0)$, $g_n(\rho_0)$ and their products, respectively.

Depth derivatives

The first three derivatives of the mean with respect to source depth z_0 are given by

$$\begin{aligned} f_n^1(z_0) = {} & i\Re\{\gamma_n\} \left[N^{(1)} \mathrm{e}^{i\Re\{\gamma_n\} z_0} + N^{(2)} \mathrm{e}^{-i\Re\{\gamma_n\} z_0} \right] \mathrm{e}^{-\Im\{\gamma_n\} z_0} \\ & - \Im\{\gamma_n\} f_n(z_0), \end{aligned} \tag{D.9a}$$

$$f_n^2(z_0) = -\left[(\Re\{\gamma_n\})^2 + (\Im\{\gamma_n\})^2 \right] f_n(z_0) - 2\Im\{\gamma_n\} f_n^1(z_0), \tag{D.9b}$$

$$f_n^3(z_0) = -\left[(\Re\{\gamma_n\})^2 + (\Im\{\gamma_n\})^2 \right] f_n^1(z_0) - 2\Im\{\gamma_n\} f_n^2(z_0). \tag{D.9c}$$

Range derivatives

The first three derivatives of the mean with respect to source range ρ_0 are given by

$$g_n^1(\rho_0) = \frac{e^{i(\xi_n+\nu_n)\rho_0}}{\sqrt{\rho_0}}\left(i(\xi_n+\nu_n)-\frac{1}{2\rho_0}\right), \tag{D.10a}$$

$$g_n^2(\rho_0) = \frac{e^{i(\xi_n+\nu_n)\rho_0}}{\sqrt{\rho_0}}\left[-(\xi_n+\nu_n)^2 - i\frac{(\xi_n+\nu_n)}{\rho_0}+\frac{3}{4\rho_0^2}\right], \tag{D.10b}$$

$$g_n^3(\rho_0) = \frac{e^{i(\xi_n+\nu_n)\rho_0}}{\sqrt{\rho_0}}\left[-(\xi_n+\nu_n)^3+\frac{3}{2\rho_0}(\xi_n+\nu_n)^2 + i\frac{9}{4\rho_0^2}(\xi_n+\nu_n)-\frac{15}{8\rho_0^3}\right]. \tag{D.10c}$$

D.1.2 Derivatives of the Covariance of the Field with Respect to Source Range and Depth

We can express the covariance of the forward propagated field in Eq. (D.4) as

$$\mathrm{Cov}(\Psi_T(\mathbf{r}_m|\mathbf{r}_0),\Psi_T(\mathbf{r}_p|\mathbf{r}_0)) \equiv \sum_{n=1}^{\infty} D_n(z_m,z_p)h_n(z_0)l_n(\rho_0), \tag{D.11}$$

where

$$D_n(z_m,z_p) = \frac{2\pi}{d^2(z_0)|\xi_n|}u_n(z_m)u_n^*(z_p), \tag{D.12a}$$

$$h_n(z_0) = |u_n(z_0)|^2, \tag{D.12b}$$

$$l_n(\rho_0) = \frac{1}{\rho_0}e^{-2\Im\{\xi_n+\nu_n\}\rho_0}\left(e^{\int_{-\rho_0}^{0}\mu_n(\rho_s)d\rho_s}-1\right). \tag{D.12c}$$

We can simplify the above expressions for $h_n(z_0)$ and $l_n(\rho_0)$ by writing

$$h_n(z_0) = \left(e^{-2\Im\{\gamma_n\}z_0}\right)\Big[\cos^2(\Re\{\gamma_n\}z_0)M1+\sin^2(\Re\{\gamma_n\}z_0)M2 + 2\cos(\Re\{\gamma_n\}z_0)\sin(\Re\{\gamma_n\}z_0)M3\Big], \tag{D.13}$$

and,

$$\begin{aligned} l_n(\rho_0) &= \frac{1}{\rho_0} \mathrm{e}^{-2\Im\{\xi_n+\nu_n\}\rho_0} \left(\mathrm{e}^{\int_{-\rho_0}^{0} \mu_n(\rho_s) \mathrm{d}\rho_s} - 1 \right) \\ &\equiv \frac{1}{\rho_0} \mathrm{e}^{-\kappa_n \rho_0} \left(\lambda_n - 1 \right), \end{aligned} \tag{D.14}$$

where

$$M1 = (\Re\{N^{(1)} - N^{(2)}\})^2 + (\Im\{N^{(1)} - N^{(2)}\})^2, \tag{D.15a}$$

$$M2 = (\Re\{N^{(1)} + N^{(2)}\})^2 + (\Im\{N^{(1)} + N^{(2)}\})^2, \tag{D.15b}$$

$$M3 = 2\left[\Re\{N^{(2)}\}\Im\{N^{(1)}\} - \Re\{N^{(1)}\}\Im\{N^{(2)}\}\right], \tag{D.15c}$$

$$\kappa_n = 2\Im\{\xi_n + \nu_n\}, \tag{D.15d}$$

$$\lambda_n = \mathrm{e}^{\int_{-\rho_0}^{0} \mu_n(\rho_s) \mathrm{d}\rho_s}. \tag{D.15e}$$

The derivatives of the covariance of the field with respect to source depth and range can then be simply expressed in terms of derivatives of $h_n(z_0)$, $l_n(\rho_0)$ and their products, respectively.

Depth derivatives

The first three derivatives of the variance with respect to source depth z_0 are given by

$$\begin{aligned} h_n^1(z_0) &= -2\Im\{\gamma_n\} h_n(z_0) \\ &\quad +2\Re\{\gamma_n\} \mathrm{e}^{-2\Im\{\gamma_n\}z_0} \left[-\cos(\Re\{\gamma_n\}z_0) \sin(\Re\{\gamma_n\}z_0)(M1 - M2) \right. \\ &\quad \left. + (\cos^2(\Re\{\gamma_n\}z_0) - \sin^2(\Re\{\gamma_n\}z_0)) M3 \right], \end{aligned} \tag{D.16a}$$

$$\begin{aligned} h_n^2(z_0) &= -2\Im\{\gamma_n\}[2h_n^1(z_0) + 2\Im\{\gamma_n\} h_n(z_0)] \\ &\quad +2(\Re\{\gamma_n\})^2 \mathrm{e}^{-2\Im\{\gamma_n\}z_0} \left[(\sin^2(\Re\{\gamma_n\}z_0) - \cos^2(\Re\{\gamma_n\}z_0))(M1 - M2) \right. \\ &\quad \left. - 4\cos(\Re\{\gamma_n\}z_0) \sin(\Re\{\gamma_n\}z_0) M3 \right], \end{aligned} \tag{D.16b}$$

$$\begin{aligned} h_n^3(z_0) &= -2\Im\{\gamma_n\}[3h_n^2(z_0) + 6\Im\{\gamma_n\} h_n^1(z_0) + 4(\Im\{\gamma_n\})^2 h_n(z_0)] \\ &\quad -4(\Re\{\gamma_n\})^2 [h_n^1(z_0) + 2\Im\{\gamma_n\} h_n(z_0)]. \end{aligned} \tag{D.16c}$$

Range derivatives

The first three derivatives of the variance with respect to source range ρ_0 are given by

$$l_n^1(\rho_0) = \frac{1}{\rho_0}\mathrm{e}^{-\kappa_n\rho_0}\left[\kappa_n + \frac{1}{\rho_0} + \lambda_n\left(-\kappa_n - \frac{1}{\rho_0} + \mu_n\right)\right], \tag{D.17a}$$

$$\begin{aligned} l_n^2(\rho_0) = \frac{1}{\rho_0}\mathrm{e}^{-\kappa_n\rho_0}\Bigg[&-(\kappa_n + \frac{1}{\rho_0})^2 - \frac{1}{\rho_0^2} \\ &+\lambda_n\left((\kappa_n + \frac{1}{\rho_0})^2 - 2\mu_n(\kappa_n + \frac{1}{\rho_0}) + \frac{1}{\rho_0^2} + \mu_n^2 + \mu_n'\right)\Bigg], \end{aligned} \tag{D.17b}$$

$$\begin{aligned} l_n^3(\rho_0) = \frac{1}{\rho_0}\mathrm{e}^{-\kappa_n\rho_0}\Bigg[&(\kappa_n + \frac{1}{\rho_0})^3 + \frac{3}{\rho_0^2}(\kappa_n + \frac{1}{\rho_0}) + \frac{2}{\rho_0^3} \\ &+ \lambda_n\Bigg(-(\kappa_n + \frac{1}{\rho_0})^3 + 3\mu_n(\kappa_n + \frac{1}{\rho_0})^2 - 3\mu_n^2(\kappa_n + \frac{1}{\rho_0}) - \frac{3}{\rho_0^2}(\kappa_n + \frac{1}{\rho_0}) \\ &+ 3\frac{\mu_n}{\rho_0^2} + \mu_n^3 - \frac{2}{\rho_0^3} - 3\mu_n'(\kappa_n + \frac{1}{\rho_0}) + 3\mu_n\mu_n' + \mu_n''\Bigg)\Bigg]. \end{aligned} \tag{D.17c}$$

Appendix E

Full Formulations in Free Space and in a Stratified Waveguide for the Statistical Moments of the Ambiguity Function for the Field Scattered from a Group of Randomly Distributed, Randomly Moving Targets

E.1 Free Space

Here, we derive analytical expressions for the statistical moments of the ambiguity function of the total acoustic field scattered from a group of moving targets in free space. We begin with an analytical expression for the acoustic field scattered from a simple harmonic source by a single moving target in free space (Appendix C of Ref. [92]), and derive expressions for the statistical moments of the received field when

the target's position and velocity are random. Fourier synthesis is then used to expand these expressions for the general case of broadband source signals and calculate the statistical moments of the ambiguity function of the received field. Accounting for the cummulative effect of a distribution of N randomly swarming targets, we note that the expected intensity of the received field consists of: (i) a variance term proportional to N due to scattering from each target, and (ii) a mean-squared term proportional to N^2 due to interaction of the fields scattered from different targets,[90] where the variance term typically dominates.[1]

E.1.1 The Back-Scattered Field

We consider a monostatic stationary source/receiver system at $\mathbf{r}$, and a group of N targets randomly distributed in volume V centered at the origin $\mathbf{0}$. The random position of the qth target at time t_q is given by $\mathbf{r}_q = \mathbf{u}_q^0 + \mathbf{v}_q t_q$, as shown in Fig. 5-1, where $\mathbf{u}_q^0$ is its random initial position, and $\mathbf{v}_q$ is the target's average velocity during the time necessary for the sound signal to travel through the remote system's resolution footprint. Since the Doppler shift due to a moving target depends only on its speed relative to the source and receiver, we assume without loss of generality that $\mathbf{v}_q = v_q \hat{\mathbf{i}}_r + v_{q\perp} \hat{\mathbf{i}}_{r,\perp}$, where $\hat{\mathbf{i}}_{r,\perp}$ denotes a unit vector perpendicular to $\hat{\mathbf{i}}_r$. Under the above conditions, the field incident on the qth target in the far field of a harmonic source of frequency f is given by adapting Eq. (C3) of Ref. [92],

$$\Phi_{i,q}(\mathbf{r}_q, t_q; f) = e^{i2\pi f(r - \hat{\mathbf{i}}_r \cdot \mathbf{u}_q^0 - v_q t_q)/c} e^{-i2\pi f t_q} \tag{E.1}$$

where $r \equiv |\mathbf{r}|$, $\hat{\mathbf{i}}_r = \mathbf{r}/|r|$, and we have used the far field approximation $|\mathbf{r}_q - \mathbf{r}| = r - \hat{\mathbf{i}}_r \cdot \mathbf{r}_q$, valid for $r \gg r_q$. To determine the field scattered from the q target, we then follow the derivation procedure detailed in Eqs. (C4-C19) of Ref. [92],

$$\begin{aligned} \Phi_{s,q}(\mathbf{r}, t; f) &= \frac{S(\bar{f})}{\bar{k}} G(\mathbf{0}|\mathbf{r}, \bar{f}(1 + 2v_q/c)^{-1}) G(\mathbf{r}|\mathbf{0}, \bar{f}) e^{-i2\pi \bar{f} t} \\ &\quad \times e^{-i2\pi \bar{f}(1+(1+2v_q/c)^{-1})\hat{\mathbf{i}}_r \cdot \mathbf{u}_q^0/c}, \end{aligned} \tag{E.2}$$

where

$$\bar{f} = \frac{f(1+v_q/c)}{1-v_q/c}, \text{ or } \bar{f} \approx f(1+2v_q/c) \tag{E.3}$$

is the Doppler-shifted frequency of the scattered field. This derivation is also consistent with the approach of Dowling and Ffowcs Williams,[32] Eqs. (9.1)-(9.7), for calculating the sound field due to a moving point source.

Let us now consider the effect of random target position and speed. Taking expectations over the random initial offset $\mathbf{u}_q^0$, we define

$$\begin{aligned} U_q(\bar{f}\hat{\mathbf{i}}_r/c, v_q) &\equiv p_{\mathbf{u}}\left(\frac{\bar{f}\hat{\mathbf{i}}_r}{c}\left[1+\frac{1}{1+2v_q/c}\right]\right) \\ &= \int_V e^{-i2\pi\bar{f}(1+(1+2v_q/c)^{-1})\hat{\mathbf{i}}_r\cdot\mathbf{u}_q^0/c} P_{\mathbf{u}}(\mathbf{u}_q^0)\mathrm{d}^3\mathbf{u}_q^0 \end{aligned} \tag{E.4}$$

where $P_{\mathbf{u}}(\mathbf{u}_q^0)$ is the probability that the target initial position is $\mathbf{u}_q^0$, and $p_{\mathbf{u}}$ is the corresponding characteristic function, i.e. the Fourier Transform of $P_{\mathbf{u}}$. Then,

$$\begin{aligned} \langle\Phi_{s,q}(\mathbf{r},t;f)\rangle &= \int \frac{S(\bar{f})}{\bar{k}} G(\mathbf{0}|\mathbf{r}, \bar{f}(1+2v_q/c)^{-1}) G(\mathbf{r}|\mathbf{0},\bar{f}) e^{-i2\pi\bar{f}t} \\ &\quad \times U_q(\bar{f}\hat{\mathbf{i}}_r/c, v_q) P_v(v_q)\mathrm{d}v_q \end{aligned} \tag{E.5}$$

where $P_v(v_q)$ is the probability that the target speed is v_q. We note that when the source frequency f becomes such that the wavelength c/f is much smaller than the length scale of the targets' spatial distribution, the variable $U_q(\bar{f}\hat{\mathbf{i}}_r/c, v_q)$ approaches zero, so that $\langle\Phi_{s,q}(\mathbf{r},t;f)\rangle \approx 0$ also.

Finally, we can derive an expression for the autocorrelation of the scattered field

from the qth target,

$$\begin{aligned}
&\langle \Phi_{s,q}(\mathbf{r},t;f)\Phi^*_{s,q}(\mathbf{r},t+\tau;f)\rangle = \\
&= \int \frac{S(\bar{f})S^*(\bar{f})}{\bar{k}\bar{k}^*} G(\mathbf{r}|\mathbf{0},\bar{f})e^{-i2\pi\bar{f}t}G^*(\mathbf{r}|\mathbf{0},\bar{f})e^{i2\pi\bar{f}(t+\tau)} \\
&\quad \times \int G(\mathbf{0}|\mathbf{r},\bar{f}(1+2v_q/c)^{-1})e^{-i2\pi\bar{f}\hat{\mathbf{i}}_r\cdot\mathbf{u}^0_q/c(1+(1+2v_q/c)^{-1})} \\
&\qquad \times G^*(\mathbf{0}|\mathbf{r},\bar{f}(1+2v_q/c)^{-1})e^{i2\pi\bar{f}\hat{\mathbf{i}}_r\cdot\mathbf{u}^0_q/c(1+(1+2v_q/c)^{-1})} \\
&\qquad \times P_{\mathbf{u}}(\mathbf{u}^0_q)P_v(v_q)\mathrm{d}^3\mathbf{u}^0_q\mathrm{d}v_q \\
&= \int \frac{|S(\bar{f})|^2}{|\bar{k}|^2}|G(\mathbf{r}|\mathbf{0},\bar{f})|^2|G(\mathbf{0}|\mathbf{r},\bar{f}(1+2v_q/c)^{-1})|^2 e^{i2\pi\bar{f}\tau}P_v(v_q)\mathrm{d}v_q \qquad \text{(E.6)}
\end{aligned}$$

E.1.2 Statistical Moments of the Ambiguity Function

For a broadband source with source function $q(t) \Leftrightarrow Q(f)$, the scattered field is found by Fourier synthesis as

$$\Psi_{s,q}(\mathbf{r},t) \;=\; \int \mathrm{d}f Q(f)\Phi_{s,q}(\mathbf{r},t;f) \qquad \text{(E.7)}$$

The ambiguity function of $\Psi_{s,q}(\mathbf{r},t)$ is defined as

$$\Psi_{s,q}(\tau,\nu) = \int_{-\infty}^{\infty} \Psi_{s,q}(\mathbf{r},t)q^*(t-\tau)e^{i2\pi\nu t}\mathrm{d}t = \int_{-\infty}^{\infty} \Psi_{s,q}(\mathbf{r},f')Q^*(f'-\nu)e^{-i2\pi(f'-\nu)\tau}\mathrm{d}f' \qquad \text{(E.8)}$$

where * signifies complex conjugate and

$$\begin{aligned}
\Psi_{s,q}(\mathbf{r},f') &= \int \mathrm{d}t e^{i2\pi f't}\int \mathrm{d}f Q(f)\Phi_{s,q}(\mathbf{r},t;f) \\
&= \int \mathrm{d}t e^{i2\pi f't}\int \mathrm{d}f Q(f)\frac{S(\bar{f})}{\bar{k}}G(\mathbf{0}|\mathbf{r},\bar{f}(1+2v_q/c)^{-1})G(\mathbf{r}|\mathbf{0},\bar{f}) \\
&\qquad \times e^{-i2\pi\bar{f}t}e^{-i2\pi\bar{f}(1+(1+2v_q/c)^{-1})\hat{\mathbf{i}}_r\cdot\mathbf{u}^0_q/c} \qquad \text{(E.9)}
\end{aligned}$$

Changing the order of integration, the integral over t results in the delta function $\delta(f' - \bar{f})$, where $\bar{f} = f(1 + 2v_q/c)$ (see Appendix E.1). Substituting for f,

$$\begin{aligned}\Psi_{s,q}(\mathbf{r}, f') &= \int \frac{\delta(f' - \bar{f})\mathrm{d}\bar{f}}{1 + 2v_q/c} Q(\bar{f}(1 + 2v_q/c)^{-1}) \frac{S(\bar{f})}{\bar{k}} G(\mathbf{0}|\mathbf{r}, \bar{f}(1 + 2v_Q/c)^{-1}) G(\mathbf{r}|\mathbf{0}, \bar{f}) \\ &\quad \times e^{-i2\pi\bar{f}(1+(1+2v_q/c)^{-1})\hat{\mathbf{i}}_r \cdot \mathbf{u}_q^0/c} \\ &\approx \frac{S(f')}{k'} G(\mathbf{0}|\mathbf{r}, f'(1 + 2v_q/c)^{-1}) G(\mathbf{r}|\mathbf{0}, f') Q(f'(1 + 2v_q/c)^{-1}) \\ &\quad \times e^{-i2\pi f'(1+(1+2v_q/c)^{-1})\hat{\mathbf{i}}_r \cdot \mathbf{u}_q^0/c} \end{aligned} \tag{E.10}$$

Plugging Eq. (E.10) into Eq. (E.8), we then have

$$\begin{aligned}\Psi_{s,q}(\tau, \nu) &= \int_{-\infty}^{\infty} \frac{S(f')}{k'} G(\mathbf{0}|\mathbf{r}, f'(1 + 2v_q/c)^{-1}) G(\mathbf{r}|\mathbf{0}, f') Q(f'(1 + 2v_q/c)^{-1}) \\ &\quad \times e^{-i2\pi f'(1+(1+2v_q/c)^{-1})\hat{\mathbf{i}}_r \cdot \mathbf{u}_q^0/c} Q^*(f' - \nu) e^{-i2\pi(f'-\nu)\tau} \mathrm{d}f' \end{aligned} \tag{E.11}$$

and we can now provide expressions for the expected value of the ambiguity function, as well as its second moment,

$$\begin{aligned}\langle \Psi_{s,q}(\tau, \nu) \rangle &= \int_{-\infty}^{\infty} \frac{S(f')}{k'} G(\mathbf{r}|\mathbf{0}, f') Q^*(f' - \nu) e^{-i2\pi(f'-\nu)\tau} \\ &\quad \times \int G(\mathbf{0}|\mathbf{r}, f'(1 + 2v_q/c)^{-1}) Q(f'(1 + 2v_q/c)^{-1}) \\ &\quad \times U_q(f'\hat{\mathbf{i}}_r/c, v_q) P_v(v_q) \mathrm{d}v_q \mathrm{d}f' \end{aligned} \tag{E.12}$$

and

$$\begin{aligned}\langle |\Psi_{s,q}(\tau, \nu)|^2 \rangle &= \int_{-\infty}^{\infty} \int_{-\infty}^{\infty} \frac{S(f_1)}{k_1} G(\mathbf{r}|\mathbf{0}, f_1) Q^*(f_1 - \nu) \frac{S^*(f_2)}{k_2^*} G^*(\mathbf{r}|\mathbf{0}, f_2) Q(f_2 - \nu) \\ &\quad \times e^{-i2\pi(f_1 - f_2)\tau} \int G(\mathbf{0}|\mathbf{r}, f_1(1 + 2v_q/c)^{-1}) Q(f_1(1 + 2v_q/c)^{-1}) \\ &\quad \times G^*(\mathbf{0}|\mathbf{r}, f_2(1 + 2v_q/c)^{-1}) Q^*(f_2(1 + 2v_q/c)^{-1}) \\ &\quad \times U_q((f_1 - f_2)\hat{\mathbf{i}}_r/c, v_q) P_v(v_q) \mathrm{d}v_q \mathrm{d}f_1 \mathrm{d}f_2 \end{aligned} \tag{E.13}$$

We note that the term U_q, which corresponds to the characteristic function of the random target position $\mathbf{u}_q^0$, is evaluated at different wavenumbers between Eqs. (E.12) and (E.13). As demonstrated in Section 5.2.1, evaluating U_q near base-band typically leads to the second moment of the ambiguity function dominating over the magnitude squared of its first moment.

For the total field scattered from the group of N targets within volume V we can write $\Psi_s(\mathbf{r}, f') = \sum_{q=1}^{N} \Psi_{s,q}(\mathbf{r}, f')$. Assuming that: (i) target positions are independent and identically distributed random variables (i.i.d.), and (ii) target speeds are also i.i.d., we then have $\langle \Psi_s(\tau,\nu) \rangle = N \langle \Psi_{s,q}(\tau,\nu) \rangle$, with the second moment given by

$$
\begin{aligned}
\langle |\Psi_s(\tau,\nu)|^2 \rangle &= \sum_{q=1}^{N}\sum_{p=1}^{N} \int_{-\infty}^{\infty}\int_{-\infty}^{\infty} \frac{S(f_1)}{k_1} G(\mathbf{r}|\mathbf{0}, f_1) Q^*(f_1-\nu) \frac{S^*(f_2)}{k_2^*} G^*(\mathbf{r}|\mathbf{0}, f_2) Q(f_2-\nu) \\
&\quad \times \int\int\int\int G(\mathbf{0}|\mathbf{r}, f_1(1+2v_q/c)^{-1}) Q(f_1(1+2v_q/c)^{-1}) \\
&\quad\quad \times G^*(\mathbf{0}|\mathbf{r}, f_2(1+2v_p/c)^{-1}) Q^*(f_2(1+2v_p/c)^{-1}) \\
&\quad\quad \times e^{-i2\pi f_1 (1+(1+2v_q/c)^{-1})\hat{\mathbf{i}}_r \cdot \mathbf{u}_q^0/c} e^{i2\pi f_2 (1+(1+2v_q/c)^{-1})\hat{\mathbf{i}}_r \cdot \mathbf{u}_p^0/c} \\
&\quad\quad \times P_{\mathbf{u}}(\mathbf{u}_q^0) P_{\mathbf{u}}(\mathbf{u}_p^0) P_v(v_q) P_v(v_p) \mathrm{d}\mathbf{u}_q^0 \mathrm{d}\mathbf{u}_p^0 \mathrm{d}v_q \mathrm{d}v_p e^{-i2\pi(f_1-f_2)\tau} \mathrm{d}f_1 \mathrm{d}f_2 \\
&= N\langle |\Psi_{s,q}(\tau,\nu)|^2 \rangle + N(N-1) |\langle \Psi_{s,q}(\tau,\nu) \rangle|^2 \qquad \text{(E.14)}
\end{aligned}
$$

The last line is arrived at by considering the distinction between the $q = p$ terms, and the $q \neq p$ terms. The second moment of the ambiguity function then consists of two terms: (i) a variance term proportional to N due to scattering from each target, and (ii) a mean-squared term proportional to N^2 due to interaction of the fields scattered from different targets,[90] where the variance term typically dominates.[1]

E.1.3 Moments of the Ambiguity Function over Time Delay and Doppler Shift

Equations (E.12) and (E.13) cannot typically be analytically evaluated. A significant simplification is however possible in the case of specially designed source spectra that can be approximated by Eq. (5.7), $Q(f) = \sum_{n=0}^{M-1} a_n e^{i2\pi(f-f_n)h_n} \delta(f-f_n)$. As we show

in Appendix E.3, a Costas sequence belongs in this set of signals. Equation (E.12) can then be rewritten as,

$$\begin{aligned}\langle \Psi_{s,q}(\tau,\nu)\rangle &= \sum_{n=0}^{M-1}\sum_{m=0}^{M-1} a_n^* a_m \int_{-\infty}^{\infty} \frac{S(f')}{k'} G(\mathbf{r}|\mathbf{0},f') e^{-i2\pi(f'-\nu-f_n)h_n}\delta(f'-\nu-f_n) \\ &\quad \times e^{-i2\pi(f'-\nu)\tau}\int G(\mathbf{0}|\mathbf{r},f'(1+2v_q/c)^{-1}) e^{i2\pi(f'(1+2v_q/c)^{-1}-f_m)h_m} \\ &\quad \times \delta(f'(1+2v_q/c)^{-1}-f_m) U_q(f'\hat{\mathbf{i}}_r/c, v_q) P_v(v_q)\mathrm{d}v_q\mathrm{d}f' \end{aligned} \quad \text{(E.15)}$$

Integrating over f' introduces the delta function

$$\delta\left(v_q - \frac{c}{2}\left[\frac{f_n+\nu}{f_m}-1\right]\right) \quad \text{(E.16)}$$

since $f' = f_n + \nu = f_m(1+2v_q/c)$, so that

$$\begin{aligned}\langle \Psi_{s,q}(\tau,\nu)\rangle &= \sum_{n=0}^{M-1}\sum_{m=0}^{M-1} a_n^* a_m \frac{S(f_n+\nu)}{2\pi(f_n+\nu)/c} G(\mathbf{r}|\mathbf{0},f_n+\nu) G(\mathbf{0}|\mathbf{r},f_m) e^{-i2\pi f_n\tau} \\ &\quad \times p_{\mathbf{u}}([f_n+f_m+\nu]\hat{\mathbf{i}}_r/c) P_v\left(\frac{c}{2}\left[\frac{f_n+\nu}{f_m}-1\right]\right) \end{aligned} \quad \text{(E.17)}$$

where we have substituted for $U_{b,q}$ using Eq. (E.4). Similarly, for the second moment of the ambiguity function we find,

$$\begin{aligned}\langle |\Psi_{s,q}(\tau,\nu)|^2\rangle &= \sum_{n=0}^{M-1}\sum_{m=0}^{M-1}\sum_{l=0}^{M-1}\sum_{j=0}^{M-1} a_n^* a_m a_l a_j^* \left[\frac{S(f_n+\nu)}{2\pi(f_n+\nu)/c}\right]\left[\frac{S^*(f_l+\nu)}{2\pi(f_l+\nu)/c}\right] \\ &\quad \times G(\mathbf{r}|\mathbf{0},f_n+\nu) G^*(\mathbf{r}|\mathbf{0},f_l+\nu) G(\mathbf{0}|\mathbf{r},f_m) G^*\left(\mathbf{0}|\mathbf{r},\frac{f_l+\nu}{f_n+\nu}f_m\right) \\ &\quad \times \delta\left(\frac{f_l+\nu}{f_n+\nu}f_m - f_j\right) p_{\mathbf{u}}\left(\left[f_n+f_m-f_l-\frac{f_l+\nu}{f_n+\nu}f_m\right]\hat{\mathbf{i}}_r/c\right) \\ &\quad \times e^{-i2\pi(f_n-f_l)\tau} P_v\left(\frac{c}{2}\left[\frac{f_n+\nu}{f_m}-1\right]\right) \end{aligned} \quad \text{(E.18)}$$

where the delta function signifies that, for given ν, only specific frequency ratios result in non-zero values for $\langle |\Psi_{s,q}(\tau,\nu)|^2\rangle$.

To evaluate the moments of the ambiguity function's expected square magnitude

along ν, we assume that the acoustic wavelength is much smaller than the spatial extent of the target swarm, so that the characteristic function of the target's position ($p_{\mathbf{u}}$) can be approximated as a delta function, whereby

$$\sum_{l=0}^{M-1}\sum_{j=0}^{M-1}\delta\left(\frac{f_l+\nu}{f_n+\nu}f_m-f_j\right)\delta\left(\left[f_n+f_m-f_l-\frac{f_l+\nu}{f_n+\nu}f_m\right]\right)$$
$$\equiv\sum_{l=0}^{M-1}\sum_{j=0}^{M-1}\delta(f_l-f_n)\delta(f_j-f_m) \tag{E.19}$$

so that

$$\langle|\Psi_{s,q}(\tau,\nu)|^2\rangle = \sum_{n=0}^{M-1}\sum_{m=0}^{M-1}|a_n|^2|a_m|^2\frac{|S(f_n+\nu)|^2}{[2\pi(f_n+\nu)/c]^2}\frac{1}{4\pi r^4}P_v\left(\frac{c}{2}\left[\frac{f_n+\nu}{f_m}-1\right]\right) \tag{E.20}$$

For low Mach number motions, we assume that the term $|S(f_n+\nu)|^2/[2\pi(f_n+\nu)/c]^2$ is approximately constant and equal to $|S(f_n)|^2/[2\pi f_n/c]^2$. The moments of Eq. (E.20) along ν for constant τ are linearly related to the moments of the target speed probability density,

$$\nu_1 \equiv \int\nu\langle|\Psi_{s,q}(\tau,\nu)|^2\rangle\mathrm{d}\nu=\sum_{n,m}^{M-1}b_{n,m}\frac{2f_m}{c}\left(f_m-f_n+f_m\frac{2\mu_v}{c}\right), \tag{E.21a}$$

$$\nu_2 \equiv \int\nu^2\langle|\Psi_{s,q}(\tau,\nu)|^2\rangle\mathrm{d}\nu=\sum_{n,m}^{M-1}b_{n,m}\frac{2f_m}{c}\left\{\left(f_m-f_n+f_m\frac{2\mu_v}{c}\right)^2+\frac{4\sigma_v^2}{c^2}f_m^2\right\} \tag{E.21b}$$

after normalizing so that $\int\langle|\Psi_{s,q}(\tau,\nu)|^2\rangle\mathrm{d}\nu=1$, where $b_{n,m}$ is a known constant, μ_v, σ_v are the mean and standard deviation of the target speed, and f_n, f_m are known constants that correspond to the distinct frequency components of the source spectrum of Eq. (5.7). For example, for the case of a continuous harmonic wave ($M=1$), we find $\nu_1=2f_0\mu_v/c$, and $\nu_2=4f_0^2(\sigma_v^2+\mu_v^2)/c^2$.

Going back to Eq. (E.18), to evaluate the moments of the ambiguity function's expected square magnitude along τ, we now write the characteristic function for $\mathbf{u}$ as

a Taylor series expansion,

$$\begin{aligned} p_{\mathbf{u}}(\gamma\hat{\mathbf{i}}_r/c) &\equiv \int P_{\mathbf{u}}(\mathbf{u}_q)e^{-i2\pi\gamma\hat{\mathbf{i}}_r\cdot\mathbf{u}_q/c}\mathrm{d}\mathbf{u}_q \\ &= \int P_{\mathbf{u}}(\mathbf{u}_q)\left(1-i2\pi\gamma\hat{\mathbf{i}}_r\cdot\mathbf{u}_q/c-\frac{4\pi^2}{2}[\gamma\hat{\mathbf{i}}_r\cdot\mathbf{u}_q/c]^2+\ldots\right)\mathrm{d}\mathbf{u}_q \\ &= 1-i2\pi\gamma(r+\hat{\mathbf{i}}_r\cdot\boldsymbol{\mu}_{\mathbf{u}})/c-\frac{4\pi^2}{2}\gamma^2\left([\hat{\mathbf{i}}_r\cdot\boldsymbol{\sigma}_{\mathbf{u}}]^2+[r+\hat{\mathbf{i}}_r\cdot\boldsymbol{\mu}_{\mathbf{u}}]^2\right)/c^2+\ldots \\ &= \sum_{d=0}^{p}c_d\gamma^d \end{aligned} \tag{E.22}$$

where $\gamma=(f_n+f_m-f_l-f_m(f_l+\nu)/(f_n+\nu))$, and $\boldsymbol{\mu}_{\mathbf{u}}$, $\boldsymbol{\sigma}_{\mathbf{u}}$ are the mean and standard deviation of the target initial position, respectively. The moments of Eq. (E.18) along τ involve integrals of the form

$$\int\tau^p e^{-i2\pi(f_n-f_l)\tau}\mathrm{d}\tau=\left(\frac{i}{2\pi}\right)^p\delta^{(p)}(f_n-f_l) \tag{E.23}$$

where $\delta^{(p)}$ is the pth derivative of the Dirac delta function and is defined by the property

$$\int h(f)\delta^{(p)}(f)\mathrm{d}f=-\int\frac{\partial h(f)}{\partial f}\delta^{(p-1)}(f)\mathrm{d}f=(-1)^p\int\frac{\partial^p h(f)}{\partial f^p}\delta(f)\mathrm{d}f \tag{E.24}$$

Before substituting into Eq. (E.18), we also note that

$$\sum_{l=0}^{M-1}\delta\left(\frac{f_l+\nu}{f_n+\nu}f_m-f_j\right)\delta(f_n-f_l)\equiv\delta(f_j-f_m) \tag{E.25}$$

The moments of Eq. (E.18) along τ are then given by

$$\begin{aligned} \int\tau^p\langle|\Psi_{s,q}(\tau,\nu)|^2\rangle\mathrm{d}\tau &= \sum_{n=0}^{M-1}\sum_{m=0}^{M-1}|a_n|^2|a_m|^2\frac{|S(f_n+\nu)|^2}{[2\pi(f_n+\nu)/c]^2}\frac{1}{(4\pi r)^4} \\ &\quad\times p!\left(\frac{i}{2\pi}\right)^p c_p P_v\left(\frac{c}{2}\left[\frac{f_n+\nu}{f_m}-1\right]\right), \end{aligned} \tag{E.26}$$

so that

$$\tau_1 \equiv \int \tau \langle |\Psi_{s,q}(\tau,\nu)|^2 \rangle \mathrm{d}\tau = (r + \hat{\mathbf{i}}_r \cdot \boldsymbol{\mu}_{\mathbf{u}}) \frac{1}{c} \sum_{n=0}^{M-1} \sum_{m=0}^{M-1} P_v \left(\frac{c}{2} \left[\frac{f_n + \nu}{f_m} - 1 \right] \right), \tag{E.27a}$$

$$\tau_2 \equiv \int \tau^2 \langle |\Psi_{s,q}(\tau,\nu)|^2 \rangle \mathrm{d}\tau = \frac{2}{c^2} \left([\hat{\mathbf{i}} \cdot \boldsymbol{\sigma}_{\mathbf{u}}]^2 + [r + \hat{\mathbf{i}}_r \cdot \boldsymbol{\mu}_{\mathbf{u}}]^2 \right) \sum_{n=0}^{M-1} \sum_{m=0}^{M-1} P_v \left(\frac{c}{2} \left[\frac{f_n + \nu}{f_m} - 1 \right] \right) \tag{E.27b}$$

Note here that, for the case of a continuous harmonic wave ($M = 1$), it is not possible to infer the statistics of target position since $\gamma = 0$, $p_{\mathbf{u}}(\mathbf{0}) = 1$, and the magnitude square of the ambiguity function does not depend on target position, as expected.

Also note that Eqs. (E.21 - E.27) were derived for the expected value of the ambiguity function magnitude squared given a single target with random position and velocity, Eq. (E.13). For a total of N targets, the expected value of the ambiguity function magnitude squared is instead given by Eq. (E.14), which also involves the magnitude squared of the expected value of the ambiguity function for a single target, Eq. (E.12). Moments of the latter along constant-τ and constant-ν axis cannot in general be expressed as linear functions of the target's position and velocity statistical moments, even for source signals that satisfy Eq. (5.7). For a group of N targets, moments of the expected value of the total ambiguity function magnitude squared can still be used to obtain estimates of the targets' position and velocity means and standard deviations, as long as the variance of the received field intensity dominates, which is typically the case.[1]

E.2 Stratified Waveguide

Here, we derive expressions for the statistical moments of the ambiguity function of the total acoustic field scattered from a group of moving targets in a stratified waveguide. Our formulation is based on analytical expressions for the Doppler shift and spread expected in long-range scattering from fish groups in the continental shelf, which in turn are based on a model for scattering from a moving target submerged

in a stratified ocean waveguide.[92] We also state conditions for modal decorrelation, since it has been shown that given a sufficiently large distribution of random volume or surface inhomogeneities, the waveguide modes will decouple in the mean forward field.[18, 90]

E.2.1 The Back-Scattered Field

As for the free space case in Appendix E.1, we consider a monostatic stationary system at range $\mathbf{r}$ from a group of N targets randomly distributed within volume V centered at the origin $\mathbf{0}$. The position of the qth target at time t_q is given by $\mathbf{r}_q = \mathbf{u}_q^0 + \mathbf{v}_q t_q$, as shown in Fig. 5-1, where $\mathbf{u}_q^0$ is the initial random target position, and $\mathbf{v}_q$ is the target's average velocity during the time needed for the sound signal to travel through the remote system's resolution footprint. We assume again that $\mathbf{v}_q = v_q \hat{\mathbf{i}}_r + v_{q\perp} \hat{\mathbf{i}}_{r,\perp}$, where $\hat{\mathbf{i}}_{r,\perp}$ denotes a unit vector perpendicular to $\hat{\mathbf{i}}_r$. Finally, we assume that for the frequency regime we consider, the targets scatter omnidirectionaly so that their scatter function has no angular dependence. Under the above conditions, we can rewrite Eq. (59) of Ref. [92] as

$$\Phi_{s,q}(\mathbf{r}, t; \Omega) = 4\pi \sum_l \sum_m \frac{S(\omega_{m,l,q})}{k(\omega_{m,l,q})} \Phi_{s,q}^{l,m}(\mathbf{r}, \Omega, \omega_{m,l,q}) e^{-i\omega_{m,l,q} t} \tag{E.28}$$

where

$$\omega_{m,l,q} = \Omega + v_q[\xi_l(\Omega) + \xi_m(\Omega)] \tag{E.29}$$

is the Doppler shifted frequency due to target motion. We have defined for convenience

$$\begin{aligned}\Phi_{s,q}^{l,m}(\mathbf{r},\Omega,\omega_{m,l,q}) &= \Big[A_l(\mathbf{r};\Omega)A_m(\mathbf{r};\omega_{m,l,q})\mathrm{e}^{i(\gamma_l(\Omega)+\gamma_m(\omega_{m,l,q}))z_q^0} \\ &\quad - A_l(\mathbf{r};\Omega)B_m(\mathbf{r};\omega_{m,l,q})\mathrm{e}^{i(\gamma_l(\Omega)-\gamma_m(\omega_{m,l,q}))z_q^0} \\ &\quad - B_l(\mathbf{r};\Omega)A_m(\mathbf{r};\omega_{m,l,q})\mathrm{e}^{-i(\gamma_l(\Omega)-\gamma_m(\omega_{m,l,q}))z_q^0} \\ &\quad + B_l(\mathbf{r};\Omega)B_m(\mathbf{r};\omega_{m,l,q})\mathrm{e}^{-i(\gamma_l(\Omega)+\gamma_m(\omega_{m,l,q}))z_q^0}\Big] \times \mathrm{e}^{i(\xi_l(\Omega)+\xi_m(\omega_{m,l,q}))\rho_q^0}\end{aligned} \tag{E.30}$$

where, other than in the expression for $\omega_{m,l,q}$, the lth mode wavenumbers are evaluated at Ω, while the mth mode wavenumbers are evaluated at $\omega_{m,l,q}$. Note that $\Phi_{s,q}^{l,m}(\mathbf{r},\Omega,\omega_{m,l,q})$ is an implicit function of v_q.

Equation (E.28) is valid when we are in the far-field of the source/receiver, which is satisfied here since we are considering scattering from targets within a resolution footprint of our monostatic system. We have already made use of this fact in deriving Eq. (E.30), where for the amplitudes of the down- and up-going plane waves of the incoming mode l, we have written

$$A_l(\mathbf{r}-\mathbf{u}_q^0;\Omega) = A_l(\mathbf{r};\Omega)\times e^{i(\xi_l(\Omega)\hat{\mathbf{i}}_\rho\cdot\mathbf{u}_q^0+\gamma_l(\Omega)\hat{\mathbf{i}}_z\cdot\mathbf{u}_q^0)}, \tag{E.31a}$$

$$B_l(\mathbf{r}-\mathbf{u}_q^0;\Omega) = B_l(\mathbf{r};\Omega)\times e^{i(\xi_l(\Omega)\hat{\mathbf{i}}_\rho\cdot\mathbf{u}_q^0-\gamma_l(\Omega)\hat{\mathbf{i}}_z\cdot\mathbf{u}_q^0)}, \tag{E.31b}$$

and similarly for the plane wave amplitudes of the outgoing mode m, we have used

$$A_m(\mathbf{r}-\mathbf{u}_q^0;\omega_{m,l,q}) = A_m(\mathbf{r};\omega_{m,l,q})\times e^{i(\xi_m(\omega_{m,l,q})\hat{\mathbf{i}}_\rho\cdot\mathbf{u}_q^0+\gamma_m(\omega_{m,l,q})\hat{\mathbf{i}}_z\cdot\mathbf{u}_q^0)}, \tag{E.32a}$$

$$B_m(\mathbf{r}-\mathbf{u}_q^0;\omega_{m,l,q}) = B_m(\mathbf{r};\omega_{m,l,q})\times e^{i(\xi_m(\omega_{m,l,q})\hat{\mathbf{i}}_\rho\cdot\mathbf{u}_q^0-\gamma_m(\omega_{m,l,q})\hat{\mathbf{i}}_z\cdot\mathbf{u}_q^0)}. \tag{E.32b}$$

For spatial cylindrical coordinates $\mathbf{k}=\xi\hat{\mathbf{i}}_\rho+\gamma\hat{\mathbf{i}}_z$, while $A_l(\mathbf{r};\Omega)$, $B_l(\mathbf{r};\Omega)$ are the amplitudes of the down- and up-going modal plane wave components incident on the target, and $A_m(\mathbf{r};\omega_{m,l,q})$, $B_m(\mathbf{r};\omega_{m,l,q})$ are the amplitudes of the down- and up-going

modal plane wave components scattered from the target,

$$A_l(\mathbf{r};\Omega) = \frac{i}{d(z)}\frac{e^{-i\pi/4}u_l(z)N_l^{(1)}}{\sqrt{8\pi\xi_l(\Omega)|\boldsymbol{\rho}|}}e^{i(\xi_l(\Omega)|\boldsymbol{\rho}|+\gamma_l(\Omega)z_t)}, \tag{E.33a}$$

$$B_l(\mathbf{r};\Omega) = \frac{i}{d(z)}\frac{e^{-i\pi/4}u_l(z)N_l^{(2)}}{\sqrt{8\pi\xi_l(\Omega)|\boldsymbol{\rho}|}}e^{i(\xi_l(\Omega)|\boldsymbol{\rho}|-\gamma_l(\Omega)z_t)}, \tag{E.33b}$$

$$A_m(\mathbf{r};\omega_{m,l,q}) = \frac{i}{d(0)}\frac{e^{-i\pi/4}u_m(z)N_m^{(1)}}{\sqrt{8\pi\xi_m(\omega_{m,l,q})|\boldsymbol{\rho}|}}e^{i(\xi_m(\omega_{m,l,q})|\boldsymbol{\rho}|+\gamma_m(\omega_{m,l,q})z_t)}, \tag{E.33c}$$

$$B_m(\mathbf{r};\omega_{m,l,q}) = \frac{i}{d(0)}\frac{e^{-i\pi/4}u_m(z)N_m^{(2)}}{\sqrt{8\pi\xi_m(\omega_{m,l,q})|\boldsymbol{\rho}|}}e^{i(\xi_m(\omega_{m,l,q})|\boldsymbol{\rho}|-\gamma_m(\omega_{m,l,q})z_t)} \tag{E.33d}$$

Before taking expectations over target position and speed in Eq. (E.28), we note that only $\Phi_{s,q}^{l,m}$ is a function of $\mathbf{u}_q^0$ and define

$$\begin{aligned} U_q^{l,m}(\omega_{m,l,q},v_q) &\equiv \frac{1}{V}\int_V \Phi_{s,q}^{l,m}(\mathbf{r},\Omega,\omega_{m,l,q})\mathrm{d}^3\mathbf{u}_q^0 \\ &= \operatorname{sinc}\left((\xi_{lx}+\xi_{mx})L_x/2\right)\operatorname{sinc}\left((\xi_{ly}+\xi_{my})L_y/2\right) \\ &\quad\times\left[\operatorname{sinc}\left((\gamma_l+\gamma_m)L_z/2\right)(A_lA_m+B_lB_m)\right. \\ &\quad\left.-\operatorname{sinc}\left((\gamma_l-\gamma_m)L_z/2\right)(A_lB_m+B_lA_m)\right] \end{aligned} \tag{E.34}$$

where we have assumed that the target position is randomly distributed within the resolution footprint of volume V, and the following shorthand notations have been employed: $A_l = A_l(\mathbf{r};\Omega)$, $B_l = B_l(\mathbf{r};\Omega)$, $A_m = A_m(\mathbf{r};\omega_{m,l,q})$, and $B_m = B_m(\mathbf{r};\omega_{m,l,q})$. Note that ξ_{lx}, ξ_{ly}, γ_l are evaluated at Ω, while ξ_{mx}, ξ_{my}, γ_m are evaluated at $\omega_{m,l,q}$. We can then write for the expected value of field scattered from the qth target,

$$\langle\Phi_{s,q}(\mathbf{r},t;\Omega)\rangle = 4\pi\int\sum_l\sum_m\frac{S(\omega_{m,l,q})}{k(\omega_{m,l,q})}U_q^{l,m}(\omega_{m,l,q},v_q)e^{-i\omega_{m,l,q}t}P_v(v_q)\mathrm{d}v_q \tag{E.35}$$

where $P_v(v_q)$ is the probability that the target speed is v_q. For small Mach numbers, the change between wavenumbers $\xi_l(\Omega)$ and $\xi_l(\omega_{m,l,q})$, as well as the change between modal amplitudes $A_l(\Omega)$ and $A_l(\omega_{m,l,q})$ are both very small, so that modal

orthogonality leads to $\sum_l \sum_m U_q^{l,m}(\omega_{m,l,q}, v_q) = \sum_l U_q^{l,l}(\omega_{l,l,q}, v_q)$, where

$$U_q^{l,l}(\omega_{l,l,q}, v_q) = \mathrm{sinc}\left(\xi_{lx} L_x\right) \mathrm{sinc}\left(\xi_{ly} L_y\right) \times \left[\mathrm{sinc}\left(\gamma_l L_z\right)\left(A_l^2 + B_l^2\right) - 2A_l B_l\right] \quad \text{(E.36)}$$

When the length scale of the resolution footprint becomes sufficiently larger than the wavelength, the mean scattered field $\langle \Phi_{s,q}(\mathbf{r}, t; \Omega) \rangle \approx 0$.

For the autocorrelation of the scattered field, we find

$$\begin{aligned}
\langle \Phi_{s,q}(\mathbf{r}, t; \Omega) \Phi_{s,q}^*(\mathbf{r}, t+\tau; \Omega) \rangle &= \frac{16\pi^2}{V} \int \int_V \sum_l \sum_m \sum_n \sum_p \frac{S(\omega_{m,l,q}) S^*(\omega_{p,n,q})}{k(\omega_{m,l,q}) k^*(\omega_{p,n,q})} \\
&\quad \times \Phi_{s,q}^{l,m}(\mathbf{r}, \Omega, \omega_{m,l,q}) \Phi_{s,q}^{*\,n,p}(\mathbf{r}, \Omega, \omega_{p,n,q}) \\
&\quad \times e^{-iv_q[\xi_l(\Omega) + \xi_m(\Omega) - \xi_n(\Omega) - \xi_p(\Omega)]t} \\
&\quad \times e^{iv_q[\xi_n(\Omega) + \xi_p(\Omega)]\tau} e^{i\Omega\tau} P_v(v_q) \mathrm{d}^3\mathbf{u}_q^0 \mathrm{d}v_q \\
&= 16\pi^2 \int \sum_l \sum_m \sum_n \sum_p \frac{S(\omega_{m,l,q}) S^*(\omega_{p,n,q})}{k(\omega_{m,l,q}) k^*(\omega_{p,n,q})} \\
&\quad \times U_q^{l,m,n,p}(\omega_{m,l,q}, \omega_{p,n,q}, v_q) e^{iv_q[\xi_n(\Omega) + \xi_p(\Omega)]\tau} e^{i\Omega\tau} \\
&\quad \times e^{-iv_q[\xi_l(\Omega) + \xi_m(\Omega) - \xi_n(\Omega) - \xi_p(\Omega)]t} P_v(v_q) \mathrm{d}v_q \quad \text{(E.37)}
\end{aligned}$$

by defining

$$\begin{aligned}
U_q^{l,m,n,p}(\omega_{m,l,q}, \omega_{p,n,q}, v_q) &\equiv \frac{1}{V} \int_V \Phi_{s,q}^{l,m}(\mathbf{r}, \Omega, \omega_{m,l,q}) \Phi_{s,q}^{*\,n,p}(\mathbf{r}, \Omega, \omega_{p,n,q}) \mathrm{d}^3\mathbf{u}_q^0 \\
&= \mathrm{sinc}\left((\xi_{lx} + \xi_{mx} - \xi_{nx} - \xi_{px}) L_x/2\right) \mathrm{sinc}\left((\xi_{ly} + \xi_{my} - \xi_{ny} - \xi_{py}) L_y/2\right) \\
&\quad \times \Big[(A_l A_m A_n^* A_p^* + B_l B_m B_n^* B_p^*) \mathrm{sinc}\left((\gamma_l + \gamma_m - \gamma_n - \gamma_p) L_z/2\right) \\
&\quad - (A_l A_m A_n^* B_p^* + B_l B_m B_n^* A_p^*) \mathrm{sinc}\left((\gamma_l + \gamma_m - \gamma_n + \gamma_p) L_z/2\right) \\
&\quad - (A_l A_m B_n^* A_p^* + B_l B_m A_n^* B_p^*) \mathrm{sinc}\left((\gamma_l + \gamma_m + \gamma_n - \gamma_p) L_z/2\right) \\
&\quad + (A_l A_m B_n^* B_p^* + B_l B_m A_n^* A_p^*) \mathrm{sinc}\left((\gamma_l + \gamma_m + \gamma_n + \gamma_p) L_z/2\right) \\
&\quad - (A_l B_m A_n^* A_p^* + B_l A_m B_n^* B_p^*) \mathrm{sinc}\left((\gamma_l - \gamma_m - \gamma_n - \gamma_p) L_z/2\right) \\
&\quad + (A_l B_m A_n^* B_p^* + B_l A_m B_n^* A_p^*) \mathrm{sinc}\left((\gamma_l - \gamma_m - \gamma_n + \gamma_p) L_z/2\right) \\
&\quad + (A_l B_m B_n^* A_p^* + B_l A_m A_n^* B_p^*) \mathrm{sinc}\left((\gamma_l - \gamma_m + \gamma_n - \gamma_p) L_z/2\right) \\
&\quad - (A_l B_m B_n^* B_p^* + B_l A_m A_n^* A_p^*) \mathrm{sinc}\left((\gamma_l - \gamma_m + \gamma_n + \gamma_p) L_z/2\right) \Big] \quad \text{(E.38)}
\end{aligned}$$

where $A_n = A_n(\mathbf{r};\Omega)$, $B_n = B_n(\mathbf{r};\Omega)$, $A_p = A_p(\mathbf{r};\omega_{p,n,q})$, and $B_p = B_p(\mathbf{r};\omega_{p,n,q})$. Also ξ_{nx}, ξ_{ny}, γ_n are evaluated at Ω, while ξ_{px}, ξ_{py}, γ_p are evaluated at $\omega_{p,n,q}$. Due to modal orthogonality, the quadruple modal sum in Eq. (E.37) reduces to a triple sum, $\sum_l \sum_m \sum_n \sum_p U_q^{l,m,n,p}(\omega_{m,l,q}, \omega_{p,n,q}, v_q) = \sum_l \sum_m \sum_p U_q^{l,m,l,p}(\omega_{m,l,q}, \omega_{p,l,q}, v_q)$. Further, following the reasoning of Ref. [90], Section IV B, Eq. (68), terms with $m \neq p$ are negligible compared to terms for which $m = p$ as long as the size of the resolution footprint is large enough, i.e.

$$\text{sinc}\left((\xi_{mx} - \xi_{px})\right) L_x/2) << 1, \text{ and} \tag{E.39a}$$

$$\text{sinc}\left((\xi_{my} - \xi_{py})\right) L_y/2) << 1, \tag{E.39b}$$

so that $\sum_l \sum_m \sum_p U_q^{l,m,l,p}(\omega_{m,l,q}, \omega_{p,l,q}, v_q) \approx \sum_l \sum_m U_q^{l,m,l,m}(\omega_{m,l,q}, \omega_{m,l,q}, v_q)$. An illustrative example for the length scales necessary for the above conditions to hold is presented in Fig. E-1 for the waveguide of Fig. 5-2 and the source signal and remote sensing system parameters of Table 5.2. We assume the targets are stationary and uniformly distributed over all depths, and that the mean range to the targets is 30 km. While the exact 'necessary' length scale will differ depending on the exact modal decomposition of the field, we may still conclude that the higher the frequency and the number of propagating modes, the larger the length scale required for the double sum approximation stated above to be valid.

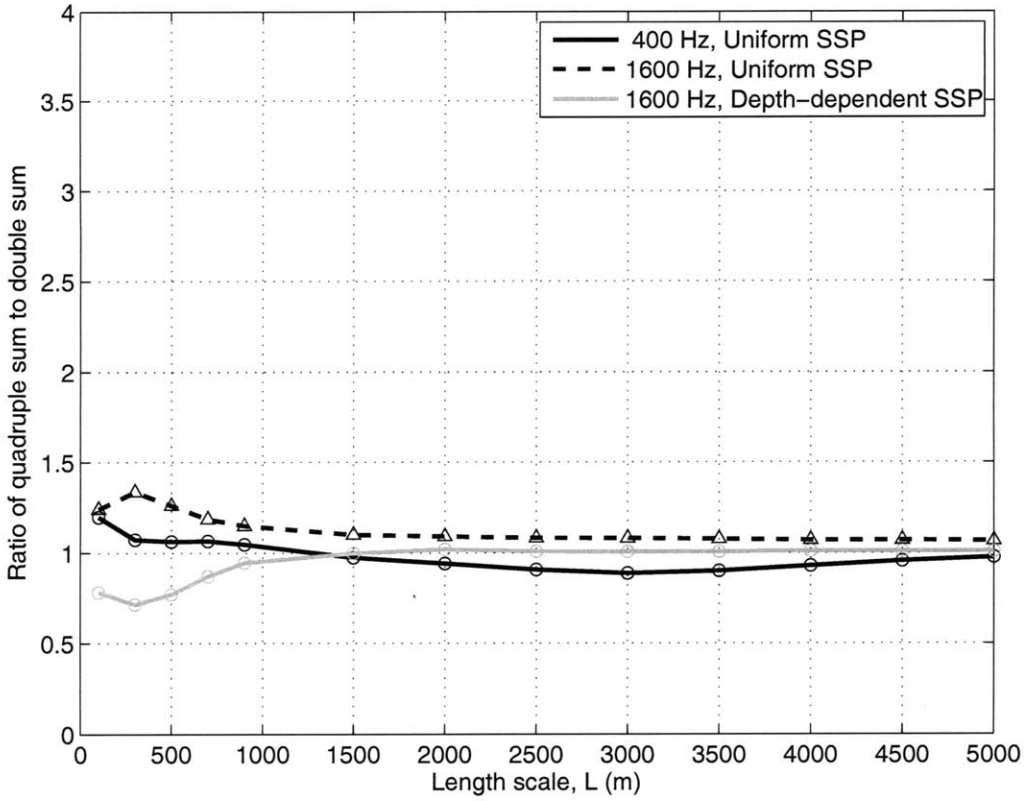

Figure E-1: Waveguide. Necessary length scales for the quadruple modal sum of Eq. (E.37) to reduce to a double modal sum, given different frequencies Ω and sound speed profiles.

Under these conditions, Eq. (E.37) simplifies to

$$\langle \Phi_{s,q}(\mathbf{r},t;\Omega)\Phi^*_{s,q}(\mathbf{r},t+\tau;\Omega)\rangle = 16\pi^2 \int \sum_l \sum_m \frac{|S(\omega_{m,l,q})|^2}{|k(\omega_{m,l,q})|^2} U_q^{l,m,l,m}(\omega_{m,l,q},\omega_{m,l,q}), \times e^{iv_q[\xi_l(\Omega)+\xi_m(\Omega)]\tau} e^{i\Omega\tau} \mathrm{d}v_q \quad \text{(E.40)}$$

E.2.2 Statistical Moments of the Ambiguity Function

For a broadband source with source function $Q(\Omega) \Leftrightarrow q(t)$, we can use Fourier synthesis to write the scattered field and its spectrum as

$$\Psi_{s,q}(\mathbf{r},t) = \frac{1}{2\pi}\int \mathrm{d}\Omega Q(\Omega)\Phi_{s,q}(\mathbf{r},t;\Omega), \quad \text{(E.41)}$$

$$\Psi_{s,q}(\mathbf{r},\omega') = \int \mathrm{d}t e^{i\omega' t}\Psi_{s,q}(\mathbf{r},t) \quad \text{(E.42)}$$

The expected values of $\Psi_{s,q}(\mathbf{r},\omega')$, and $|\Psi_{s,q}(\mathbf{r},\omega')|^2$, can then be calculated in a manner similar to the process described in Appendix E.1.2 for the free space case. The expressions are given below

$$\langle \Psi_{s,q}(\mathbf{r},\omega')\rangle = 2\frac{S(\omega')}{k(\omega')}\int \sum_l \sum_m Q(\omega'(1+v_q(1/v_l^G+1/v_m^G))^{-1}) \times U_q^{l,m}(\omega',v_q)P_v(v_q)\mathrm{d}v_q \quad \text{(E.43)}$$

$$\langle |\Psi_{s,q}(\mathbf{r},\omega')|^2\rangle = 4\frac{|S(\omega')|^2}{|k(\omega')|^2}\int \sum_l \sum_m \sum_n \sum_p Q(\omega'(1+v_q(1/v_l^G+1/v_m^G))^{-1}) \times U_q^{l,m,n,p}(\omega',\omega',v_q)Q^*(\omega'(1+v_q(1/v_n^G+1/v_p^G))^{-1})P_v(v_q)\mathrm{d}v_q \quad \text{(E.44)}$$

where v_l^G denotes the group velocity of the lth mode. Similarly, for the statistical moments of the ambiguity function, $\Psi_{s,q}(\tau,\nu)$ and $|\Psi_{s,q}(\tau,\nu)|^2$, we find

$$\langle \Psi_{s,q}(\tau,\nu)\rangle = \frac{1}{\pi}\int_{-\infty}^{\infty}\frac{S(\omega')}{k(\omega')}Q^*(\omega'-2\pi\nu)e^{-i(\omega'-2\pi\nu)\tau} \times \int \sum_l \sum_m Q(\omega'(1+v_q(1/v_l^G+1/v_m^G))^{-1})U_q^{l,m}(\omega',v_q)P_v(v_q)\mathrm{d}v_q\mathrm{d}\omega' \quad \text{(E.45)}$$

and

$$\begin{aligned}\langle|\Psi_{s,q}(\tau,\nu)|^2\rangle &= \frac{1}{\pi^2}\int_{-\infty}^{\infty}\int_{-\infty}^{\infty}\frac{S(\omega_1)}{k(\omega_1)}Q^*(\omega_1-2\pi\nu)\frac{S^*(\omega_2)}{k^*(\omega_2)}Q(\omega_2-2\pi\nu)e^{-i(\omega_1-\omega_2)\tau} \\ &\quad\times\int\sum_l\sum_m\sum_n\sum_p Q(\omega_1(1+v_q(1/v_l^G+1/v_m^G))^{-1})U_q^{l,m,n,p}(\omega_1,\omega_2,v_q) \\ &\quad\times Q^*(\omega_2(1+v_q(1/v_n^G+1/v_p^G))^{-1})P_v(v_q)\mathrm{d}v_q\mathrm{d}\omega_1\mathrm{d}\omega_2 \qquad \text{(E.46)}\end{aligned}$$

We note that the term $U_q^{l,m}$, which corresponds to the characteristic function of the random target position $\mathbf{u}_q^0$, is evaluated at different wavenumbers between Eqs. (E.45) and (E.46). As demonstrated in Section 5.2.2, evaluating $U_q^{l,m}$ near base-band typically leads to the second moment of the ambiguity function dominating over the magnitude squared of its first moment.

The total field $\Psi_s(\mathbf{r},\omega')$ is given by summing over all targets, $\Psi_s(\mathbf{r},\omega')=\sum_{q=1}^N\Psi_{s,q}(\mathbf{r},\omega')$. We assume that: (i) target positions are independent and identically distributed random variables (i.i.d.), and (ii) target speeds are also i.i.d. It then follows that $\langle\Psi_s(\tau,\nu)\rangle = N\langle\Psi_{s,q}(\tau,\nu)\rangle$, and the expected value of the magnitude squared of the ambiguity function is given by

$$\begin{aligned}\langle|\Psi_s(\tau,\nu)|^2\rangle &= \sum_{q1=1}^N\sum_{q2=1}^N\frac{1}{\pi^2}\int_{-\infty}^{\infty}\int_{-\infty}^{\infty}\frac{S(\omega_1)}{k(\omega_1)}Q^*(\omega_1-2\pi\nu)\frac{S^*(\omega_2)}{k^*(\omega_2)}Q(\omega_2-2\pi\nu)e^{-i(\omega_1-\omega_2)\tau} \\ &\quad\times\frac{1}{V^2}\int\int\int\int\sum_l\sum_m\sum_n\sum_p\Phi_{s,q1}^{l,m}(\mathbf{r},\omega_1(1+v_{q1}(1/v_l^G+1/v_m^G))^{-1},\omega_1) \\ &\quad\times Q(\omega_1(1+v_{q1}(1/v_l^G+1/v_m^G))^{-1})Q^*(\omega_2(1+v_{q2}(1/v_n^G+1/v_p^G))^{-1}) \\ &\quad\times\Phi_{s,q2}^{n,p}(\mathbf{r},\omega_2(1+v_{q2}(1/v_n^G+1/v_p^G))^{-1},\omega_2) \\ &\quad\times P_v(v_{q1})P_v(v_{q2})\mathrm{d}\mathbf{u}_{q1}^0\mathrm{d}\mathbf{u}_{q2}^0\mathrm{d}v_{q1}\mathrm{d}v_{q2}\mathrm{d}\omega_1\mathrm{d}\omega_2 \\ &= N\langle|\Psi_{s,q}(\tau,\nu)|^2\rangle + N(N-1)|\langle\Psi_{s,q}(\tau,\nu)\rangle|^2 \qquad \text{(E.47)}\end{aligned}$$

where the last line is arrived at by considering the distinction between the $q2=q1$ terms, and the $q2\neq q1$ terms. Again, the second moment of the ambiguity function for the total group of N targets consists of two terms: (i) a variance term proportional to N due to scattering from each target, and (ii) a mean-squared term proportional

to N^2 due to interaction of the fields scattered from different targets,[90] where the variance term typically dominates.[1]

E.2.3 Moments of the Ambiguity Function over Time Delay and Doppler Shift

Equations (E.45) and (E.46) cannot typically be analytically evaluated. A significant simplification is however possible in the case of specially designed source spectra that can be approximated by Eq. (5.7), $Q(\Omega) = \sum_{n'=0}^{M-1} a_{n'} e^{i(\Omega-\Omega_{n'})H_{n'}} \delta(\Omega - \Omega_{n'})$. As we show in Appendix E.3, a Costas sequence belongs in this set of signals. Equation (E.45) can then be rewritten as,

$$\begin{aligned}\langle \Psi_{s,q}(\tau,\nu)\rangle &= \sum_{n'}^{M-1}\sum_{m'}^{M-1} \frac{a^*_{n'}a_{m'}}{\pi} \int_{-\infty}^{\infty} \frac{S(\omega')}{k(\omega')} e^{-i(\omega'-2\pi\nu-\omega_{n'})H_{n'}} \delta(\omega'-2\pi\nu-\omega_{n'}) \\ &\quad \times e^{-i(\omega'-2\pi\nu)\tau} \int \sum_l \sum_m e^{i(\omega'(1+v_q(1/v_l^G+1/v_m^G))^{-1}-\omega_{m'})H_{m'}} U_q^{l,m}(\omega', v_q) \\ &\quad \times \delta(\omega'(1+v_q(1/v_l^G+1/v_m^G))^{-1}-\omega_{m'}) P_v(v_q) \mathrm{d}v_q \mathrm{d}\omega' \end{aligned} \tag{E.48}$$

Integrating over ω' introduces the delta function

$$\delta\left(v_q(1/v_l^G+1/v_m^G) - \left[\frac{\omega_{n'}+2\pi\nu}{\omega_{m'}} - 1\right]\right) \equiv \delta\left(v_q - \tilde{v}_q\right) \tag{E.49}$$

since $\omega' = \omega_{n'} + 2\pi\nu = \omega_{m'}(1 + v_q(1/v_l^G + 1/v_m^G))$, so that

$$\langle \Psi_{s,q}(\tau,\nu)\rangle = \sum_{n'}^{M-1}\sum_{m'}^{M-1} \frac{a^*_{n'}a_{m'}}{\pi} \frac{S(\omega_{n'}+2\pi\nu)}{(\omega_{n'}+2\pi\nu)/c} e^{-i\omega_{n'}\tau} \sum_l \sum_m U_q^{l,m}(\omega_{n'}+2\pi\nu, \tilde{v}_q) P_v(\tilde{v}_q) \tag{E.50}$$

Similarly, for the second moment of the ambiguity function we find,

$$\begin{aligned}\langle|\Psi_{s,q}(\tau,\nu)|^2\rangle &= \sum_{n'}^{M-1}\sum_{m'}^{M-1}\sum_{l'}^{M-1}\sum_{j'}^{M-1}\frac{a_{n'}^* a_{m'} a_{l'} a_{j'}^*}{\pi^2}\left[\frac{S(\omega_{n'}+2\pi\nu)}{(\omega_{n'}+2\pi\nu)/c}\right]\left[\frac{S^*(\omega_{l'}+2\pi\nu)}{\omega_{l'}+2\pi\nu)/c}\right] \\ &\quad\times\delta\left(\frac{\omega_{j'}}{\omega_{m'}}-\frac{\omega_{l'}+2\pi\nu}{\omega_{n'}+2\pi\nu}\right)e^{-i(\omega_{n'}-\omega_{l'})\tau} \\ &\quad\times\sum_{l}\sum_{m}\sum_{n}\sum_{p}U_q^{l,m,n,p}(\omega_{n'}+2\pi\nu,\omega_{l'}+2\pi\nu,\tilde{v}_q)P_v(\tilde{v}_q)\end{aligned} \tag{E.51}$$

where the delta function signifies that, for given ν, only specific frequency ratios result in non-zero values for $\langle|\Psi_{s,q}(\tau,\nu)|^2\rangle$.

Contrary to the free space case in Appendix E.1.3, the moments of Eq. (E.51) over time delay τ and Doppler shift ν cannot be analytically expressed as linear functions of the target's position and velocity statistical moments. This is because the characteristic function for target position is not separable from the propagation effects in a waveguide, but both are instead contained within the term $U_q^{l,m,n,p}$, which in Eq. (E.51) is also a function of the Doppler shift ν. Nevertheless, we may still expect that the moments of the ambiguity function magnitude squared over ν and τ relate to the statistics of target velocity and position, respectively. In fact, we show in Section 5.3.2 that calculations of these moments can indeed be used to obtain estimates of target velocity and position statistics.

E.2.4 Evaluating the Volume Integral

The following integral

$$\frac{1}{V}\int_V e^{i[\xi\rho+\gamma z]}\mathrm{d}^3\mathbf{r} = \frac{1}{V}2\pi\int_\rho e^{i\xi\rho}\rho\mathrm{d}\rho\int_z e^{i\gamma z}\mathrm{d}z \tag{E.52}$$

is more easily evaluated by changing into a cartesian coordinate system, where $\mathbf{k} = \xi_x\hat{\mathbf{i}}_x + \xi_y\hat{\mathbf{i}}_y + \gamma\hat{\mathbf{i}}_z$ and $\mathrm{d}^3\mathbf{r} = \mathrm{d}x\mathrm{d}y\mathrm{d}z$. If the characteristic lengths of the resolution

footprint along dimensions x, y and z are L_x, L_y and L_z respectively, then

$$\begin{aligned}\frac{1}{V}\int_V e^{i[\xi\rho+\gamma z]}\mathrm{d}^3\mathbf{r} &= \frac{1}{L_x}\int_{-L_x/2}^{L_x/2} e^{i\xi_x x}\mathrm{d}x\frac{1}{L_y}\int_{-L_y/2}^{L_y/2} e^{i\xi_y y}\mathrm{d}y\frac{1}{L_z}\int_{-L_z/2}^{L_z/2} e^{i\gamma z}\mathrm{d}z \\ &= \operatorname{sinc}\left(\frac{\xi_x L_x}{2}\right)\operatorname{sinc}\left(\frac{\xi_y L_y}{2}\right)\operatorname{sinc}\left(\frac{\gamma L_z}{2}\right) \qquad \text{(E.53)}\end{aligned}$$

so that

$$\begin{aligned}\int_V \Phi_{s,q}(\mathbf{r},t)\mathrm{d}^3\mathbf{r}_q^0 &= 4\pi\sum_l\sum_m \frac{1}{k(\omega_{m,l})}e^{-i\omega_{m,l}t} \\ &\times \operatorname{sinc}\left((\xi_{lx}+\xi_{mx})L_x/2\right)\operatorname{sinc}\left((\xi_{ly}+\xi_{my})L_y/2\right) \\ &\times \left[A_l(\mathbf{r}_0^0;\omega_l)A_m(\mathbf{r}_0^0;\omega_{m,l})S(\ldots)\times\operatorname{sinc}\left((\gamma_l-\gamma_m)L_z/2\right)\right. \\ &- A_l(\mathbf{r}_0^0;\omega_l)B_m(\mathbf{r}_0^0;\omega_{m,l})S(\ldots)\times\operatorname{sinc}\left((\gamma_l+\gamma_m)L_z/2\right) \\ &- B_l(\mathbf{r}_0^0;\omega_l)A_m(\mathbf{r}_0^0;\omega_{m,l})S(\ldots)\times\operatorname{sinc}\left((\gamma_l+\gamma_m)L_z/2\right) \\ &+ \left.B_l(\mathbf{r}_0^0;\omega_l)B_m(\mathbf{r}_0^0;\omega_{m,l})S(\ldots)\times\operatorname{sinc}\left((\gamma_l-\gamma_m)L_z/2\right)\right] \qquad \text{(E.54)}\end{aligned}$$

This represents a three-dimensional *sinc* pattern that approaches unity as L_x, L_y, $L_z \to 0$. The first zero in the x direction lies at $L_x = \lambda_x/2$, in the y direction at $L_y = \lambda_y/2$ and in the z direction at $L_z = \lambda_z/2$. The first sidelobes are 13 dB down from the mainlobe, and for $L_x \gg \lambda_x$ or $L_y \gg \lambda_y$ or $L_z \gg \lambda_z$, the integral goes to zero. In our case, L_x, L_y are on the order of 100 m and L_z on the order of 20 m, while $|\mathbf{k}|$ is on the order of 1 m^{-1}.

E.3 Signal Design

The range-velocity ambiguity function provides a graphical representation of the resolution capacity of a given signal and is typically used to quantify the signal's performance in terms of resolving target range and relative velocity from measurements of the scattered field.[66] The ambiguity function characteristics for several 'basic' signals have been reviewed extensively in literature.[47, 25, 66, 50] In terms of clutter discrimination and reverberation suppression in the presence of ambient noise, the fol-

lowing signals are among the best options: pulse trains, linear frequency modulated (LFM) signals, and pseudo-random noise signals, such as Costas sequences. Here, we describe the design of a Costas sequence signal motivated by the need to resolve the position and velocity of a large group of underwater biological targets. We assume that the desired range resolution is around 50 m, while the velocity resolution should be better than 0.2 m/s. Finally, the signal's center frequency should be on the order of hundreds of Hz or a few kHz, to allow for remote sensing on the order of tens of km.[40]

A Costas sequence is defined in terms of the number M of CW pulses in the sequence, the duration T_{cw} of each pulse, the base frequency f_b, and the sequence used to generate each CW pulse. To determine appropriate values for the above parameters, we consider the range $\Delta u = c\Delta\tau/2$, and velocity $\Delta v = c\Delta\nu/(2f_c)$ resolutions we want to achieve, where $\Delta\tau$, $\Delta\nu$ are the time-delay and Doppler shift resolutions of the signal,[66]

$$\Delta\tau = \frac{1}{B} = \frac{T_{cw}}{M}, \tag{E.55a}$$

$$\Delta\nu = \frac{1}{T_{tot}} = \frac{1}{MT_{cw}}, \tag{E.55b}$$

$f_c \equiv f_b + B/2$ is the center frequency and c is the speed of sound in the medium. Given then a Costas sequence of $M = 7$ pulses, a pulse length of $T_{cw} = 0.4$ s leads to a range resolution of approximately 43 m in water ($c = 1500$ m/s). The desired velocity resolution of 0.2 m/s or better can then be achieved by choosing $f_c = 1600$ Hz to get $\Delta v \approx 0.17$ m/s.

For this specific design of a 7-pulse Costas sequence, the total signal duration is $T_{tot} = MT_{cw} = 2.8$ s and the bandwidth is $B = M/T_{cw} \approx 20$ Hz. Each of the seven consequent pulses is a CW at frequency $f_n = f_b + \alpha_n/T_{cw}$ for $n = 0, 1, \ldots M-1$, where f_b is the signal 'base' frequency $(f_c - B/2)$, and α_n is the $(n+1)$th element of the Costas sequence, here chosen to be [4, 7, 1, 6, 5, 2, 3]. The normalized time

domain expression is given by[66]

$$q(t) = \frac{1}{\sqrt{MT_{cw}}} \sum_{n=0}^{M-1} q_n(t - nT_{cw}) \tag{E.56}$$

where

$$q_n(t) = \begin{cases} e^{-i2\pi f_n t}, & 0 \leq t \leq T_{cw} \\ 0, & \text{otherwise} \end{cases} \tag{E.57}$$

The complex signal spectrum is then given by the Fourier Transform of Eq. (E.56),

$$\begin{aligned} Q(f) &= \sqrt{\frac{T_{cw}}{M}} \sum_{n=0}^{M-1} e^{i2\pi f(nT_{cw})} e^{i2\pi(f-f_n)T_{cw}/2} \text{sinc}\left(\pi(f - f_n)T_{cw}\right) \\ &= \sum_{n=0}^{M-1} a_n e^{i2\pi(f-f_n)h_n} \text{sinc}\left(\pi(f - f_n)T_{cw}\right) \\ &\approx \sum_{n=0}^{M-1} a_n e^{i2\pi(f-f_n)h_n} \delta(f - f_n) \end{aligned} \tag{E.58}$$

where $a_n = \sqrt{\frac{T_{cw}}{M}} e^{i2\pi f_n n T_{cw}}$ and $h_n = (n + 1/2)T_{cw}$, so that Eq. (E.58) is in the form of Eq. (5.7). Note that the last line of Eq. (E.58) strictly requires $|f - f_n| > 1/T_{cw}$. It is still aproximately valid otherwise.

Appendix F

Reciprocity Examples

F.1 Plane Wave Incident on Rigid Plate

Suppose we have a rigid plate at the origin. The plate lies in the x-y plane and is of size L_x by L_y. A plane wave with direction vector k_i is incident on the rigid plate, as shown in Fig. F-1. The scattered field is given by

$$\Phi_s(\mathbf{r},t) = -\int_0^{t^+} \mathrm{d}t_\sigma \int \mathrm{d}\mathbf{S}_\sigma \cdot (\Phi_T(\mathbf{r}_\sigma,t_\sigma)\nabla_\sigma G(\mathbf{r},t|\mathbf{r}_\sigma,t_\sigma)) \tag{F.1}$$

where Φ_T equals 2 $\Phi_i|_{z=0}$ on the left hand side, and is 0 on the right hand side. Assuming the receiver is at the far field of the plate, such that $\mathbf{r} >> \mathbf{r}_\sigma$, we can write

$$\nabla_\sigma G(\mathbf{r}|\mathbf{r}_\sigma;\omega) \equiv \hat{i}_z \frac{\partial}{\partial z} G(\mathbf{r}|\mathbf{r}_\sigma;\omega) = -jk_z \hat{i}_z G(\mathbf{r}|\mathbf{0};\omega) e^{-jk\mathbf{r}_\sigma \cdot \hat{i}_r} \tag{F.2}$$

where $G(\mathbf{r}|\mathbf{r}_0;\omega)$ is the free space Green's function,

$$G(\mathbf{r}|\mathbf{r}_0;\omega) = \frac{e^{jk|\mathbf{r}-\mathbf{r}_0|}}{4\pi|\mathbf{r}-\mathbf{r}_0|} \tag{F.3}$$

which in the far field ($\mathbf{r} >> \mathbf{r}_0$) can be approximated as $G(\mathbf{r}|\mathbf{r}_0;\omega) \approx \frac{e^{jkr}}{4\pi r} e^{-j\mathbf{k}\cdot\mathbf{r}_0}$, and $\mathbf{k} \equiv k\hat{i}_r$.

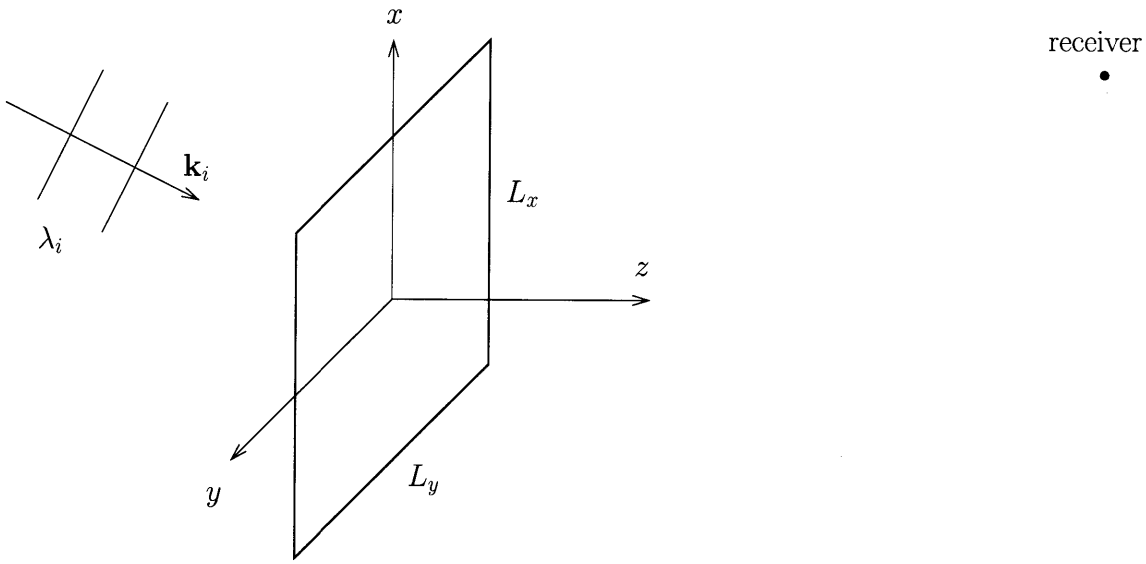

Figure F-1: Rigid plate.

For 'general' incident field, given a harmonic source of frequency Ω at position $\mathbf{r}_0$,

$$\Phi_i(\mathbf{r}_\sigma, t_\sigma) = \int_0^{t_\sigma^+} \mathrm{d}t_0 \int \mathrm{d}V_0 G(\mathbf{r}_\sigma, t_\sigma | \mathbf{r}_0, t_0) q(\mathbf{r}_0, t_0) \tag{F.4}$$

where for a stationary source, $q(\mathbf{r}_0, t_0) = e^{-j\Omega t_0}$, so that assuming the source is also in the far field ($\mathbf{r}_0 >> \mathbf{r}_\sigma$),

$$\Phi_i(\mathbf{r}_\sigma, t_\sigma) = \int_0^{t_\sigma^+} \mathrm{d}t_0 e^{-j\Omega t_0} \frac{1}{2\pi} \int_{-\infty}^{\infty} G(\mathbf{0}|\mathbf{r}_0; \omega_i) e^{-j\omega_i(t_\sigma - t_0)} e^{jk_i \mathbf{r}_\sigma \cdot \hat{i}_{r_0}} \mathrm{d}\omega_i \tag{F.5}$$

Putting it all together,

$$\begin{aligned} \Phi_s(\mathbf{r}, t) \;=\; & 2jk_z \int_0^{t^+} \mathrm{d}t_\sigma \int \mathrm{d}\mathbf{S}_\sigma \cdot \hat{i}_z \left[\int_0^{t_\sigma^+} \mathrm{d}t_0 e^{-j\Omega t_0} \frac{1}{4\pi^2} \right. \\ & \times \int_{-\infty}^{\infty} G(\mathbf{0}|\mathbf{r}_0; \omega_i) e^{-j\omega_i(t_\sigma - t_0)} e^{jk_i \mathbf{r}_\sigma \cdot \hat{i}_{r_0}} \mathrm{d}\omega_i \\ & \left. \times \int_{-\infty}^{\infty} G(\mathbf{r}|\mathbf{0}; \omega) e^{-j\omega(t - t_\sigma)} e^{-jk \mathbf{r}_\sigma \cdot \hat{i}_r} \mathrm{d}\omega \right] \end{aligned} \tag{F.6}$$

where k_i and k are evaluated at ω_i and ω, respectively, which are 'dummy' variables. Finally, for a plate moving with constant velocity v_σ in the z direction, $\mathbf{r}_\sigma = \mathbf{r}_\sigma^0 + v_\sigma t_\sigma \hat{i}_z$, where $\mathbf{r}_\sigma^0$ denotes the initial position of points on the rigid plate at time $t = 0$. The integral over t_0 introduces the delta function $\delta(\omega_i - \Omega)$.[92] Similarly, the integral over t_σ introduces the delta function $\delta(\omega - \omega_i - kv_\sigma \hat{i}_z \cdot \hat{i}_{r_0} + k_i v_\sigma \hat{i}_z \cdot \hat{i}_r)$. Integrating over ω_i and ω, we then obtain,[92, 32]

$$\Phi_s(\mathbf{r}, t) = 2j\tilde{k}_z G(\mathbf{0}|\mathbf{r}_0; \Omega) G(\mathbf{r}; \tilde{\omega}) e^{-j\tilde{\omega}t} \int \mathrm{d}\mathbf{S}_\sigma \cdot \hat{i}_z \left[e^{j\left(\frac{\Omega}{c} \mathbf{r}_\sigma^0 \cdot \hat{i}_{r_0} - \tilde{k} \mathbf{r}_\sigma^0 \cdot \hat{i}_r\right)} \right] \tag{F.7}$$

where $\tilde{k}_z$ is evaluated at $\tilde{\omega}$, and

$$\tilde{\omega} = \Omega \left(1 - \frac{v_\sigma}{c} \hat{i}_z \cdot \hat{i}_{r_0}\right) \left(1 - \frac{v_\sigma}{c} \hat{i}_z \cdot \hat{i}_r\right)^{-1} \tag{F.8}$$

The scattering function for the moving rigid plate is found by evaluating the

surface integral in Eq. (F.7) and substituting for the scattering function $S()$ in

$$\Phi_s(\mathbf{r},t) = \Phi_i(\mathbf{0},\Omega)\frac{S(\mathbf{k}_i,\mathbf{k})}{k}\frac{e^{jkr}}{r}e^{-j\omega t} \tag{F.9}$$

where $\Phi_i(\mathbf{0},\Omega) = G(\mathbf{0}|\mathbf{r}_0;\Omega)$, so that

$$S(\mathbf{k}_i,\mathbf{k}) = j\cos\theta\frac{k^2L_xL_y}{2\pi}\text{sinc}\left(\left[\frac{L_x}{2}(k_{ix}-k_x)\right]\right)\text{sinc}\left(\left[\frac{L_y}{2}(k_{iy}-k_y)\right]\right) \tag{F.10}$$

where $k_i = \Omega/c$ and k is evaluated at $\tilde{\omega}$. The scattering function is then that of a stationary rigid plate evaluated at the Doppler-shifted frequency $\tilde{\omega} \approx \Omega\left[1+\frac{v_\sigma}{c}\hat{i}_z\cdot(\hat{i}_r-\hat{i}_{r_0})\right]$. This example proves that the scattering function should be evaluated at the frequency calculated by Lai and Makris.[92]

Now we can also check reciprocity by swaping source receiver positions, reversing time and repeating the process above, whereby we have

$$\Phi_s(\mathbf{r}_0,-t_0) = -\int_{-\infty}^{-t_0^+}\mathrm{d}t_\sigma\int\mathrm{d}\mathbf{S}_\sigma\cdot(\Phi_T(\mathbf{r}_\sigma,-t_\sigma)\nabla_\sigma G(\mathbf{r}_0,-t_0|r_\sigma,-t_\sigma)) \tag{F.11}$$

where, on the left hand side of the plate

$$\Phi_T(\mathbf{r}_\sigma,-t_\sigma) = 2\Phi_i(\mathbf{r}_\sigma,-t_\sigma)|_{z=0} = 2\int_{-\infty}^{-t_\sigma^+}\mathrm{d}te^{j\Omega' t}\frac{1}{2\pi}\int_{-\infty}^{\infty}G(\mathbf{0}|\mathbf{r};\omega)e^{-j\omega(t-t_\sigma)}e^{jk\mathbf{r}_\sigma\cdot\hat{i}_r}\mathrm{d}\omega \tag{F.12}$$

for a source at $\mathbf{r}$ that is harmonic at Ω'. We can then write for the scattered field

$$\begin{aligned}\Phi_s(\mathbf{r}_0,-t_0) &= 2jk_{iz}\int_{-\infty}^{-t_0^+}\mathrm{d}t_\sigma\int\mathrm{d}\mathbf{S}_\sigma\cdot\hat{i}_z\left[\int_{-\infty}^{-t_\sigma^+}\mathrm{d}te^{j\Omega' t}\frac{1}{4\pi^2}\right.\\ &\quad\times\int_{-\infty}^{\infty}G(\mathbf{r}_0|\mathbf{0};\omega_i)e^{-j\omega_i(t_\sigma-t_0)}e^{-jk_i\mathbf{r}_\sigma\cdot\hat{i}_{r_0}}\mathrm{d}\omega_i\\ &\quad\left.\times\int_{-\infty}^{\infty}G(\mathbf{0}|\mathbf{r};\omega)e^{-j\omega(t-t_\sigma)}e^{jk\mathbf{r}_\sigma\cdot\hat{i}_r}\mathrm{d}\omega\right]\end{aligned} \tag{F.13}$$

Which expression we can evaluate for a moving plate such that $\mathbf{r}_\sigma = -v_\sigma t_\sigma\hat{i}_z$, and we

get

$$\Phi_s(\mathbf{r}_0, -t_0) = 2j\bar{k}_z \int \mathrm{d}\mathbf{S}_\sigma \cdot \hat{i}_z G(\mathbf{r}_0|\mathbf{0};\bar{\omega}) G(\mathbf{0}|\mathbf{r};\Omega') e^{j\bar{\omega}t_0} \tag{F.14}$$

where

$$\bar{\omega} = \Omega' \left(1 - \frac{v_\sigma}{c}\hat{i}_z \cdot \hat{i}_r\right)\left(1 - \frac{v_\sigma}{c}\hat{i}_z \cdot \hat{i}_{r_0}\right)^{-1} \tag{F.15}$$

Setting the source frequency equal to the received frequency at $\mathbf{r}$ from before, i.e. $\Omega' = \tilde{\omega}$, then $\bar{\omega} = \Omega$, so that

$$\Phi_s(\mathbf{r}_0, -t_0) = 2jK_z \int \mathrm{d}\mathbf{S}_\sigma \cdot \hat{i}_z G(\mathbf{r}_0|\mathbf{0};\Omega) G(\mathbf{0}|\mathbf{r};\tilde{\omega}) e^{j\Omega t_0} \tag{F.16}$$

Comparing with the expression derived earlier, we find that reciprocity is conserved, as expected. In particular, the terms inside the surface integrals are equal in both cases, so that we have

$$\frac{\Phi_s(\mathbf{r}, t)}{2j\tilde{k}_z} e^{j\tilde{\omega}t} = \frac{\Phi_s(\mathbf{r}_0, -t_0)}{2jK_z} e^{-j\Omega t_0} \tag{F.17}$$

and reciprocity holds.

F.2 Pressure Release Sphere

Bubble of radius a at distance $\mathbf{r}_c$ from the origin. We will assume it moves with velocity $\mathbf{v}_c = v_c\hat{r}_c$, where $\hat{r}_c$ lies on the x-y plane, for convenience. A plane wave is incident along direction $\hat{k}_i$, as shown in Fig. F-2. The spectrum of the field scattered from the bubble and received at position $\mathbf{r}$ can be written as

$$\Psi_s(\mathbf{r}|\mathbf{r}_c;\omega) = \frac{S(\omega)}{k} P_I(\mathbf{r}_c) \frac{e^{jk|\mathbf{r}-\mathbf{r_c}|}}{|\mathbf{r}-\mathbf{r}_c|}, \tag{F.18}$$

and the boundary condition on the surface of the bubble is

$$P_I(\mathbf{r}_c + a\hat{i}_r)\left[1 + \frac{S(\omega)}{k}\frac{e^{jka}}{a}\right] = 0 \tag{F.19}$$

so that $S(\omega) = -ka = -\omega a/c$ (because $e^{jka} \approx 1$). Making a far field approximation, i.e. $\mathbf{r} > \mathbf{r}_c$,

$$\Psi_s(\mathbf{r}|\mathbf{r}_c;\omega) = -\frac{a}{r}e^{jk_i r_0}e^{jkr}e^{j(\mathbf{k}_i - \mathbf{k})\cdot\mathbf{r}_c} \tag{F.20}$$

where $e^{jk_i r_0}$ is some 'artificial' phase that we apply to the incident plane wave for the purpose of proving reciprocity, as we show next. The position $\mathbf{r}_0$ can be thought of as the 'origin' of the plane wave, since its phase is zero at that point.

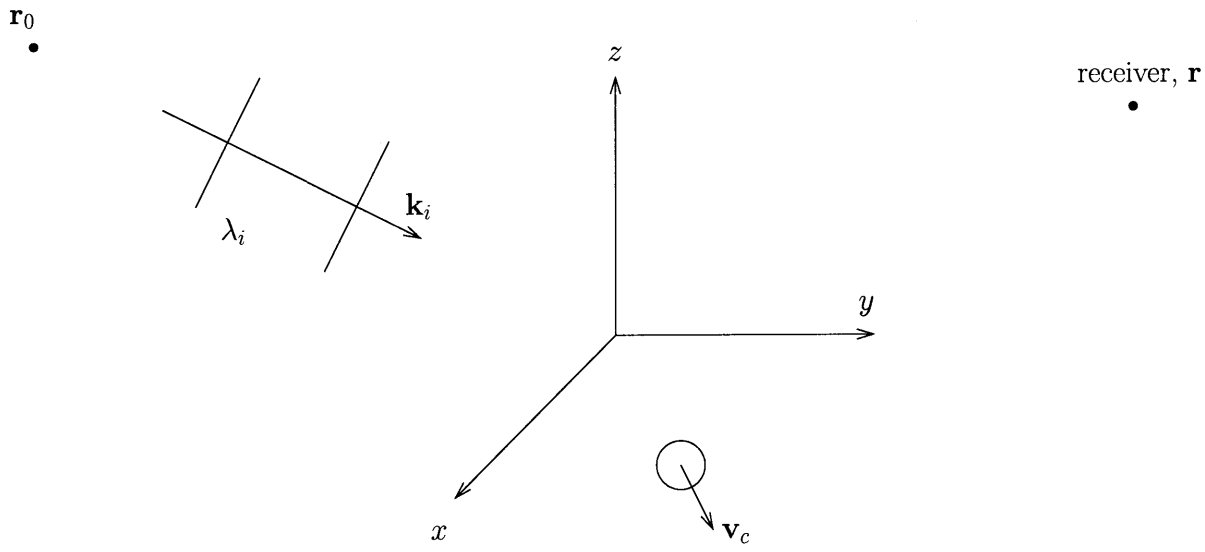

Figure F-2: Pressure release sphere.

We plug the above into Eq. C15 of [Lai and Makris] and get

$$\Phi_s(\mathbf{r},t) = \int_0^{t^+} \mathrm{d}t_c \int \mathrm{d}V_c \Psi_s(\mathbf{r},t|\mathbf{r}_c,t_c) q(\mathbf{r}_c,t_c) \tag{F.21}$$

where $q(\mathbf{r}_c,t_c) = e^{-j\omega_i t_c}\delta(\mathbf{r}_c - \mathbf{v}_c t_c)$, because we have a assumed a harmonic source at ω_i and the target moves with velocity $\mathbf{v}_c$ as described earlier. Then

$$\begin{aligned}\Phi_s(\mathbf{r},t) &= \int_0^{t^+} \mathrm{d}t_c \frac{1}{2\pi}\int_{-\infty}^{\infty} \mathrm{d}\omega \Psi_s(\mathbf{r}|\mathbf{v}_c t_c;\omega) e^{-j\omega(t-t_c)} e^{-j\omega_i t_c} \\ &= \int_0^{t^+} \mathrm{d}t_c \frac{1}{2\pi}\int_{-\infty}^{\infty} \mathrm{d}\omega \frac{S(\omega)}{kr} e^{jk_i r_0} e^{jkr} e^{-j\omega t} \left[e^{jt_c(\omega-\omega_i+(\mathbf{k}_i-\mathbf{k})\cdot\mathbf{v}_c)}\right] \end{aligned} \tag{F.22}$$

In a manner similar to that of the [Lai and Makris] paper, the integral over t_c leads to the delta function $\delta(\omega - \omega_i + (\mathbf{k}_i - \mathbf{k})\cdot\mathbf{v}_c)$, and subsequently the integral over ω results in the above expression evaluated at ω^*, where

$$\omega^* = \frac{\omega_i\left[1 - \frac{v_c}{c}\hat{k}_i\cdot\hat{r}_c\right]}{1-\frac{v_c}{c}\hat{k}\cdot\hat{r}_c} \approx \omega_i\left[1 - \frac{v_c}{c}(\hat{k}_i - \hat{k})\cdot\hat{r}_c\right] \tag{F.23}$$

So we have, finally,

$$\Phi_s(\mathbf{r}.t) = \frac{S(\omega^*)}{k^* r} e^{jk_i r_0} e^{j\omega^*(r/c-t)} \frac{1}{1-\frac{v_c}{c}\hat{k}\cdot\hat{r}_c} \tag{F.24}$$

where the last fraction is due to the delta function property, as explained in the Ffowcs Williams book (note that this terms is approximately equal to one, and in fact we neglect it in the future).

For the reciprocal problem, we evaluate the spectrum of the field scattered from the bubble at frequency ω' instead. We then have $S = -k'a$, and

$$\Psi_s(\mathbf{r}_0|\mathbf{r}_c;\omega') = -\frac{a}{r_0} e^{jk'r} e^{jk'_i r_0} e^{j(\mathbf{k}'-\mathbf{k}'_i)\cdot\mathbf{r}_c} \tag{F.25}$$

where the plane wave is now incident along vector $\hat{k}'$. The scattered field is given by

$$\begin{aligned}\Phi_s(\mathbf{r}_0,-t_0) &= \int_{-\infty}^{-t_0^+} \mathrm{d}t_c \frac{1}{2\pi}\int_{-\infty}^{\infty} \mathrm{d}\omega' \Psi_s(\mathbf{r}_0|\mathbf{v}_c t_c;\omega') e^{-j\omega'(t_c-t_0)} e^{j\omega_i' t_c} \\ &= \int_{-\infty}^{-t_0^+} \mathrm{d}t_c \frac{1}{2\pi}\int_{-\infty}^{\infty} \mathrm{d}\omega' \frac{S(\omega')}{k' r_0} e^{jk'r} e^{jk_i' r_0} e^{j\omega' t_0} \left[e^{jt_c(\omega_i'-\omega'+(\mathbf{k}_i'-\mathbf{k}')\cdot\mathbf{v}_c)}\right] \quad \text{(F.26)}\end{aligned}$$

because the source frequency is now ω_i' and the target position is now $\mathbf{r}_c = -\mathbf{v}_c t_c$. Like before we integrate over t_c and ω' to get

$$\Phi_s(\mathbf{r}_0,-t_0) = \frac{S(\tilde{\omega})}{\tilde{k} r_0} e^{j\tilde{k}_i r_0} e^{j\tilde{\omega}(r/c+t_0)} \frac{1}{1+\frac{v_c}{c}\hat{\tilde{k}}\cdot\hat{r}_c} \quad \text{(F.27)}$$

where

$$\tilde{\omega} = \frac{\omega_i'\left[1+\frac{v_c}{c}\hat{k'}_i\cdot\hat{r}_c\right]}{1+\frac{v_c}{c}\hat{k}'\cdot\hat{r}_c} \approx \omega_i'\left[1+\frac{v_c}{c}(\hat{k'}_i-\hat{k}')\cdot r_c\right] \quad \text{(F.28)}$$

Now, let ω' be the received frequency from before, i.e. $\omega' = \omega^*$. Then,

$$\tilde{\omega} = \omega_i \frac{\left[1-\frac{v_c}{c}\hat{k}_i\cdot\hat{r}_c\right]}{\left[1-\frac{v_c}{c}\hat{k}\cdot\hat{r}_c\right]} \frac{\left[1+\frac{v_c}{c}\hat{k'}_i\cdot\hat{r}_c\right]}{\left[1+\frac{v_c}{c}\hat{k}'\cdot\hat{r}_c\right]} \approx \omega_i \quad \text{(F.29)}$$

since $\hat{k}_i = \hat{k'}_i$, $\hat{k} = \hat{k}'$ because they are just unit vectors, and we have assumed small Mach numbers so that terms of the order $(v_c/c)^2$ can be neglected. We then find that the reciprocal example gives us the reverse shift in frequency, as expected: reciprocity holds!

F.3 Pressure Release Boundary

Pressure release boundary on the $x-y$ plane, moving with velocity v_B in the direction of the z-axis, as shown in Fig. F-3. A plane wave with direction vector $\mathbf{k}_i$ is incident

on this boundary at angle θ_i, so that the incident field *on the boundary* is given by

$$P_i(\mathbf{r}_B;\omega_i) = e^{jk_{iz}z_B}e^{jk_{ix}x_B} \tag{F.30}$$

where subscript B denotes a point on the boundary and we have neglected the y direction without loss of generality. The reflected field is a plane wave propagating along direction $\mathbf{k} = k_{ix}\hat{i}_x - k_z\hat{i}_z$ at reflection angle θ_R and frequency ω,

$$P_R(\mathbf{r};\omega) = RP_i(\mathbf{r}_B;\omega_i)e^{-jk_z(z-z_B)}e^{jk_{ix}x} \tag{F.31}$$

where $R = -1$ is the reflection coefficient that satisfies the boundary condition ($P_i + P_R = 0$) on ($\mathbf{r} = \mathbf{r}_B$).

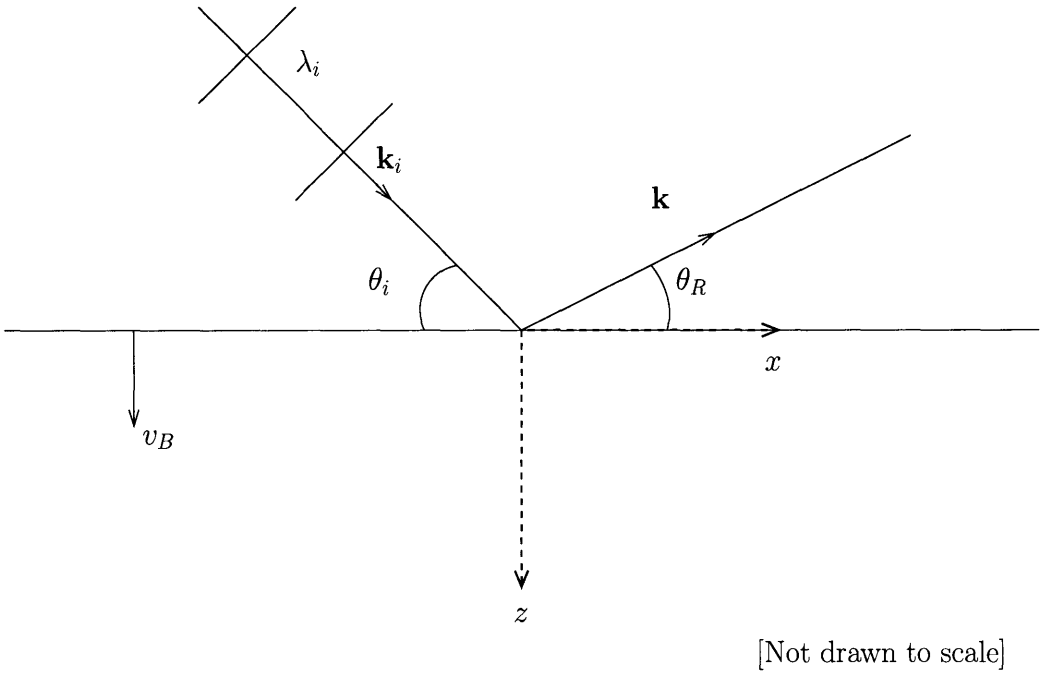

Figure F-3: Pressure release boundary.

Plugging into Eq. C15 of [Lai and Makris], we find

$$\Phi_s(\mathbf{r},t) = \int_0^{t^+} \mathrm{d}t_B \int \mathrm{d}S_B P_R(\mathbf{r},t|\mathbf{r}_B,t_B) q(\mathbf{r}_B,t_B) \tag{F.32}$$

where the source term is $q(\mathbf{r}_B,t_B) = e^{-j\omega_i t_B}\delta(\mathbf{r}_B - v_B t_B \hat{i}_z)$, so that

$$\Phi_s(\mathbf{r},t) = \int_0^{t^+} \mathrm{d}t_B \frac{1}{2\pi} \int_{-\infty}^{\infty} \mathrm{d}\omega e^{-j\omega(t-t_B)} \left[-e^{jk_{iz}v_B t_B} e^{-jk_z z} e^{jk_z v_B t_B} e^{-j\omega_i t_B} e^{jk_{ix}(x_B+x)} \right] \tag{F.33}$$

The integral over t_B then leads to the delta function $\delta(\omega - \omega_i + k_{iz}v_B + k_z v_B)$, so that integrating over ω, we get

$$\Phi_s(\mathbf{r},t) = -e^{-j\omega^* t} e^{j\frac{\omega^*}{c}[(x+x_B)\cos\theta_R - z\sin\theta_R]} \tag{F.34}$$

where

$$\omega^* = \frac{\omega_i \left[1 - \frac{v_B}{c}\sin\theta_i\right]}{1 + \frac{v_B}{c}\sin\theta_R} \approx \omega_i \left[1 - \frac{v_B}{c}\sin\theta_i - \frac{v_B}{c}\sin\theta_R\right] \tag{F.35}$$

Notice that the reflection angle is different from the incident angle because of the moving boundary,

$$\omega_i \cos\theta_i = \omega^* \cos\theta_R \tag{F.36}$$

For the reciprocal problem, we define a plane wave incident on the pressure release boundary along direction $\mathbf{k}'_i = -k'_{ix}\hat{i}_x + k'_{iz}\hat{i}_z$, at frequency ω'_i, so that the *incidence* angle is θ_R. The reflected field propagates along direction $\mathbf{k}' = -k'_{ix}\hat{i}_x - k'_z\hat{i}_z$ at reflection angle θ' and frequency ω', so that for a receiver in the far-field

$$P'_R(\mathbf{r}_0;\omega') = -e^{-jk'_{ix}(x_B+x_0)} e^{jk'_{iz}z_B} e^{-jk'_z(z_0-z_B)} \tag{F.37}$$

where $z_B = v_B t_B$. Reversing time also, the scattered field is given by

$$\begin{aligned}\Phi_s(\mathbf{r}_0, -t_0) &= \int_{-\infty}^{-t_0^+} \mathrm{d}t_B \frac{1}{2\pi} \int_{-\infty}^{\infty} \mathrm{d}\omega' e^{-j\omega'(t_B - t_0)} \left[-e^{jk'_{iz} v_B t_B} e^{-jk'_z z_0} e^{jk'_z v_B t_B} e^{j\omega'_i t_B} e^{-jk'_{ix}(x_B + x_0)} \right] \\ &= -e^{j\tilde{\omega} t_0} e^{j\frac{\tilde{\omega}}{c}[-(x_0 + x_B)\cos\theta' - z_0 \sin\theta']} \end{aligned} \tag{F.38}$$

where

$$\tilde{\omega} = \frac{\omega'_i \left[1 + \frac{v_B}{c} \sin\theta_R\right]}{1 - \frac{v_B}{c}\sin\theta'} \approx \omega'_i \left[1 + \frac{v_B}{c}\sin\theta_R + \frac{v_B}{c}\sin\theta'\right] \tag{F.39}$$

where $\omega'_i \cos\theta_R = \tilde{\omega}\cos\theta'$. If we now set the frequency of the incident wave to that of the received wave in the previous example, i.e. $\omega'_i = \omega^*$, then $\omega^* \cos\theta_R = \omega_i \cos\theta_i$ from before, and

$$\tilde{\omega} = \frac{\omega_i \cos\theta_i}{\cos\theta'} \tag{F.40}$$

$$\tilde{\omega} = \frac{\omega_i \left[1 - \frac{v_B}{c}\sin\theta_i\right]}{1 - \frac{v_B}{c}\sin\theta'} \tag{F.41}$$

whereby $\theta' = \theta_i$ and $\tilde{\omega} = \omega_i$, i.e. we get the reverse shift in frequency and reciprocity holds.

Bibliography

[1] M. Andrews, Z. Gong, and P. Ratilal. High resolution population density imaging of random scatterers with the matched filter scattered field variance. *J. Acoust. Soc. Am.*, 126:1057–1068, 2009.

[2] H. H. Arsenault and G. April. Properties of speckle integrated with a finite aperture and logarithmically transformed. *J. Opt. Soc. Am.*, 66:1160–1163, 1976.

[3] A. B. Baggeroer, W. A. Kuperman, and P. N. Mikhalevsky. An overview of matched field methods in ocean acoustics. *IEEE J. Ocean. Eng.*, 18:401–424, 1993.

[4] A. B. Baggeroer, W. A. Kuperman, and Henrik Schmidt. Matched field processing: Source localization in correlated noise as an optimum parameter estimation problem. *J. Acoust. Soc. Am.*, 83:571–587, 1988.

[5] O. E. Barndorff-Nielsen and D. R. Cox. *Inference and Asymptotics.* Chapman and Hall, London, 1994.

[6] J. F. III Bell, M. S. Rice, J. R. Johnson, and T. M. Hare. Surface albedo observations at gusev crater and meridiani planum, mars. *J. Geophys. Res.*, 113:E06S18, 2008.

[7] J. W. Bergstrom, W. A. Delamere, and A. McEwen. Mro high resolution imaging science experiment (hirise): Instrument test, calibration and operating constraints. 55th International Astronautic Federation Congress, IAC-04-Q.3.b.02, unpublished, 2004.

[8] Ioannis Bertsatos and Nicholas C. Makris. Statistical biases and errors inherent in photoclinometric surface slope estimation with natural light. *Icarus*, in press.

[9] D. P. Bertsekas and J. N. Tsitsiklis. *Introduction to Probability.* Athena Scientific, Belmont, MA, 2nd edition, 2008.

[10] M. Betke, D. E. Hirsh, N. C. Makris, G. F. McCracken, M. Procopio, N. I. Hristov, S. Tang, A. Bagchi, J. Reichard, J. Horn, S. Crampton, C. J. Cleveland, and T. H. Kunz. Thermal imaging reveals significantly smaller brazilian free-tailed bat colonies than previously estimated. *Journal of Mammalogy*, 89:18–24, 2008.

[11] M. Betke and N. Makris. Recognition, resolution and complexity of objects subject to affine transformation. *Int. J. Comput. Vis.*, 44:5–40, 2001.

[12] R. A. Beyer, A. S. McEwen, and R. L. Kirk. Meter-scale slopes of candidate mer landing sites from point photoclinometry. *J. Geophys. Res.*, 108:8085, 2003.

[13] E. Bonabeau, G. Theraulaz, J.-L. Deneubourg, S. Aron, and S. Camazine. Self-organization in social insects. *Trends Ecol. Evol.*, 12:188–193, 1997.

[14] M. Born and E. Wolf. *Principles of Optics.* Cambridge University Press, Cambridge, U.K., 7th edition, 1999.

[15] L. M. Brekhovskikh and Y. Lysanov. *Fundamentals of Ocean Acoustics.* Springer, New York, 3rd edition, 2003.

[16] N. T. Bridges and K. E. Herkenhoff. Topography and geologic characteristics of aeolian grooves in the south polar layered deposits of mars. *Icarus*, 156:387–398, 2002.

[17] D. Brillinger. The calculation of cumulants via conditioning. *Annals of the Institute of Statistical Mathematics*, 21:215–218, 1969.

[18] H. P. Bucker and Halcyon E. Morris. Normal-mode reverberation in channels or ducts. *J. Acoust. Soc. Am.*, 44:827–828, 1968.

[19] S. Camazine, J. L. Deneubourg, N. R. Franks, J. Sneyd, G. Theraulaz, and E. Bonabeau. *Self-organization in biological systems. Princeton studies in complexity.* Princeton University Press, Princeton, NJ, 2001.

[20] B. A. Cantor, P. B. James, M. Caplinger, and M. J. Wolff. Martian dust storms: 1999 mars orbiter camera observations. *J. Geophys. Res.*, 106:23653–23687, 2001.

[21] T. Chen, P. Ratilal, and N. C. Makris. Mean and variance of the forward field propagated through three-dimensional random internal waves in a continental-shelf waveguide. *J. Acoust. Soc. Am.*, 118:3560–3574, 2005.

[22] Tianrun Chen. *Mean, Variance, and Temporal Coherence of the 3D Acoustic Field Forward Propagated through Random Inhomogeneities in Continental-shelf and Deep Ocean Waveguides.* PhD thesis, Massachusetts Institute of Technology, February 2009.

[23] S. D. Chuprov. Interference structure of a sound field in a layered ocean. In L. M. Brekhovskikh and I. B. Andreevoi, editors, *Acoustics of the Ocean: Current Status (in Russian)*, pages 71–91. Nauka, Moscow, 1982.

[24] M. D. Collins and W. A. Kuperman. Focalization: Environmental focusing and source localization. *J. Acoust. Soc. Am.*, 90:1410–1422, 1991.

[25] T. Collins and P. Atkins. Doppler-sensitive active sonar pulse designs for reverberation processing. *IEEE Proc-Radar. Sonar Navig.*, 145(6):347–353, 1998.

[26] M. V. Trevorrow D. M. Farmer and B. Pedersen. Intermediate range fish detection with a 12-khz sidescan sonar. *J. Acoust. Soc. Am.*, 106:2481–2490, 1999.

[27] J. C. Dainty, editor. *Laser Speckle and Related Phenomena.* Springer-Verlag, Berlin, 2nd edition, 1984.

[28] P. A. Davis and A. S. McEwen. Photoclinometry: Analysis of inherent errors and implications for topographic measurements. *Planet. Sci.*, IV:194–195, 1984.

[29] P. A. Davis and L. A. Soderblom. Modeling crater topography and albedo from monoscopic viking orbiter images, 1. methodology. *J. Geophys. Res.*, 89:9449–9457, 1984.

[30] O. Diachok, A. Caiti, P. Gerstoft, and H. Schmidt, editors. *Full Field Inversion Methods in Ocean and Seismic Acoustics.* Kluwer, Dordrecht, 1995.

[31] Richard J. Doviak, Dusan S. Zrnic, and Dale S. Sirmas. Doppler weather radar. In *Proceedings of the IEEE*, volume 67, 1979.

[32] A. P. Dowling and J. E. Ffowcs Williams. *Sound and Sources of Sound.* Horwood, Chichester, 1983.

[33] S. A. Drury. *Image interpretation in Geology.* Chapman and Hall, 2nd edition, 1993.

[34] J. A. Dunne. Mariner 1969 television image processing. *Pattern Recognition*, 2:261–266, 1970.

[35] E. Eastwood. *Radar Ornithology.* Methuen, London, 1967.

[36] N. D. Efford. Sources of error in the photoclinometric determination of planetary topography: A reappraisal. *Earth Moon Planets*, pages 19–58, 1991.

[37] W. G. Egan. *Optical Remote Sensing Science and Technology.* Marcel Dekker, Inc., 2004.

[38] Nicholas C. Makris et al. Fish population and behavior revealed by instataneous continental shelf-scale imaging. *Science*, 311:660–663, 2006.

[39] Nicholas C. Makris et al. Critical population density triggers rapid formation of vast oceanic fish shoals. *Science*, 323:1734–1737, 2009.

[40] S. Jagannathan et al. Ocean acoustic waveguide remote sensing (oawrs) of marine ecosystems. *Mar. Ecol. Prog. Ser.*, 395:137–160, 2009.

[41] J. A. Fawcett and B. H. Maranda. Localization accuracies for a moving source in an oceanic waveguide. *J. Acoust. Soc. Am.*, 96:1047–1055, 1994.

[42] John A. Fawcett, M. L. Yeremy, and N. R. Chapman. Matched-field source localization in a range-dependent environment. *J. Acoust. Soc. Am.*, 99:272–282, 1996.

[43] Laurie T. Fialkowski, Michael D. Collins, Josh S. Perkins, and W. A. Kuperman. Source localization in noisy and uncertain ocean environments. *J. Acoust. Soc. Am.*, 101:3539–3545, 1997.

[44] R. A. Fisher. *Statistical Methods and Scientific Inference.* Hafner, New York, 1956.

[45] A. E. Gill. *Atmosphere-Ocean Dynamics.* Academic Press, San Diego, 1982.

[46] D. F. Gingras. Methods for predicting the sensitivity of matched-field processors to mismatch. *J. Acoust. Soc. Am.*, 86:1940–1949, 1989.

[47] Tildon H. Glisson and Andrew P. Sage. On sonar signal analysis. *IEEE Transactions on Aerospace and Electronic Systems*, AES-6(1):37–50, 1969.

[48] J. W. Goodman. Statistical properties of laser speckle patterns. In J. C. Dainty, editor, *Laser Speckle and Related Phenomena*, pages 9–75. Springer-Verlag, Berlin, 2nd edition, 1984.

[49] J. W. Goodman. *Statistical Optics.* Wiley, New York, 1985.

[50] Simon Haykin, Brian Currie, and Thia Kirubarajan. Adaptive radar for improved small target detection in a maritime environment. Technical Report 03-01, DRDC Ottawa, April 2003.

[51] J. Hillier, P. Helfenstein, and J. Veverka. Miranda: Color and albedo variations from voyager photometry. *Icarus*, 82:314–335, 1989.

[52] D. J. Hoare, G. D. Ruxton, J.-G. J. Godin, and J. Krause. The social organization of free-ranging fish shoals. *Oikos*, 89:546–554, 2000.

[53] B. K. P. Horn. *Robot Vision.* MIT Press, Cambridge, 1986.

[54] A. D. Howard. Photoclinometric determination of the topography of the martian north polar cap. *Icarus*, 50:245–258, 1982.

[55] I. Huse and E. Ona. Tilt angle distribution and swimming speed of overwintering norwegian spring spawning herring. *ICES J. Mar. Sci.*, 53:863–873, 1996.

[56] J. R. Janesick. *Scientific Charge-Coupled Devices.* SPIE Press, 2001.

[57] D. G. Jankowski and S. W. Squyres. Sources of error in planetary photoclinometry. *J. Geophys. Res.*, 196:20907–20922, 1991.

[58] F. B. Jensen, W. A. Kuperman, M. B. Porter, and H. Schmidt. *Computational Ocean Acoustics.* American Institute of Physics, New York, 1994.

[59] Shahab Kalantar and Uwe R. Zimmer. Distributed shape control of homogeneous swarms of autonomous underwater vehicles. *Auton. Robot*, 22:37–53, 2007.

[60] S. M. Kay. *Fundamentals of Statistical Signal Processing: Estimation Theory.* Prentice Hall, New Jersey, 1993.

[61] R. L. Kirk, J. M. Barrett, and L. A. Soderblom. Photoclinometry made simple...? In *Advances in Planetary Mapping*, Houston, 2003.

[62] R. L. Kirk, E. Howington-Kraus, B. Redding, D. Galuszka, T. M. Hare, B. A. Archinal, L. A. Soderblom, and J. M. Barrett. High-resolution topomapping of candidate mer landing sites with mars orbiter camera narrow-angle images. *J. Geophys. Res.*, 1080:8088, 2003.

[63] R. L. Kirk, K. T. Thompson, and E. M. Lee. Photometry of the martian atmosphere: An improved practical model for cartography and photoclinometry. In *Lunar Planet. Sci. XXXII*, 2001.

[64] W. A. Kuperman and J. F. Lynch. Shallow-water acoustics. *Phys. Today*, 11:55–61, 2004.

[65] Sunwoong Lee and Nicholas C. Makris. The array invariant. *J. Acoust. Soc. Am.*, 119:336–351, 2006.

[66] Nadav Levanon. *Radar Principles.* John Wiley & Sons, New York, 1988.

[67] J. Lighthill. *Waves in Fluids.* Cambridge University Press, Cambridge, 1978.

[68] E. Naftali M. Zanolin and N. Makris. Second order bias of a multivariate gaussian maximum likelihood estimate with chain-rule for higher moments. Technical report, Massachusetts Institute of Technology, 2001.

[69] David N. MacLennan and D. V. Holliday. Fisheries and plankton acoustics: past, present, and future. *ICES J. Mar. Sci.*, 53:513–516, 1996.

[70] N. C. Makris. A foundation for logarithmic measures of fluctuating intensity in pattern recognition. *Optics Lett.*, 20:2012–2014, 1995.

[71] N. C. Makris. The effect of saturated transmission scintillation on ocean acoustic intensity measurements. *J. Acoust. Soc. Am.*, 100:769–783, 1996.

[72] N. C. Makris. Parameter resolution bounds that depend on sample size. *J. Acoust. Soc. Am.*, 99:2851–2861, 1996.

[73] N. C. Makris. Estimating surface orientation from sonar images. In *SACLANT Conference Proceedings Series CP-45*, pages 339–346, 1997.

[74] N. C. Makris, F. Ingenito, and W. A. Kuperman. Detection of a submerged object insonified by surface noise in an ocean waveguide. *J. Acoust. Soc. Am.*, 96:1703–1724, 1994.

[75] Nicholas C. Makris, Purnima Ratilal, Yisan Lai, Sunwoong Lee, Deanelle T. Symonds, Lilimar A. Ruhlmann, Redwood W. Nero, John R. Preston, Edward K. Scheer, and Michael T. Sundvik. Long-range acoustic imaging of the continental shelf environment reveals massive fish schools: 2003 main acoustic clutter experiment. *J. Acoust. Soc. Am.*, 114:2375, 2003.

[76] M. C. Malin, G. E. Danielson, A. P. Ingersoll, H. Masursky, J. Veverka, M. A. Ravine, and T. A. Soulanille. Mars observer camera. *J. Geophys. Res.*, 97:7699–7718, 1992.

[77] M. C. Malin and K. S. Edgett. Mars global surveyor mars orbiter camera: Interplanetary cruise through primary mission. *J. Geophys. Res.*, 106:23429–23570, 2001.

[78] L. Mandel. Fluctuations of photon beams: The distribution of photo-electrons. *Proc. Phys. Soc.*, 74:233–243, 1959.

[79] R. McCluney. *Introduction to Radiometry and Photometry.* Artech House, Massachusetts, 1994.

[80] P. McCullagh. *Tensor Methods in Statistics (Monographs on Statistics and Applied Probability).* Chapman and Hall, London, 1987.

[81] A. McEwen and 14 colleagues. Mro's high resolution imaging science experiment (hirise): Science expectations. In *6th International Conference on Mars*, Pasadena, California, 2003.

[82] A. S. McEwen. Exogenic and endogenic albedo and color patterns on europa. *J. Geophys. Res.*, 91:8077–8097, 1986.

[83] A. S. McEwen. Photometric functions for photoclinometry and other applications. *Icarus*, 92:298–311, 1991.

[84] E. Naftali and N. C. Makris. Necessary conditions for a maximum likelihood estimate to become asymptotically unbiased and attain the cramerrao lower bound. part i. general approach with an application to time-delay and doppler shift estimation. *J. Acoust. Soc. Am.*, 110:1917–1930, 2001.

[85] T. Pitcher O. A. Misund, A. Ferno and B. Totland. Tracking herring schools with a high resolution sonar. variations in horizontal area and relative echo intensity. *ICES J. Mar. Sci.*, 55:58–66, 1998.

[86] G. Parry. Speckle patterns in partially coherent light. In J. C. Dainty, editor, *Laser Speckle and Related Phenomena*, pages 77–122. Springer-Verlag, Berlin, 2nd edition, 1984.

[87] C. A. Poynton. 'gamma' and its disguises: The nonlinear mappings of intensity in perception, crts, film and video. *SMPTE Journal*, 1993.

[88] K. J. Ranson, J. R. Irons, and C. S. T. Daughtry. Surface albedo from bidirectional reflectance. *Remote Sens. Environ.*, 35:201–211, 1991.

[89] C. R. Rao. *Linear Statistical Inference and its Applications.* Wiley, New York, 1966.

[90] P. Ratilal and N. C. Makris. Mean and covariance of the forward field propagated through a stratified ocean waveguide with three-dimensional random inhomogeneities. *J. Acoust. Soc. Am.*, 118:3532–3559, 2005.

[91] Yi san Lai and Nicholas C. Makris. Estimating the velocity of a moving object submerged in an ocean waveguide with active sonar. *J. Acoust. Soc. Am.*, 112:2407, 2002.

[92] Yi san Lai and Nicholas C. Makris. Spectral and modal formulations for the doppler-shifted field scattered by an object moving in a stratified medium. *J. Acoust. Soc. Am.*, 113:223–244, 2003.

[93] P. Schenk. Landing site characteristics for europa 1: Topography. In *Lunar Planet. Sci. XXXVI*, 2005.

[94] Henrik Schmidt, A. B. Baggeroer, W. A. Kuperman, and E. K. Scheer. Environmentally tolerant beamforming for high-resolution matched field processing: Deterministic mismatch. *J. Acoust. Soc. Am.*, 88:1851–1862, 1990.

[95] L. R. Shenton and K. O. Bowman. *Maximum Likelihood Estimation in Small Samples.* Griffin, New York, 1977.

[96] J. A. Shorey and L. W. Nolte. Wideband optimal a posteriori probability source localization in an uncertain shallow ocean environment. *J. Acoust. Soc. Am.*, 103:355–361, 1998.

[97] G. B. Smith, H. A. Chandler, and C. Feuillade. Performance stability of high-resolution matched-field processors to sound-speed mismatch in a shallow-water environment. *J. Acoust. Soc. Am.*, 93:2617–2626, 1993.

[98] Cristiano Soares and Sergio M. Jesus. Broadband matched-field processing: Coherent and incoherent approaches. *J. Acoust. Soc. Am.*, 113:2587–2598, 2003.

[99] D. J. T. Sumpter. The principles of collective animal behaviour. *Phil. Trans. R. Soc. B*, 361:5–22, 2005.

[100] Deanelle T. Symonds, Purnima Ratilal, Redwood W. Nero, and Nicholas C. Makris. Fish schools are the dominant cause of long-range active sonar clutter in the new jersey continental shelf: Quantitative correlations. *J. Acoust. Soc. Am.*, 114:2375, 2003.

[101] T. L. Szabo. *Diagnostic Ultrasound Imaging: Inside Out.* elsevier Science, Boston, 2004.

[102] A. Thode, M. Zanolin, E. Naftali, I. Ingram, P. Ratilal, and N. C. Makris. Necessary conditions for a maximum likelihood estimate to become asymptotically unbiased and attain the cramerrao lower bound. part ii. range and depth localization of a sound source in an ocean waveguide. *J. Acoust. Soc. Am.*, 112:1890–1910, 2002.

[103] A. Tolstoy. Sensitivity of matched field processing to sound speed profile mismatch for vertical arrays in a deep water pacific environment. *J. Acoust. Soc. Am.*, 85:2394–2404, 1989.

[104] L. L. Van Trees. *Detection, Estimation and Modulation Theory*, volume IV. Wiley, New York, 1970.

[105] Robert J. Urick. *Principles of Underwater Sound.* McGraw-Hill, New York, 1983.

[106] H. C. van du Hulst. *Light Scattering by Small Particles.* Dover, New York, 1981.

[107] Evan K. Westwood. Broadband matched-field source localization. *J. Acoust. Soc. Am.*, 91:2777–2789, 1992.

[108] Wen Xu, Arthur B. Baggeroer, and Henrik Scmidt. Performance analysis for matched-field source localization: Simulations and experimental results. *IEEE Journal of Oceanic Engineering*, 31:325–344, 2006.

[109] M. Zanolin, S. Vitale, and N. Makris. Asymptotic expansions of maximum likelihood estimators errors, with an application to gravitational waves generated in the inspiral phase of binary mergers, 2009. arXiv:0912.0065v2 [gr-qc].

[110] Michele Zanolin, Ian Ingram, Aaron Thode, and Nicholas C. Makris. Asymptotic accuracy of geoacoustic inversions. *J. Acoust. Soc. Am.*, 116:2031–2042, 2004.

[111] Renhe Zhang, Zhenglin Li, Jin Yan, Zhaohui Peng, and Fenghua Li. Broadband matched-field source localization in the east china sea. *IEEE J. Oceanic Eng.*, 29:1049–1054, 2004.